Clumped isotopes in planktonic foraminifera: application in a multiproxy North Atlantic study

Stuart Umbo

PhD Thesis

University of East Anglia
School of Environmental Sciences
2020

Abstract

Robust experimental protocols for the clumped isotope analysis of foraminifera are established using the University of East Anglia's Multi-Isotopologue-Ratio-Analyser (MIRA). Key advances include sample cleaning and preparation, development of a corrective algorithm to overcome a persistent sample size effect, and optimisation of standard measurements for projection of Δ47 values onto the absolute reference frame.

A foraminifera clumped isotope temperature calibration is derived through measurement of 25 Atlantic core top samples:

$$\Delta 47 = 0.0314\ (\pm 0.0027) \times \frac{10^6}{T^2} + 0.3171\ (\pm 0.0332)$$

The calibration shows good agreement with previous studies. However, measurement uncertainty remains too large for reliable temperature reconstructions.

In addition, a high-resolution, multiproxy study of North Atlantic core MD99-2251 is conducted, offering exceptional resolution through MIS 4 – 2. It shows highly variable surface temperatures with numerous cold excursions. Comparison with nearby benthic $\delta^{13}C$ records has provided additional detail on the relationship between ice rafting and oceanic ventilation. The AMOC shows evidence of suppression following H10, H6 and H4.

The new ice rafting record has provided enhanced detail on specific Heinrich Stadial events, offering improved clarity on the timing and nature of H3 and H6 — as well as showing H5a, H7a, and H7b exhibit suppressed magnitude in comparison to other Heinrich events. The onset of cooling is shown to precede ice rafting, supporting the growing body of evidence that Greenland cooling acted as a driver of ice rafting, as opposed to being a symptom of it.

Finally, a new multispecies stable isotope record of core U1302 from the Labrador Sea is presented, offering improved resolution and timing restraints on the Termination II transition and MIS 5e Plateau. Short lived isotopic excursions during Termination II reveal a 'step-like' transition. Comparison of the isotopic signatures of epipelagic and mesopelagic foraminifera species support earlier findings of a highly stratified water mass during the last interglacial.

Access Condition and Agreement

Each deposit in UEA Digital Repository is protected by copyright and other intellectual property rights, and duplication or sale of all or part of any of the Data Collections is not permitted, except that material may be duplicated by you for your research use or for educational purposes in electronic or print form. You must obtain permission from the copyright holder, usually the author, for any other use. Exceptions only apply where a deposit may be explicitly provided under a stated licence, such as a Creative Commons licence or Open Government licence.

Electronic or print copies may not be offered, whether for sale or otherwise to anyone, unless explicitly stated under a Creative Commons or Open Government license. Unauthorised reproduction, editing or reformatting for resale purposes is explicitly prohibited (except where approved by the copyright holder themselves) and UEA reserves the right to take immediate ‘take down’ action on behalf of the copyright and/or rights holder if this Access condition of the UEA Digital Repository is breached. Any material in this database has been supplied on the understanding that it is copyright material and that no quotation from the material may be published without proper acknowledgement.

Contents

Figures

Tables

Acknowledgements

The last four years has been an amazing journey. I've learnt so much, worked with some incredible people, and finished uncountable mugs of coffee. In years to come, I'll look back with fondness. So before the memories of torment and pain fade completely, I'd like to say thank you to those that helped me get through — especially when I doubted I ever would.

First, I'd like to thank my three supervisors: Mark, Paul and Alina. Your wealth of knowledge and expertise never fails to amaze me. Mark – thank you for always being positive in the face of setbacks and for your constant encouragement. Your intellectual rigour challenged me to delve deeper into the literature and think in new ways. I know this thesis is better for it. Paul – without your drive and vision MIRA wouldn't exist! Thank you for solving so many of my laboratory woes. I'll miss chatting about sixties psychedelia and commiserating over Spurs. A couple more seasons and Barnet will be challenging Charlton! Alina – thank you for your patience, for putting up with my gripes, and for always being there to lend a hand. For all the hours you've been with me in the lab and the hours beyond. No task is too big. Thank you.

Thank you to all those who have supported me in the lab with their expertise and guidance, especially Bertie Leze, Graham Chilvers and Andy McDonald — and to Ruth Kirk and Leila Hume for your support and guidance, having trodden this path before me.

I am indebted to those who have kindly given data to this project, particularly Mark Chapman, Leila Hume, Liz Farmer, Katie Miller and Christopher Ellison for their work on MD99-2251, alongside Claude Hillaire-Marcell, Stephanie Kaboth and Leila Hume for their work on U1302.

Thank you to the office gang: Dan, Denis, Helen, Marina, Michael, Peter, Philip and Ryan. I couldn't have asked for a better bunch to be around every day. Special thanks to Philip for letting me sleep on his sofa after uncountable late nights in the lab.

Finally, I'd like to thank the University of East Anglia and all those at EnvEast, as well as the Natural Environment Research Council for supporting this study.

Chapter 1. Introduction

The climate underpins countless aspects of human society. Our architecture, agricultural systems, disaster preparedness, diet, infrastructure and countless other aspects of our culture have all been shaped by the particular climate in which we live. The relative climatic stability of the Holocene has allowed human civilisation to flourish and global population to expand to unprecedented levels. Yet anthropogenic climate change over the coming decades and centuries threatens these climatically fine-tuned elements of society that have developed over thousands of years.

The extent of societal impacts, and humanity's preparedness for the forthcoming climatic changes, rely heavily on our ability to predict how the climate will evolve under anthropogenic forcing. Looking to the past can provide context to constrain model projections and provide historical analogies to the modern day.

No study of the climate would be complete without a look to the oceans, which play a major role in transporting and distributing heat through the thermohaline circulation. This vast global conveyor carries volumes of water equivalent to 20 times the combined discharge from all the world's rivers (Broeker, 1991). In the Atlantic, heat is transported from the equator to the high latitudes, where it is released to the atmosphere from surface waters before they sink to the abyss.

Changes in this oceanic circulation have played a major role in the millennial scale (e.g. Barber et al., 1999; Clark et al., 2001) and long term (Lynch-Stieglitz et al., 2007) climatic changes of the Quaternary Earth. Better understanding of the drivers of circulation change, and the subsequent climatic response will help inform predictions of the future — when increased precipitation and temperature over the high latitudes (Meehl et al., 2007), combined with freshwater input from Greenland Ice Sheet melt may act to significantly alter the modern day thermohaline circulation (Hu et al., 2009; Jungclaus et al., 2006).

This study looks to improve our understanding of the Quaternary Ocean by developing a novel new method to quantify palaeo-ocean temperatures using the clumped isotope analysis of fossilised foraminifera. It then produces high resolution records of the Quaternary Ocean from two sites that are highly influenced by the thermohaline circulation — the North Atlantic and South Labrador Sea — to inform our understanding of historical oceanic changes.

1.1 Aims and thesis outline

Objective 1: The development of a foraminifera clumped isotope palaeothermometer

Chapters 2 – 3 of this study aim to produce a foraminifera clumped isotope calibration for use in palaeoclimate reconstructions. Measurements were made using the University of East Anglia's (UEA) Multi-Isotopologue-Ratio-Analyser (MIRA) — the first mass spectrometer specifically designed for clumped isotope analysis. The ubiquity of foraminifera throughout the world's oceans make them an ideal proxy for palaeoclimate reconstructions, and the clumped isotope method has the potential to overcome many of the problems with existing temperature reconstruction methods — namely a lack of knowledge of the isotopic and chemical composition of the palaeo-ocean.

The development of a foraminifera calibration will first require robust experimental protocols to be established for the measurement of foraminifera. These are explored in further detail in chapter 2. Objectives include:

1.1 *Development of sample preparation techniques for foraminifera clumped isotope measurements*. Existing clumped isotope foraminifera studies employ a variety of techniques for the removal of contaminants prior to measurement (e.g. Grauel et al., 2013; Tripati et al., 2010). This study will investigate the impact of different pre-cleaning treatments and the post dissolution CO_2 purification process to ensure consistent and reliable data acquisition. This is explored further in sections 2.3.3 and 3.5.2.

1.2 *Minimisation of sample size*. At the beginning of this study, standard sample mass was approximately 6 mg. This is equivalent to 600 – 700 foraminifera tests. In order to reduce microscope based sample collection time and maximise the resolution of future palaeo-studies, this must be reduced. This is discussed in section 2.4.

1.3 *Streamlining of standard measurements and establishment of a robust methodology by which sample data can be reported against other laboratories.* Section 2.5 explores different methods by which measurements of laboratory standards can be used to project UEA laboratory data onto the ‘absolute reference frame’ (Dennis et al., 2011), minimising error and running time devoted to standard measurements.

Objective 2: The creation of a high resolution multiproxy record of the North Atlantic during the last glacial cycle

Chapters 5 explores the multiproxy analysis of North Atlantic core MD99-2251. The study site sits below the northerly flowing limbs of the North Atlantic Current, at the southern tip of the Gardar Drift, where exceptionally high sedimentation rates offer the opportunity for extremely high resolution environmental reconstructions (Ellison et al., 2006).

Additional study of this area has the potential to inform our understanding of many of the long term and millennial scale climatic fluctuations over the Quaternary, their causes and effects. Improved understanding of the AMOC response to historical freshwater forcing can be used to contextualise predictions under anthropogenic climate change. Specifically, this study aims to:

2.1 *Establish a high resolution chronology for north Atlantic ice rafting events.* Much uncertainty still exists as to timing and magnitude of Heinrich events. In particular, Heinrich events 3 (H3) and 6 (H6) which appear as prolonged and less pronounced in much of the sedimentary record (Hemming, 2004). Recent studies have postulated the existence of an additional event H5a between H6 and H5 (Rashid, Hesse, & Piper, 2003; S. Van Kreveld et al., 2000). This study aims to provide clarity on the magnitude and timing of this event compared with ‘better established’ Heinrich events. A detailed ice rafting chronology is constructed in section 5.7.

2.2 *Improve understanding of the relationship between Heinrich Events and cooling intervals.* Better understanding of the timing of Greenland cooling in relation to ice rafting events can help determine whether Heinrich events were a driver of Greenland cooling or merely a response. This is explored in detail in section 5.7.2.

2.3 *Improve understanding of the role of the AMOC in long term and millennial climatic fluctuations?* There is strong evidence to suggest that the AMOC slowed, or reconfigured in response to a H10, H6, H4 and H3 (Vidal et al., 1997; Wary et al., 2015). However, limited response has been observed during rafting intervals. This study aims to provide clarity on whether AMOC response was uniform across all

Heinrich events and whether AMOC alteration was a driver of, or response to, Greenland cooling. This is explored further in section 5.8.

2.4 *Provide clarity on the timing and nature of major climatic transitions.* Questions still remain as to the nature of transitions between major palaeoclimatic stages. In particular, this record will look to improve understanding as to the magnitude of temperature transition and deep ocean response to the MIS 5/4 transition and the timing and cause of high frequency climatic fluctuations during the transition out of full glacial conditions and into the Holocene.

Objective 3: Production of a high resolution isotope record of the Labrador Sea over Termination II and the last interglacial

A high resolution isotope record from the Labrador Sea during the last interglacial is produced in chapter 6. The region is a key site of NADW formation which drives the modern day thermohaline circulation. This study aims to improve understanding of Termination II and MIS 5e – the last interglacial where environmental conditions were analogous to the modern day. Key objectives:

3.1 *Provide clarity on the timing and nature Termination II.* Section 6.2.1 looks to provide detail on Termination II, providing improved estimates for start and end dates and detailing the nature of the transition. Did Termination II exhibit cold reversals such as the Younger Dryas, observed during Termination I?

3.2 *Improve understanding of the environmental conditions during MIS 5e in the Labrador Sea*. Were conditions in the last interglacial similar to those of today? Did the region act as a site of deepwater formation as it does today and was the climate stable, or did it undergo climatic fluctuations similar to those observed in the early Holocene? This is addressed in section 6.2.2

Chapter 2. Clumped isotope instrumentation and methodology

2.1 Introduction: Background and chapter outline

The University of East Anglia’s Multi-Isotopologue-Ratio-Analyser (MIRA) came online in 2011 after five years of development. It is the world’s first mass spectrometer specifically designed for clumped isotope analysis (Dennis et al., 2013). Previous studies had used modified Thermo-Finnegan 253 (Affek & Eiler, 2006; Eiler & Schauble, 2004; Ghosh et al., 2006) or Elementar Analysensysteme Isoprime (Rosenheim et al., 2013) instruments which, whilst capable of producing high quality data, required extensive non-linearity corrections and often large sample volumes. The MIRA design and setup, described in detail in section 2.3, promised unparalleled measurement precision, reduced data correction procedures, and enhanced throughput compared with existing instruments.

In the intervening years, much effort has gone into refining the experimental procedure and standardising the methodology to ensure the production of consistent, high quality data. 2017 saw the establishment of a laboratory calibration, produced largely from modern brachiopod carbonates and a limited number of controlled temperature precipitates (Kirk, 2017). This was followed by the first published data to come from the instrument, a study of a calcite vein system from the Derbyshire Platform in the Southern Pennines, UK (Dennis et al., 2019).

This chapter details the experimental methodology employed on the UEA clumped isotope system, and the many instrumental and procedural improvements that have occurred since the inception of this project in October 2015. The majority of work has focused on sample preparation, particularly the cryogenic gas cleaning line (section 2.3.3) with the aim of finalising a methodology which can eventually be automated.

Since the eventual aim of this project is to apply the clumped isotope technique to foraminifera, of central importance has been the need to reduce sample sizes from the 6 – 8 mg which were being used at the project inception. This has proved extremely challenging because of a persistent offset in measured Δ47 between large and small samples. Such sample size effects have been observed in previous studies (Guo & Eiler, 2007; Wacker & Mainz, 2013) but remain largely unexplored within the scientific literature. Section 2.4 explores this phenomenon, and the efforts to eliminate it.

Additional investigations into data processing techniques are also explored, in particular refining projections of Δ47 measurements onto the absolute reference frame (ARF). Most laboratories have now adopted the ARF projection procedures outlined in Dennis et al*. (*2011) that allows data to be compared between laboratories. This methodology requires development of a transfer function, derived from regular measurement of laboratory standards with known Δ47 values. Yet the timeframes over which transfer functions are applied, and the regularity of standard measurements for their construction, are seldom reported within the literature. Section 2.5 explores these question further, developing a robust methodology for UEA absolute reference frame reporting and a method for assessing transfer function accuracy that can readily be adopted by other laboratories.

2.1.1 Overview of existing research into clumped isotope palaeothermometers

Clumped isotope analysis offers a means by which palaeotemperatures can be deduced which is independent of the isotopic and chemical composition of calcite precipitation waters. The basis of clumped isotope geochemistry dates back to the discovery that the substitution of a heavy isotope into a chemical bond lowers its vibrational frequency, and accordingly, its zero point energy (Bigeleisen & Mayer, 1947; Urey, 1947). Thus bonds between two heavy isotopes have a lower zero point energy than bonds between light isotopes (Figure 2.1). As such, a higher degree of heavy-heavy isotope bonding should occur in low energy environments – i.e. at lower temperatures. Thus clumped isotope analysis looks at the degree to which heavy isotopes bond (or clump) together within the calcite lattice.

Molecules with two heavy isotopes bonded together (known as doubly substituted isotopologues) remain relatively rare within the natural environment. For example, the most common doubly substituted isotopologue of carbon dioxide, $^{13}C^{18}O^{16}O$, is present at just 44.4 ppm, assuming stable isotopic composition equal to VSMOW (Eiler, 2007). $^{12}C^{17}O^{18}O$ and $^{12}C^{18}O_2$ are present at even lower abundances of 1.5 ppm and 1.6 ppb respectively (Eiler, 2007). Until recently this rendered their detection and measurement beyond the realms of technological possibility.

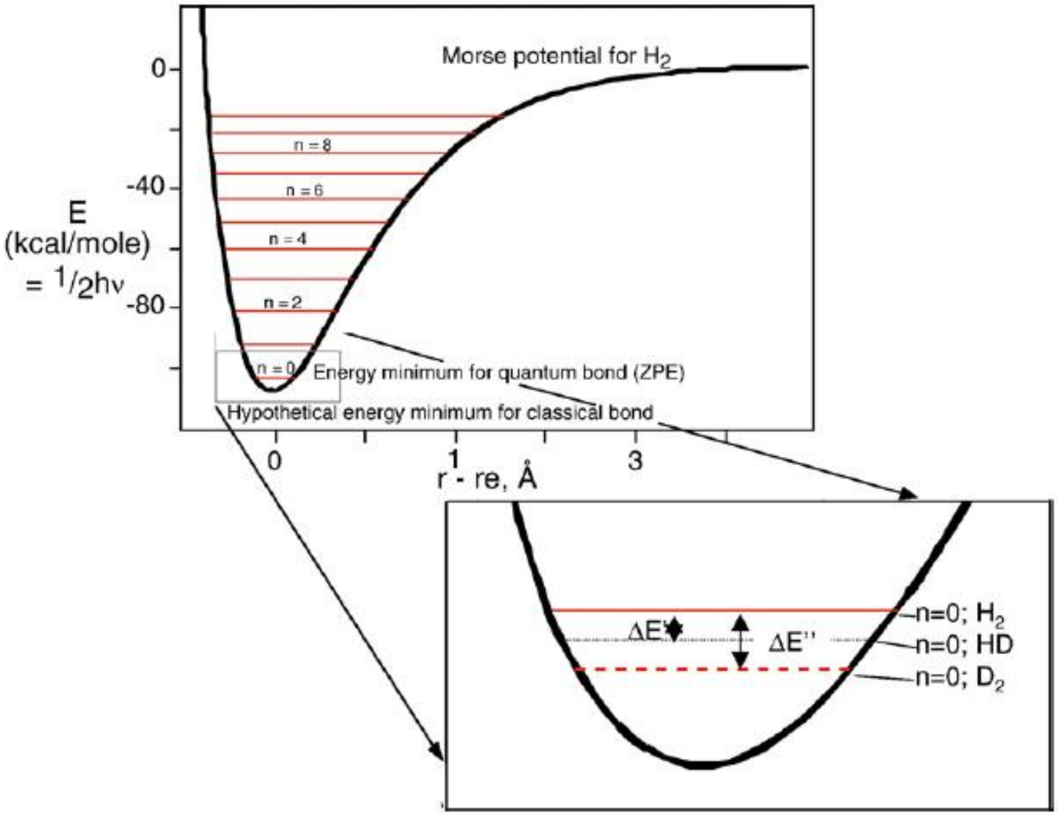

Figure 2.1 Energy content of a hydrogen molecule with bond distance. The red lines represent the morse potential (the potential energy of a diatomic molecule) at different quantum states. The expanded window shows that at the zeroth level, the morse potential of the hydrogen molecule is roughly double that of a deuterium molecule. (Source: Eiler, 2007))

However the adaptation of a Thermo MAT 253 mass spectrometer at Caltech's Division of Geological and Planetary Sciences in the early 2000s to include an additional three Faraday collectors at masses 47 – 49 paved the way for the first clumped isotope measurements (Eiler & Schauble, 2004). Since then successful mass spectrometer measurements have been made on Elementar Analysensysteme Isoprimes (Rosenheim et al., 2013) Nu-instruments Perspectives (Lacroix et al., 2018) and the University of East Anglia's Multi-Isotopologue-Ratio-Analyser (MIRA) (Dennis et al., 2019). Laser spectroscopy has been applied to clumped measurements of methane (Ono et al., 2014) and the recently deployment of the MAT 253 ultra, promises measurement of isotopologues and their fragments with unprecedented resolution (Eiler et al., 2013).

The first carbonate based clumped isotope temperature calibration derived the relationship between calcite precipitation temperatures and heavy isotope clumping from a combination of laboratory and naturally precipitated inorganic calcites, as well as tropical and deep sea corals (Ghosh et al., 2006). As the field of clumped isotopes has developed, further calibrations have been derived from numerous carbonate sources including, but not limited to, fish otoliths (Ghosh et al., 2007), brachiopods (Came et al., 2014), molluscs (Eagle et al., 2013), travertines and tufas (Kele et al., 2015), laboratory precipitates (Jautzy et al., 2020), and sedimentary siderite (Fernandez et al., 2014).

Until recently the number of foraminifera based calibrations remained limited. The large sample sizes required for clumped isotope analysis (typically in the order of several milligrams) made foraminifera measurements time consuming and impractical. The few existing foraminifera calibrations combined foraminiferal calcite alongside other bulk carbonates (Grauel et al., 2013; Tripati et al., 2010) and exhibited considerable variation in their gradient and intercept. However, the last few years have seen the publication of the first solely foraminifera derived calibrations and these show much closer agreement with each other (Breitenbach et al., 2018; Piasecki et al., 2019; Peral et al., 2018). Indeed several recent studies have now successfully used clumped isotope analysis of foraminifera to infer palaeotemperatures (Evans et al., 2017; Henkes et al., 2018; Piasecki et al., 2019; Thornalley et al., 2015; Rodríguez-Sanz et al., 2017).

2.1.2 Definition of Delta values

Since clumped isotope measurements employ gas source mass spectrometry, if a carbonate sample is used it must be converted to a gas phase prior to measurement. This is achieved through reaction with ortho-phosphoric acid to produce carbon dioxide, according to the standard procedure outlined by McCrea (1950). Doubly substituted bonds within the carbonate lattice produce carbon dioxide of mass 47, as opposed to mass 44, the mass of CO_2 with no heavy isotope substitutions. Thus clumped isotope carbonate thermometry measures the concentration of carbon dioxide with mass 47.

As with conventional stable isotopes, the measurement is made relative to a standard, normally a laboratory produced carbon dioxide of known bulk isotopic composition. The measurement of mass 47 of the sample relative to mass 47 of the standard is defined as δ^{47}.

$$\delta^{47} = \frac{\frac{N47}{N44}_{sample}}{\frac{N47}{N44}_{standard}}$$

Where N is the number of isotopes present. However, the concentration of mass 47 ions within a sample is dependent on the stable, or bulk, isotopic composition — i.e. more doubly substituted isotopologues would be expected in a sample with a high concentration of heavy isotopes. Thus to account for this, Δ47 is calculated by normalising δ^{47} to the N47/N44 ratio that would be expected from a sample with the same stable isotopic composition, given a random (or stochastic) distribution of ions within the calcite lattice. This is calculated theoretically according to (Wang et al., 2004)

$$\delta^{47} = \left[\frac{\frac{N47}{N44}_{sample}}{\frac{N47}{N44}_{standard}}\right] \Bigg/ \left[\frac{\frac{N47}{N44}_{stochastic}}{\frac{N47}{N44}_{standard}}\right]$$

Thus

$$\Delta 47 = \left(\frac{\frac{N47}{N44}_{sample}}{\frac{N47}{N44}_{stochastic}} - 1\right) \times 1000$$

With the subtraction of 1 and multiplication of 1000 to put into ‰ notation. Values for N45 – N49 can be substituted for calculation of Δ45 - Δ49.

2.2 Reporting methods and terminology

Prior to exploring the field of clumped isotopes further it is necessary to define some basic reporting methods and terminology.

2.2.1 Clumped isotope error reporting

Throughout this study 95 % confidence intervals shall be used when reporting clumped isotopic measurements as recommended by Müller et al. (2017), with the exception of laboratory standards and foraminiferal measurements measured under standard procedures. Müller et al. (2017) suggest that the standard error, commonly used as a measure of analytical precision in clumped isotope studies, cannot adequately capture the full variance of most measurements where only a few repeats are possible due to the large sample sizes required.

The findings of Müller et al. (2017) were corroborated in this study using the dataset of 146 laboratory standard UEACMST measurements obtained between January 2018 to May 2019. This large dataset allows establishment of the mean Δ47 with a high degree of certainty (-0.396 ± 0.006 ‰, standard deviation = 0.067 on the local reference frame). If 3 random hypothetical measurements are generated around a mean of -0.3964 with a standard deviation of 0.067, it can be determined whether the standard error of this small hypothetical dataset encapsulates the well-established UEACMST mean. By repeating this thought experiment 5000 times it is shown that the standard error will only encapsulate the true mean 78.5 % of the time. Thus 95 % confidence intervals are required when reporting MIRA measurements to ensure true means are captured.

A limited number of exceptions are made. The large number of laboratory standard measurements, conducted under standard experimental procedure, allow the reporting of standard deviation with a high degree of confidence. For standards measured under novel or test procedures, 95 % confidence intervals shall be used.

For foraminiferal samples measured under standard procedures, the pooled standard deviation is calculated according to the formula:

$$S_{pooled} = \sqrt{\frac{(n_1 - 1){s_1}^2 + (n_2 - 1){s_2}^2 + \ (n_3 - 1){s_3}^2 + .. + (n_k - 1){s_k}^2}{n_1 + n_2 + n_3 + .. + n_k - k}}$$

Where:
k = number of samples
S_1, S_2 etc. = sample standard deviations
n_1, n_2 etc. = number of repeat measurements for a single sample.

The pooled Δ47 standard deviation for all foraminifera measurements in this study is 0.034 ‰ on the absolute reference frame. The pooled standard deviation is then used to calculate a standard error for each foraminifera sample based on the number of measurements made.

2.2.2 Reference frame reporting and acid temperature corrections

Unless otherwise stated, all Δ47 measurements are reported on the absolute reference frame (Dennis et al., 2011) to allow comparison with values in the published literature. Section 2.5 details how Δ47 measurements can be projected from a local laboratory frame (denoted throughout as LRF) to an 'absolute' reference frame (denoted ARF) used for inter-laboratory comparisons. $\delta^{13}C$ and $\delta^{18}O$ of carbonate samples are reported on the VPDB scale unless otherwise stated.

Clumped and stable isotopic values are corrected to an acid reaction temperature of 25°C. For the 87 °C reaction employed throughout this study, a correction of 0.062 ‰ is applied to Δ47 values, assuming a temperature sensitivity of 0.001 ‰/°C as reported by (Guo et al., 2009).

$\delta^{18}O$ is corrected using a fractionation factor calculated from the common acid bath temperature relationship defined by Swart et al. (1989):

$$\alpha_T = \frac{5.25 \times 10^2}{T^2} + 1.003970$$

This gives a fractionation factor of 1.008 at the laboratory reaction temperature of 87°C.

2.2.3 Laboratory standards

UEACMST (**UEA**-**C**arrara-**M**arble-**ST**andard)

UEACMST is the most commonly used standard, sourced from BDH marble chips which have been crushed, homogenised and sieved to a grain size 125 – 200 µm. It is a natural carbonate standard with no obvious signs of discolouration, suggesting it is relatively pure. UEACMST is used predominantly as a means to test day-to-day drift in MIRA and the sample purification line, as well as to construct the transfer function with which samples are projected onto the absolute reference frame. The laboratory accepted Δ47 value is 0.381 ± 0.005 ‰ based on 129 measurements between January 2018 and May 2019.

ETH1

A fine powdered Carrara Marble heated to 600 °C at a pressure of 155 mpa for 10 hours (Meckler et al., 2014). The standard was obtained from ETH Zurich as part of an inter-laboratory calibration project in 2013. ETH1 is used predominantly to construct the transfer function with which samples are projected onto the absolute reference frame. Published estimates of Δ47 values for ETH1 have recently been revised down from 0.267 (Meckler et al., 2014) to 0.258 (Bernasconi et al., 2018). The UEA long term average measured value is 0.280 ‰ (ARF) based repeated measurements against heated gases. This is closer to the recent 0.302 ‰ estimate from Fiebig et al. (2019).

ETH3

A cretaceous chalk from Northern Germany, obtained alongside ETH1 from ETH Zurich. Both ETH3 and ETH1 were chosen to have a stable isotopic composition close to that of most marine carbonates (Bernasconi et al., 2018). ETH3 is predominantly used as a laboratory standard with which samples are projected onto the absolute reference frame. As with ETH1, accepted Δ47 values for ETH3 have recently been revised from Meckler et al's. (2014) estimate of 0.705 ‰, to 0.691 ‰ (Bernasconi et al., 2018) and 0.707 ‰ (Fiebig et al., 2019). The UEA long term average measured value is 0.662 ‰ (ARF) based on repeated measurements against heated gases.

BDH-RT

Carbon dioxide produced from acid digestion of BDH marble chips and equilibrated with water at room temperature before being dehydrated and cleaned. BDH-RT is a clean gas and thus can be measured to a high precision to monitor day-to-day drift in MIRA.

UEAOES (**UEA**-**O**strich-**E**gg-**S**hell)

A modern ostrich egg shell which has been ground to a fine powder. It contains proteins native to the egg shell structure making it a useful standard with which to assess the performance of the sample purification line.

UEATHC (**UEA T**urkish **H**ydrothermal **C**arbonate)

An internal laboratory standard, UEATHC is an inorganic hydrothermal carbonate, precipitated in concentric rings within a pipe at the Kamara Fissure Ridge in Turkey at a constant temperature of 56 ±2 ^{o}C. The material was ground into a fine powder and homogenised prior to measurement. A noticeable discolouration suggests presence of iron oxide with such impurities making it ideal for testing the performance of the MIRA purification line. The long term average Δ_{47} value is 0.564 ±0.033 ‰ based on 42 measurements (Kirk, 2017).

2.3 Experimental setup

2.3.1 Instrument setup and design

The MIRA (Multiple Isotopologue Ratio Analyser) isotope ratio mass spectrometer at the University of East Anglia is the first mass spectrometer specifically designed for clumped isotope analysis. A detailed description of MIRA can be found in Dennis et al*. (*2013) which is summarised in the following section.

Sample gas is inputted via a VG micro dual inlet system for SIRA series II instruments, consisting of variable volume sample and reference bellows, matched 50 cm capillaries and a changeover-valve for switching between sample and reference input (Figure 2.2). Dual inlet systems have been widely employed in clumped isotope measurements (e.g. Eagle et al., 2015; Tang et al., 2014; Zhang et al., 2018) since they provide stable conditions over the long measurement times required.

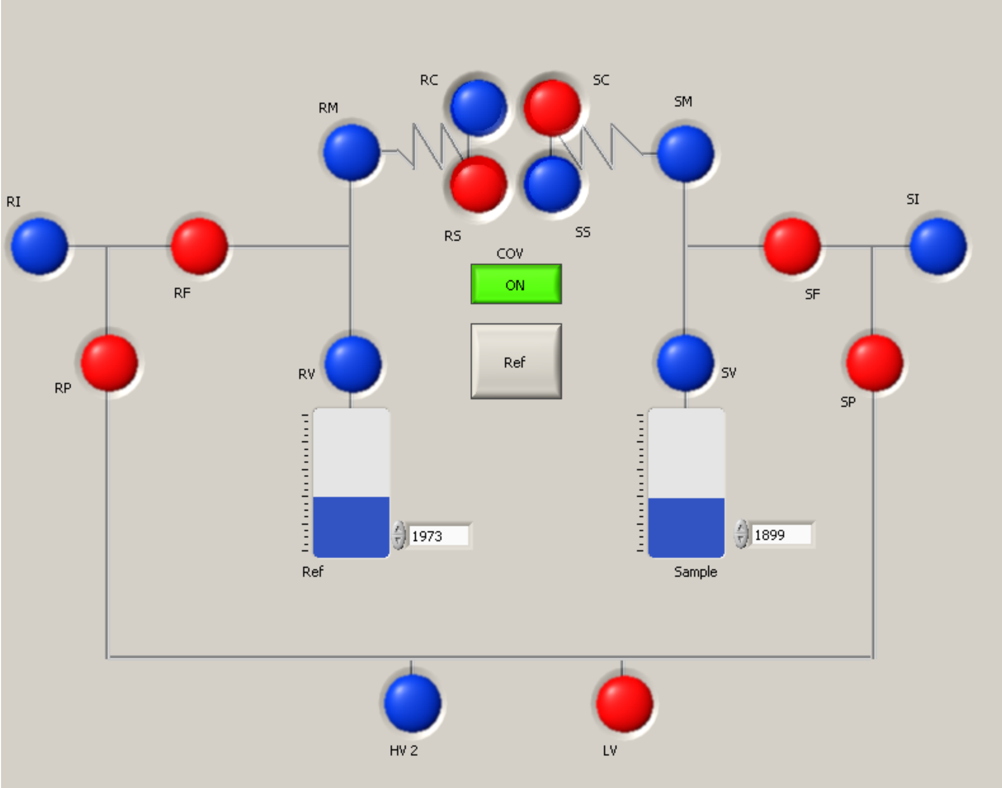

Figure 2.2 MIRA dual inlet system as operated in Labview software. Sample and reference gases inputted through valves SI and RI respectively. Input bellows can be manually adjusted. Analyte gases inputted into MIRA through valves RC (reference) and SC (sample). HV2 and LV are connected to high and low vacuum pumps respectively for evacuating the system.

The ion source is modified from a standard Nier type (Nier, 1947) to give improved collimation of the ionising electron beam and matching of the source emittance window with the acceptance window of the magnetic analyser. It consists of an ionisation cavity traversed by an electron beam. A repeller plate at the rear of the chamber propels the ions through a three component immersion lens consisting of an ion exit slit (5 mm x 0.6 mm), focusing plates and ion source slit (5 mm = 0.5 mm), each separated by a 2 mm gap. A final α slit 50 mm beyond the source slit acts to limit dispersion in the X-Y plane.

The instrument geometry is shown in Figure 2.3. A 120° magnetic sector minimises overall path length between the ion source and resolving slits. This acts to limit ion-ion interactions in the flight tube and reduce beam broadening which may give rise to secondary electron generation through ion collision with the instrument hardware (flight tube, lens slits etc.).

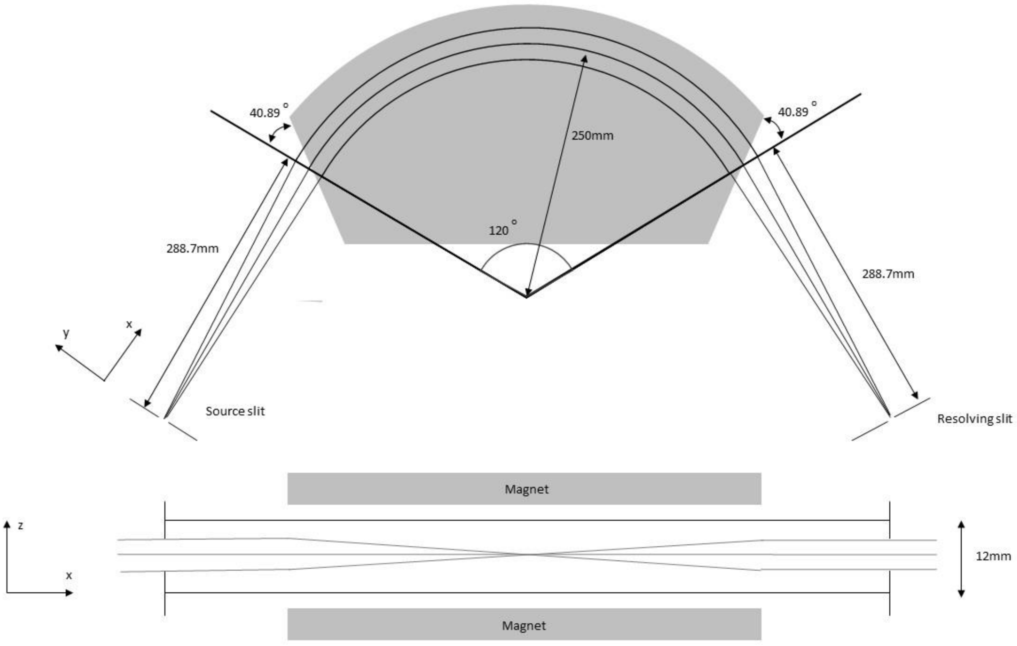

Figure 2.3 MIRA instrument geometry (Adapted from Dennis et al. (2013))

The electromagnet is constructed from 10 cm thick high purity iron plates with 2 x 600 turn coils made from 2 mm diameter polyester resin copper coated wire. A resistance based feedback mechanism ensures field stability is maintained to better than 1 in 5000 during ambient temperature fluctuations.

Six faraday cups allow detection of ions of mass 44 – 49. The array has a front resolving aperture of 2 mm width prior to an election supression plate and final screening aperture. A deep aperture in the front faraday support provides screening against secondary electrons scattered from the resolving slits.

System vacuum is maintained with five Leybold TW70H 70L.s−1 drag stage turbomolecular pumps — two on the source block, one at the detector housing, one on the changeover valve and one on the inlet. The five pumps are backed by two Leybold DiVac 0.8T diaphragm pumps running in series. In this configuration, vacuum pressures as low as 3 x 10^{-9} hPa are readily achieved.

2.3.2 MIRA instrumental performance

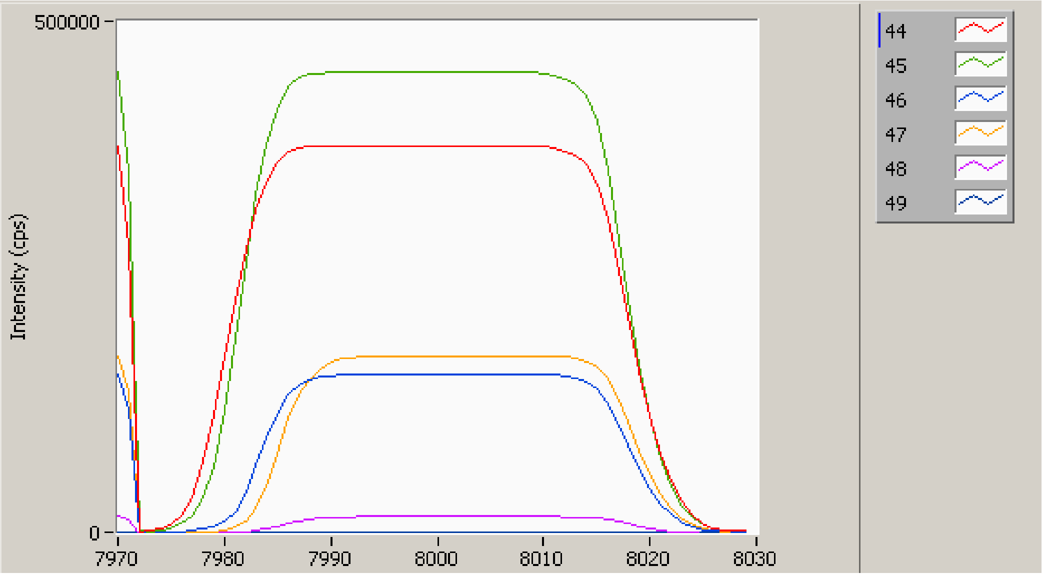

Figure 2.4 MIRA peak shapes with a major beam intensity of 7.5x10-^{8}A and source vacuum of 3x10-^{7} hPa. X-axis is accelerated potential in volts.

Instrumental stability is evident in the exceptional beam quality and shape shown in Figure 2.4. MIRA achieves mean routine measurement precision of 0.008 ‰ with a linear response in Δ47 across a range in δ^{47} from -60 ‰ to +60 ‰ (Figure 2.5), reducing the number of standards needed for non-linearity corrections and increasing sample throughput (Dennis et al., 2013). Minimal interaction of sample ions with instrumental hardware eliminates the generation of secondary electrons and thus no pressure baseline effect is observed. Instrument sensitivity of one ion detected per ~300 sample gas molecules enables measurement of small sample volumes over short integration times.

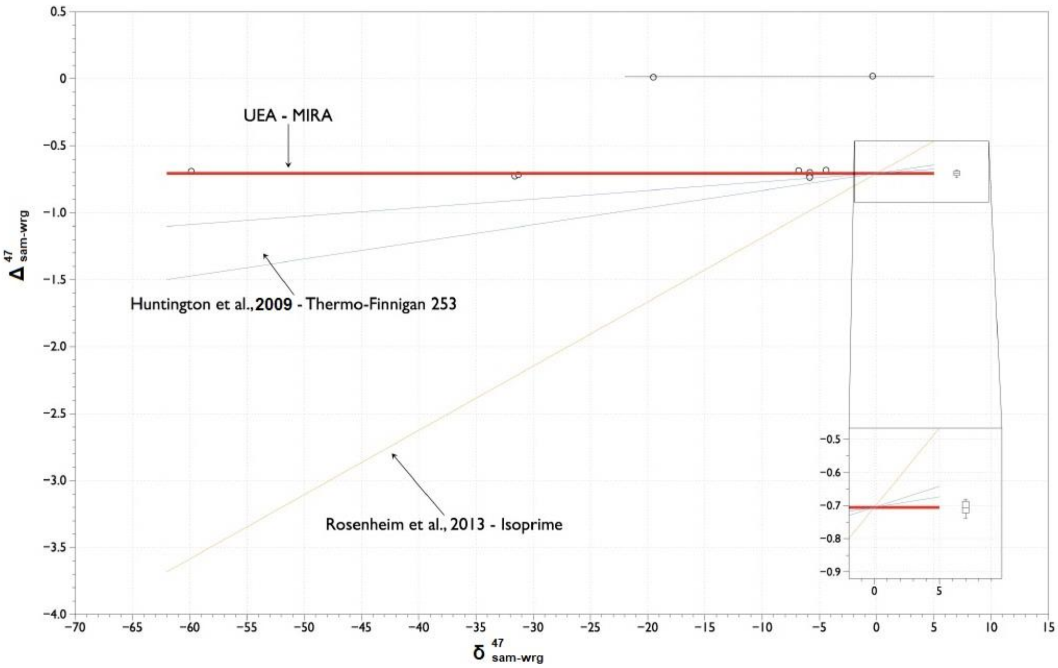

Figure 2.5 The zero gradient obtained from plotting $\delta^{47}_{\text{sample-working reference gas}}$ vs $\Delta47_{\text{sample-working reference gas}}$ for a suite of gases heated to 1000 °C (stochastically distributed) with variable bulk composition demonstrates the long term linearity of MIRA (adapted from Dennis (2014)). Compared alongside Thermo-Finnigan 253 (Huntington et al., 2009) and Isoprime (Rosenheim et al., 2013) instruments.

The three most regularly measured laboratory standards, UEACMST, ETH1 and ETH3, exhibit a long term drift on the local reference frame (Figure 2.6). Average monthly drift across a 17-month operational period between January 2018 and 8 March 2019 was 0.01 ‰ per month. This drift was thought to arise from a gradual build-up of water within the instrument source. Further evidence to support this assertion comes from a reversal in the upward trend observed after the installation of additional water traps on the MIRA sample purification line in March 2019 (See section 2.3.3 for details).

Average long term standard deviation for the three laboratory standards was 0.058 ‰ over the period January 2018 – May 2019. For detrended data, prior to March 8 2019, the average standard deviation was 0.036 ‰.

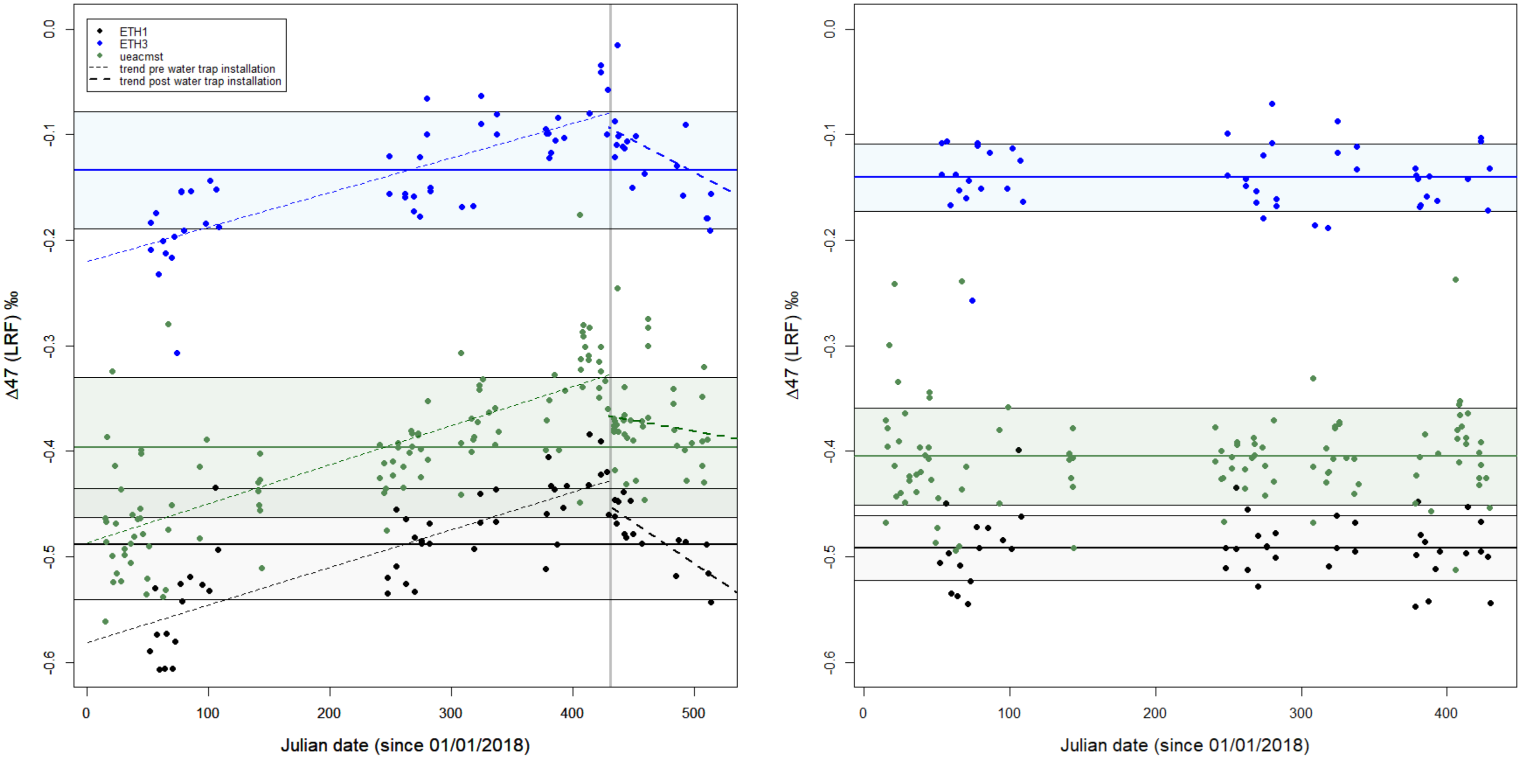

Figure 2.6 Δ47 (LRF) for three laboratory standards (ETH1, ETH3 and UEACMST) measured between January 2018 and May 2019. Left panel shows long term instrumental drift and right panel detrended data prior to the installation of additional water traps. Solid horizontal lines show the measurement means, shaded areas the standard deviation. The grey vertical bar at day 431 marks the installation of additional water traps on the sample purification line. Dashed lines are linear trends through each standard, prior to and subsequent to the installation of additional water traps.

2.3.3 Sample purification line

The low abundances of mass 47 CO_2 (typically 46ppm in stochastically distributed samples with $^{18}O/^{16}O$ and $^{13}C/^{12}C$ concentrations equal to VMSOW and VPDB respectively (Eiler, 2007)) mean that exceptionally pure samples are required for clumped isotope analysis. Contamination of just 4 -5 ppb at mass 47 will result in an approximately 0.01 ‰ shift in Δ47, equivalent to a ~3 ^{o}C temperature shift at earth surface temperatures (Eiler, 2007).

Figure 2.7 shows the current setup of the MIRA manual CO_2 purification line through which all samples are prepared for clumped isotope analysis. Throughout this study, the purification line has been through many iterations which are summarised in Table 2.1 and explored in detail below. In the current setup, hot 102 % phosphoric acid, is pumped under vacuum via a dedicated turbomolecular pump, down to a base pressure of 6×10^{-7} mbar. This acts to remove water vapour from the system prior to sample reaction. Samples dropped into a common acid bath held at 87.0 ± 0.2 ^{o}C with temperature maintained via a water jacket and circulation system. Samples are left to react for 30 minutes. Liberated CO_2 is immediately passed over three cold traps held at -110 ^{o}C with liquid nitrogen pumps, which act to dehydrate the sample. Liberated gas is continually frozen into a subsequent coldfinger held under liquid nitrogen throughout the reaction, which provides sufficient temperature gradient to aid gas transfer. At the end of the reaction, the first of the three cold traps is defrosted and water vapour pumped away via the dedicated acid vacuum pump, ensuring that minimal water vapour passes into the main section of the purification line.

The clean sample gas is sublimated at room temperature into a coldfinger of known volume and the pressure recorded for use in a post measurement sample size correction. The sample is frozen into a second coldfinger (transfer time 5 minutes) which acts to increase pressure and reduce sample transfer time through the next step of the line. The sample is now passed through a 24 cm long glass tube of 4 mm internal diameter, filled with Porapak Q adsorbent material to remove halocarbon and hydrocarbon contaminants. A further two coldfingers act to increase pressure and aid gas transfer, before the sample is loaded into the mass spectrometer. At each coldfinger, the sample is held under liquid nitrogen and non-condensable gases pumped away. Liquid nitrogen traps connected between the purification line and the vacuum manifold prevent water from entering the purification line via the vacuum system.

The majority of samples in this study were run between October 2018 and May 2019. During this period the purification line remained largely unchanged from the format described above. The only changes being the installation of an additional water trap immediately after the acid reaction vessel, the addition of liquid nitrogen water traps between the purification line and vacuum manifold, and installation of a dedicated acid pumping line (prior to this the acid was pumped via the same system as the rest of the line). The evolution of the purification line is described in detail below and summarised in Table 2.1.

Acid reaction vessel

Clumped isotope studies generally employ one of three reaction methods: individual reaction vessels (e.g. Dennis & Schrag, 2010; Tripati et al., 2010), common acid baths (e.g. Eagle et al., 2015; Tang et al., 2014) or Kiel devices (e.g. Breitenbach et al., 2018; Meckler et al., 2014). Reaction temperatures range from 25 ^{o}C to 90 ^{o}C, with Δ47 values corrected for acid fractionation to a reaction temperature of 25 ^{o}C when reporting on the absolute reference frame. At the beginning of this study, samples were reacted overnight at 25 ^{o}C in individual reaction vessels. In September 2016 the decision was made to install a common acid bath after evidence of sample re-equilibration with water vapour over prolonged periods of close proximity within the reaction vessel. In the absence of an automated system for individual reaction vessels, all samples were reacted at the same time, generally late in the evening on the day before analysis. This meant little control over reaction time, and those samples analysed late the following day remaining in contact with water vapour in the reaction vessel for extended periods. This resulted in an offset between standards run earlier in the day and those run later. Increased Δ47 spread when reacting at 25 ^{o}C compared with a common acid bath has been observed previously by Wacker & Mainz (2013), who noted that the effect was most extreme in smaller ~4 mg samples, similar to those analysed at UEA. Recent analysis by Swart et al. (2019) has confirmed these findings, showing that variable contact time between sample CO_2 and acid has a measurable impact on Δ47.

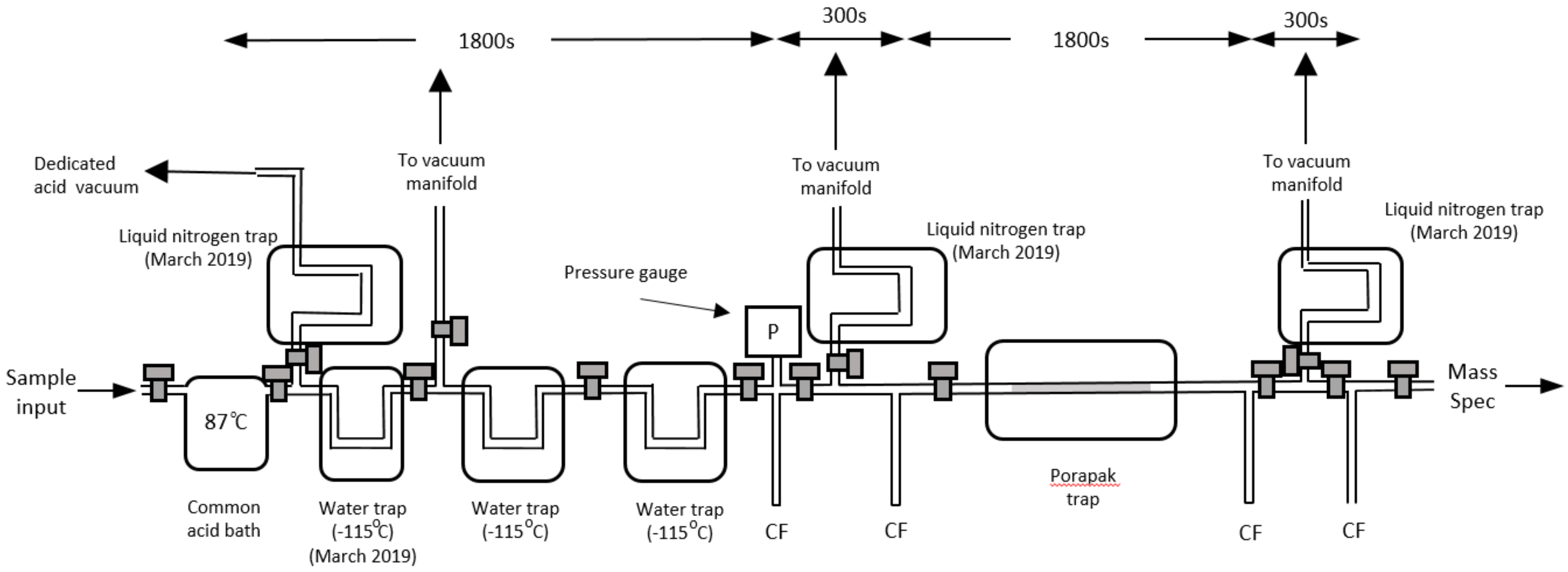

Figure 2.7 The current MIRA purification line setup. CF = coldfinger. Times at the top of the diagram indicate transfer times through each stage of the line

Table 2.1 Chronological summary of the MIRA purification line changes

Line section	Dates	Description	Temperature	Transfer time
Acid reaction	Sep 2015	Samples reacted offline in individual reaction vessels in a water bath	25 °C	overnight
	Sep 2016	Common acid bath installed. Heated with water circulator from water mains	56 °C	60 minutes
	Jan 2017	Additional water circulator installed	87 °C	30 minutes
	April 2018	Separate acid vacuum pumping line installed	N/A	N/A
Water traps	Sep 2015	2 x ethanol cooled coil traps	-110 ± 5 °C	With acid reaction
	May 2018	Liquid nitrogen pump cooling system installed	-80 ± 5 °C	
	March 2019	Third cold trap installed, ethanol cooled, evacuated via dedicated vacuum line	-115 ± 5 °C	
		Liquid nitrogen traps installed between vacuum manifold and purification line		
Porapak trap	Sep 2015	21 cm length, 9 mm diameter U trap. Cooled with liquid nitrogen pumps	-25 °C ± 5 °C	60 minutes
	Nov 2015	7 cm length, 4 mm diameter linear trap, cooled with Peltier devices	-7 ± 1 °C	20 minutes
	Oct 2016	24 cm length, 4 mm diameter linear trap, cooled with Peltier devices and water jackets	-20 ± 1 °C	60 minutes
	March 2017	12 cm and 7 cm, 4 mm diameter linear traps both tested	-20 ± 1 °C	30 and 20 minutes respectively
	Jan 2018	24 cm length, 4 mm diameter linear trap, cooled with Peltier devices and water jackets	-20 ± 1 °C	60 minutes
	May 2018	12 cm length, 9 mm diameter U trap, cooled with liquid nitrogen pumps	-20 ± 2 °C	30 minutes

The first iteration of the common acid bath was heated with hot water directly from the water mains to a temperature of 56 ± 2 ^{o}C. Reacting online allowed more flexibility over the number of samples run each day and ensured all samples were reacted for the same duration. However, system stability was compromised by fluctuations in mains water temperature. Thus a hot water circulator, at 87 ± 1 ^{o}C was installed in January 2017.

Water traps

In September 2015, at the start of this study, water was removed from reactant gas with two coil traps cooled to -110 ^{o}C with ethanol. After each reaction, the traps were warmed to room temperature and continually evacuated with vapour pressure recorded as the traps defrosted. Negligible rise in vapour pressure from defrosting of the second trap suggested that the vast majority of water was removed in the initial trap such that the sample could be considered dry.

In May 2018 the ethanol cooling system was replaced with a liquid nitrogen system featuring continuous temperature monitoring and automated nitrogen pumping to improve temperature stability. Trap temperatures were raised to -80 ^{o}C in an attempt to address the greater degree of scale compression observed on MIRA compared with other instruments (Dennis et al., 2013). A potential source of scale compression arises from fragmentation and recombination of carbon dioxide molecules through electron bombardment in the ion source. When water is present, hydroxide ions, produced from fragmentation of water in the ion source, preferentially combine with carbon monoxide ions, preventing their recombination back into CO_2 molecules. Thus through this reaction, it is hypothesised that water may act to reduce scale compression.

Increasing the temperature of the water traps to -80 oC, brought the UEA system more in line with existing experimental setups where scale compression is less pronounced (Dennis & Schrag, 2010; Guo & Eiler, 2007). The hope was that by allowing small quantities of water into MIRA, this would saturate the ion source and reduce scale compression. Unfortunately, no such reduction was observed. Table 2.2 shows MIRA scale compression during periods of freezing at -80 ^{o}C and – 110 ^{o}C with almost identical scale compression observed over the two phases.

Table 2.2 Scale compression with water trap temperature. No reduction is scale compression is observed with a shift to warmer (-80 °C) temperatures

Month	Stretch factor	Trap temperature (°C)
Mar-18	0.9928	-110
Apr-18	1.115887	-110
Sep-18	1.108377	-80
Oct-18	1.05095	-80

In March 2019 water trap temperature was decreased to – 115 °C in an attempt to limit the amount of water in the MIRA system since it was thought to be a potential cause of the ongoing size effect being observed between large and small samples (See section 2.4 for more details). An additional water trap was installed immediately after the acid reaction vessel and pumped via a separate vacuum line to ensure that minimal water entered the main vacuum manifold through which the rest of the purification line was evacuated. Additional liquid nitrogen traps were also installed between the purification line and the vacuum manifold to stop water passing from the manifold to the later parts of the purification line (Figure 2.7 The current MIRA purification line setup. CF = coldfinger. Times at the top of the diagram indicate transfer times through each stage of the).

Porapak trap changes

At the start of this study the Porapak trap was constructed from a 9 mm inner diameter, 21 cm length glass tube filled with Porapak Q absorbent material and cooled to -20 ± 5 °C with liquid nitrogen pumping. In October 2016, following the publication of (Petersen et al, 2015) — which showed running Porapak traps at temperatures below -20 °C resulted in sample fractionation — the decision was taken to move to a design with improved temperature stability, just 7 cm in length, 4 mm inner diameter and cooled to -7.0 ± 1.0 °C with Peltier devices.

Testing of the shorter trap suggested that it was insufficient to effectively remove contamination from ‘dirtier’ samples (Figure 2.8). Thus the trap was lengthened to a 24 cm version a month later.

This configuration remained unchanged, aside from brief alterations of trap length to investigate the sample size effect (section 2.4) until May 2018 when the decision was made to revert back to a liquid nitrogen cooled system as was present at the start of the study. The decision to abandon a Peltier device cooled trap was taken because of poor reliability of the devices which needed continual replacement and would lead to extended periods when the purification line was out of operation.

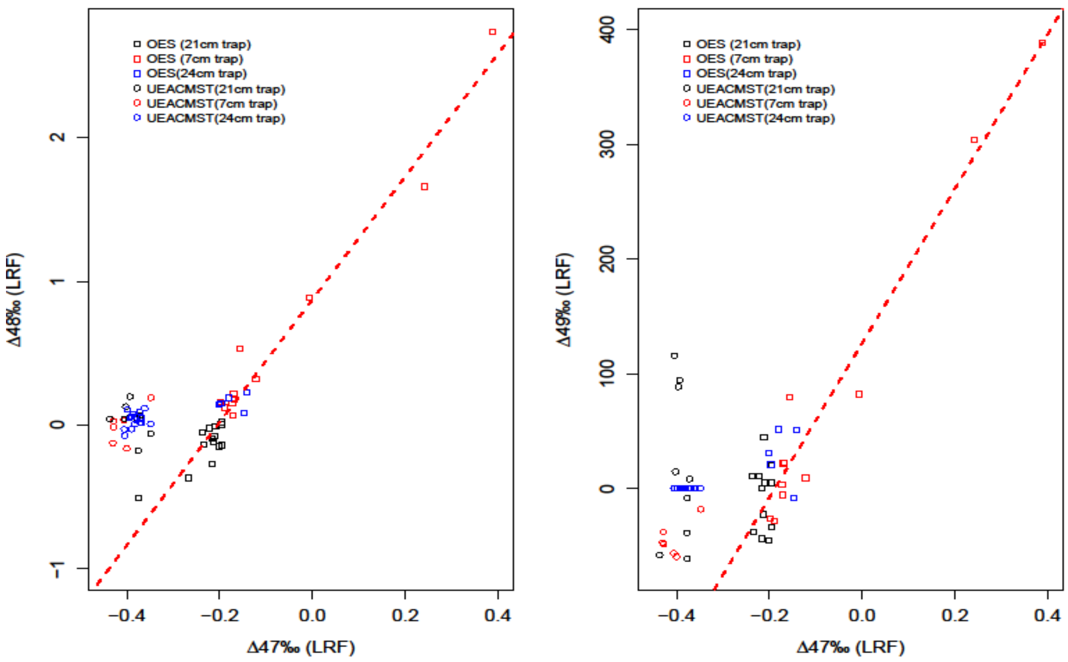

Figure 2.8 Testing of short (7cm) vs longer (21 and 24cm) Porapak traps. ‘Clean’ UEACMST sample show a tightly constrained data cloud in all trap configurations. However, ‘dirtier’ ostrich egg shell (OES) samples show increased Δ48 (LRF) and Δ49 (LRF) values when purified with the 7 cm trap suggesting contamination is present.

2.3.4 Calculating Δ values from MIRA output data

A single measurement consists of four 20 minute acquisitions throughout which mass spectrometer input is alternated between sample and reference gases every 30 seconds. Peak centering and pressure balancing was performed before each measurement with a 7.5 x 10^{-8} A signal yielded from the mass 44 beam through volume adjustment of the input bellows. Thereafter pressures are balanced automatically after each 20-minute acquisition.

MIRA output data files consist of total ion counts at masses 44 - 49 in single second intervals. The first 10 seconds of each 30 second integration is left unrecorded to remove the effect of gas mixing in the input capillaries and ion source. Thus the output file contains blocks of 20 single second counts which alternate between sample and reference, giving a total of 3200 single second counts.

Delta values were calculated using an algorithm written in the R programming language as part of this study, based on an original script developed by Paul Dennis in Wolframm Mathematica. R is a free, open source software and thus was chosen so that it could be accessed and edited by multiple users. A schematic overview is given in Figure 2.9. Values of R_{13}, R_{17} and λ are taken from Brand et al*. (*2010) as recommended by Daëron et al*. (*2016). Recent work by Petersen et al. (2019) has shown that universal adoption of the so called 'Brand parameters' acts to reduce interlaboratory discrepancies in Δ47 temperature sensitivities.

Collector counts at each mass were averaged over 20 second intervals.

$$C^*_{av} = \frac{1}{20}\sum_1^{20} C^*, \frac{1}{20}\sum_{21}^{40} C^* \dots \frac{1}{20}\sum_{n-19}^{n} C^* \qquad (1)$$

Where C* is the collector count at mass * in one second intervals and C^*_{av} is a 160 term variable containing averaged collector counts over 20 second intervals. R values, the ratio of heavy isotopologues counts to mass 44 counts were then calculated for each mass for both sample and reference gas.

$$R^* = \frac{C^*_{av}}{C^{44}_{av}} \qquad (2)$$

$$\delta^*_{running=} \frac{2.R^*_i - (R^*_{i-1} + R^*_{i+1})}{(R^*_{i-1} + R^*_{i+1})}, \frac{(R^*_{i-1} + R^*_{i+1}) - 2.R^*_{i+2}}{2.R^*_{i+2}} \dots \frac{2.R^*_n - (R^*_{n-1} + R^*_{n+1})}{(R^*_{n-1} + R^*_{n+1})} + \frac{(R^*_{n-1} + R^*_{n+1}) - 2.R^*_{n+2}}{2.R^*_{n+2}} \qquad (3)$$

Where $\delta^*_{running}$ is a 160 term variable defined physically as the mass * to mass 44 ratio of the sample relative to the mass * to mass 44 ratio of the reference gas calculated in 20 second intervals. Outlying values ± 2 standard deviations were removed before an average δ value over the whole run was calculated at each mass:

$$\delta^* = \frac{1}{160}\sum \delta^*_{running} \tag{4}$$

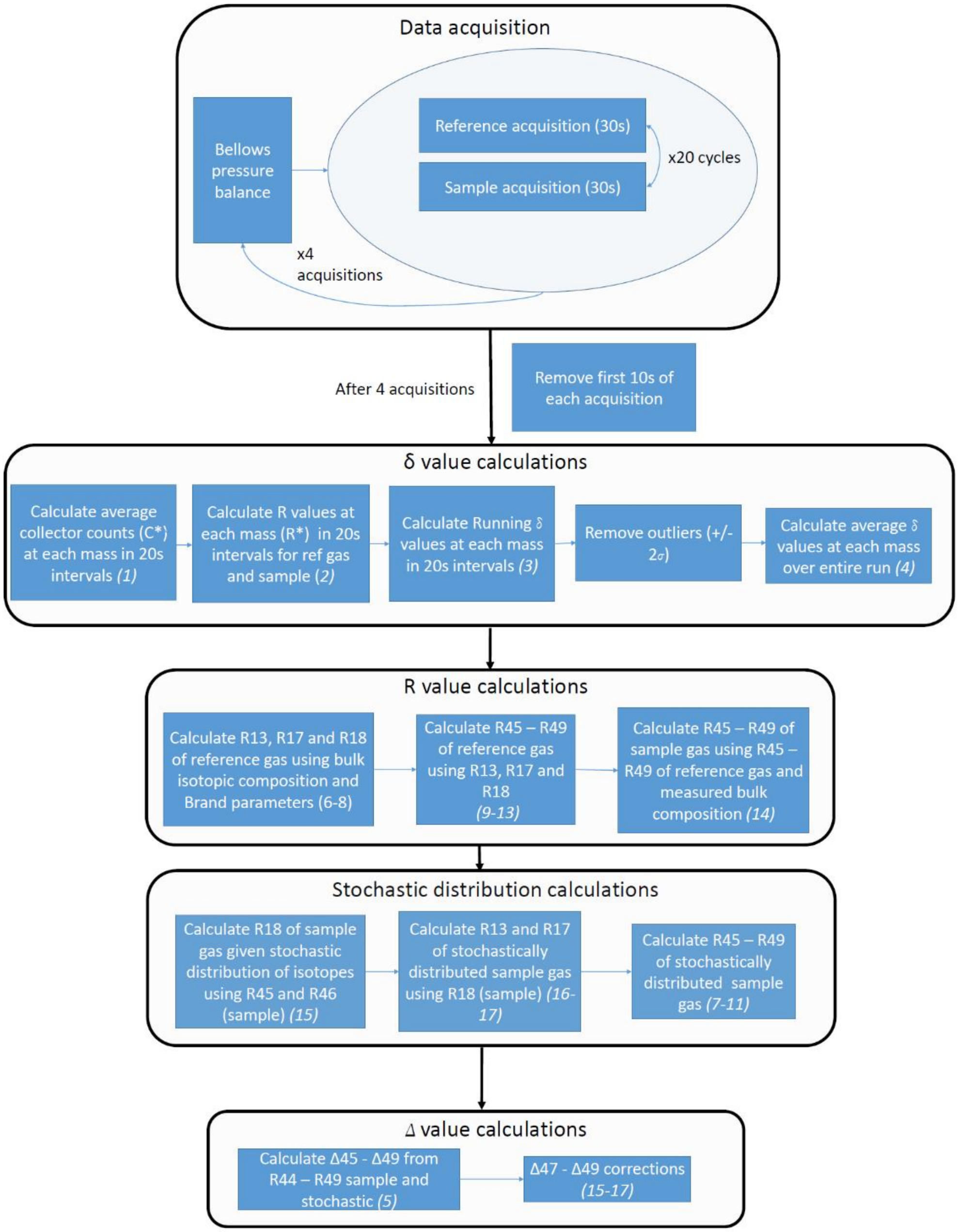

Figure 2.9 Schematic of MIRA data reduction algorithm. Bracketed numbers refer to equations detailed below.

Since… $$\Delta^{*} = \left(\frac{R^{*}_{sam}}{R^{*}_{stochastic}} - 1\right).1000 \qquad (5)$$

where R* = the ratio of counts at mass * relative to the counts at mass 44, it was necessary to obtain single values at each mass for R^{*}_{sam} and $R^{*}_{stochastic}$. R^{*}_{sam} is determined using equation (14) and substituting the δ^{*} value determined in equation (4) and the R* of the reference gas (R^{*}_{ref}). R^{*}_{ref} was first calculated from equations (9-13) (Eiler, 2007) using values of R^{13}_{ref}, R^{17}_{ref} and R^{18}_{ref} calculated from equations (6-8) and R^{13}_{VPDB}, R^{17}_{VSMOW} and R^{18}_{VSMOW} values as outlined by Brand et al. *(*2010). These describe the ratio of $^{13}C/^{12}C$ in VPDB and $^{18}O/^{16}O$ in VSMOW international standards. λ = -0.528, and is a constant characteristic of the relationship between ^{17}O and ^{18}O in the terrestrial water pool (Brand et al., 2010).

$$R^{13}_{ref} = \left(\frac{\delta^{13}C_{ref}}{1000} + 1\right) \times R^{13}_{VPDB} \qquad (6)$$

$$R^{18}_{ref} = \left(\frac{\delta^{18}O_{ref}}{1000} + 1\right) \times R^{18}_{VSMOW} \qquad (7)$$

$$R^{17}_{ref} = K \times R^{18}_{ref}{}^{\lambda} \qquad (8)$$

The stable isotopic compositions of the reference gas used in equations (6 – 8) must first be independently measured. K is calculated according to the equation $k = (R^{17}_{VSMOW} \times R^{18}_{VSMOW})^{\lambda}$

$$R^{45} = R^{13} + 2.R^{17} \qquad (9)$$

$$R^{46} = R^{18} + 2.R^{13}.R^{17} + R^{17}_{ref}{}^{2} \qquad (10)$$

$$R^{47} = 2.R^{13}.R^{18} + 2.R^{18}.R^{17} + R^{13}.R^{17^2} \qquad (11)$$

$$R^{48} = R^{18^2} + 2.R^{13}.R^{18}.R^{17^2} \qquad (12)$$

$$R^{49} = R^{13}.R^{18^2} \qquad (13)$$

With R^*_{ref} values obtained, they were substituted into (14) with δ values from (4) used to obtain R^*_{sam} — which can in turn be substituted into (5).

$$R^*_{sam} = R^*_{ref}.(1 + \delta^*) \tag{14}$$

$R^*_{stochastic}$ - the ratio of CO_2 at the mass of interest to the ratio of CO_2 at mass 44, given a stochastic distribution of isotopes within the sample, was calculated theoretically according to equations (9-13) using sample R values in place of reference values. Values for R^{18}_{sam}, R^{17}_{sam} and R^{13}_{sam} were calculated according to equations (15-17). $R^{18}_{sam}$the ratio of ^{18}O to ^{16}O in the sample, was derived from the root of equation (12) given by Santrock et al,. (1985) to account for isobaric interferences – interactions of beams consisting of several, indistinguishable isotopologues of the same mass. R^{45}_{sam} and R^{46}_{sam} are calculated previously using equation (9).

$$-3.K^2.{R^{18}_{sam}}^{2\lambda} + 2.K.R^{45}_{sam}.{R^{18}_{sam}}^{\lambda} + 2.R^{18}_{sam} - R^{46}_{sam} = 0 \tag{15}$$

R_{17} and R_{13} of the stochastically distributed sample gas were calculated with the following equations derived by Santrock et al. (1985) using values for R^{18}_{sam} and R^{45}_{sam} calculated in equations (15) and (9) respectively.

$$R^{17}_{sam} = -K.{R^{18}_{sam}}^{\lambda} \tag{16}$$

$$R^{13}_{sam} = R^{45}_{sam} - 2.R^{17}_{sam} \tag{17}$$

Values for R^{13}_{sam} , $R^{17}_{sam}\ and\ R^{18}_{sam}$ were then inputted into equations (9-13) to obtain $R^*_{stochastic}$ values. With values for R^*_{sam} and $R^*_{stochastic}$ obtained, calculations of Δ values from mass 45 – 49 using equation (5) could be made.

Δ values were then corrected using equations (15-17), derived from (Wang et al., 2004).

$$\Delta 47_{cor} = \Delta 47 - \Delta 46 - \Delta 45 \tag{15}$$

$$\Delta 48_{cor} = \Delta 48 - 2.\Delta 46 \tag{16}$$

$$\Delta 49_{cor} = \Delta 49 - 2.\Delta 46 - \Delta 45 \tag{17}$$

2.3.5 Contaminant screening

The primary contaminants at mass 47 in carbon dioxide liberated from phosophoric acid digestion of carbonates have been identified as oganic and sulfur compounds (Guo & Eiler, 2007), $^{15}N^{16}O_2$, $^{15}N^{14}N^{18}O$ and $^{14}N^{15}N^{18}O$, fragments and recombination products from halocarbons (e.g. CCl^+ from CH_3Cl or CH_2Cl_2) and other hydrocarbons (Eiler & Schauble, 2004). These can arise from a number of potential sources including leaks during the CO_2 purification procedure, sample and reagent impurities and background contaminants in the mass spectrometer – arising from memory effects between samples or cleaning agents used to service hardware.

Background currents through masses 44 – 49 were recorded at the beginning of each day to monitor for long term contamination build-up within MIRA, and peak shape scans on all masses prior to each run were used to highlight pressure sensitive backgrounds (Figure 2.4). Any contamination identified from these procedures was then corrected for in the output data processing algorithm by subtracting background counts from the measured values.

Sample specific contaminants were identified through monitoring of Δ48 and Δ49. Eiler & Schauble (2004) showed that addition of N_2O and NO_2 to pure CO_2 resulted in systematic interferences at masses 44-49. Thus noticable offsets in Δ48 vs Δ47 and Δ49 vs Δ47, that deviate from those expected from a purely temperature driven signal can be indicative of contamination from these two gases. They also showed that addition of CH_2Cl_2 and pentane to purified CO_2 produced highly linear trends between Δ47, Δ48 and the intensity of the mass 49 ion beam. Halocarbon and hydrocarbon contamination should therefore be evident in elevated Δ48 and Δ49 values.

Thus contaminated samples were identified as outliers on a plot of Δ48 against Δ47 – i.e. samples deviating from a purely temperature driven signal. Outliers were defined as those laying outside a tukey fence on a single pass Tukey filter. Figure 2.10 shows that whilst this method is affective for idenitifying contamination at mass 48, limited precision on measurements at mass 49 mean that a temperature driven relationship between Δ47 and Δ49 could not be determined ($r^2=0.00184$ for non-pressure corrected and $r^2=0.0169$ for pressure corrected samples). Thus it was necessary to apply a threshold filtering, identifying those samples with Δ49 > 2 standard deviations from the mean as contaminated (corresponding to Δ49 > 577 ‰ for non-pressure corrected data and Δ49 > 78 ‰ for pressure corrrected data). When applied to all samples between january 2018 and May 2019, these methods identified 9.5 % of samples as contaminated.

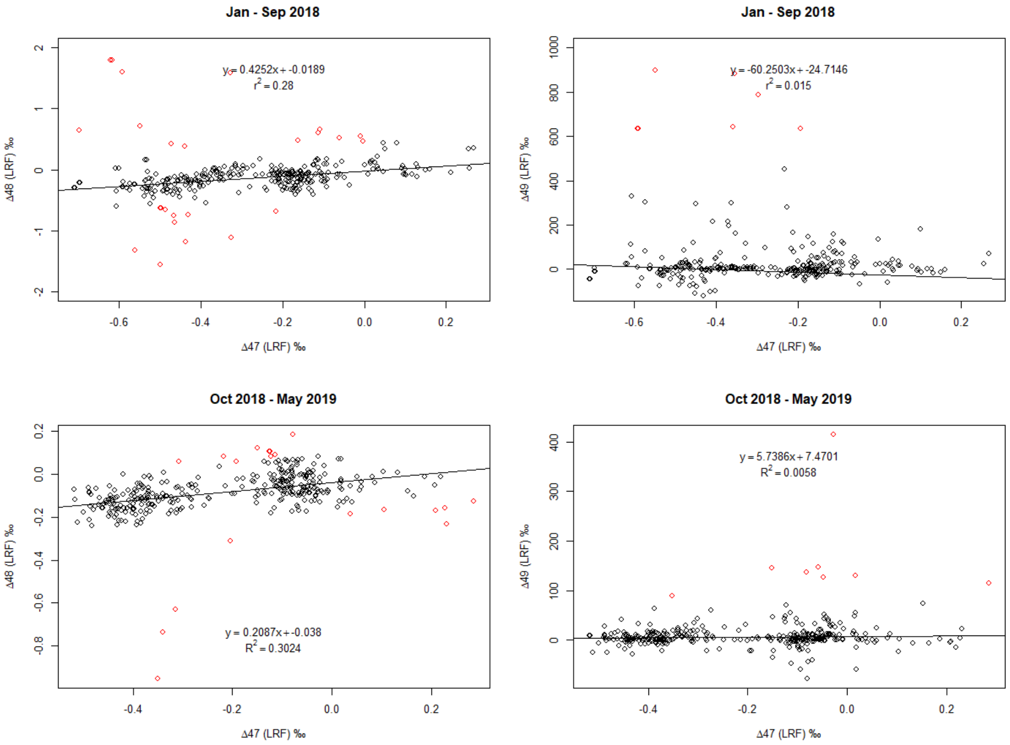

Figure 2.10 Δ47 vs Δ48 (left) and Δ47 vs Δ49 (right) plots for non-pressure corrected (top) and pressure corrected (bottom) data. Outliers (contaminated) samples are shown in red.

2.4 Sample size effect

2.4.1 Quantifying the sample size effect

Much of the changes to the purification line described in section 2.3.3 were driven by attempts to overcome a persistent offset in measured Δ47 between large and small sample volumes. Similar offsets have been observed in previous studies (Guo & Eiler, 2007; Wacker & Mainz, 2013) but have remained largely unexplored within the scientific literature. Resolving the issue is of central importance to foraminifera studies where smaller sample sizes will reduce sample picking requirements and increase the achievable resolution of palaeo-studies.

Typical sample masses required for the operation of MIRA were around 6-8 mg at the start of this study. By doubling the trap current in the ion source from 600 to 1200 µA and introducing an additional focusing plate for the ionisation beam, ion production was increased nearly four fold, amplifying the signal obtained from smaller gas volumes. This reduced the theoretical minimum sample mass of pure carbonate to approximately 1.5 mg, however a mass of 4 mg was generally measured for bulk carbonates where sample quantity was not limited. In theory it would have been possible to reduce the minimal sample size further through bypassing the sample input bellows and expanding the sample gas directly into the ion source. However, this method provides reduced control over the ion beam intensity and a trade off with measurement precision must be made.

Table 2.3 Clumped and bulk isotopic compositions for 2 mg and 4 mg UEACMST samples run between February and March 2017. Uncertainties are 95 % confidence intervals. N = number of measurements

Sample mass	N	Δ47 ‰ (LRF)	Δ48 ‰	δ^{13}C ‰ (VPDB)	δ^{18}O ‰ (VPDB)
2 ± 0.2 mg	7	-0.337 ± 0.027	-0.043 ± 0.036	2.051 ± 0.017	-2.057 ± 0.020
4 ± 0.2 mg	16	-0413 ± 0.008	-0.130 ± 0.021	2.061 ± 0.016	-2.085 ± 0.027

Measurements of 2 mg UEACMST samples exhibited a shift to higher Δ47 values compared with 4 mg samples with no comparable offset in stable isotopic compositions (Figure 2.11 and Table 2.3). This effect was seen across all laboratory standards suggesting that it is independent of both clumped and bulk composition.

Guo & Eiler (2007) postulated that the sample size effect observed in their system was likely due to isotopic exhange with water on glassware surfaces. This was ruled out for the UEA system since samples exhibited constant stable isotopic compositions regardless of sample volume. It is postulated that the effect could have arisen from either a constant background contaminant at mass 47 or an isotopic re-equilibration to lower temperatures.

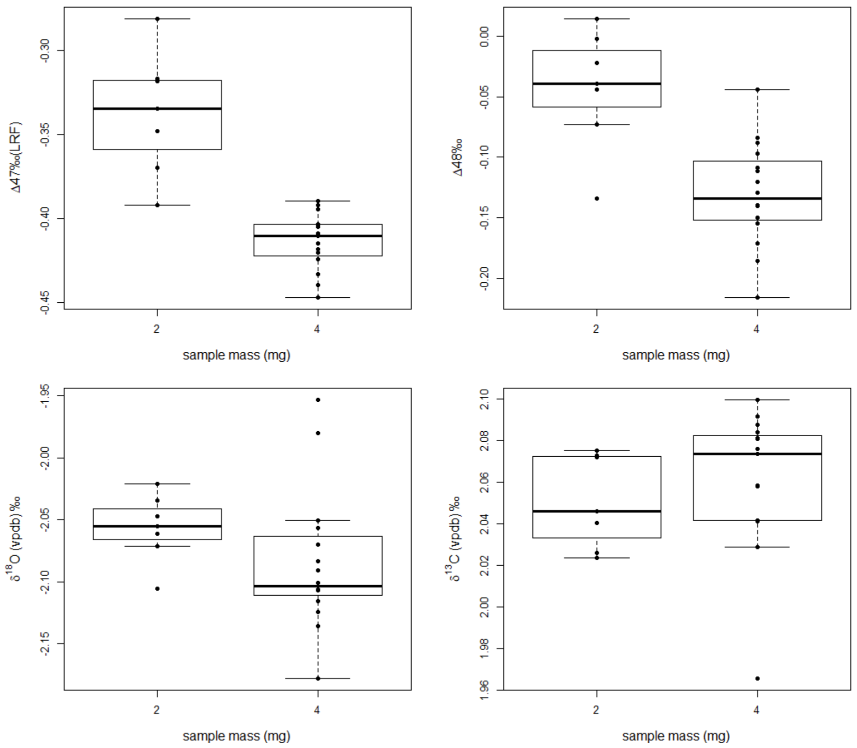

Figure 2.11 Small (2 mg) vs standard (4 mg) UEACMST samples run between February and March 2017. A persistent offset is observed in Δ47 measurements that is not seen in stable compositions. Δ47 is shown on the local reference frame

2.4.2 Identifying the source of the sample size effect

MIRA instrumentation

To test whether the sample size effect arises on MIRA or on the sample purification line, a 4 mg UEACMST sample was purified and measured according to standard procedure. After this initial measurement, the remaining sample was split on the MIRA sample input system and ~half of the sample pumped away. The remaining half size sample was measured again, achieving Δ47 values of 0.301 ‰ and 0.292 ‰ (ARF) respectively. Since no offset was observed, the source of the size effect could be attributed to the MIRA purification line.

Porapak trap

The Porapak trap was identified as the most obvious site at which a re-equilibration to lower temperatures might arise within the purification line. Monitoring pressure of the sample gas in the isolated poropak trap showed that a significant proportion of sample gas is absorbed onto the Poropak surface. Absorption exhibited a Langmuir behaviour with the quantity absorbed proprotional to gas pressure given a constant absortion surface area (Langmuir, 1918). At -20 °C nearly 25 % of CO_2 liberated from a typical sample was absorbed onto a trap of 7 cm length, 4 mm diameter, demonstrating the potential for isotopic exchange at the Porapak site, where gas molecules are held in close proximity on the PorapakQ surface.

To test whether re-equilibration occurs on the Porapak surface, a ~6 mg UEACMST sample was reacted and dehydrated before being split on the purification line into ~1/3 and 2/3 proporations to simulate the rough quantities liberated from 2 mg and 4 mg samples respectively. These two gas samples were subsequently taken through the Porapak trap separately before being measured. This experiment was repeated, giving an average Δ47 of 0.467 ± 0.02 ‰ (ARF) for the larger sample and 0.309 ± 0.03 ‰ (ARF) for the smaller sample, confirming that the size affect was present and arising on the purification line after the acid reaction and dehydration stages.

Table 2.4 Examples of Porapak trap setups in the published literature

Laboratory	Temperature	Dimensions	Reference
Caltech	-20 oC	Not given	(Eagle et al., 2015)
ETH Zurich/ Cambridge University	-20 oC	2 cm L x 6 mm ϕ	(Grauel et al., 2016; Meckler et al., 2014)
Harvard	-10 oC	Not given	(Dennis & Schrag, 2010)
Imperial College London	-35°C	13 cm L x 8 mm ϕ	(Kluge et al., 2015)
Tulane University	-15°C	18.5 cm L x 12.5 mm ϕ	(Rosenheim et al., 2013)

In laboratories that use Porapak trap setups — as opposed to gas chromatograph columns — for sample purification, considerable variability exists over the trap configuration (Table 2.4). Thus if the Porapak trap was driving isotopic re-equilibration, it may provide some explanation for the considerable variability observed between laboratories in interlaboratory calibration studies (Bonifacie et al., 2017). The recent work of Swart et al. (2019) showed strong evidence that stainless steel gas prep lines provided a medium for isotopic exchange, and it would seem reasonable that a similar exchange may occur on the glassware and Porapak Q material used in the UEA system. However, with the exception of temperature

(Petersen et al., 2015) there has been little research into the impact of differing poropak configurations.

To investigate the impact of Porapak trap configuration on Δ47, numerous trap dimensions and temperatures were investigated. In each configuration, the sample size effect was quantified with repeat measurements of UEACMST. Results are summarised in 0.

No discernible trend between sample size offset and trap length was observed (Figure 2.120). This would suggest either:

- Re-equilibration was occurring elsewhere on the latter part of the purification line, perhaps on glassware surface or,
- Even very small quantities of Porapak Q material were sufficient to cause a noticeable offset. However, since samples cleaned with a 1 cm trap showed signs of contamination in Δ48 and Δ49, it would have been impossible to overcome this effect whilst still using a Porapak trap setup.

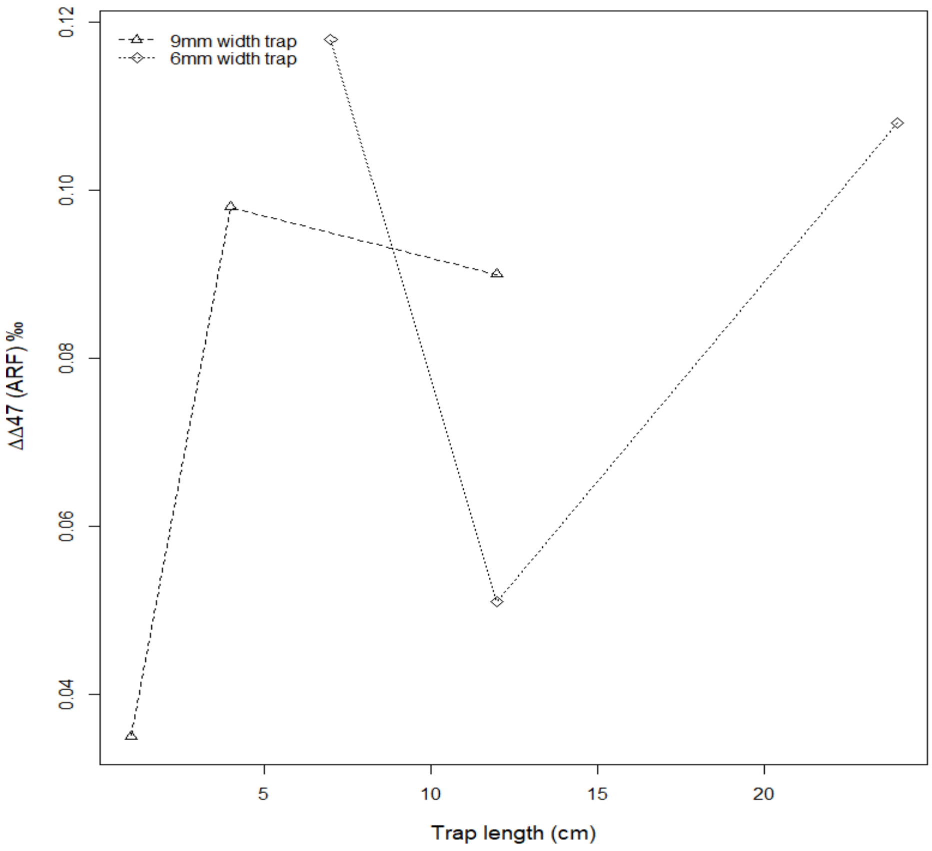

Figure 2.12 ΔΔ47 ‰, the offset in Δ47 between 4 mg and 2 mg samples with differing trap setup

Trap temperature also had little impact on reducing the offset. It was hypothesised that lower temperatures could have slowed kinetics of isotopic exchange thus reducing the offset. Traps run at -50 °C, exhibited exactly the same offset as those run at -20 °C. Similarly raising the temperature to -10 °C had no impact on measured Δ47. When the trap was run at room temperature, samples exhibited signs of contamination in the Δ48 and Δ49 signal.

A limited number of samples were also run with shorter transfer time through the Porapak trap to investigate whether reduced contact time with the Porapak Q material would impact the offset, however these samples exhibited signs of fractionation in their stable isotopic signatures.

Table 2.5 Porapak trap configurations and UEACMST isotopic measurements. Errors are 95 % confidence intervals. For single measurements, error is twice long term UEACMST standard deviation. Δ47 is not corrected for sample size (section 2.4.5). Temperature and transfer time variations are in bold.

Length (cm)	Inner Diameter (mm)	Temp (^{o}C)	Transfer time (mins)	Sample mass (mg)	N	Δ47 ‰ (ARF)	Δ48 ‰ (LRF)	δ^{18}O ‰ (VPDB)	δ^{13}C ‰ (VPDB)
24	4	-20± 0.5	60	4 ± 0.2	16	0.250 ±0.011	-0.130 ± 0.021	-2.08 ±0.03	2.06 ± 0.02
24	4	-20± 0.5	60	2 ± 0.2	7	0.358± 0.03	-0.130 ± 0.021	-2.09 ± 0.03	2.06 ± 0.02
12	4	-20± 0.5	30	4 ± 0.2	11	0.255 ± 0.02	15.89 ± 6.0	-2.06 ± 0.02	2.07 ± 0.02
12	4	-20± 0.5	30	2 ± 0.2	3	0.306 ± 0.02	24.7 ± 10.5	-2.10 ± 0.03	2.06 ± 0.003
12	4	**-10 ± 0.5**	30	2 ± 0.2	2	0.39 ± 0.03	-0.06 ± 0.06	-1.98 ± 0.09	2.09 ± 0.01
12	4	-20± 0.5	**25**	4 ± 0.2	1	0.271 ± 0.13	-0.03 ± 0.51	-2.15 ± 0.26	2.05± 0.10
12	4	-20± 0.5	**15**	4 ± 0.2	1	0.268 ± 0.13	-0.08 ± 0.51	-2.36 ± 0.26	1.97 ± 0.10
7	4	-20± 0.5	20	4 ± 0.2	4	0.247 ± 0.03	-0.09± 0.02	-2.12 ± 0.11	2.07 ± 0.04
7	4	-20± 0.5	20	2 ± 0.2	4	0.365 ± 0.06	-0.08± 0.04	-2.18± 0.14	2.07 ± 0.06
12	9	-20± 0.5	30	4 ± 0.1	8	0.325 ± 0.03	-0.14 ± 0.16	-2.03± 0.02	1.93 ± 0.02
12	9	-20± 0.5	30	2 ± 0.1	4	0.450 ± 0.04	-0.06 ± 0.1	-2.02± 0.04	1.96 ± 0.01
12	9	**+10± 0.5**	30	2 ± 0.1	1	0.540 ± 0.13	0.009 ± 0.51	-1.99 ± 0.26	1.99 ± 0.11
4	9	-20± 0.5	30	4 ± 0.1	1	0.287± 0.13	0.06 ± 0.51	-2.06 ± 0.26	1.99 ± 0.10
4	9	-20± 0.5	30	2 ± 0.1	1	0.385 ± 0.13	-0.23 ± 0.51	-2.09 ± 0.26	1.99 ± 0.10
4	9	**-50± 0.5**	30	4 ± 0.1	1	0.27 2± 0.13	-0.41 ± 0.51	-2.21 ± 0.26	1.98 ± 0.10
4	9	**-50± 0.5**	30	2 ± 0.1	1	0.385 ± 0.13	-0.31 ± 0.51	-2.09 ± 0.26	1.97 ± 0.10
1	9	-20± 0.5	6	4 ± 0.1	2	0.442 ± 0.02	0.14 ± 0.06	-2.04 ± 0.0009	1.99± 0.01
1	9	-20± 0.5	6	2 ± 0.1	2	0.475± 0.22	0.16 ± 0.23	-2.02 ± 0.02	1.97 ± 0.001
Trap bypassed				4 ± 0.1	2	0.32 ± 0.02	4.46± 0.16	-2.09± 0.01	2.04 ± 0.03

Reaction vessel

With little progress in reducing the sample size effect achieved through altering the parameters of the Porapak trap, investigations were made into whether contaminants were arising in the acid reaction vessel. To test this theory, full and half aliquots of laboratory reference gas (BDH-RT) were left overnight in reaction vessels with 1 cm^3 of phosphoric acid to allow potential impurities from the acid to migrate into sample gas. These were compared with full and half aliquots of reference gas that had been put straight through the purification line with no acid contact. Results are summarised in Table 2.6.

Table 2.6 Isotopic measurements of BDH reference gas acid equilibration test

Sample	n	Δ47 (ARF, ‰)	Δ48 (LRF, ‰)	Mean $\delta^{13}C$ (VPDB, ‰)	Mean d18O (VSMOW, ‰)
Half aliquot	2	0.950 +/- 0.007	0.10 +/- 0.07	2.04 +/- 0.08	33.74 +/- 0.09
Half aliquot acid equilibrated	2	1.00 +/- 0.06	0.23 +/- 0.20	2.08 +/- 0.04	33.81 +/- 0.04
Full aliquot	3	0.90 +/- 0.01	0.20 +/- 0.30	2.04 +/- 0.04	33.78 +/- 0.03
Full aliquot acid equilibrated	2	0.90 +/- 0.06	0.08 +/- 0.24	2.08 +/- 0.04	33.78 +/- 0.04

Little variation in Δ47 was observed between acid equilibrated and non-acid equilibrated samples, nor between large or small samples. It is interesting that these experiments yielded no sample size offset despite samples being taken through the Porapak trap prior to being measured. This would indicate that the offset cannot purely be due to a re-equilibration on the Porapak surface and that it is dependent on the presence of an acid reaction. Outgassing of an acid derived contaminant would account for such behaviour. Since the effect was also observed in samples reacted in individual reaction vessels at 25 °C it is not dependent on acid temperature, simply the occurrence of a reaction.

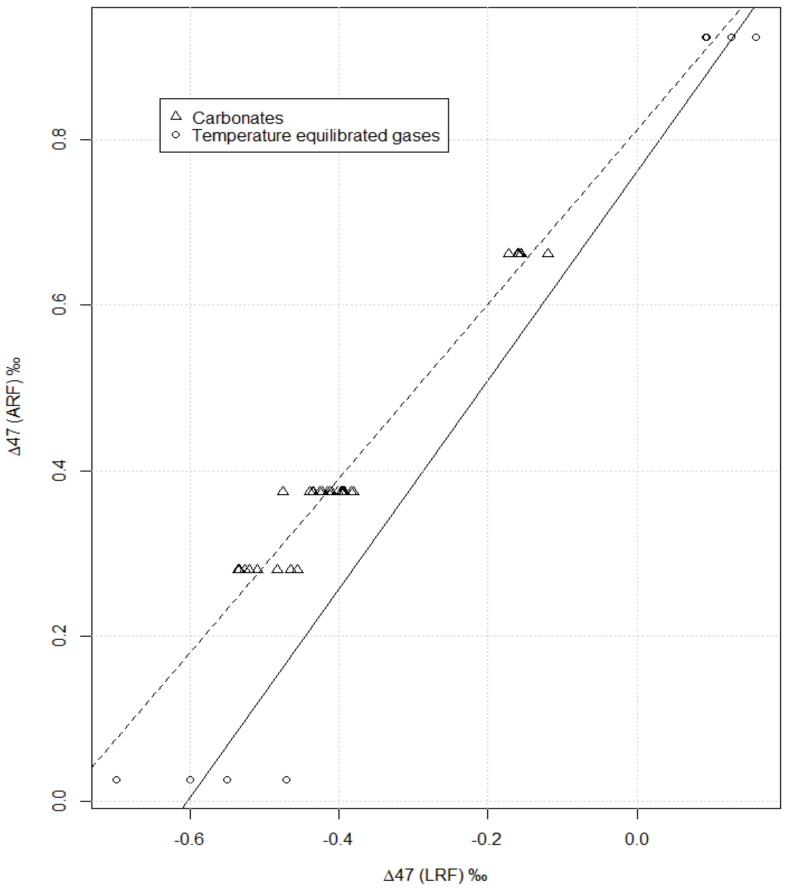

Figure 2.13 Transfer functions for August – September 2018 derived from carbonates (dashed line) and temperature equilibrated gases (solid line). Δ47 (ARF) values for temperature equilibrated gases are calculated from (Wang et al., 2004)

Further evidence that a contaminant arises from the acid reaction was obtained from comparison of laboratory transfer functions derived from temperature equilibrated gases as opposed to carbonate material (Figure 2.13). The carbonate derived transfer function exhibited a persistent intercept offset consistent with a shift to higher Δ47 (ARF) values – potentially from the presence of an acid derived contaminant.

Conclusions

The absence of the sample size effect in equilibrated gases run through the purification line suggests that the cause of the sample size effect must ultimately lay in the acid reaction (since equilibrated gases have not undergone an acid reaction). Yet the acid reaction alone cannot account for the fact that the effect was observed when a large sample, from a single reaction, was split into large and small sizes. Any contaminant present in the sample should have been present in equal concentrations in both small and large volumes since they will have been well mixed in the reaction phase.

Thus it is suggested that the sample size effect arises from an interplay between the acid reaction and the Porapak trap. The suggested mechanism arises from a constant rate of contaminant outgassing during the reaction phase which results in higher concentrations at lower sample volumes. As samples are subsequently transferred through the Porapak trap stage of the purification line, this contaminant is more readily removed in larger volume samples, since absorption onto the Porapak Q material is proportional to pressure. This acts to further amplify the sample size effect.

2.4.3 The sample size effect: candidate contaminants

Two types of contaminant could have lead to the offset that has thus far been described:

1. A carbonate derived contaminant, such as dolomite or carboxylic acids that react with phosphoric acid to produce CO_2, which mixes with sample CO_2. This seems unlikely since the sample size effect is observed across three laboratory standards (ETH1, ETH3, UEACMST) as well as in coldwater coral samples and there is no known single contaminant that could affect both organic and inorganic samples in this manner. Such CO_2 mixing would also likely lead to offsets at other masses and this is not observed.
2. An acid derived contaminant gas with a mass 47 component.

This second option would account for the persistence of the sample size offset across multiple carbonates and the fact that the offset is observed solely at mass 47. Such a contaminant must arise in the acid reaction (since no offset is seen in equilibrated gases) and is more readily absorbed by the Porapak trap in large samples (since the offset has been shown to arise at the Porapak stage of the purification line). Such behaviour seems plausible given that absorption of sample gas onto the Porapak Q surface is proportional to pressure.

Background scans during bake out of the MIRA inlet system have revealed large quantities of CCl being degassed. Chlorine is thought to arise within the MIRA inlet system from di-chloromethane, a cleaning agent used in manufacture of system valves. Whilst CCl leads to contamination at mass 47, it is thought to derive from the MIRA system rather than the purification line. Thus CCL contamination would cause an observable sample size offset in equilibrated gases, rather than solely carbonate derived gases, as well as causing a sample size shift between large and small samples split on the MIRA input system, and this is not observed.

Observation of the background pressure within the reaction vessels showed that the acid is continually outgassing water. Despite the presence of the water traps, recent analysis of background masses on the purification line conducted by Paul Dennis and Alina Marca using a quadrupole analyser showed that there is a continuous background level of water present which could give rise to the sample size offset.

It is theorised that water could dissociate within the Mass spectrometer source to form hydronium, H_3O, which then combines with carbon monoxide (dissociated from carbon dioxide) in the source, forming $H_3O\cdots CO+$ at mass 47.

$$H_2O + H_2O \rightarrow H_3O^+ + OH^-$$

$$H_3O^+ + CO \rightarrow H_3O \dots CO^+$$

Further evidence to support this theory comes from the concurrent increase of signals at both mass 18 (water) and 19 (hydronium) when the purification line was opened to the quadrupole analyser. This would suggest that water was introduced to the system and with it, the production of hydronium ions. Protonation of carbon dioxide from disassociated water derived hydrogen has been shown to cause measurable enrichments at masses 45 and 46 (Leckrone & Hayes, 1998). This may be the first evidence that water derived products also cause interference at higher masses.

Further work is required to determine whether this hypothesis holds up to robust scrutiny and the recent acquisition of a quadrupole analyser by the stable isotope laboratory should allow this. Should water be the cause of the sample size effect, a contribution to $\delta^{18}O$ from water derived oxygen should be observable between small and large samples. So far this has not been observed.

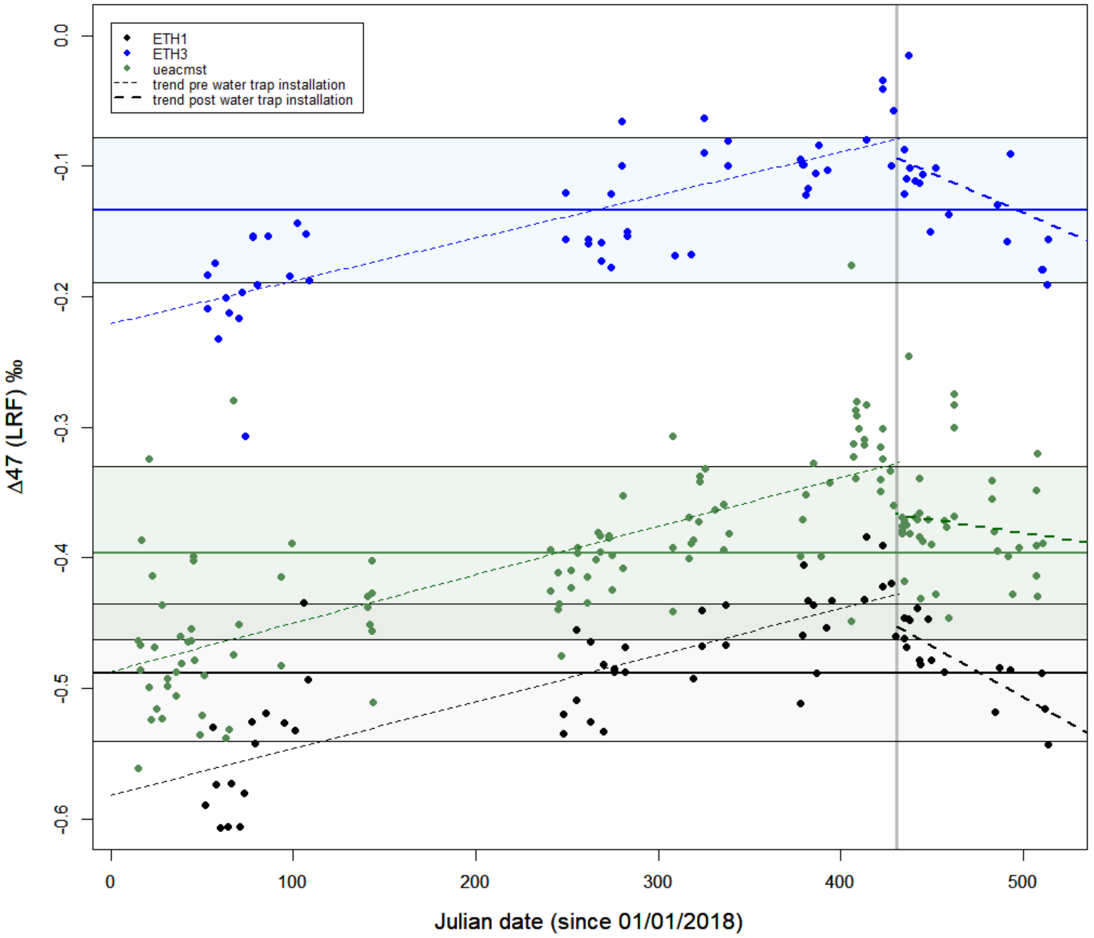

Figure 2.14 Δ47 (LRF) for three laboratory standards (ETH1, ETH3 and UEACMST) measured between January 2018 and May 2019. Solid horizontal lines show the measurement means, shaded areas the standard deviation. The grey vertical bar at day 431 marks the installation of the additional water traps on the sample purification line in March 2019. Dashed lines are linear trends through each standard, prior to and subsequent to the installation of additional water traps.

Efforts to eliminate the sample size effect are ongoing. Most recently, three additional water traps were installed on the purification line in an attempt to limit the amount of water passing between the vacuum manifold and the latter stages of the line (section 2.3.3). Initial measurements of standards immediately after installation showed a decreasing trend in Δ47 as would be expected with the ongoing removal of water (Figure 2.14). Ongoing monitoring of the sample size effect will determine whether installing these additional traps has been successful.

It is worth noting that a water derived mass 47 component may provide some explanation for the differing intercepts observed between laboratories in Δ47 calibration studies (Bonifacie et al., 2017). Sample drying methodology varies dramatically between labs. This will give rise to variable water derived Δ47 signals, and subsequently, variable degrees of offset from the theoretical calibration line.

2.4.4 Choice of sample mass

The continued persistence of the sample size effect required that all samples are measured at constant mass. Generally, clumped isotope measurements require comparatively large sample gas volumes for extended integration times that allow part per million enrichments to be resolved. Desired precision is generally achieved through 2-3 repeat measurements of 4-5 mg with prolonged integrations times (Tripati et al., 2010) or through pooling a large number (51-99) of small (~120 µg) adjacent samples from relatively stable climatic periods (e.g Leutert et al., 2019). Both methods require between 6 – 15 mg of sample. However, if it is desirable to achieve high resolution palaeoclimate records from foraminifera, rivalling those obtained from more established proxies like stable isotopes or Mg/Ca ratios, it will be necessary to dramatically reduce samples masses even further.

Table 2.7 Standard deviations for 2 mg and 4 mg laboratory standards.

	n	**Δ47 σ (LRF,‰)**	**d13C σ (‰ VPDB)**	**d18O σ (‰ VPDB)**
ETH1 2 mg	9	0.0576	0.0131	0.0450
ETH1 4 mg	10	0.0307	0.0087	0.0409
ETH3 2 mg	10	0.0404	0.0295	0.0711
ETH3 4 mg	11	0.0196	0.0155	0.0567
UEACMST 2 mg	9	0.0536	0.0252	0.0557
UEACMST 4 mg	9	0.0242	0.0242	0.0375

In order to investigate the impact of reduced sample masses on measurement precision, repeated measurements of laboratory standards ETH1, ETH3 and UEACMST were conducted at masses 2 mg and 4 mg over a three-month period between November 2018 and January 2019. The standard deviations are presented in Table 2.7.

Standard deviation in Δ47 of 2 mg samples increases in all three standards when compared to 4 mg and more than doubles in ETH3 and UEACMST (Table 2.7). This suggests that any reductions in uncertainty gained from additional repeat measurements of 2 mg samples will be more than negated by decreased measurement precision. Poorer precision is also observed on 2 mg samples for stable isotope measurements.

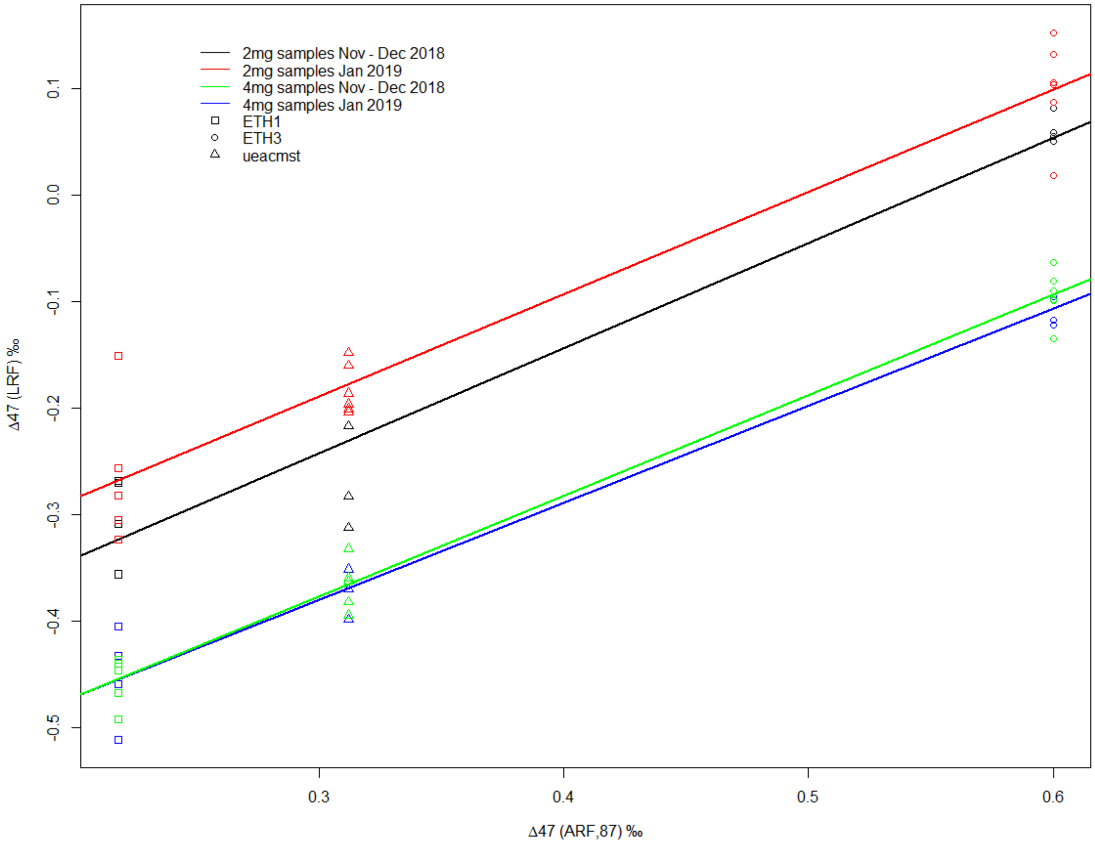

Figure 2.15 Transfer functions constructed from 2 mg and 4 mg standard samples November 2018 – January 2019. A migrating intercept is seen in smaller, 2 mg samples.

The impact of increased variability of 2 mg samples can be seen by constructing transfer functions for samples run between November and December 2018 versus those run in

January 2019 (Figure 2.15). 2 mg samples exhibited a 0.2 ‰ offset in intercepts between the two periods whereas 4 mg samples were within error. Since the sample size effect is thought to arise from a constant background contamination at mass 47, smaller samples will therefore exhibit a larger shift as contamination levels drift over time. Thus in a small sample system, standards will need to be run at more regular intervals in order to construct regularly updated transfer functions.

The results of these experiments suggest that 4 mg samples should be run in preference to 2 mg samples. This will act to reduce the spread in measurements and limit the need for additional standard measurements and more regular transfer function updates. 4 mg of carbonate corresponds to about 500 foraminifera tests in the 300-355 µm size fraction.

2.4.5 Correcting for the sample size effect

As outlined throughout this section, a persistent trend towards elevated Δ47 was observed with decreasing sample size. The impact was reduced by measuring samples of consistent mass (4 mg), yet the quantity of sample gas liberated through acid digestion remained unpredictable, varying with the concentration of non-carbonate impurities.

Table 2.8 Relationship between Δ47 (LRF) and sample size for UEACMST calculated by calendar month. Limited data prior to October 2018 and throughout March 2019 mean the relationship cannot be reliably established during these periods.

Month	Gradient	Intercept	R^2	Sample size range ($mbar^{-1}$)
Jan-18	13.84	-0.78	0.03	0.002
Feb-18	7.68	-0.65	0.19	0.010
Mar-18	41.21	-1.46	0.98	0.002
Apr-18	7.66	-0.58	0.55	0.008
May-18	-6.85	-0.30	0.02	0.002
Sep-18	4.59	-0.51	0.07	0.006
Oct-18	6.09	-0.53	0.76	0.024
Nov-18	2.29	-0.41	0.13	0.043
Dec-18	25.42	-0.93	0.97	0.001
Jan-19	8.41	-0.55	0.92	0.026
Feb-19	18.85	-0.73	0.70	0.009
Mar-19	-16.16	0.00	0.09	0.004
Apr-19	6.68	-0.52	0.98	0.039
May-19	6.98	-0.56	0.66	0.018

With little success in eradicating this sample size effect, it was necessary to quantify and correct for it after measurement. The correction was obtained from the gradient of the plot of inverse of the barrocell pressure (proportional to sample gas volume), recorded during purification, against Δ47 on the local reference frame.

Analysis of long running laboratory standard datasets (Figure 2.16 and Table 2.8) showed the relationship between Δ47 (LRF) and sample size changed over time, with the shifting local laboratory reference frame, and it was therefore necessary to measure and define at regular temporal intervals. Prior to October 2018 and throughout February - March 2019, limited spread in sample volume (barrocell pressure range <0.01 mbar^{-1}) meant there was insufficient data to reliably define the relationship during these periods.

Selected Δ47 (LRF) vs inverse barrocell pressure plots for four laboratory standards from October 2018 to May 2019 are presented in Figure 2.16 and Figure 2.17. The spread in sample sizes (inverse pressure range > 0.01 mbar^{-1}) and regression fit (R^2 > 0.75) for the relationships plotted in Figure 2.17 were considered large enough to infer a reliable sample size correction. The gradients for each of the four standards are presented in Table 2.9. For a given month, gradients across the four standards fall within error of each other, suggesting that the effect is independent of the isotopic composition of the sample. Significant offsets in the gradients between months for a single standard highlighted the need to regularly quantify the effect by measuring standards of different volumes.

Table 2.9 Monthly gradients for the relationship between Δ47 (LRF) and sample size for four laboratory standards where R2> 0.75 and sample volume range > 0.01 mbar-1 (as measured on purification line barrocell).

Month	UEACMST	ETH1	ETH3	Coral	monthly mean
Oct-18	6.09 (± 1.03)				6.09
Dec-18		6.47 (± 1.17)	7.11 (±0.51)		6.79
Jan-19	8.41 (± 0.80)	8.76 (± 0.82)	9.08 (±0.67)	8.61 (±0.64)	8.71
Apr-19	6.68 (± 0.33)				6.68
May-19				5.75 (±0.59)	5.75

It is clear that the magnitude of the effect is sufficient to have a dramatic impact on measured Δ47 for even small volume variations. Foraminifera measurements are particularly susceptible given the variable amount of sediment contamination present in each sample, making the quantity of gas liberated through acid digestion highly variable. For a given Δ47 the typical pressure, measured on the purification line, ranged between 30 and 47 mbar for 4 mg foraminifera samples. This gives rise to an offset of approximately 0.1 ‰.

Thus for the purposes of this study, samples run between October 2018 and May 2019 had a sample volume correction applied before they were projected onto the absolute reference frame. This time period encompassed the majority of foraminifera samples measured in this study. Prior to October 2018, where insufficient data exists to reliable quantify the sample size effect, no correction was applied.

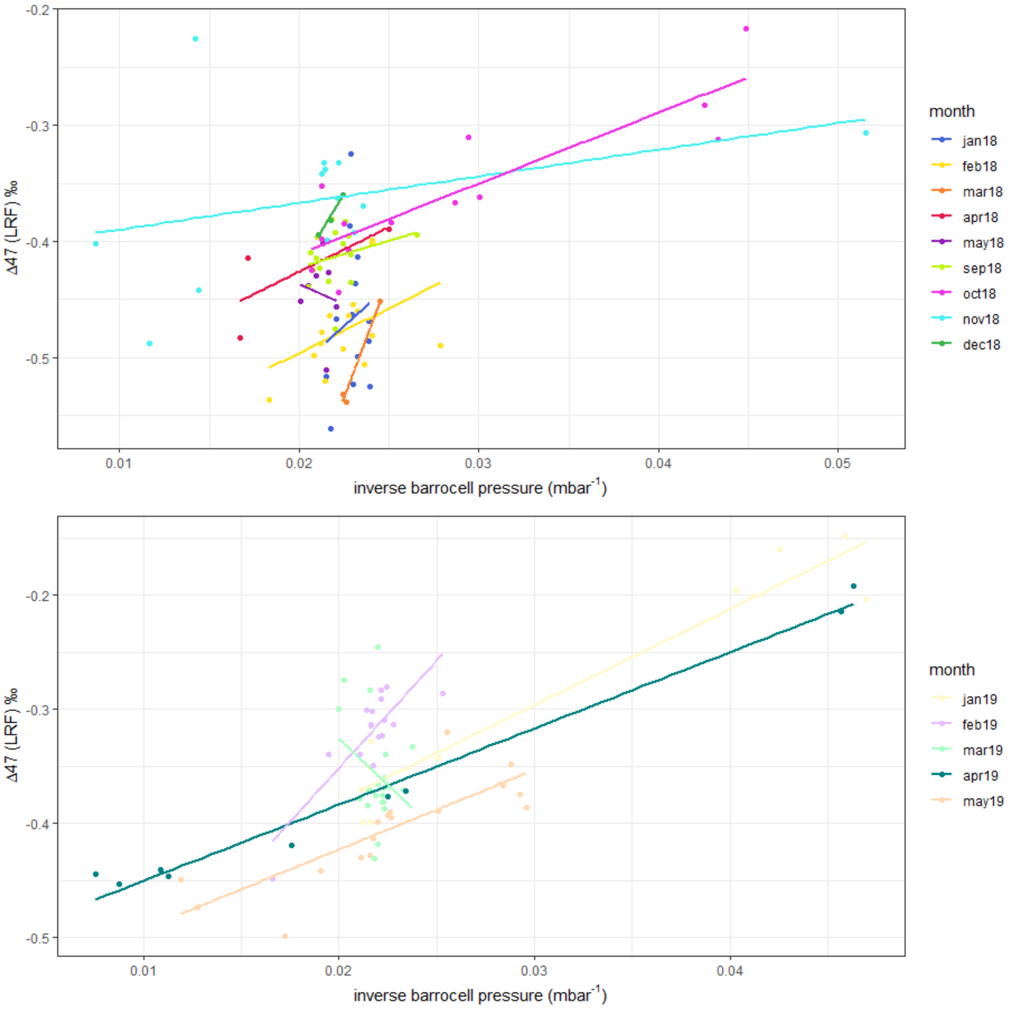

Figure 2.16 Relationship between Δ47 (LRF) and sample size for UEACMST calculated by calendar month for 2018 (top) and 2019 (bottom)

Since the size effect was shown to shift with time, it was desirable to minimise the temporal window of the standard database from which the correction is calculated around the date on which the sample is run. This time window selection was achieved with an algorithm, written in the programming language R, which adheres to the following steps:

1. Standards from the four listed in Table 2.9 were iteratively selected ± one day around the date on which the sample was run. This creates four standard databases.
2. Each time a standard was added to the database, the relationship between Δ47 and sample volume was calculated for each standard.
3. For a given standard, once the sample volume range exceeds 0.01 mbar^{-1} (as measured on purification line barrocell) AND $R^2 > 0.75$ for a single standard, the gradient of the relationship was used to correct Δ47 of the sample on the LRF as follows:

$$\Delta 47_c = \Delta 47_m - \left(\frac{1}{P_b} \times m\right)$$

Where $\Delta 47_c$ and Δ47 m are the corrected and measured sample Δ47 values, P_b is the sample barrocell pressure and m is the gradient of the Δ47 vs barrocell pressure^{-1} standard plot.

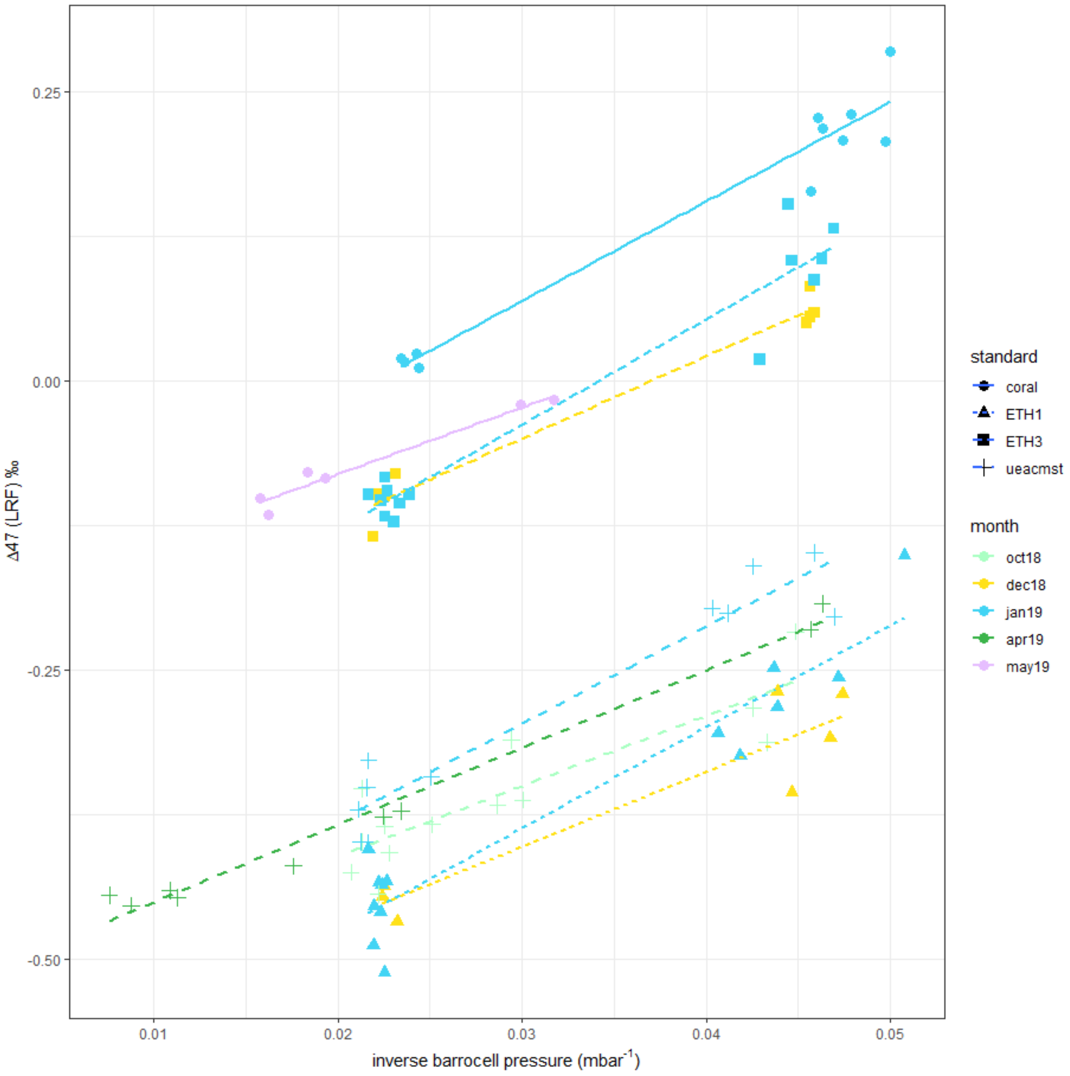

Figure 2.17 Δ47 (LRF) vs inverse barrocell pressure for four laboratory standards where R^2 > 0.75 and range in barrocell pressures > 0.01 mbar^{-1}, calculated by calendar month.

Applying the correction to UEACMST, ETH1, ETH3 and coldwater coral standard measurements run between October 2019 – May 2019 reduced the spread in Δ47 (LRF) for all samples (Figure 2.18 & Table 2.10 Corrected and uncorrected Δ47 (LRF) mean and standard deviations for four laboratory standards). A shift to lower Δ47 (LRF) values was observed in all standards. The mean corrected Δ47 (LRF) can be considered the ‘true’ Δ47 (LRF) value, equal to the intercept of the Δ47 (LRF) vs inverse pressure plot. Theoretically this value represents an infinite quantity of sample gas (since $\lim_{P_b \to \infty} \left(\frac{1}{P_b}\right) = 0$) and the sample measurement given negligible contamination.

Table 2.10 Corrected and uncorrected Δ47 (LRF) mean and standard deviations for four laboratory standards

Standard	Mean Δ47 (LRF) uncorrected	Mean Δ47 (LRF) corrected	Uncorrected Δ47 σ	Corrected Δ47 σ
UEACMST	-0.361	-0.545	0.069	0.055
ETH1	-0.407	-0.637	0.094	0.082
ETH3	0.069	-0.178	0.134	0.055
coral	-0.059	-0.292	0.089	0.051

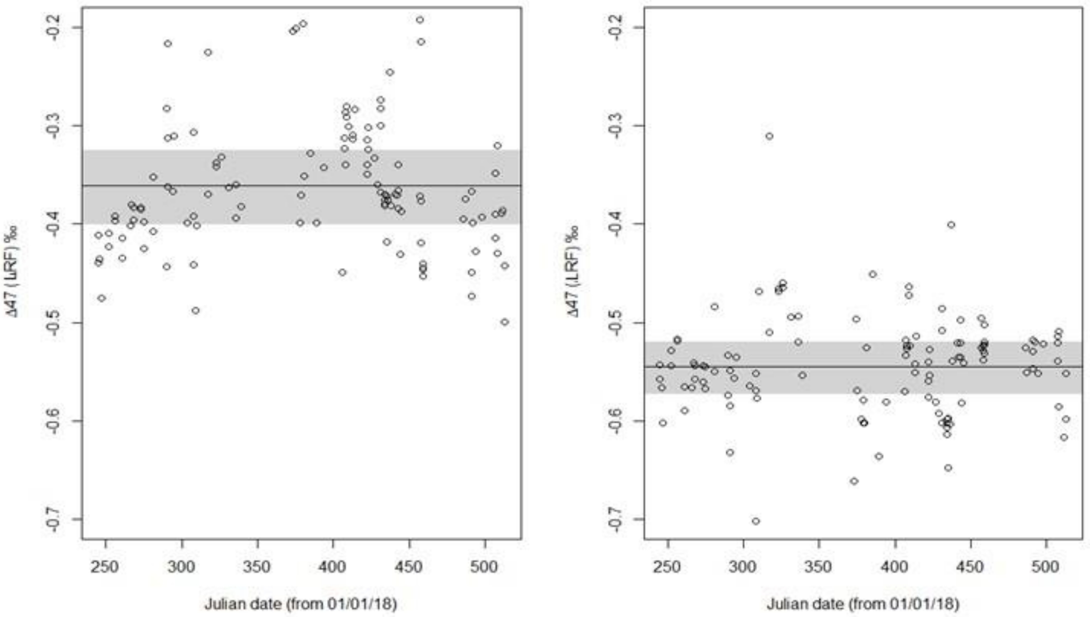

Figure 2.18 Uncorrected (left) and pressure corrected (right) UEACMST samples run between October 2018 – May 2019 showing the shift to reduced Δ47 (LRF) and reduction in data spread when the pressure correction is applied. Horizontal bar is the sample mean and shaded regions, the interquartile range.

2.5 Projection onto the absolute reference frame

Dennis et al. *(*2011) highlighted the need for an absolute reference frame (ARF) onto which clumped isotope measurements could be reported to enable comparison between laboratories. Since each mass spectrometer exhibits a unique degree of non-linearity and scale compression, raw Δ values cannot be directly compared between instruments. Even within a single laboratory, instrument parameters can change over time as components wear and ambient conditions change. Thus it is necessary to project measurements from a local laboratory reference frame onto a single, universal reference frame, herein known as the absolute reference frame (ARF).

The projection method outlined in Dennis et al. *(*2011) describes a twostep process beginning with the quantification of instrumental non-linearity with respect to bulk isotopic composition. This describes the relationship between Δ47 and Δ48, and the bulk composition of an analytical sample with respect to the laboratory's working reference gas ($δ^{47}$). Linearity quantification is achieved via the measurement of a suite of gases, differing in bulk isotopic composition, that have been equilibrated to the same, known, temperatures. The linear regressions obtained when plotting Δ values against $δ^{47}$ (both measured with respect to the laboratory working reference gas) describe the non-linearity of the specific instrument (Figure 2.19, top). The intercept of each regression line is the difference in Δ value between the equilibrated gas and working reference gas when both have the same bulk isotopic composition ($\Delta_{[EG\text{-}WG]0}$).

$\Delta_{[EG\text{-}WG]0}$ at multiple temperatures is then plotted against the accepted theoretical Δ values (Figure 2.19, bottom), calculated according to quantum mechanical and statistical thermodynamic predictions (Wang et al., 2004). The resulting transfer function is then used to project laboratory measurements onto the absolute reference frame.

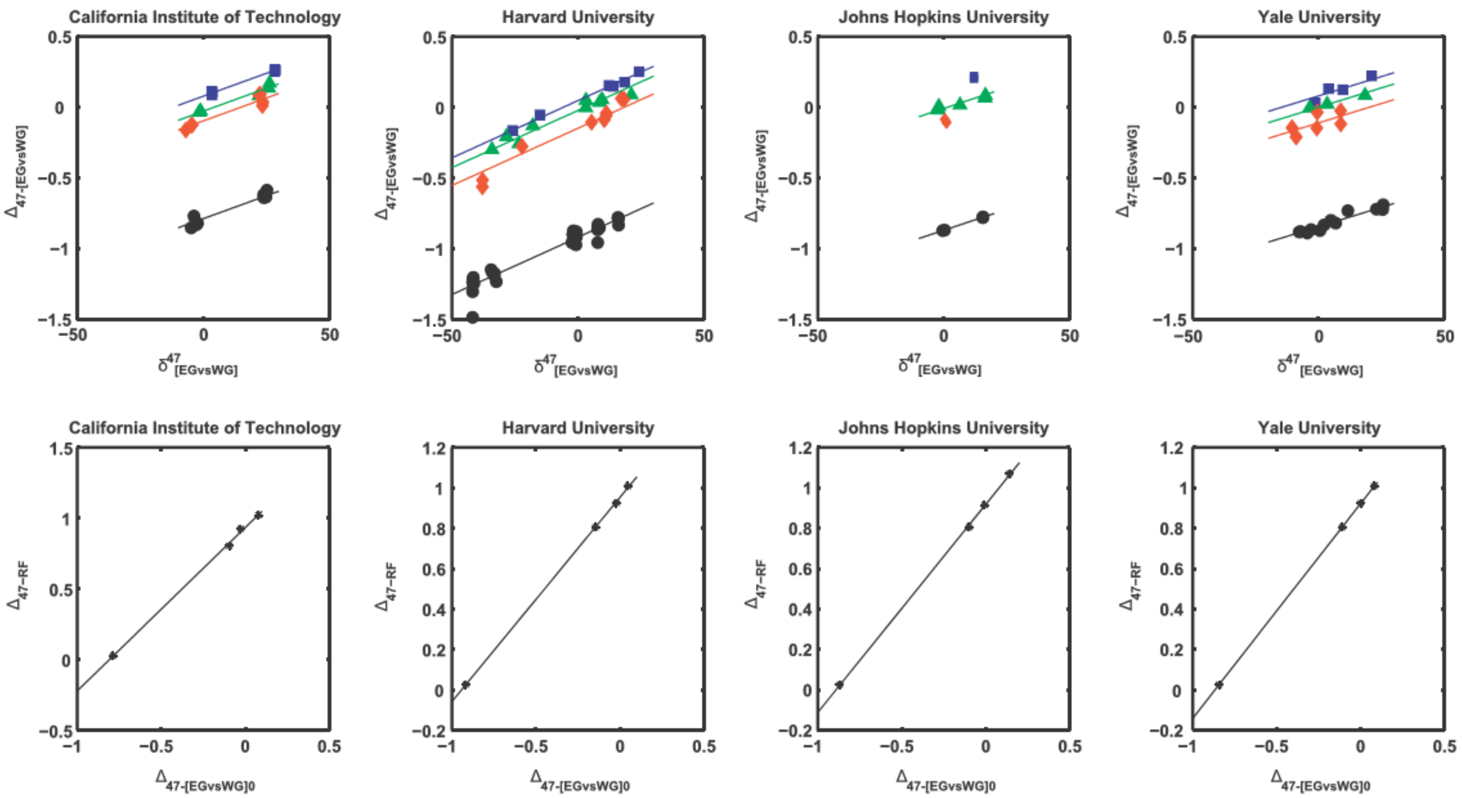

Figure 2.19 Top: Non-linearity plots for four clumped isotope laboratories. Δ47 of temperature equilibrated gases with respect to the working reference gas are plotted against δ47. The resulting regression line describes the non-linearity of the instrument. The different coloured lines correspond to gases equilibrated to different temperatures: 0-10 oC, 25-27°C, 50 °C + and 1000 °C correspond to blue, green, red and black lines respectively. Bottom: Δ[EG-WG]0 against known theoretically calculated Δ47 (Source: Dennis et al. *(*2011)).

Dennis et al. (2011) acknowledge the impracticalities of continual measurement of suite gases and suggest instead measuring just a few laboratory standard gases, equilibrated to known temperatures on a regular basis. This data can be used to adjust the underlying linearity correction and monitor short-term shifts in non-linearity.

Dennis, P (2014) showed that MIRA exhibits no systematic offset in Δ values with bulk isotopic composition under measurement of such a suite of gases (Figure 2.20), demonstrating the linearity of the instrument. As such, regular assessment of non-linearity through gas suite measurements is not required to interpret MIRA data, making day-to-day projection onto the absolute reference frame a single step process.

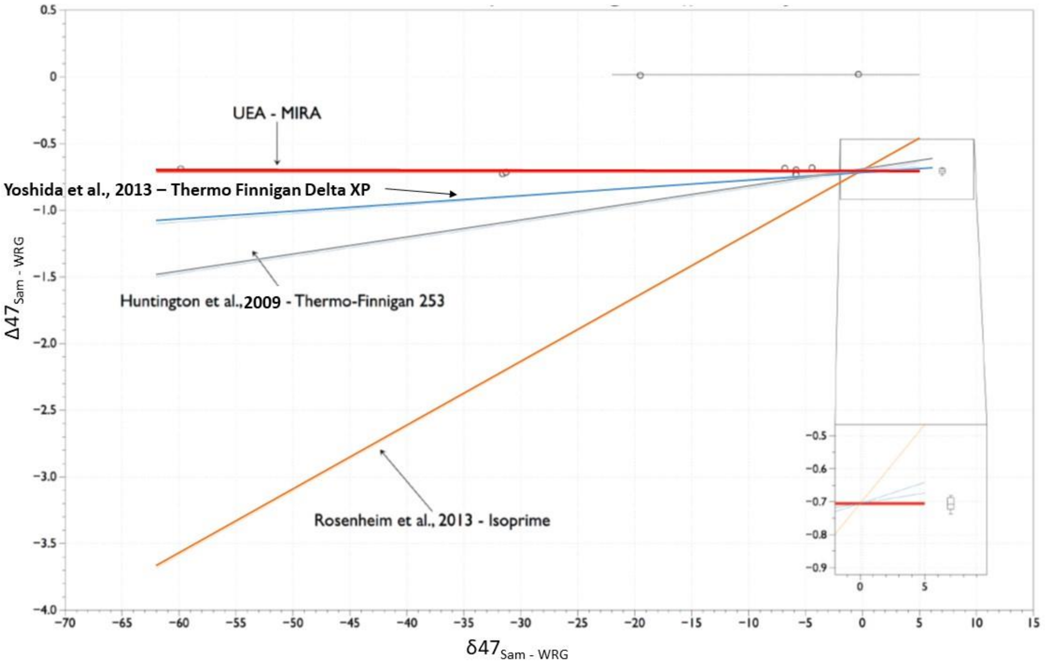

Figure 2.20 The zero gradient obtained from plotting $\delta^{47}_{\text{sample-working reference gas}}$ vs $\Delta47_{\text{sample-working reference gas}}$ for a suite of gases heated to 1000 °C (stochastically distributed) with variable bulk composition demonstrates the linearity of MIRA (adapted from Dennis (2014)). Compared alongside Thermo-Finnigan 253 (Huntington et al., 2009), Thermo- Finnigan Delta Plus (Yoshida et al., 2013), and Isoprime (Rosenheim et al., 2013) instruments.

At the beginning of this study, transfer functions were constructed from a suite of gases equilibrated to known temperatures, predominantly 25 °C and 1000 °C. Absolute Δ47 values were obtained from the theoretical calculations of Wang et al. *(*2004). In early 2018, following the publication of Bernasconi et al*.* *(*2018), in which the variation in gas preparation and sample treatment were highlighted as a potential cause of discrepancy between laboratories, the decision was taken to move to a carbonate derived transfer function. This has coincided with the period over which the vast majority of samples in this study have been measured.

The UEA transfer function is constructed from the daily measurement of at least one of three laboratory standards: ETH1, ETH3, or UEACMST. These standards are of known but differing Δ47 (ARF), established through long term measurement against equilibrated gases. Laboratory Δ47 (ARF) values of ETH1 and ETH3 were used in preference to published values (Bernasconi et al., 2018; Meckler et al., 2014) since the latter are found to give rise to erroneously high Δ47 (ARF) values for samples of known temperature. The plot of measured Δ47 (Δ47(LRF)) against known Δ47 (Δ47 (ARF)) defines a transfer function which is used to project measurements from the local to the absolute reference frame.

Whilst Dennis et al*. (*2011) outline the generalised protocol with which to construct Δ47 transfer functions, there is little published research on the number of standard measurements required or the ideal time window over which a transfer function should be constructed for robust projections. The time window must be of sufficient length to encompass enough standard measurements to define a robust relationship, whilst being short enough to limit the impact of instrumental drift over time. With a variable number of standards run each day, and instrumental downtime leading to an unequal temporal spread in standard measurements, the optimum timeframe over which to calculate the transfer function is not obvious. Nor is it apparent whether each sample should be treated in the same fashion, instead it may be more effective to vary the transfer function time window depending on the concentration of standards run in the days surrounding it.

To further investigate the optimum transfer function time window, four methods where explored for constructing the transfer function:

1. Daily optimum method
2. 19 nearest neighbours
3. Monthly transfer functions
4. Rolling window

These are explored in more detail throughout this section.

2.5.1 Daily optimum method

All 4 mg standard data between January 2018 and May 2019 was pooled into a single dataset (herein the standard dataset. Note this dataset has not been corrected for sample size effect due to insufficient data making this impossible prior to October 2018 (section 2.4.5)). In order to limit the spread in Δ47 (LRF) caused by the sample size effect, only standards weighing 4 mg ± 0.2 mg were considered. Each standard in the standard dataset was iteratively selected (called the sample standard) and a transfer function dataset created for it by iteratively adding standards run ± n days either side of the sample standard run date, with n increasing in integers from one to 30. Each time a new standard was added to the transfer function dataset, a transfer function was calculated and used to project the sample standard onto the ARF. The percentage error between the projected sample standard value and the ‘accepted’ value was then calculated. In this way it was possible to deduce the optimum number of samples to include in the transfer function for each day that gave the minimum offset between standard sample Δ47 (projected) and the accepted value. These ‘daily optimum’ transfer functions were then used to project sample data onto the ARF. Samples were then corrected to a 25 °C reaction temperature using the theoretical correction of 0.001 ‰°C^{-1}, calculated by Guo et al. *(*2009).

This method is particularly vulnerable to outliers – if the daily standard sample is anomalous it will lead to an erroneous transfer function, in turn causing a poor projection of real sample data onto the ARF. To minimise this effect, a 2-pass 30-day rolling Tukey filter (Tukey, 1977) was first applied to the standard dataset. This acts to remove standard samples lying more than 1.5 times the interquartile range away from the standard sample mean. Six percent of measurements were filtered out in this process, reducing the mean standard deviation for the three standard samples from 0.067 ‰ to 0.064 ‰.

For a given sample standard, the percentage error from the ‘accepted’ value decreases as additional measurements are added to the transfer function and a more robust fit is achieved (Figure 2.21). Error gradually decreases to a minimum, at which point the optimum transfer function is obtained, and subsequently increases as temporally distant datapoints are added, and the impact of instrumental drift is observed. The ‘optimum’ number of data points to include in a transfer function varied dramatically between 6 and 63 for the standard dataset — the larger numbers being obtained after prolonged periods of instrumental downtime during which substantial instrumental drift occured. Averaging the percentage error across all samples shows no obvious ‘universal’ optimum number of samples to include (Figure 2.21) therefore each day should have its own bespoke transfer function. The average minimum percentage error across the entire standard dataset was 5.4 %.

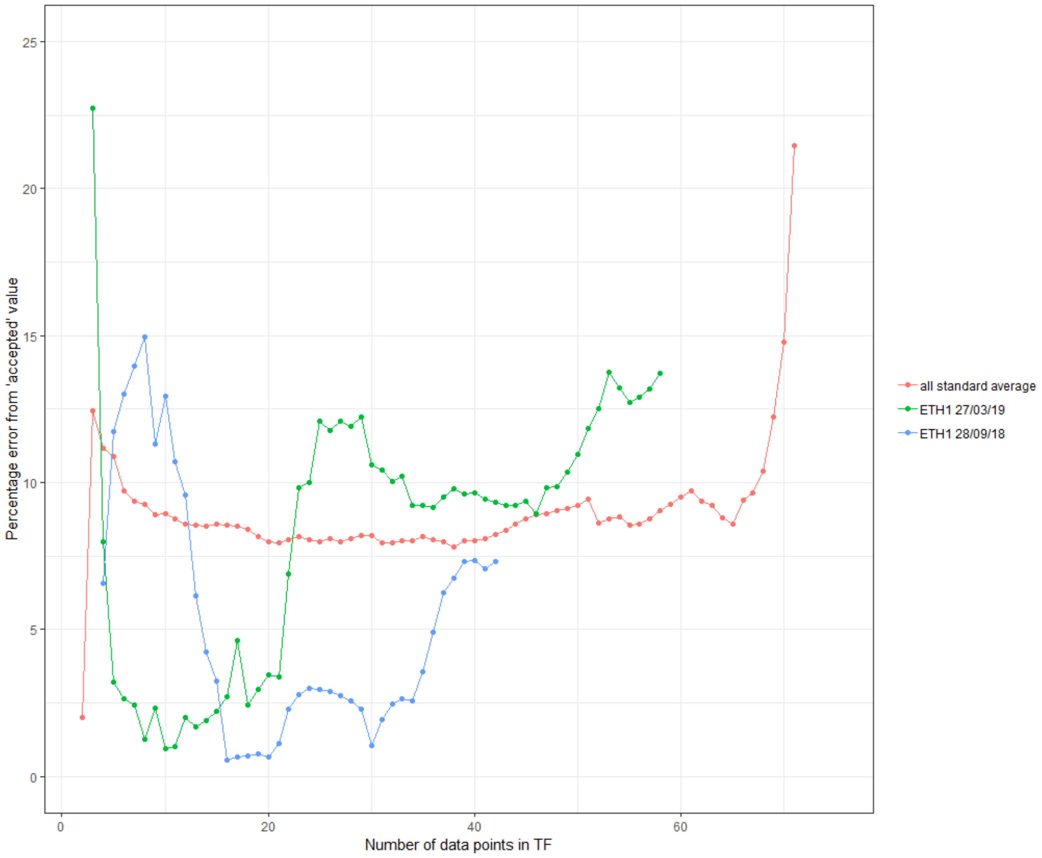

Figure 2.21 The variability in percentage error of calculated standard sample ARF from the 'accepted' value. Two ETH1 samples have been selected at random and shown to illustrate how the 'optimum' number of standards to include varies considerably between samples. The all standard average shows the average percentage error across all standard samples for a given number of data points included in the transfer function.

2.5.2 19 nearest neighbours

The daily optimum method outlined in 2.5.1 revealed that the median optimal number of standards to include in a transfer function is 19. However, the optimum time window over which to calculate the transfer function varied considerably between 4 and 30 days (Figure 2.22). Following from these findings, the 'nearest neighbours' method selects the 19 temporally closest standards to the sample run to calculate a transfer function unique to the sample. If the pool of 19 standards does not include at least one of each of the three laboratory standards, additional standards are iteratively added to the standard pool ± n days either side of the sample run date, until this condition is met. A 2-pass Tukey filter (Tukey, 1977) is then applied to the standard pool standards to remove outliers before the transfer function is calculated.

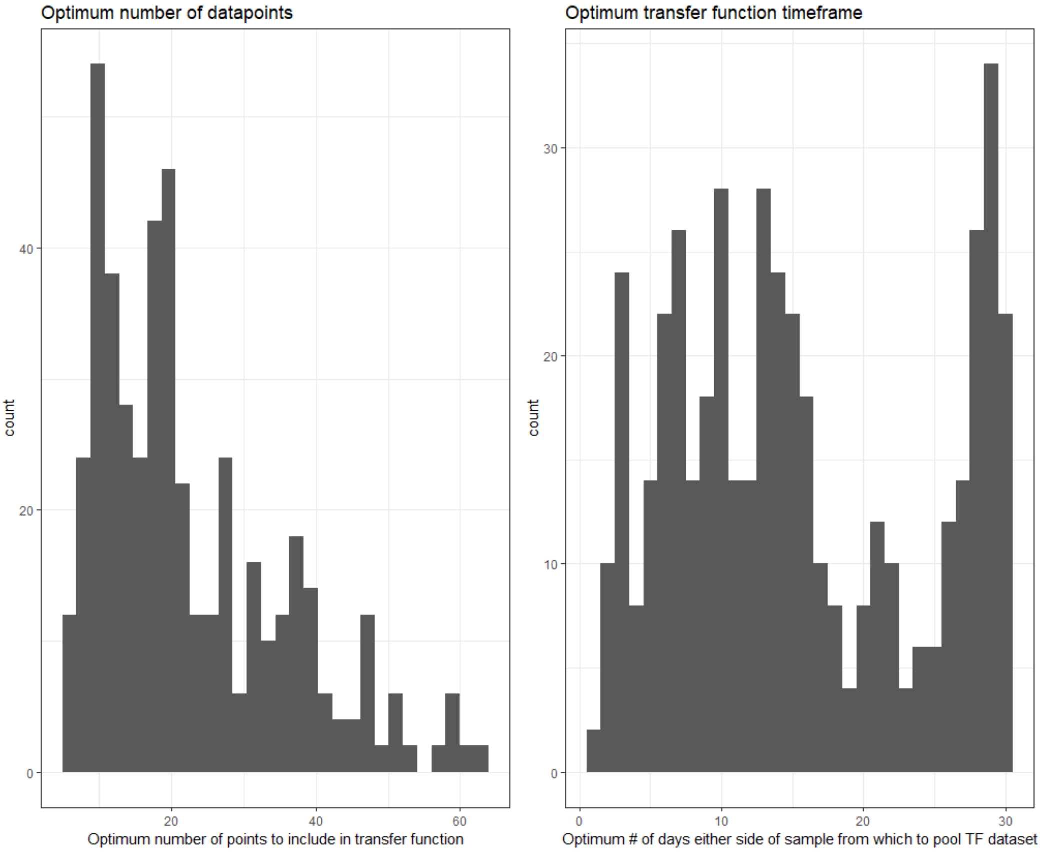

Figure 2.22 Histograms showing the idealised number of standards which minimise offset in projected Δ47 against accepted value (left) and the idealised timespan for the transfer function (right)

2.5.3 Transfer function calculated by calendar month

The standard dataset was split into monthly pools and a 2-pass Tukey filter (Tukey, 1977) applied to each month. A single, monthly transfer function was then calculated. The transfer functions show little fluctuation between months, demonstrating the long term stability of MIRA. Only February 2019 is significantly different from preceding and subsequent months.

Whilst such limited monthly fluctuations suggest the monthly transfer function method may provide reliable projections, this method is vulnerable to including temporally distant standards in the transfer function pool since a sample run towards the beginning or end of the calendar month is likely be temporally closer to standards run in the preceding or subsequent months. In addition, in months that features only a few days running time, such as January 2018, it was necessary to pool data with the previous/subsequent month.

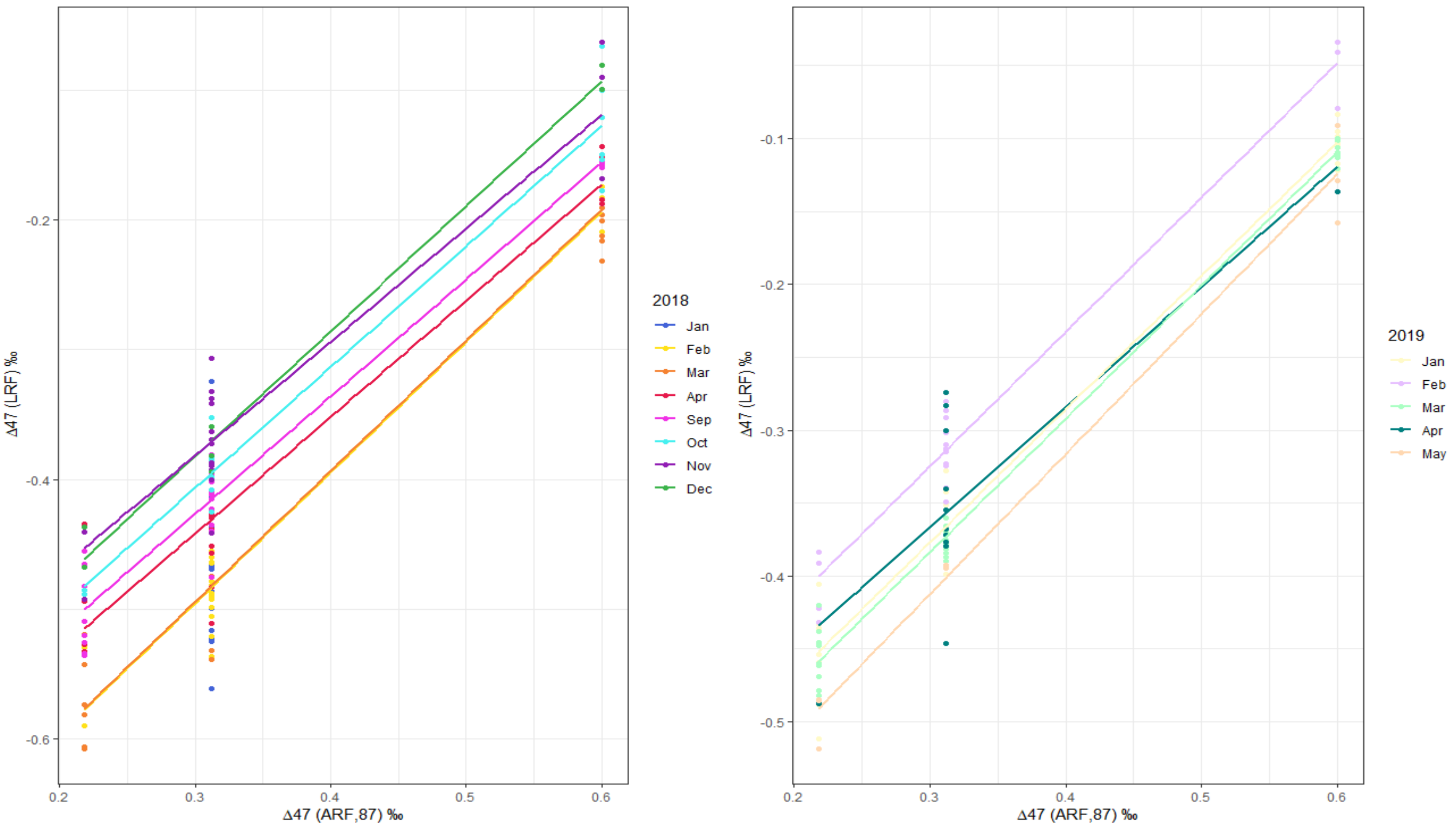

Figure 2.23 Monthly transfer functions for 2018 (left) and 2019 (right)

Table 2.11 Monthly transfer functions Jan 2018 – May 2019

Month	Gradient	Intercept
Jan-18	Only UEACMST run	
Feb-18	1.05 (± 0.049)	-0.797 (± 0.018)
Mar - 18	1.02 (± 0.043)	-0.796 (± 0.019)
Apr-18	0.896 (± 0.064)	-0.710 (± 0.064)
Sep-18	0.902 (± 0.040)	-0.697 (± 0.014)
Oct-18	0.930 (± 0.048)	-0.685 (± 0.021)
Nov-18	0.874 (± 0.068)	-0.644 (± 0.026)
Dec-18	0.964 (± 0.045)	-0.671 (± 0.018)
Jan-19	0.914 (± 0.033)	-0.65 (±0.014)
Feb-19	0.922 (± 0.042)	-0.601 (±0.014)
Mar-19	0.915 (± 0.014)	-0.658 (±0.005)
Apr-19	0.824 (± 0.18)	-0.614 (±0.061)
May-19	0.961 (±0.043)	-0.701 (±0.018)

Applying the transfer functions above to project the standard dataset onto the ARF gave an average percentage error from the 'accepted' values of 8.8 ‰. January 2018 UEACMST data was projected using the February 2018 transfer function since insufficient data existed to construct a transfer function for January.

2.5.4 Rolling window transfer function

All the standards in a limited temporal window, centred on the sample run date, were pooled. If the pool did not contain at least one of each of the transfer function standards, additional standards were iteratively added to the standard pool ± n days either side of the sample run date, until this condition was met. A 2-pass Tukey filter (Tukey, 1977) was then applied to the standard pool to remove outliers before the transfer function was calculated.

Windows from 8 – 40 days were tested and used to project each of the samples in the standard dataset onto the ARF. The average percentage difference between the projected and 'accepted' Δ47 (ARF)) was calculated and presented in Figure 2.24. A transfer function window of 22 days, centred on the sample run date is estimated to give the lowest percentage error of 8.80 ‰ on average.

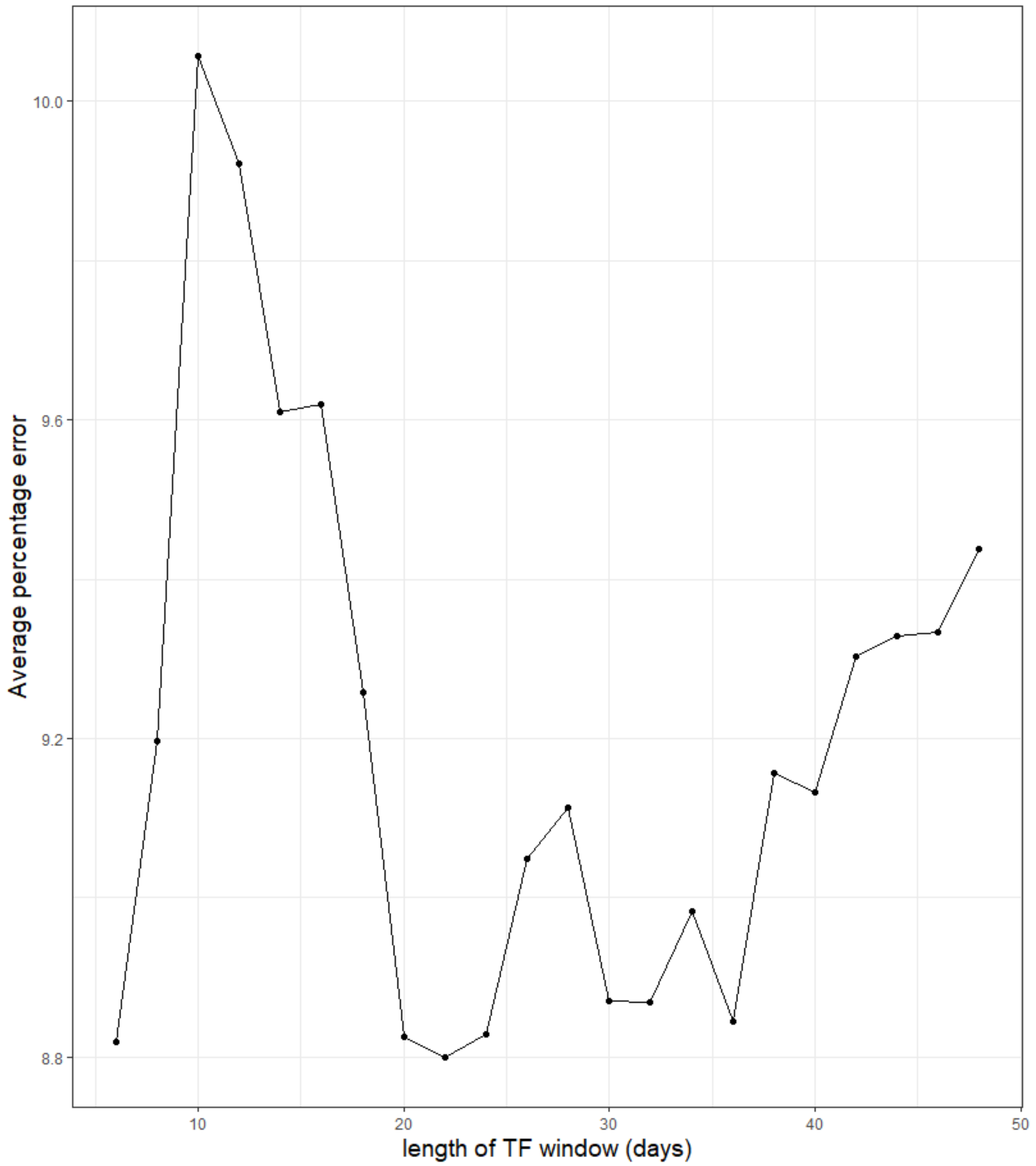

Figure 2.24 Percentage error in projected samples with length of rolling transfer function window.

2.5.5 Evaluation of Transfer function methods

Using each transfer function method to calculate the average percentage offset between the projected and the accepted values for the standard dataset, as above, is insufficient to accurately assess the reliability of each method on independent standards. In this instance the daily optimum method will clearly outperform the other methods since, by its very definition, it obtains the lowest possible error for the standard dataset. However, it does not necessarily obtain the lowest possible error for sample measurement projection. Where an erroneous standard sample is run, this is likely to lead to construction of an unreliable transfer function constructed from other erroneous standard measurements (as these are most likely to project the original standard sample back towards the 'accepted' value). Whilst this will minimise the projected error in the standard sample, it's likely to lead to a false projection for other samples run on the same day.

Thus in order to fairly compare the reliability of each transfer function method, an independent dataset of samples with known Δ47 (ARF) values is required. This was obtained from the full standard dataset by removing a random standard measurement on days when multiple standard measurements are made. Randomly selecting the measurement eliminated any bias that might arise from the ordering in which standards are run. Thus two datasets are obtained: the first containing 110 randomly selected standards run on days when multiple standard measurements are made and the second containing the remaining 152 standard measurements. The second dataset is then used as the standard pool from which transfer functions are constructed and the first (the randomly selected standard dataset), the sample pool, from which samples are projected onto the ARF. The percentage error of these projected values from the 'accepted' value was then calculated and used to assess the accuracy of the transfer function method. Results are presented in Table 2.12.

Table 2.12 Comparison of four transfer function methods.

Method	Average % error using full standard dataset	Average % error using randomly selected dataset	Standard deviation foraminifera data
Daily optimum	5.4	10.7	0.028
19 nearest neighbours	10.3	11.5	0.025
Calendar month	8.8	9.9	0.023
22-day rolling	8.8	11.3	0.033

Using the randomly selected standard dataset as the data pool to construct transfer functions allows the daily optimum method to be fairly compared with the other three methods. Its error is still lower than both the 19-nearest neighbours and 22-day rolling transfer function methods, however is outperformed by the calendar month method. Comparison of the other three methods is most reliable using the larger full standard dataset projections. Both the calendar month method and 22-day rolling window perform equally well here, outperforming the 19 nearest neighbour method.

A final evaluation is applied by using each transfer function methodology to project a suite of 15 foraminiferal samples (the calibration dataset, see section 3.6) onto the ARF. The average standard deviation for each sample is calculated. A strong performing transfer function should reduce the spread in data between samples. Results are summarised in Table 2.12. In this capacity the calendar month method performs the strongest, although there may be some bias here as the majority of foraminifera core top measurements were taken in a short time window between January – March 2019, meaning the impact of instrumental drift will be minimal.

2.5.6 Choice of transfer function methodology

With the calendar month methodology performing well in all three evaluation tests, it was employed for use throughout this study.

For samples measured between October 2018 and May 2019, which encompasses the majority of samples run in this study, calendar monthly transfer functions were constructed from a pressure corrected standard dataset. Standard Δ47 measurements were first corrected for sample volume on the local reference frame (See section 2.4.5 for methodology) prior to being regressed against Δ47 on the absolute reference frame to create a transfer function. Samples must then also be pressure corrected on the local reference frame prior to application of the transfer function.

For samples run prior to October 2018, no prior pressure correction was applied since insufficient data exists for reliable corrections (section 2.4.5). Thus measured Δ47 was directly regressed against Δ47 (ARF) to create the transfer function. Sample data is not pressure corrected.

2.6 Conclusions and further work

This study has explored the impact of sample size on Δ47 measurements for clumped isotope analysis. Water contamination is suggested as the most likely cause of a persistent offset between large and small samples, and several attempts to eliminate it are explored. Although the effect has been noted previously (Guo & Eiler, 2007; Wacker & Mainz, 2013) it is seldom reported in clumped isotope studies and it is unclear the extent to which it is observed in other laboratories.

Although this study was unsuccessful in attempts to overcome the effect, it has identified both the acid reaction vessel and the Porapak separation trap as playing an influential role. The effect appears to arise from continual water outgassing during the acid reaction. It is suggested that the water molecules dissociate to form hydronium ions, which react with carbon monoxide, giving rise to a mass 47 contaminant. The Porapak Q trap plays a further role in enhancing the effect by preferentially removing water from large samples. With a potential cause of the effect now known, this can inform further efforts towards its elimination.

The introduction of three additional water traps and a separate, dedicated, acid vacuum line in March 2019 gave rise to a declining trend in Δ47 (Figure 2.14) which was observed over the following month. This trend was consistent with a decline in the background volume of water within sample measurements. It is unfortunate that the timeframe of this study did not allow for further analysis of the sample size effect subsequent to the installation of these traps and it is suggested that this would be a beneficial exercise to help determine whether water is indeed the cause of the sample size effect as postulated above.

It is clear that elimination of the sample size effect is vital if high resolution foraminifera studies are to be achieved, and sample masses reduced beyond the 4 mg used here. Whilst the correction developed in this study provides a means of correcting for the effect, it introduces an additional layer of uncertainty to measurements, making it an inferior option to eliminating the effect entirely, such that smaller samples can be measured to the same degree of precision as larger ones.

If the sample size effect can be eliminated, additional refinements to the instrumental setup will allow for further reductions in sample sizes below the ~1.5 mg of the current instrumental limit. The MIRA inlet is equipped with a liquid nitrogen cooled coldfinger which makes it possible to isolate the entire volume of sample gas within the sample bellow, as opposed to the current method of sample input which relies on room temperature passive transport from the purification line, leaving an unused volume of sample within the inlet system. With the elimination of the sample size effect, this apparatus will make it possible to yield the same volume of gas from smaller masses of sample.

Further reduction in the volume of the inlet system could also allow for measurement of smaller gas volumes. Previous studies have made use of mercury bellows for pressure balancing of small samples and reference gases on dual inlet systems (Coplen, 1981). The installation of similar apparatus would vastly reduce the volume of the MIRA inlet system such that significantly smaller gas volumes could achieve the required ion beam intensity.

More speculatively, a wider issue for IRMS in general is the low ion yields compared with the quantity of sample gas inputted into the ion source. MIRA has a high yield of one ion liberated per ~300 CO_2 sample molecules, yet even this represents a vast 'waste' of potential ions. For each increase in the concentration of ions yielded, a proportional decrease in sample volume could be achieved.

Recent studies have demonstrated the potential of optical laser spectroscopy in clumped isotope analysis (Prokhorov et al., 2019). The method has the potential to vastly reduce sample sizes with sample volumes as low as 10 µmol being theoretical possible to achieve. This order of magnitude change would bring sample volumes in line with those of more established foraminifera temperature thermometers such as Mg/Ca ratios. It is still a technique very much in its infancy but it will be exciting to see how it unfolds in the coming years.

Aside from inroads into the sample size effect, this study has also shown that the choice of timeframe over which a transfer function is compiled, to project samples onto the absolute reference frame, has a substantial impact on the ARF value calculated. For the MIRA setup it is suggested that monthly transfer functions produce the most reliable data. However, the choice of timeframe will vary between laboratories, dependent on the frequency of standard measurements and the rate of instrumental drift. It is hoped that the methodology and algorithms developed here could be of further use in helping other laboratories refine the accuracy of their ARF transfer functions in the future.

Chapter 3. Defining the foraminifera clumped isotope calibration

3.1 Introduction

In the sixty years since the pioneering work of Emiliani (1953), fossilised foraminifera have become one of the most wisely utilised tools for inferring palaeoceanographic temperatures. Their geographical ubiquity and continual presence within sediment archives, dating back tens of millions of years, make them an ideal tool for such purposes. Yet despite the thousands of studies utilising foraminifera for temperature reconstructions, establishment of a reliable, authoritative palaeothermometer has remained elusive. The methods and limitations of some of these methods are outlined in this introduction, highlighting the need for a new accurate means of quantifying palaeo-temperatures such as clumped isotopes.

3.1.1 Overview of stable isotope studies of foraminifera

In his the pioneering studies of isotopic ratios in natural materials, Urey (1947) noted the temperature dependence of ^{18}O concentration, stating his discovery could be…

> *'… of particular interest to geology… Accurate determinations of the 0^{l8} [sic] content of carbonate rocks could be used to determine the temperature at which they were formed.'*

A short while later, alongside his colleague Samuel Epstein and others, he had determined the temperature dependence of ^{18}O in marine shells (Epstein et al., 1951), noting that…

> *'The Foraminifera should be investigated for, even if not useful over long periods of time, they may be of interest for the investigation of more recent temperatures.'*

Just two years later, Emiliani & Epstein (1953) derived the first palaeoceanographic temperature estimates from foraminifera, and with the publication of Emiliani's idealised curve (Emiliani, 1966) came the first long term record of oceanographic temperatures using δ^{18}O measurements of foraminifera.

It was with the first isotopic measurements of the polar ice sheets came the realisation that the relationship between δ^{18}O and temperature was far from straightforward. Ice sheets exhibited large $\delta^{18}O$ fluctuations throughout the Pleistocene, reflective of changing $\delta^{18}O$ of precipitation - itself dependent upon the isotopic composition of the ocean from which it derives (Shackleton, 1967).

Were these oceanic $\delta^{18}O$ fluctuations in fact the driver of Emiliani's 'palaeothermometer'? Dansgaard & Tauber (1969) showed that up to 70 % of fluctuations in the record could be attributed to shifts in ice sheet volume. Further confirmation of the ice volume/isotope relationship was provided by Shackleton & Opdyke (1973) who showed that the isotopic record from a Pacific core correlated well with estimates of sea level from coral archives (Broecker et al., 1968) during the last glacial cycle. Thus the $\delta^{18}O$ composition of foraminifera was largely driven by the isotopic composition of the palaeo-ocean, a characteristic that is extremely difficult to measure. Obtaining absolute temperatures from $\delta^{18}O$ would be further hindered by species vital effects whereby poorly understood processes lead to differing degrees of isotopic fractionation in the precipitation of foraminifera tests between species (Ziveri et al., 2003). Over 70 years on from the pioneering studies of Urey, Epstein and Emiliani, a reliable $\delta^{18}O$ palaeo-thermometer is yet to be established.

3.1.2 Overview of other foraminifera based temperature reconstructions

In the absence of an absolute $\delta^{18}O$ palaeo-thermometer, attention turned to other means by which temperatures could be derived. Imbrie and Kipp's seminal 1971 paper used multivariate analysis of fossilised foraminifera assemblages to derive estimates of sea surface temperature during the late Cenzoic. By assuming that environmental variables were the determinant of species abundances, they created mathematical relationships, or transfer functions, that described the relationship between foraminifera assemblages and environmental conditions in the modern day. These relationships could then be applied back in time. This approach was adopted by the CLIMAP group (Climap Project Members, 1976) in their efforts to infer conditions during the LGM.

Later improvements adapted the mathematical techniques used to derive the relationships between species and environmental variable (Morey et al., 2005; Roux, 1979). The modern analogue technique (MAT) works on a similar premise to transfer functions by assuming modern relationships between environmental variables and species assemblages applied back in time (Hutson, 1980). But instead of deriving mathematical relationships, MAT techniques compare fossil assemblages to a database of modern analogues and deduce environmental parameters based upon those which most closely resemble the fossil assemblage.

Whilst methods based on fossil assemblages provide a powerful method from which to derive palaeotemperatures, they suffer some drawbacks. It is particularly difficult to estimate uncertainty within a given reconstruction, and competing factors such as nutrient availability and salinity make it difficult to untangle a purely temperature derived signal. This becomes increasingly problematic going back further in time when vastly different environmental conditions may result in relatively few suitable modern analogues for comparison. Furthermore, the timeframe over which the technique can be applied is limited when it is considered that approximately 40 % of North Atlantic foraminiferal species present during the late Pliocene have since become extinct (Chapman, 2000).

In the mid-1990s Nurnberg published several papers looking at the temperature dependence of magnesium incorporation into foraminifera tests (Nürnberg et al., 1996; Nurnberg, 1995). Advancements in analytical technique and contaminant removal meant that he was able to show a clear temperature dependence for the first time, something which had eluded earlier efforts (Delaney & Boyle, 1985; Savin and Douglas, 1973).

Before long numerous calibration studies were published detailing the relationship between Mg/Ca content of foraminiferal calcite and calcification temperature (e.g. Elderfield & Ganssen, 2000; Kozdon et al., 2009; Lea et al., 1999). These appeared to show a high degree of variability between species. Furthermore, there appeared considerable variation in Mg/Ca temperature dependence even within species, according to the particular locality or methods by which the calibration was derived. Farmer et al. (2011) were able to show that the choice of calibration gave rise to temperature offsets up to 10 ^{o}C for North Atlantic *G. inflata* samples. Further difficulty in deriving absolute temperatures from Mg/Ca analysis arises from the fact that salinity has been shown to play a role in determining Mg/Ca content (Kisakürek et al., 2008) and, deeper in geological time, the Mg/Ca ratio of the ocean is known to vary (Evans & Mller, 2012).

Three dominant methodologies for deriving temperatures have arisen: stable isotope analysis, magnesium/calcium ratios and fossilised assemblage derived temperature estimates. Yet all suffer from competing influences which make it hard to untangle the temperature signal.

Mg/Ca ratios emerged as a means of establishing palaeotemperatures towards the end of the last century (Nuernberg, 1995; Nürnberg et al., 1996), reliant on the much earlier discovery that the degree of magnesium substitution into the carbonate lattice of foraminifera tests is a function of temperature (Chave, 1954). Over the following decade, a flurry of studies suggested that untangling the temperature signal might not be as simple as first envisaged. It became apparent that rate of magnesium substitution was species-specific, giving rise to numerous calibrations which showed variable temperature sensitivity between species, and even geographical locality (e.g. Elderfield & Ganssen, 2000; Ganssen & Kroon, 2000; Kozdon et al., 2009; Skinner & Elderfield, 2005). Just as with stable isotope analysis, additional factors aside from temperature have now been shown to play a role in determining Mg/Ca content including salinity (Kisakürek et al., 2008) and, deeper in geological time, variation in oceanic Mg/Ca ratio (Evans & Mller, 2012).

3.1.3 Summary of foraminiferal clumped isotope work to date

The recent development of clumped isotope analysis provides an exciting new method for deriving palaeotemperatures. It overcomes the issues associated with competing environmental influences, such as water chemistry and isotopic composition, since the clumped isotopic signature of a foraminifera is thought to be a sole function of temperature.

Several recent studies have successfully used clumped isotope analysis of foraminifera to infer palaeotemperatures (Evans et al., 2017; Henkes et al., 2018; Piasecki et al., 2019; Thornalley et al., 2015; Rodríguez-Sanz et al., 2017). Yet the large sample sizes required mean that its application has remained limited until the last few years. Not only does it make it a time consuming measurement to take, with extended sample picking times, it also limits the resolution at which a study can be conducted due to limited sample material. Many studies are forced to group stratigraphically adjacent samples to obtain sufficient measurement material (e.g. Leutert et al., 2019; Rodríguez-Sanz et al., 2017).

The first foraminifera derived palaeothermometers showed considerable variability in their temperature sensitivity (Grauel et al., 2013; Tripati et al., 2010) and were reported on their local laboratory reference frame only, making inter-laboratory comparison and utilisation difficult. In the intervening years, additional foraminifera calibrations have been published, yet all show considerable variability in their temperature sensitivity and offset (Table 3.1).

The most obvious source of discrepancy between laboratories lies in variability between instrumental setups. Yet reporting the calibration onto the absolute reference frame (as is the case in all the calibrations listed in Table 3.1 aside from Grauel et al*. (*2013) and Tripati et al*. (*2010)) should overcome this.

Table 3.1 Published foraminifera clumped isotope calibrations to date.

Calibration	Calibration material	Reference
$\Delta47 = 0.0315 \times \frac{10^6}{T^2} + 0.313$	Planktonic foraminifera	(Breitenbach et al., 2018)
$\Delta47 = 0.0537 \times \frac{10^6}{T^2} + 0.092$	Slope derived from laboratory inorganic precipitates, offset from modern day benthic foraminifera	(Evans et al., 2017)
$\Delta47 = 0.0506 \times \frac{10^6}{T^2} + 0.0807$	Foraminifera, coccoliths, otoliths, inorganic carbonate, deep sea coral, enamel biopatite	(Grauel et al., 2013)
$\Delta47 = 0.0397 \times \frac{10^6}{T^2} + 0.2259$	Planktonic foraminifera	(Meinicke et al., 2020)
$\Delta47 = 0.0416 \times \frac{10^6}{T^2} + 0.206$	Benthic and Planktonic foraminifera	(Peral et al., 2018)
$\Delta47 = 0.046 \times \frac{10^6}{T^2} + 0.159$	Benthic foraminifera	(Piasecki et al., 2019)
$\Delta47 = 0.0587 \times \frac{10^6}{T^2} + 0.014$	Foraminifera, otoliths, Laboratory precipitated carbonate	(Tripati et al., 2010)
$\Delta47 = 0.0327 \times \frac{10^6}{T^2} + 0.3030$	Foraminifera, ostrich egg shell, tropical bivalves, brachiopod, cold seep carbonate	(Wacker et al., 2014)

Other sources of discrepancy may arise in the different calibration materials utilised or the different species of foraminifera measured. Whilst the theory suggests that the clumped isotope thermometer is purely temperature dependent, it may yet be shown to be as vulnerable to ‘vital effects’ as the earlier proxy methods explored above. Coral samples have been shown to exhibit Δ47 vital effects (Spooner et al., 2016) and it is certainly possible that other biogenic carbonates do the same. Recent analysis by Meinicke et al. (2020) measured 14 species of planktonic foraminifera and found evidence of species specific offsets only in *G. ruber* specimens. Yet further research into the phenomenon in foraminifera is required.

3.1.4 Chapter aims and outline

The unique instrumental setup at UEA (Chapter 2) means that it is necessary to establish a laboratory specific calibration for foraminiferal calcite, derived as far as possible from the planktonic species with which palaeotemperatures will subsequently be derived.

This chapter outlines efforts to deduce such a calibration. Section 3.2 – 3.4 detail calibration material, including experiments to precipitate inorganic calcite at controlled temperatures, alongside foraminiferal species descriptions and temperature estimates.

Considerable thought is given to foraminifera sample preparation in section 3.5. Existing studies employ differing techniques to remove sediment clays and biogenic calcite, with contradictory findings as to the impact each method has on Δ47 signal preservation. Thus this study evaluates the differing methods and defines a protocol for measuring all foraminifera samples. The concluding sections (3.6 – 3.7) evaluate the calibration and compare to other studies.

3.2 Non-foraminiferal calibration material

3.2.1 Inorganic calcite precipitates

For additional calibration material, inorganic calcite was precipitated at known temperatures using a method adapted from Dietzel et al. (2009), in turn adapted from Dietzel et al. (2004) and Usdowski et al. (1991).

35g of sodium bicarbonate was placed inside a 500 ml low density polyethylene bottle and filled with distilled water. The solution was saturated with carbon dioxide by bubbling through CO_2 gas for one hour. pH was regularly measured throughout the bubbling with saturation signified by a cessation of pH reduction. This was achieved at pH 7.5. The bottle was immediately sealed to limit outgassing and placed inside a large 5L glass vessel filled with 0.01 molar calcium chloride solution, prepared by dissolving $CaCl_2.2H_2O$ in distilled water. The headspace of the outer vessel was purged with nitrogen to remove atmospheric CO_2 which might otherwise migrate into the solution.

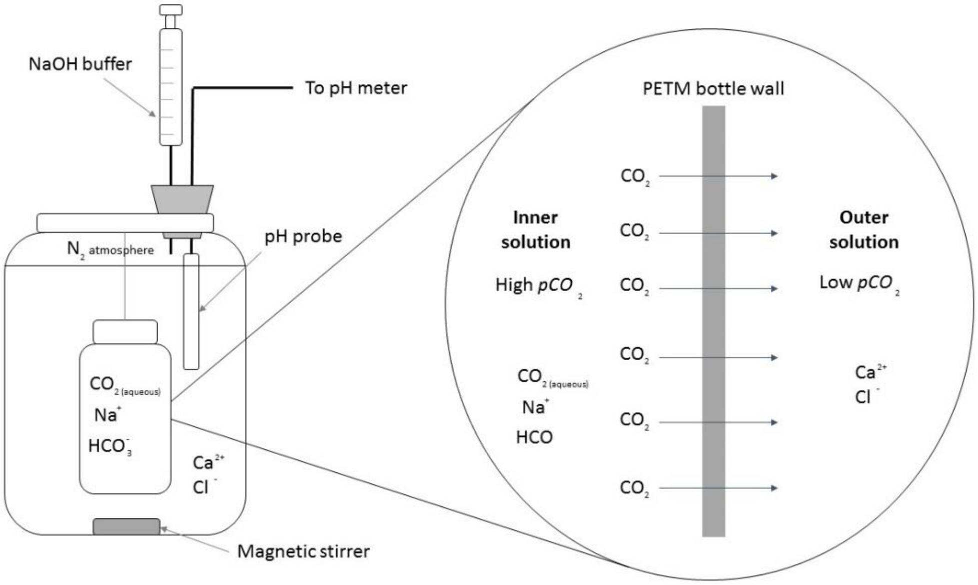

Figure 3.1 Experimental setup for calcite precipitation experiments. Adapted from Dietzel et al., (2004).

The outer vessel was sealed and maintained at constant temperature in an incubator or temperature controlled room. The outer solution was stirred continuously to ensure even migration of CO_2 throughout. As the experiment progresses, the pCO_2 gradient between the two solutions resulted in a migration of CO_2 through the walls of the polyethylene bottle from the inner to the outer solution (Figure 3.1), where it formed calcium carbonate precipitate according to the reaction:

$$Ca^{2+} + OH^- + CO_2 \rightarrow CaCO_3 + H^+$$

pH was continually monitored throughout the experimental run with a pH probe inserted through a rubber bung at the top of the container to maintain an airtight seal. The solution was maintained at pH 9 ± 0.5 with the daily addition of small quantities of 2 M NaOH solution inputted with a syringe inserted through the rubber bung. Calcite was precipitated at four temperatures: 5°C, 10 °C, 20 °C and 40 °C. The reaction was considered to have reached completion when the rate of pH decline equalled 0. The time to reach completion ranged from 124 days in the 40 °C precipitation experiment to 164 in the 5 °C experiment. At completion, precipitated carbonate was removed from suspension via vacuum filtration and physically removed from the sides of the reaction vessel with a plastic spatula.

Precipitation of calcites in isotopic equilibrium is notoriously difficult to achieve under laboratory conditions (Watkins & Hunt, 2015). This method was chosen as the slow precipitation rate, limited by the rate of osmosis of carbon dioxide from the inner to the outer solution, was considered likely to lead to the formation of calcite precipitated in isotopic equilibrium (Watkins et al., 2013). Enhanced precipitation rates have been shown to cause kinetic fractionation effects (Dietzel et al., 2009; Watkins et al., 2014) and isotopic disequilibrium (Watkins & Hunt, 2015; Watkins et al., 2013). Earlier studies employed active degassing techniques whereby nitrogen is bubbled through sodium bicarbonate solutions to remove CO_2 and trigger calcite precipitation (Kim & O'Neil, 1997; Tarutahi & Clayton, 1969) or precipitation directly from calcium chloride and sodium bicarbonate solutions mixes (Jimenez-Lopez et al., 2001; Kim et al., 2006). These studies have been unable to prove that under such conditions, calcite is precipitated in isotopic equilibrium. Coplen (2007) and Daëron et al. (2019) both suggested that in fact most studies that employ these methods gave persistently low estimates of fractionation factors, consistent with kinetic effects — through the study of a slow growing calcite from Devil's Hole, Nevada and Corchia Cave, for which they provided strong evidence that they had been precipitated in isotopic equilibrium. Additional studies have employed passive degassing techniques (Affek & Zaarur, 2014; Kim et al., 2007) where longer precipitation timescales are achieved, in line with those of this study.

Results

Between 1.6 and 2.9 grams of calcium carbonate was precipitated across the range of temperatures. Purity was assessed using X-ray diffraction and X-ray fluorescence analysis. This was conducted on the room temperature precipitate only using a Thermo Scientific ARL XTRA Powder Diffractometer and Bruker AXS S4 Pioneer XRF spectrometer at the University of East Anglia. The final product was confirmed as >99 % calcite with minor traces (<0.5 %) of chlorine, sodium, iron, phosphorus and silicon (Figure 3.2).

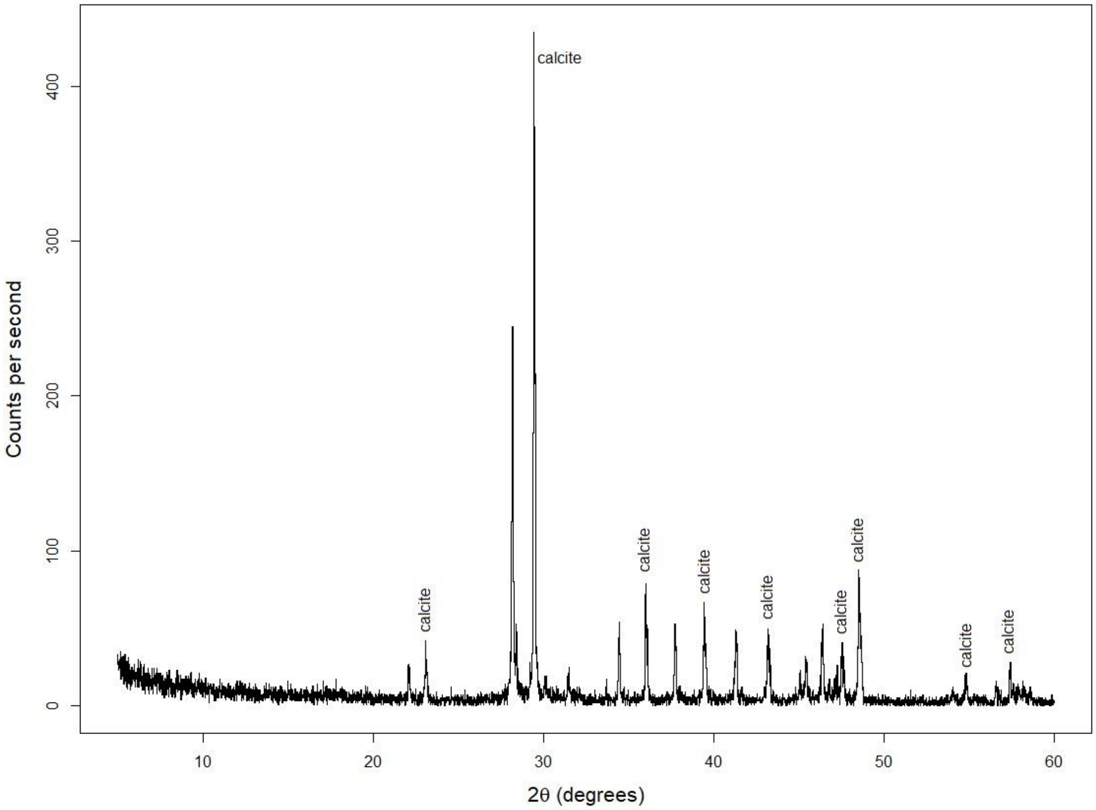

Figure 3.2 XRD analysis for 20 °C carbonate precipitate experiment. Although the predominant peaks indicate the majority is calcite, some unidentified material is present.

Precipitation water isotopic compositions were measured on the Piccaro Cavity Ringdown Spectrometer at the Stable Isotope laboratory at the University of East Anglia and used to calculate isotopic fractionation factors at different temperatures. 28 clumped isotope measurements were taken of the precipitate samples, with six samples (three 40 °C and three 20 °C samples) rejected from the final analysis because they exhibited signs of contamination through elevated Δ48 signals (see section 2.3.5). Results are presented in Table 3.2.

Calculated fractionation factors for 10 °C and 40 °C vary significantly from the equilibrium values determined experimentally by Coplen (2007) and Kim & O'Neil (1997) (Figure 3.3), suggesting that these samples have not been precipitated in isotopic equilibrium. Only the 5 °C precipitate lies within error of the Coplen line and thus is deemed to have been precipitated in equilibrium. Further evidence to support this idea comes from the Δ47 measurements in which 10, 20, and 40 °C values are higher than those measured in the 5 °C sample, when lower values are expected at warmer temperatures from equilibrium precipitation. This contradicts the findings of Watkins & Hunt (2015) who suggested that disequilibrium effects have little impact on the Δ47 signature of carbonates precipitated at Earth surface tempatures.

Table 3.2 Experimental data for inorganic calcite precipitation experiments. N = total number Δ47 of measurements with rejected measurements in brackets, t_r = is reaction time. Delta values corrected to 25 °C reaction temperature. Errors are 95 % confidence intervals.

Temp (°C)	**N (Δ47)**	**t_r (days)**	**$\delta^{18}O_{Carb}$ ‰ (VPDB)**	**$\delta^{18}O_{water}$ ‰ (VSMOW)**	**α**	**Δ47 (ARF) ‰**
5	9	164	-6.43 (± 0.06)	-6.14	1.031	0.778(± 0.06)
10	6	129	-10.55(±0.07)	-7.12	1.027	0.901(± 0.05)
20	6 (3)	125	-12.66(±0.09)	Not measured		0.814(± 0.02)
40	7 (3)	124	-12.07(±0.09)	-6.48	1.025	0.741(± 0.05)

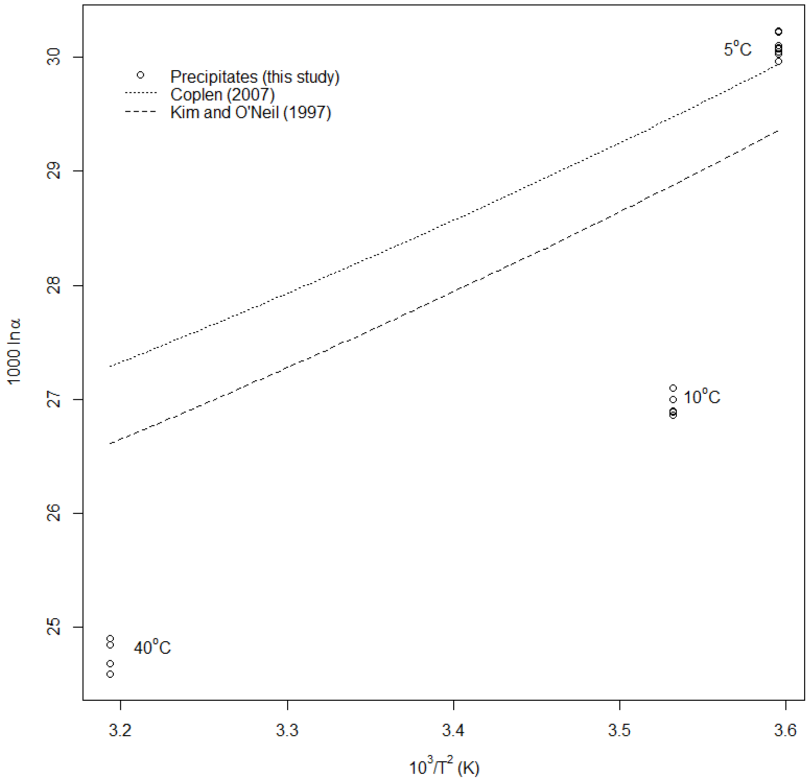

Figure 3.3 Inorganic precipitation sample fractionation factors and experimentally determined isotopic equilibrium fractionation lines from Coplen (2007) and Kim & O'Neil (1997)

The cause of the disequilibrium in higher temperature samples is uncertain, however it is postulated that the faster reaction time may be a contributing factor. This may have been further exacerbated by manual buffering in the absence of an autotitrator. Buffering was conducted on a daily basis by slowly injecting small quantities of NaOH into the outer solution, instead of constant monitoring and addition throughout the day as in Dietzel et al. (2009). It is suggested that gradual migration of CO_2 from the inner to the outer solution over each 24-hour period led to a CO_2 saturated environment which triggered rapid precipitation, and kinetic fractionation, once NaOH was added.

3.2.2 Coldwater coral calibration material

Additional material was sourced from a North Sea coldwater coral, Lophelia pertusa, collected in 2005 from the BP Magnus Platform (61.575N, 1.583E; depth = 140 – 165 m) and kindly donated for use in this study by The Deep aquarium in Hull, United Kingdom. The specimen appears visibly pristine with no obvious signs of discolouration (Figure 3.4). The bulk sample was milled to a fine powder and homogenised prior to measurement.

In order to obtain a growth temperature for the specimen, it was necessary to first establish age and seasonality of growth. Age is estimated from the length of skeletal extensions which measured up to 66 mm in length, although the distance of the breaking point along the skeleton from the base is unknown, meaning actual length may be longer. Average skeletal growth rates of 26 $mmyr^{-1}$ have been observed in *Lophelia pertusa* specimens on anthropogenic substrates, including North Sea oil rigs (Bell & Smith, 1999; Gass & Roberts, 2006). Aquarium and natural substrate observations exhibit slower growth rates with skeletal extensions of 9.4 $mmyr^{-1}$ observed in samples collected from Norwegian Fjords (Mortensen et al., 2001). Since the specimen is thought to have been growing at time of collection, these growth rates suggest an age of between 2.5 and 7.0 years when obtained in 2005.

Figure 3.4 Photograph of the coldwater coral, showing a typical skeletal extension prior to milling. Length shown is in cm.

To date, there has been little published literature on the influence of seasonality on *Lophelia pertusa* growth in natural environments. Aquarium studies suggest that rates are highly influenced by food supply (Mortensen et al., 2001), itself a reflection of seawater origin and rates of detrital deposition (Frederiksen et al., 1992). In *Flabellum alabastrum* populations on the Newfoundland coast, maximum growth rates are observed during the late summer and early autumn, during maxima of temperature, zooplankton levels and deposition of suspended detritus (Hamel & Mercier, 2010).

Unfortunately no *in situ* observations of North Sea growth seasonality exist, in part due to the rarity of *Lophelia pertusa* in the region, where the mud and sand of the surface geology makes a poor substrate for population establishment (Davies et al., 2008). Gass & Roberts (2006) postulate that growth is likely to occur predominantly in the spring and autumn when nutrient supply is increased during spring algal blooms.

Growth temperature was thus calculated from 6 CTD profiles obtained from the British Oceanographic data Centre, taken from within 50km of the growth site in spring and autumn between 1992 and 2004. The average temperature between 140 – 165 m depth was calculated, giving an estimated growth temperature of 8.9 ± 2.1°C, with the error obtained from the maximum and minimum observed temperatures.

Statistical modelling studies predict a theoretical offset between the Δ47 values of calcite and aragonite, with a greater degree of heavy isotope clumping in aragonite, compared with calcite precipitated at the same temperature (Hill et al., 2014; Schauble et al., 2006). For the temperature range 0 – 30 °C, Guo et al. (2009) calculated a $\Delta47_{aragonite\text{-}calcite}$ of approximately 0.02 ‰. The aragonite structure of coral suggests that such an offset should be accounted for when calculating Δ47 values. However multiple experimental studies have failed to observe statistically significant offsets in Δ47 between the mineral structures (Dennis & Schrag, 2010; Ghosh et al., 2006; Zaarur et al., 2013). Thus no correction for the aragonite structure is applied in this study.

3.2.3 Laboratory standards: ETH3 and UEATHC

Laboratory standards ETH3 and UEATHC provided additional calibration material with well constrained growth temperatures and Δ47 values. UEATHC provided additional material at the high end of the temperature range with a known growth temperature of 56 ± 2 °C. Further detail is given in section 2.2.3.

3.3 Foraminifera calibration material

3.3.1 Core sites

Foraminifera calibration samples were taken from eight North Atlantic core tops, spanning latitudes 19 °N to 61.6 °N (Figure 3.5). Selection of multiple planktonic species from individual core tops (eight species were used in total), created a database of 25 unique foraminiferal temperatures. Locations are given in Figure 3.5 and Table 3.3.

Figure 3.5 Calibration core top locations used in this study.

Table 3.3 Core locations used for clumped isotope calibration

Core	Latitude (°N)	Longitude (°E)
MD99-2251	57.448	-27.908
NEAP-04B	61.367	-24.172
NEAP-16B	56.37	-27.82
NEAP-19B	52.765	-30.343
NEAP-20B	42.488	-28.415
MD99-2252	57.48	-27.93
BOFS31K	19	-21.167
Rapid26-14B	59.593	-41.167
Rapid29-18B	58.8	-44.872
Coral	61.57	1.58

3.3.2 Foraminifera species descriptions

The morphology and habitats of the foraminifera species used to establish the clumped isotope calibration are described below. Morphology descriptions are largely taken from (Kennett & Srinivasan, 1983). Calcification temperatures are inferred from World Ocean Atlas data, Mg/Ca measurements, and isotopic temperatures — explored in further detail in sections 3.4.1 to 3.4.3. Note *G. scitula, G. quinqueloba* and *G. glutinata* are not utilised as part of the calibration dataset but are included here due to their use in infering temperatures through the modern analogue technique (See chapter 5).

Globigerina bulloides **(d'Orbigny, 1826)**

Description: A spinose species with low trochospiral test, usually with four spherical chambers in the final whorl. An Umbilical aperture with a high spherical arch. Chambers increase in size as they are added. Surface of fossilised tests is uniformly, and densley, perforated (Figure 3.6).

Distribution: *G. bulloides* is widely distributed in temperate regions with numbers decreasing towards the tropics (Kennett and Srinivansan, 1983). Duplessy et al. (1991) used *G. bulloides* as a proxy for summer sea surface temperatures, demonstrating that it matched the summer SST isotopic temperature derived from core top samples between an optimum temperature range of 7 – 22^{o}C. These findings have been questioned by Ganssen & Kroon (2000) who suggested *G. bulloides* isotopic temperatures showed greater correlation with the northerly migrating spring bloom, reflecting the lowest surface temperatures in February – March between 30 – 40 ^{o}N and May – June temperatures further north. Ganssen & Kroon provided further evidence to support this by showing that *G. bulloides* exhibits a strong correlation between its carbon isotopic composition and surface phosphates. Reproduction and calcification are thought to occur mainly in the upper 60 m of the water column (Schiebel et al., 1997; Bauch & Kandiano, 2007).

Globigeranita glutinata **(Egger 1893)**

Description: A non-spinose *s*mall, medium to low trochospiral test consisting of three to four spherical chambers in the final whorl which increase rapidly in size. Smooth surface with fine perforations, that often appears shiny under the microscope in well preserved samples.

Sutures are depressed and approximately radial. Low arched interiomarginal umbilical aperture with a thin lip. In many samples the aperture is covered by irregular bulla (Figure 3.8).

Distribution: A widely dispersed species from tropical to subpolar waters although widely associated with Nutrient rich, subtropical waters. *G. glutinata* feeds on diatoms and is therefore often associated with the spring bloom (Ottens, 1992).

Globigerinoides ruber **(white and pink) (d'Orbigny, 1826)**

Description: A small to medium test with 3 globular chambers in the final whorl. An umbilical primary aperture with additional apertures situated in the sutures between chambers. In the modern ocean, *G. ruber* is found in both white and pink forms, with the latter variety found solely in the Atlantic ocean (Figure 3.7).

Distribution: A warm dwelling species. The white variety is readily observed throughout the summer months in the upper 60 m of the Atlantic, with numbers declining after late September (Schiebel et al., 2001). Found in tropical waters up to 45^{o}N, it's isotopic composition has been shown to reflect summer surface waters (Ganssen & Kroon, 2000), generally calcifying at depths of 0 – 30 m (Jonkers & Kucera, 2016). The pink variety tend to occupy shallower waters at 0-10 m depth (Jonkers & Kucera, 2016).

Globigerinoides sacculifer **(Brady 1877)**

Description: A medium to large spinose species with trochospirally coiled test and three globular chambers in the final whorl. The final chamber is often elongated with a 'sack-like' shape. The main aperture is interiomarginal, with small, suplementary, apertures in the sutures between chambers (Figure 3.7**)**.

Distribution: Dominant in warm subtropical to tropical waters, generally south of 45^{o}N (Ottens, 1992), common in late summer (Chapman, 2010) in the upper 60 m of the water column (Schiebel et al., 2001).

Globoratalia Inflata **(d'Orbigny, 1826)**

Description: A non-spinose, smooth surfaced test, trochospirally coiled with 4 spherical to trapezoid chambers, larger on the umbilical side than the spiral side. A high arched aperture (Figure 3.6).

Distribution: *G. inflata* is a subtropical species, generally found in areas between 4 and 11^{o}C. It has been used in palaeo-studies as an indicator or North Atlantic Current influx (Staines-urías et al., 2013). Highest abundances in the north Atlantic are observed in the late summer months (Ottens, 1992). Cleroux et al*. (*2007) suggested that specimens tended to dwell at the base of the summer thermocline (around 100 m depth north of 35^{o}N) until temperatures exceed 16^{o}C, at which point they migrate to depths reflective of conditions in the main thermocline. Specimens have been observed calcifying down to depths of 400 m (Ganssen & Kroon, 2000).

Globoratalia truncatulinoides (sinistral) **(d'Orbigny, 1826)**

Description: A non-spinose, medium to large conical shaped test with 5 triangular chambers in the final whorl. Has an interiomarginal, thick rimmed aperture with a low arch. Exhibits both right and left coiling forms (Figure 3.6).

Distribution: *G. truncatulinoides* is found at depth, down to 400 m but average calcification occurs about 250 m (Mulitza et al., 1997; Ganssen & Kroon, 2000). Isotopic temperatures are found to reflect those between 100 and 400 m (Ganssen & Kroon, 2000), with the majority of calcification taking place in the base of the summer thermocline, migrating to around 250 m depth when temperatures exceed 16 ^{o}C (Cleroux et al., 2007).

Neoglobquadrina **pachyderma (*sinistral*) (Bandy et al., 1967)**

Description: A non-spinose, low trochospiral test with four to four and a half tightly coiled spherical to ovate chambers in the final whorl, increasing in size as they are added. A low arched and thick rimmed aperture is situated at the suture between the final and preceding chamber (interiomarginal) which extends from the umbilicus to the periphery. A cancellate surface with radial sutures on both umbilical and spiral sides. Some specimens have a thickened surface of calcite crystals giving a rosette pattern (Figure 3.6).

Distribution: *N. pachyderma (s)* is a cold dwelling species, widely found in the polar latitudes (Darling et al., 2004) with some relict species in non-polar upwelling systems such as the Peru-Chile current and Oman margin (Darling et al., 2006). *N. pachyderma (s)* are commonly associated with summer blooming (Duplessy et al., 1991; Jonkers et al., 2010; Simstich et al., 2003). Calcification depth is variable, being observed at the sea surface in the western Nordic seas to 250 m off the Norwegian coast (Simstich et al., 2003). More generally, $\delta^{18}O$ of *N. pachyderma (s)* is thought to reflect that of waters just below the seasonal summer mixing zone (Jonkers et al., 2010).

Neoglobquadrina *incompta*

Numerous studies have assumed *N. incompta* and *N. pachyderma* (s) to be opposite coiling phenotypes of a single species. Coiling direction has been assumed a symptom of environmental stress and thus to be used as an indicator for palaeoenvironment (e.g. Ericson, 1959; Boltovskoy, 1973). However, recent analysis suggests that coiling direction is inherited (Norris & Nishi, 2001) and that the two phenotypes represent separate species. Darling, et al. (2006) suggest that the two species diverged in the late Miocene. For this study the Darling et al. attribution of the name Neoglobquadrina *Incompta* shall be adopted to describe the dextral coiling species. *N. pachyderma (s)* will be used solely to describe the sinistral coiling morphology (Figure 3.7).

Distribution: *N. incompta* is prominent in the temperature north Atlantic (Darling et al., 2006) in shallow (top 100 m) mixed layer depths (Schiebel et al., 2001), generally peaking in late spring and the summer seasons in the higher latitudes (Jonkers & Kucera, 2016; Chapman, 2010).

Globorotalia *scitula* (d'Orbigny, 1826)

Description: A non-spinose species with 4 – 5 compressed biconvex chambers in the final whorl. The test is medium to low trochospiral with chamber inflation on the umbilical side and a narrow interiomarginal aperture with a pronounced lip. The spiral side exhibits strongly curved sutures, occasionally penetrated by circular pores (Figure 3.8).

Distribution: *G. scitula* is a deep dwelling species associated with the spring bloom (Chapman, 2010). Commonly found in tropical waters south of 38°N but can also been found further north, up to 60°N (Ottens, 1992).

Globigerina quinqueloba (Natland, 1938)

Description: Small, slightly depressed trochospiral test with five chambers in the final whorl. The aperture is a small slit, often hidden under a flap-like extension on the final chamber. Early chambers have a reticulate surface and the final chamber is often spinose. Widely distributed (Figure 3.8).

Distribution: Most common in warm-subtropical and temperate areas but also known to occurs in polar regions (Carstens et al., 1997). Thought to calcify at depths within the pycnocline (25 – 75 m) (Simstich et al., 2003).

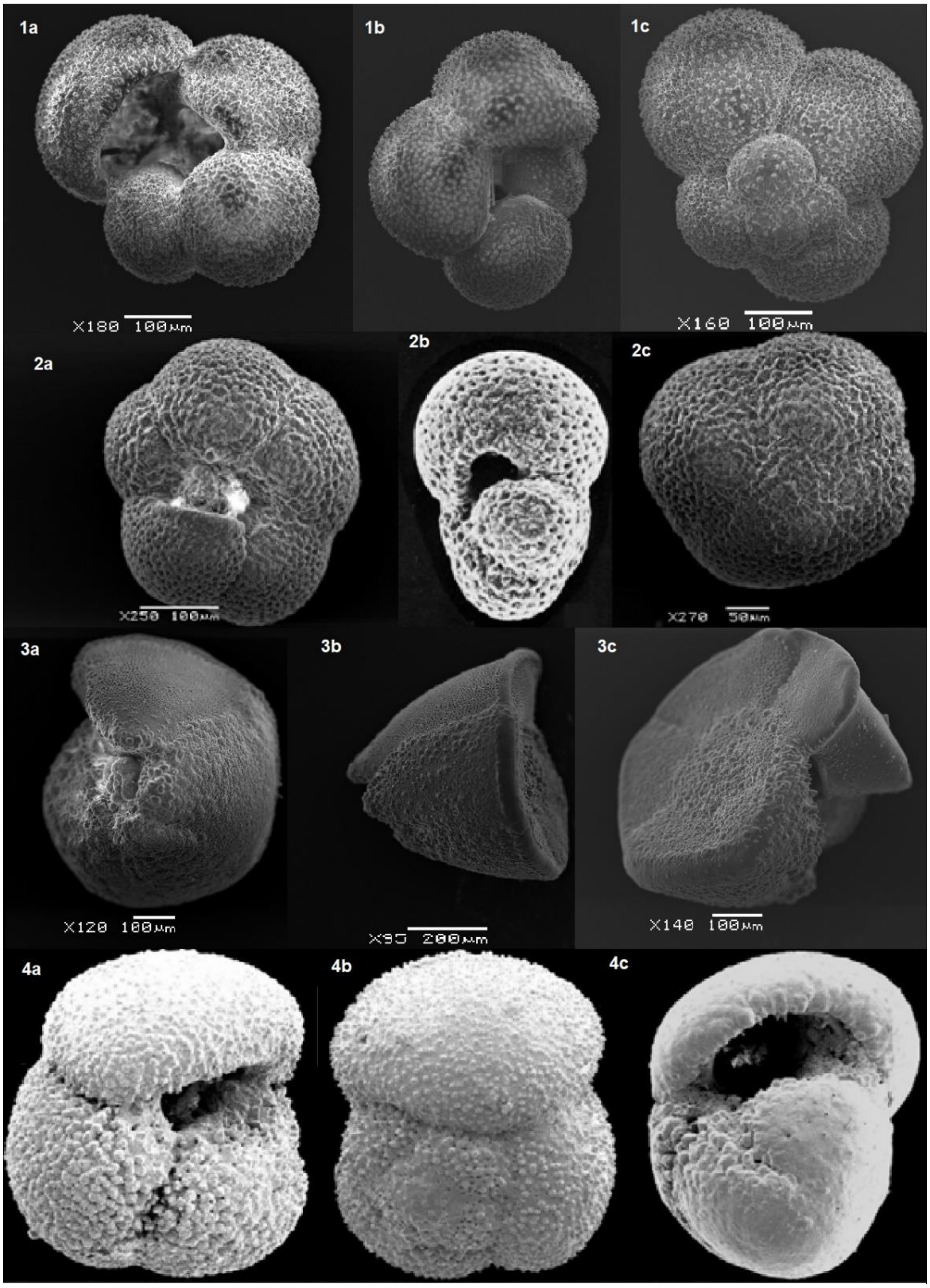

Figure 3.6 Foraminifera species used in this study a) umbilical view, b) axial view, c) spiral view. 1) *G. bulloides*, 2) *N. pachyderma (s)* (axial view source: Kennett & Srinivasan, 1982), 3) G. *truncatulinoides (dextral coiling)* 4) *G. inflata* (all images: Bruce Hayward)

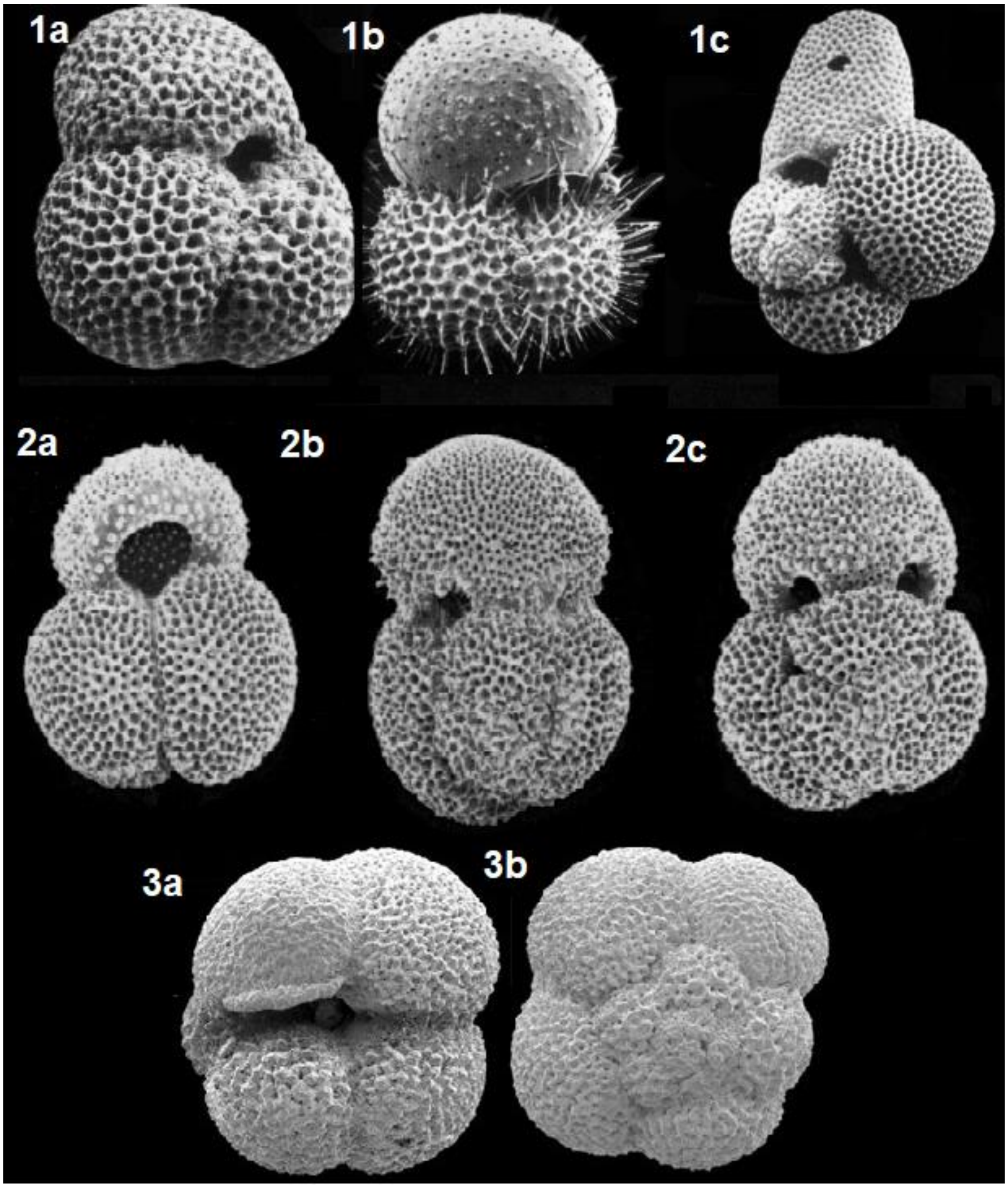

Figure 3.7 Foraminifera species used in this study (continued) a) umbilical view, b) axial view, c) spiral view. 1) G. *sacculifer* (Image: Bruce Hayward), 2) G. *ruber* (Source: Kennett & Srinivasan, 1982). 3) *N. incompta* (Image: Bruce Hayward)

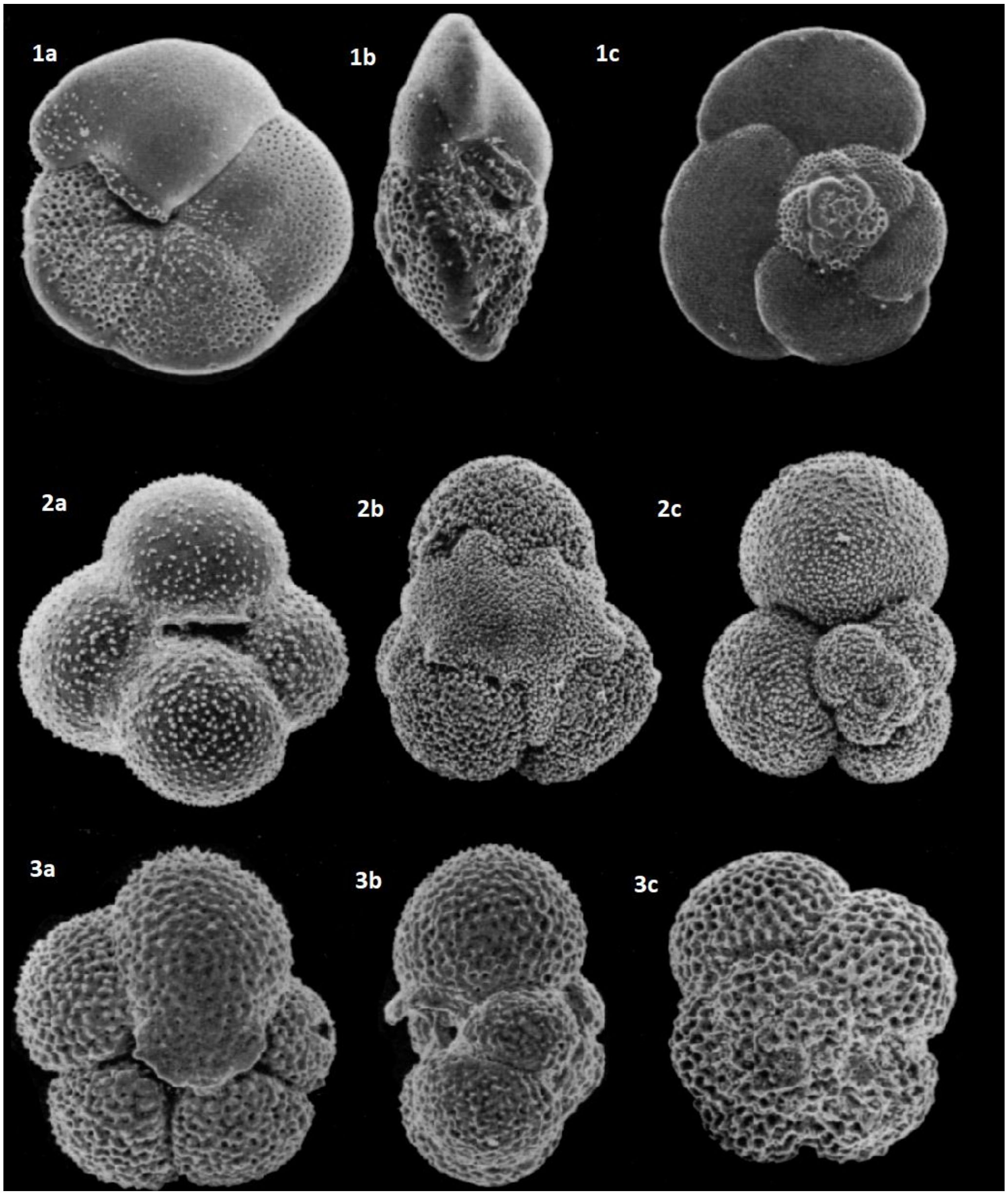

Figure 3.8 Foraminifera species used in this study 1) G. *scitula* a) umbilical view, b) axial view, c) spiral view. 2) G. *glutinata* a) umbilical view b) umbilical view with aperture covered by bulla c) spiral view. 3) G. *glutinata* a) umbilical view, b) axial view, c) spiral view. (Images sourced from Kennet and Srinivansan (1983))

3.4 Estimating foraminifera calcification temperatures

3.4.1 World ocean Atlas temperatures of foraminifera calibration samples

Calcification temperatures were calculated using species predicted habitat depths and seasonality (described in section 3.3.2) from the World Ocean Atlas 1994 (herein WOA) (Table 3.40) (Conkright et al., 1994). For species which migrate throughout the water column (e.g. *G. truncatulinoides* and *G. inflata*) the calcification depth was inferred from the depth of the summer mixing layer at the core top site (Figure 3.9). When temperatures exceed 16 °C, a variale thermocline calcification depth was assumed (Cleroux et al., 2007). Temperatures were calculated by interpolating between the four nearest WOA data locations to the core site.

Use of the 1994 dataset allowed direct comparison with other assemblage based foraminifera temperature reconstructions (e.g. Pflaumann et al., 2003). The 1994 dataset provides global average temperature estimates at 1° resolution between 1900 and 1992. Such an extended time period is thought to be more reflective of the top 1-2 cm of core sediment from which samples are taken, than latterly published World Ocean Atlas datasets which offer more recent, and constrained time periods.

Table 3.4 Calcification depths and seasonality for core top foraminifera samples. *G. inflata* and *G. truncatulinoides* (s) depths based on depth of the summer thermocline at each location (Figure 3.9)

Species	Depth	Seasonality	Reference
G. bulloides	0-50 m	NEAP-04B, MD99-2252, NEAP-16B, NEAP-20B May – Jun BOFS 31K Feb – March Rapid 26-14B Jul – Aug	Ganssen & Kroon (2000) Schiebel et al. *(*1997) Bauch & Kandiano (2007)
G *inflata*	NEAP-16B, NEAP-19B, NEAP-20B 75 – 100 m BOFS31K 150 - 400 m	Jun - Aug	Cleroux et al. *(*2007) Ganssen & Kroon (2000)
G *ruber* (p)	0-30 m	Jun - Aug	Ganssen & Kroon (2000) Jonkers & Kucera (2016)
G *ruber* (w)	0-10 m	Jun - Aug	Ganssen & Kroon (2000) Jonkers & Kucera (2016)
G *sacculifer*	0-50 m	Jul - Sep	Chapman (2010) Schiebel et al. *(*2001)
G *truncatulinoides* (s)	150 - 250 m	Jun - Aug	Cleroux et al. *(*2007)
N. pachyderma (s)	75 - 100 m	Jun - Aug	Jonkers et al. *(*2010)
N *incompta*	0-100 m	May-Aug	Chapman (2010) Schiebel et al. *(*2001) Jonkers & Kucera (2016)

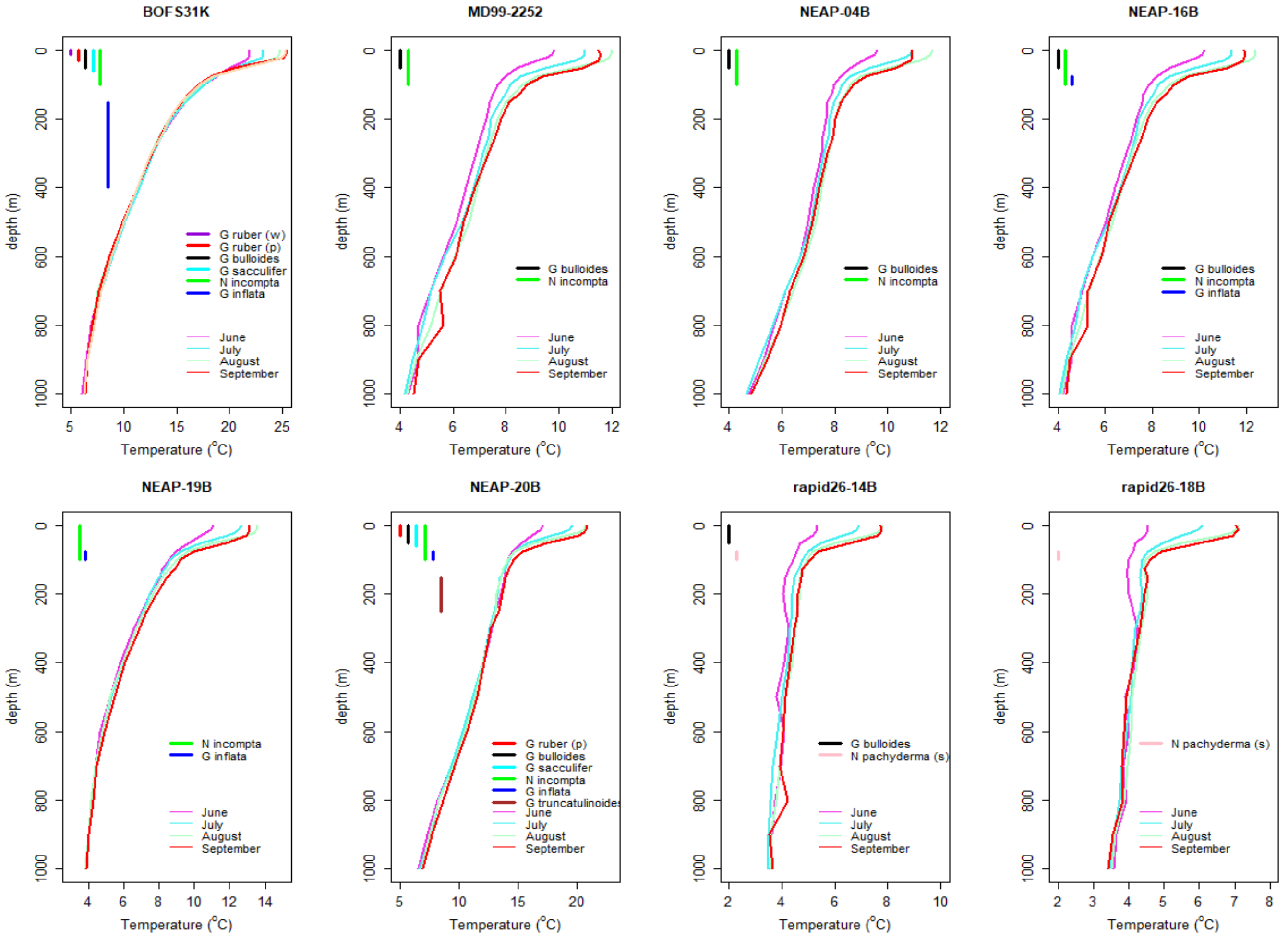

Figure 3.9 Temperature vs depth profiles at the 8 calibration sites used in this study. Calcification depths for different species are indicated by the vertical coloured bars

3.4.2 Mg/Ca ratio inferred temperatures of foraminifera calibration samples

Additional calcification temperature estimations were constructed from Mg/Ca ratio measurements on nine core top samples (See Chapter 5 for methodology) where sufficient sample remained after clumped isotope analysis. Inferring temperatures from foraminifera Mg/Ca ratios is hindered by varying degrees of temperature sensitivity to Mg uptake between species (Elderfield et al., 2002; Anand et al., 2003; Thornalley et al., 2008) and considerable variability in published temperature calibrations.

Table 3.4 Calcification depths and seasonality for core top foraminifera samples. *G. inflata* and *G. truncatulinoides* (s) depths based on depth of the summer thermocline at each location (Figure 3.9) shows calcification temperatures for Mg/Ca measured core tops in this study, calculated using several published calibrations and compared alongside WOA temperatures. Temperature inferences vary considerably, with a range of up to 12.7 °C observed in *G. bulloides.* Thus it can be shown that the Mg/Ca calibration chosen will have a dramatic impact on the subsequent clumped isotope calibration constructed from it. Generally higher temperature estimates tend to come from calibrations derived from subtropical cores (e.g. Anand et al., 2003; Elderfield et al., 2002) and lower estimates from those derived from multiple North Atlantic mid latitude core tops (e.g. Barker et al., 2002).

Comparison of Mg/Ca temperature inferences against WOA temperature was used to assess the validity of each calibration (Table 3.4 Calcification depths and seasonality for core top foraminifera samples. *G. inflata* and *G. truncatulinoides* (s) depths based on depth of the summer thermocline at each location (Figure 3.9)). In seven out of the nine core samples analysed, the minimum offset between WOA and Mg/Ca inferred temperatures was observed when the geographically closest derived Mg/Ca calibration was used (Table 3.6). In the two instances where the geographically closest calibration did not provide closest agreement with WOA derived temperatures (*G. sacculifer* in NEAP 20B and *G. ruber* (p) in BOFS 31K), it is the second latitudinally closest calibration that provides the best match.

Thus the proximity, particularly latitudinal distance, of calibration sites to core top location was shown to be the most important factor when choosing which calibration to use in Mg/Ca temperature reconstructions. For the purposes of the clumped isotope thermometer developed in this study, those calibrations producing the smallest offset from WOA temperatures are used. Errors quoted are calculated from calibration uncertainties in the printed literature.

Table 3.5 Inferred Mg/Ca temperatures for Mg/Ca core top measurements using published calibrations. Bracketed number is the offset from the World Ocean Atlas 1994 estimated temperature (WOA). All temperatures are in °C. Values in bold exhibit the smallest offset from the WOA estimate for a given sample. Calibrations from left to right: Lea et al. (1999), Elderfield & Ganssen (2000) (Single species (SS) and multi species calibrations), Barker & Elderfield (2002), Thornalley et al 2008, Kozdon et al. (2009), Cleroux et al. (2008)(Single species (SS) and multi species calibrations), Farmer (2010), Anand et al. (2003) (Single species (SS) and multi species calibrations), Elderfield et al. (2002). Errors calculated from calibration uncertainties.

Core	species	WOA	Mg /Ca	Lea	E+G (SS)	E + G (multi)	B+E	Thornally et al.	Kozdon et al.	Cleroux (SS)	Cleroux (Multi)	Farmer	Anand et al. (multi)	Anand et al. (SS)	Elderfield et al.	Temp Range
NEAP-16B	*G. bulloides*	9.1	2.6	15.8 (6.7)	15.3 (6.2)	16.0 (6.9)	**12.8 (3.7)**	16.0 (6.9)		14.6 (5.5)	23.5 (14.4)				21.3 (12.2)	10.7
NEAP-20B	*G. bulloides*	15.7	2.9	16.9 (1.2)	16.4 (0.7)	17.1 (1.4)	13.9 (1.8)	12.9 (2.8)		**15.9 (0.2)**	25.6 (9.9)				23.5 (5.6)	12.7
NEAP-04B	*G. bulloides*	8.7	2.2	14.0 (5.3)	13.5 (4.8)	14.2 (5.5)	10.9 (2.2)	**10.0 (1.3)**		12.4 (3.7	19.9 (11.2)				17.6 (8.9)	9.9
Rapid 26-14B	*N. pachyderma (s)*	4.8	1.2		8.9 (4.1)	8.5 (3.7)			**6.7 (1.9)**							2.2
NEAP-20B	*G truncatulinoides (s)*	13.5	2.1		**13.4 (0.1)**	13.8 (0.3)				19.9 (6.4)	19.1 (5.6)		18.8 (5.3)	19.4 (5.9)	16.8 (3.3)	6.4
NEAP-20B	*G inflata*	14.5	2.0		**14.1 (0.4)**	13.5 (1.02)				18.5 (4.0)	18.5 (4.0)	20.0 (5.5)	18.5 (4.0)	22.0 (7.5)	16.2 (1.7)	8.5
NEAP-20B	*G.sacculifer*	19.2	2.7		17.0 (2.2)	16.6 (2.6)		14.0 (5.2)					22.0 (2.8)	**20.5 (1.3)**	22.5 (3.3)	8.5
BOFS 31K	*G.sacculifer*	23.3	2.9		17.6 (5.7)	17.2 (6.1)		14.6 (8.7)					22.6 (0.7)	21.2 (2.1)	**23.6 (0.3)**	9.0
BOFS 31K	*G. ruber (p)*	23.2	3.0		17.6 (5.6)					19.7 (3.5)	26.5 (3.3)		**23.0 (0.2)**	21.3 (1.9)	24.4 (1.2)	9.0

Table 3.6 Geographical range of published Mg/Ca calibrations (top) and their proximity to Mg/Ca sample core top locations (bottom). Distance is calculated from the mid-point of the calibration longitude/latitude range where appropriate.

Calibration	Calibration type	Latitudinal range (°N)	Longitudinal range (°E)
Lea et al. *(*2009)	Laboratory culture	-	-
Elderfield and Ganssen (2000)	Core top	30 - 60	-25
Barker and Elderfield (2002)	Downcore	59.46	-23.53
Thornally et al. (2009)	Core top	62.1	-17.8
Kozdon et al. (2009)	Core top	62.27 – 79.40	-25.95 – 13.11
Cleroux et al. (2008)	Core top	17.4 – 60.6	-92.9 - -8.5
Farmer (2010)	Core top	17.4 – 60.6	-92.9 - -8.5
Anand et al 2003	Sediment trap	32.08	-64.25
Elderfield et al. *(*2002)	Downcore	19	-21.167

Core	Latitude (°N)	Longitude (°E)	Geographically closest calibrations	Distance (km)
NEAP-04B	61.367	-24.172	Thornally et al. *(*2009)	345
NEAP-16B	56.37	-27.82	Barker and Elderfield (2002)	354
NEAP-20B	42.488	-28.415	Elderfield and Ganssen (2000)	391
BOFS31K	19	-21.167	Elderfield et al. *(*2002)	0
Rapid26-14B	59.593	-41.167	Kozdon (2009)	1586

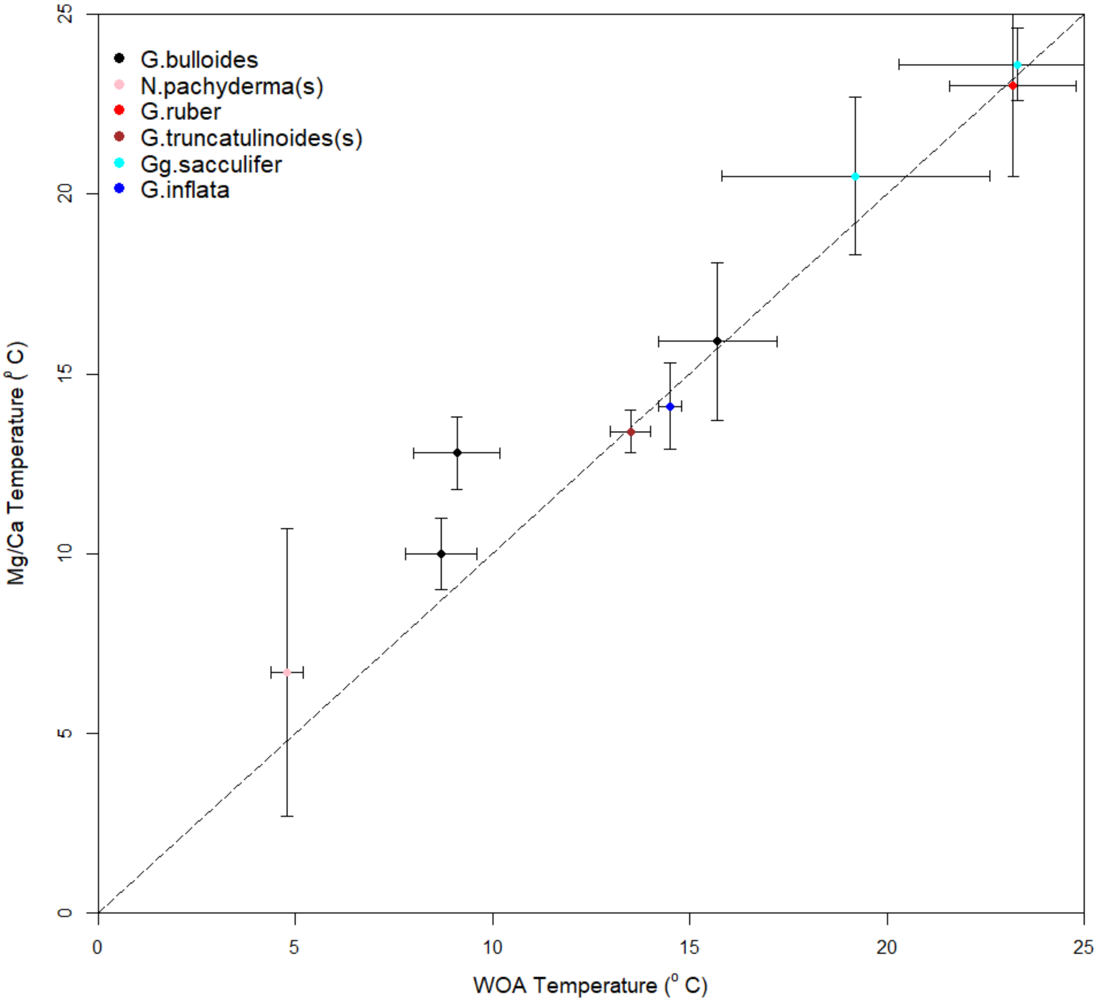

Figure 3.10 Paired Mg/Ca and WOA temperatures. Dashed line is 1:1 line

Mg/Ca temperatures show good agreement with WOA inferred temperatures (Figure 3.10), with 7 out of 9 samples falling within calculated errors. Below 12 °C, there is a slight tendency for warmer Mg/Ca temperature estimates compared with those from the World Ocean Atlas.

3.4.3 Stable isotopic inferred temperatures of foraminifera calibration samples

Additional core top temperature estimates were calculated from stable isotopic temperatures using the Shackleton equation (Shackleton, 1974):

$$T = 16.9 - 4.38 \times (\delta^{18}O_{foraminifera} - \delta^{18}O_{seawater}) + 0.1 \times (\delta^{18}O_{foraminifera} - \delta^{18}O_{seawater})^2$$

$\delta^{18}O_{seawater}$ is then calculated according to the relationship derived by Cleroux et al*. (*2008):

$$\delta^{18}O_{sw}(vsmow) = -19.264 + 0.558 \times salinity$$

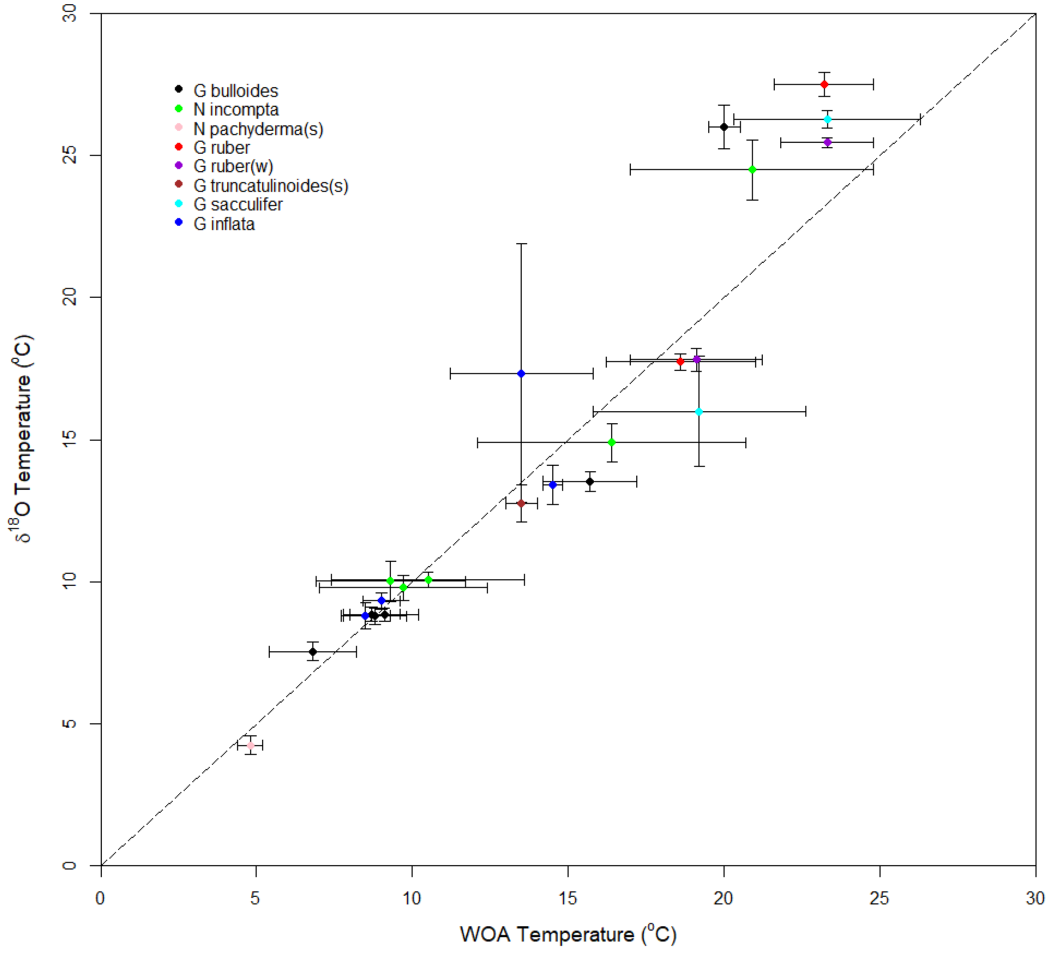

Figure 3.11 Paired $\delta^{18}O$ and WOA temperatures. Dashed line is 1:1 line

This methodology was used in preference to obtaining $\delta^{18}O_{seawater}$ directly from observational datasets such as Legrande & Schmidt (2006) and NASA GEOSECs, since it enabled calculation of $\delta^{18}O_{seawater}$ at multiple depths and eradicated uncertainty arising from sparse measurement sites within the databases.

Salinity data was obtained from the World Ocean Atlas 1994 (Conkright et al., 1994) at the relevant calcification depths and seasonality (Table 3.4) by interpolating between the four nearest WOA data points. $\delta^{18}O_{seawater}$ errors were calculated from the salinity range over species depths and seasonality at each core location in the WOA database. This was used, alongside $\delta^{18}O_{foraminifera}$ to calculate temperature error.

Isotopic temperatures show good agreement with WOA temperatures (Figure 3.11) with some disparity above 20 °C where isotopic temperatures tend to predict warmer conditions than those observed in the WOA dataset.

3.5 Foraminifera sample preparation

Bulk core top material was sieved into constrained size fractions and individual species picked under binocular optical microscope. Between 450 and 600 individual tests provided sufficient material for a single clumped isotope measurement, dependent on the density of calcite and size fraction of the particular species.

3.5.1 Consideration of diagenesis

Post depositional diagenesis has long been known to alter isotopic and chemical signatures of foraminiferal calcite (Delaney, 1989 ; Kozdon et al., 2013) and has been suggested as the cause of 'cool tropic paradox' (Crowley & Zachos, 2000) whereby erroneously cool temperatures are inferred from foraminiferal calcite compared with modelling studies during the mid-Cretaceous.

Recent work has suggested that diagenetic effects are also measurable in clumped isotopic signatures (Stolper et al., 2018). This is problematic since primary Δ47 signatures must be preserved in fossilised calcite in order to accurately infer palaeoceanographic temperatures. Negative temperature offsets up to 12 °C have been observed, reflecting the cooler depositional environment under which diagenesis occurs (Leutert et al., 2019). Furthermore, the effect is most prominent in planktonic species, such as those studied here, where the temperature gradient between primary calcification, and depositional, environment is greatest (Edgar et al., 2013).

At earth surface temperatures, diagenesis arises from one of three processes: carbonate dissolution, cementation of minerals in carbonate pores and neomorphism, or recrystallization (Killingley, 1983).

In situ measurements from the Sargasso Sea (Honjo & Erez, 1978) and laboratory experiments (Subhas et al., 2018) suggest that foraminiferal calcite can be subjected to substantial dissolution over just a few months in oceanic waters. Hence care was taken to ensure that only pristine specimens were obtained, with no visual evidence of fragmentation or dissolution. For the two Rapid cores located off the Greenland margin, it was not possible to obtain sufficient pristine material and a small number of tarnished specimens had to be used, however their inclusion was limited as far as possible.

Carbonate cementation and neomorphism require further consideration. Both have been shown to impact foraminiferal calcite during early stages of burial and therefore may be important to the relatively 'modern' samples utilised throughout this study (Rudnicki et al., 2001). Sexton et al*.* *(*2006) suggested that samples subjected to such diagenetic effects tended to exhibit a 'frosty' appearance under the binocular microscope compared with a 'glassy' appearance from pristine specimens. Thus effort was made to obtain only samples with clear, glassy appearances. Yet stippled surfaces in spinose species are common and this often gives a 'frosty' appearance even for pristine samples. Thus it is not always possible to authoritatively identify non-diagenetically altered specimens with a binocular microscope alone. Here it is necessary to examine specimens under scanning electron microscope (SEM) for signs of calcite overgrowths and infillings (Figure 3.12).

SEM analysis of core top samples of *G. bulloides* from core NEAP-19B and *G. truncatulinoides* (s) from NEAP-20B revealed no visual evidence of calcite overgrowths or infillings (Figure 3.13 and Figure 3.140), suggesting that diagenesis effects are negligible in core top samples. This agrees with the findings of Stolper et al. (2018) who proposed that diagenesis effects are most prominent in burial sites below 1km in depth below the sea floor. As such, fossilised samples could be assumed to be void of digenetic effects due to their relatively shallow burial depths (between 10 – 40 m). All cores in this study from which palaeo samples were taken exhibit high sedimentation rates, limiting contact with oceanic waters and potential sources of secondary calcite. Furthermore, all palaeo-cores exhibit a high clay concentration which has been shown to limit secondary calcite formation by 'entombing' the specimen and limiting contact with pore waters (Sexton et al., 2006).

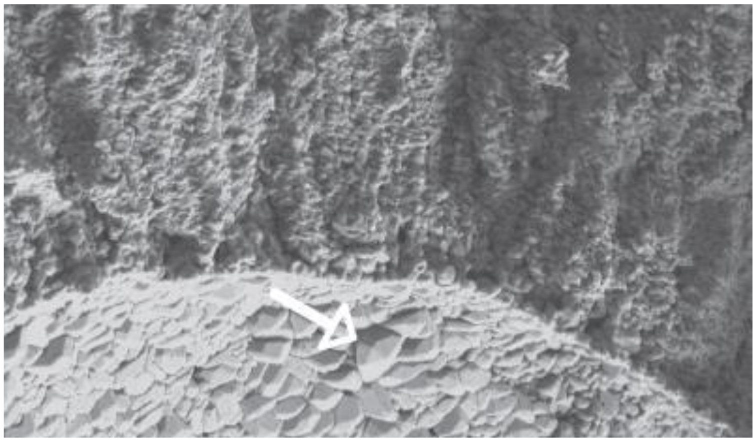

Figure 3.12 SEM image of *N. truempyi* showing calcite overgrowths (indicated by arrow) as a results of diagenesis (source: Leutert et al., 2019)

Fiebig et al. (2019) showed that diagenetic alteration gives rise to deviation in the Δ47 vs Δ48 relationship from that expected from a purely temperature driven signal. Deviations from this relationship are used to screen all samples for contamination (section 2.3.5) and thus any diagenetically altered samples should be identified and eliminated through this process.

3.5.2 Foraminifera pre-cleaning procedure

Scanning electron microscope (SEM) analysis of crushed foraminifera core samples revealed extensive contamination from coccolithophores and other detrital material captured within test chambers (Figure 3.13 and Figure 3.14). The slow settling rate of coccolithophores (on average 13.8 cm day^{-1} (Winter & Siesser, 1994)) results in yearly to decadal deposition. Honjo (1976) theorised that such slow settling rates could result in translational displacement of up to 10^5 km in oceanic waters of 5km depth. Thus coccolithophores provide a potential secondary source of sample calcite which may have been formed at sites with very different temperatures from those at the core location. Their removal prior to analysis is clearly desirable to exclude potential alien temperature signals.

A second potential source of contamination comes from sedimentary minerals and residue test proteins, which have the potential to react with phosphoric acid and create contaminants at masses of interest — although the precise nature of such reactions remains largely unstudied. It is clear therefore that a sample cleaning procedure to remove sediment contamination prior to acid digestion should be considered.

Existing studies have adapted one of two similar pre-cleaning treatments developed for trace element analysis: (Boyle & Keigwin, 1985) and Barker et al*.* *(*2003). Broadly similar, the methods physically crush tests and remove large chamber debris under the microscope, before repeated washing in distilled water and methanol to remove fine sediment. An NaOH buffered H_2O_2 wash is applied for removal of organic matter on the calcite surface before a final leach with dilute acid to remove secondary surface calcite. Existing clumped isotope studies have tended to omit the final acid leach step, presumably to avoid sample fractionation through dissolution. Solution concentrations, as well as the number and duration of each wash differs between studies. See Table 3.7 for details.

Whilst these cleaning procedures have been adopted, little research has been published into their impact on foraminifera samples. Tripati et al. (2010) confirm the validity of the method by showing that the procedure has no measurable impact on laboratory standards, but provide no detail of the effect on more porous foraminiferal calcite.

In addition, there is much conflicting evidence on the impact of hydrogen peroxide washing. Grauel et al. (2013) observe significant calcite dissociation and recombination from peroxide washing - apparent under SEM analysis, whereas Tripati et al. (2010) report no such effect. It is likely that the disparity arises from the more aggressive 5-minute wash in 10 % H_2O_2 solution at 100 ^{o}C, tested by Grauel et al. (2013), compared with the 15 – 60 minute rinse in 1 % solution favoured by Tripati et al. (2010). Thus Grauel et al. (2013) chose to omit this stage from their final cleaning procedure.

The recent study of Peral et al. (2018) tested both of these hydrogen peroxide treatments, concluding that both the Grauel et al. (2013) and Tripati et al. (2010) treatments led to some degree of carbonate dissolution on foraminiferal calcite, evident under scanning electron microscope analysis. Despite the differing degrees of dissolution, no offset in either clumped or stable isotopic signatures between the two methodologies was measured, suggesting that the impact was below instrumental detection. Such disparities in the existing literature, and the lack of published data give rise to the need for further research.

In this study, laboratory standard UEACMST and foraminiferal samples from two North Atlantic core tops were subjected to each stage of a cleaning procedure adapted from Barker et al. (2003). UEACMST samples were cleaned in both powdered and granulated forms, with the former thought to more closely resemble finer foraminiferal calcite. UEACMST is known to be a relatively clean sample and thus was used to assess the impact of the procedure on pure calcite, removing any signal from contaminant removal. The core top samples NEAP 19B *G. bulloides* and NEAP 20B *G. truncatulinoides* (s) were chosen since their high abundance allowed for multiple measurements and the two species reflected both open (*G. bulloides)* and tightly coiled (*G. truncatulinoides*) test morphology – with the former considered more susceptible to sediment capture in open test chambers. For *G. bulloides,* 600 specimens from the 300 - 355 µm size fraction were picked and for *G. truncatulinoides,* 400 from the 355 – 500 µm size fraction. This was sufficient for a 4 mg clumped isotope measurement.

Table 3.7 Pre-acid digestion cleaning procedures for existing clumped isotope studies of foraminifera

	(Grauel et al., 2013)	**(Tripati et al., 2010)**	**(Evans et al., 2017)**	**(Breitenbach et al., 2018)**
Ultrasonication in ultrapure water	2 x 60s (repeat if necessary)	5 x 60s (pre methanol rinse) 3 x 60s (post methanol rinse)	Once. Time unspecified (fossil samples only)	Conducted (duration unspecified)
Ultrasonication in methanol	2 x 30s	5 repeats (duration unspecified)	Once. Time unspecified (fossil samples only)	Conducted (duration unspecified)
H_2O_2 rinse	Not used. 10 % solution fixed at pH 8 seen to induce dissolution	15 – 60-minute reaction (dependent on organic concentration) in 1 % solution	Ultrasonicated for 30 mins in 7 % H_2O_2 (modern samples only)	5 % H_2O_2 buffered by 0.1 m NaOH at room temperature
Final rinse/drying	No detail given	Centrifuged and decanted before being rinsed four times in distilled water, twice in methanol and twice more in distilled water	Rinsed three times in distilled water and dried overnight in vacuum at 25°C	Secondary silica grain removal under microscope before drying in vacuum at room temperature overnight and powdering between glass plates.

Prior to finalising a methodology, investigation was conducted into the impact of ultra-sonication on sample loss and contaminant removal. Ultra-sonication is a key part of the cleaning procedure, aiding the release of contaminants tightly bound to the calcite surface. In less robust *G. bulloides* however, it leads to enhanced test fragmentation and undesirable sample loss during surfactant removal. Each foraminifera sample was ultra-sonicated in ultrapure water in ten second increments before surfactant was removed, the sample dried overnight in a drying oven, and finally weighed to gain an estimate of sample retention. The results are presented in Table 3.8.

Table 3.8 Foraminifera sample retention after repeated ultrasonication

Sonication time (seconds)	*G. bulloides* **% of sample remaining**	***G truncatulinoides* (s) % of sample remaining**
Start	100	100
10	90	96
20	81	97
30	79	96
40	76	82
50	72	80
60	69	79
70	68	79
80	65	79
90	64	79
100	64	79

Mass loss is greatest in *G. bulloides* samples, likely a reflection of the higher concentration of contaminant being removed from open test morphology compared to *G. truncatulinoides* (s), as well as enhanced fragmentation of less robust test calcite leading to increased sample loss during surfactant removal. SEM images of samples subjected to 60 seconds of ultra-sonication suggest that this is sufficient to remove all visible evidence of sediment contamination (Figure 3.13 and Figure 3.14). SEM images of foraminiferal calcite subjected to longer periods of ultra-sonication show enhanced fragmentation (Figure 3.15). Thus any mass loss beyond 60s was considered to be due to sample removal alone. This is confirmed in a plateauing of mass loss in *G. truncatulinoides* samples beyond 60s as contaminant removal ceased and the more robust calcite tests exhibited reduced vulnerability to removal in surfactant compared with *G. bulloides*.

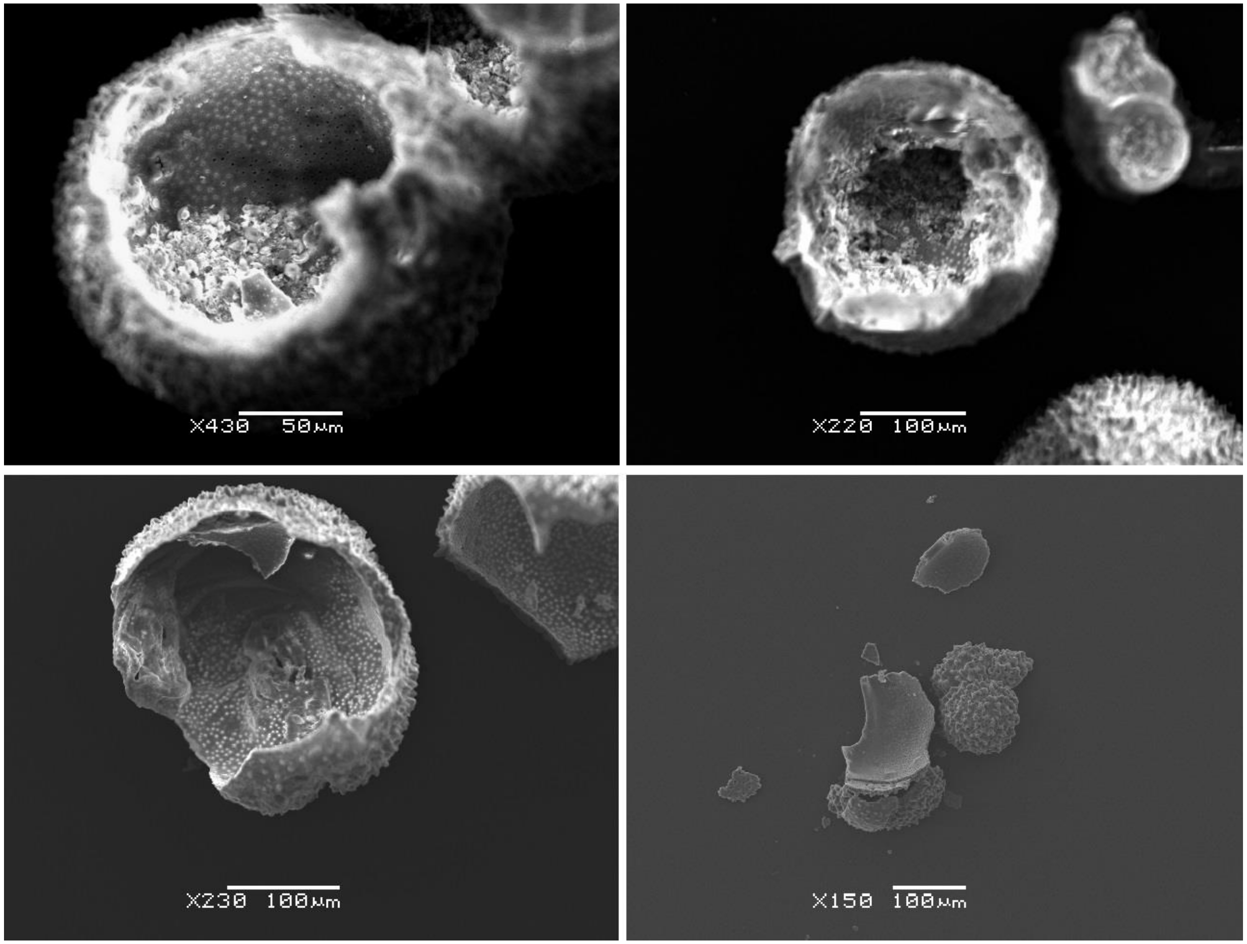

Figure 3.13 SEM images of *G. bulloides* from core NEAP19B. Top) Chambers have been crushed to allow internal investigation under SEM. No further cleaning has been conducted. Detrital matter, including a large concentration of coccolithophores calcite is clearly present. Bottom) Sample subjected to 6 x 10 second rinsing in ultrapure water (3x10s) and methanol (3x10s). No further visible sign of contamination.

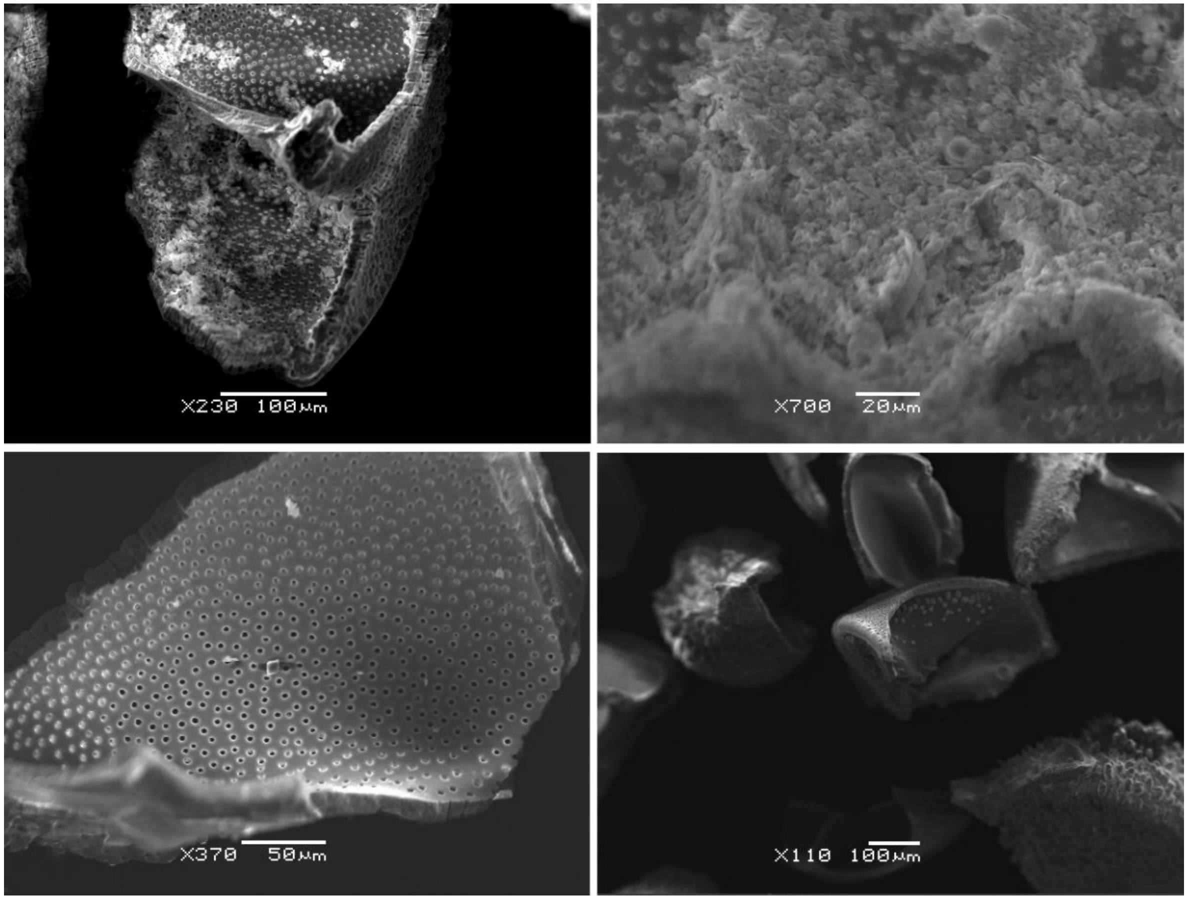

Figure 3.14 SEM images of G *truncatulinoides*. Top: Crushed with no further cleaning. Detrital coccolithophores contamination clearly present. Below. Sample subjected to 6 x 10 second rinsing in ultrapure water (3x10s) and methanol (3x10s). No further visible sign of contamination.

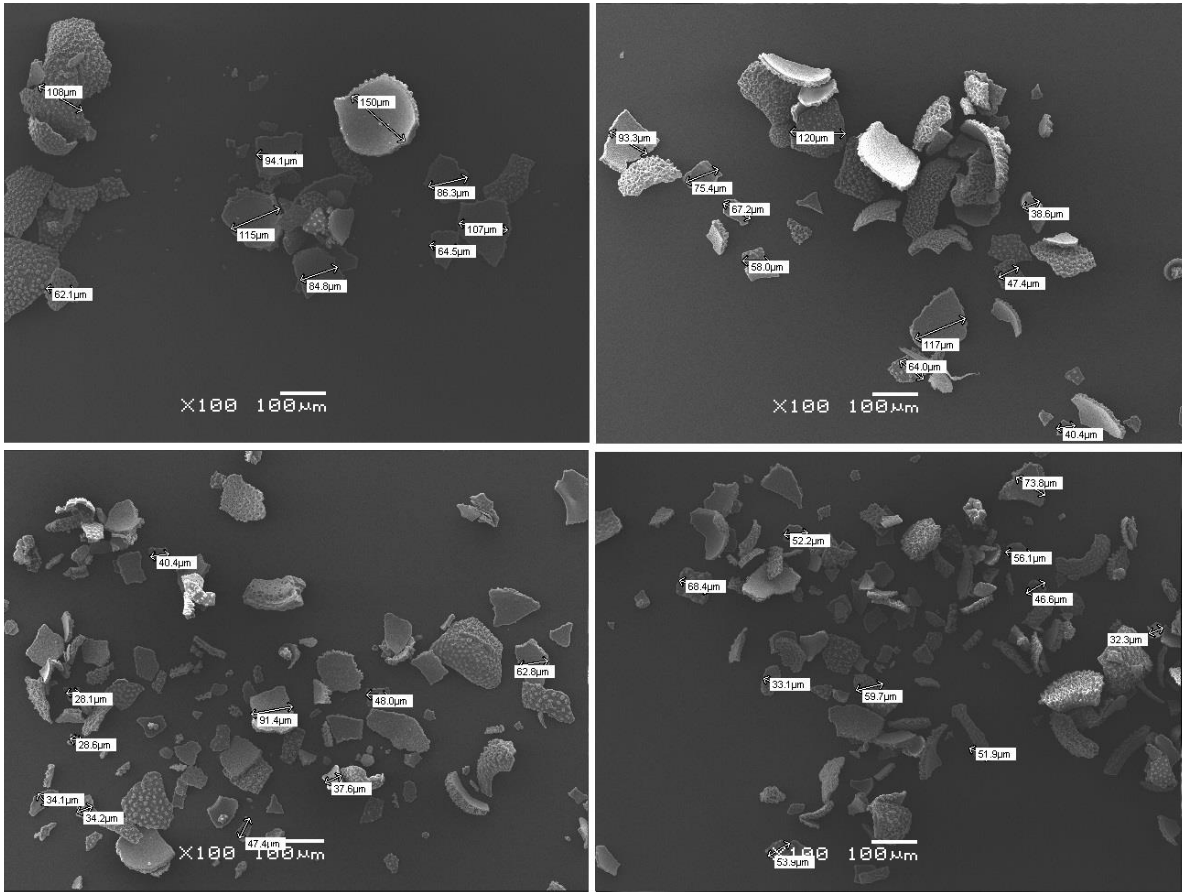

Figure 3.15 SEM images of NEAP 19B *G. bulloides* showing the effect of lengthening sonication time on increasing fragmentation. Total sonication time clockwise from top left: 60s, 90s, 120s, 150s

Once idealised ultrasonication time had been derived, the following pre-cleaning procedure was defined:

Foraminifera tests were fragmented by gently pressing between two glass plates to free sediment trapped in test chambers. Care was taken to avoid extreme fragmentation during this process by using minimal force and thus avoiding additional sample loss. Large sediment grains or discoloured tests were removed with a paintbrush under a binocular stage microscope. The sample was then transferred to a micro-centrifuge tube.

Samples were rinsed using the 'minimum settling technique' by first covering in 500 µL of ultrapure water and allowing to settle for 30 seconds. Supernatant was then removed by pipette, taking away clay particles in suspension and leaving behind ~50 µL of fluid in the micro-centrifuge tube. The sample was then ultrasonicated for ten seconds to release contaminants tightly bound to the calcite surface, before rinsing again in ~300 µL of ultrapure water, allowing to settle for 30 seconds and removing surfactant. This process was repeated a minimum of two times with additional rinses if visible signs of contamination remained under the binocular microscope.

This rinsing process was repeated a minimum of two times using 300 µL of Aristar methanol. The lower viscosity of the methanol, compared with water, encourages finer particulates into suspension. Repeat rinses were conducted if visible signs of contamination remained. Residue methanol was removed by rising twice in 500 µL of ultrapure water.

Next, 300 µL of alkali buffered 10 % H_2O_2 was added to the sample and the tube inverted several times to ensure good mixing between the reagent and sample. Air bubbles were removed by agitating the solution, ensuring constant contact between reagent and sample.

Two peroxide methodologies were tested:

1. A 20-minute room temperature reaction. The sample is agitated after ten minutes to remove air bubbles
2. A more aggressive, 20 minute 100 ^{o}C reaction, more closely matching the methodology of Barker et al. (2003) but rejected by Grauel et al. (2013) as it was seen to cause secondary calcite overgrowth. This step is repeated twice.

After both methods, supernatant was removed by pipetting and excess reagent removed by rinsing twice in 500 µL of ultrapure water.

A final acid leach to remove calcite overgrowths was conducted with the addition of 500 µL of 0.01 m nitric acid, after which the sample was ultrasonicated for 30 seconds and allowed to settle before surfactant was removed. The sample was rinsed twice in ultrapure water, transferred to a durham tube using a wide nozzle pipette and left to dry overnight at 50 °C.

Clumped isotope measurements of UEACMST (powdered and granulated) and *G. bulloides* were conducted after the following stages of the procedure to monitor the effects on isotopic composition:

- Uncleaned
- Water covered only and dried overnight in a drying oven. This test was conducted to monitor for isotopic exchange between surfactant water and calcite
- Rinsed only: After water and methanol rinsing and allowed to dry overnight
- After weak peroxide clean (rinse / weak peroxide clean)
- After the more aggressive peroxide clean (rinse / aggressive peroxide clean)
- After full treatment (rinse / Aggressive peroxide clean / acid leach)

The same measurements were conducted for *G. truncatulinoides* (s) samples, omitting water covered and full treatments.

Table 3.9 UEACMST and foraminifera core top measurements conducted after each stage of the pre-cleaning procedure. n = number of clumped isotope measurements. Errors are 95 % confidence intervals.

	No treatment	**Water covered**	**Rinse**	**Weak peroxide**	**Aggressive peroxide**	**Full treatment**
UEACMST						
n	16	8	8	8	3	3
Δ47 ‰ (ARF)	0.403 (± 0.02)	0.387 (± 0.01)	0.426 (± 0.02)	0.406 (± 0.04)	0.354 (± 0.02)	0.366 (± 0.009)
Δ48 ‰	0.081 (± 0.04)	0.058 (± 0.15)	0.147 (± 0.07)	-0.379 (± 0.09)	-0.093 (± 0.03)	-0.047(± 0.06)
δ^{13}C‰ (VPDB)	1.930 (± 0.04)	1.969 (± 0.03)	1.986 (± 0.03)	1.985 (± 0.06)	1.961 (± 0.004)	1.980 (± 0.01)
δ^{18}O‰ (VPDB)	8.225 (± 0.20)	8.225 (± 0.08)	8.229 (± 0.07)	8.369 (± 0.22)	8.606 (± 0.01)	8.534 (± 0.07)
G. bulloides						
n	4	4	4	4	4	4
Δ47 ‰ (ARF)	0.579 (± 0.06)	0.624 (± 0.04)	0.698 (± 0.03)	0.625 (± 0.07)	0.721 (± 0.01)	0.721 (± 0.02)
Δ48 ‰	-0.219 (± 0.16)	-0.044 (± 0.09)	-0.169 (± 0.12)	-0.194 (± 0.17)	-0.009 (± 0.05)	0.026 (± 0.05)
δ^{13}C‰ (VPDB)	-0.234 (± 0.05)	-0.307 (± 0.07)	-0.375 (± 0.05)	0.037 (± 0.04)	0.089 (± 0.09)	-0.252 (± 0.04)
δ^{18}O‰ (VPDB)	1.454 (± 0.08)	1.454 (± 0.05)	1.510 (± 0.07)	1.525 (± 0.04)	1.554 (± 0.05)	1.5789 (± 0.04)
G. *truncatulinoides*						
n	3		5	3	3	
Δ47 ‰ (ARF)	0.557 (± 0.02)	N/A	0.693 (± 0.05)	0.634 (± 0.04)	0.76 (± 0.07)	N/A
Δ48 ‰	-0.284 (± 0.10)	N/A	-0.102 (± 0.12)	-0.322 (± 0.03)	-0.013 (± 0.06)	N/A
δ^{13}C‰ (VPDB)	0.937 (± 0.15)	N/A	0.962 (± 0.03)	0.928 (± 0.05)	0.965 (± 0.09)	N/A
δ^{18}O‰ (VPDB)	0.986 (± 0.22)	N/A	0.986 (± 0.08)	0.984 (± 0.06)	0.990 (± 0.09)	N/A

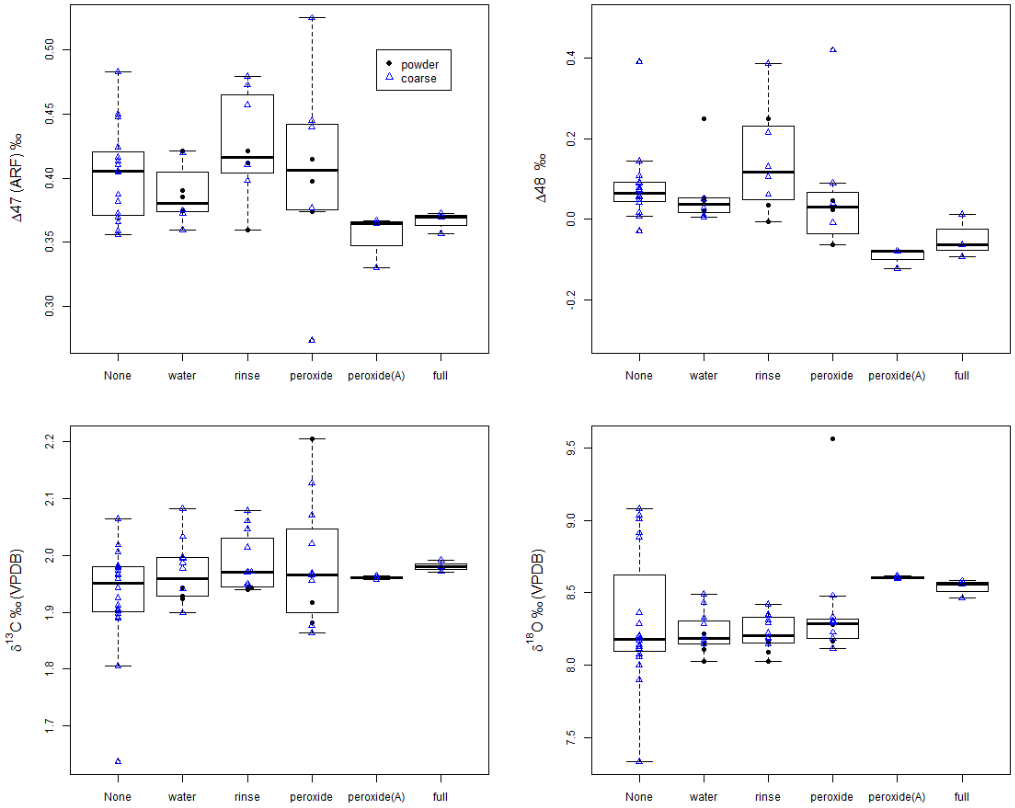

Figure 3.16 Isotopic measurements after each stage of the pre-cleaning procedure for UEACMST laboratory standard. Peroxide (A) is the more aggressive of the two peroxide treatments. $\delta^{18}O$ values corrected to 25 ^{o}C using fractionation factor of 1.008 at 87 ^{o}C and 1.01025 at 25 ^{o}C, calculated according to (Swart et al., 1989).

Clumped isotope measurements were conducted sporadically between April 2016 and November 2018 due to significant instrumental downtime. Throughout this period, the MIRA purification line underwent multiple changes (section 2.3.3), most notably migrating from reacting samples at 25 ^{o}C in individual reaction vessels to using an 87 ^{o}C common acid bath. All data has been corrected to 25 ^{o}C according to the method of Swart et al. (1989) yet an undesirably large spread in the data remains, likely arising from the different processes each has been subjected to on the purification line. Data is summarised in Table 3.9.

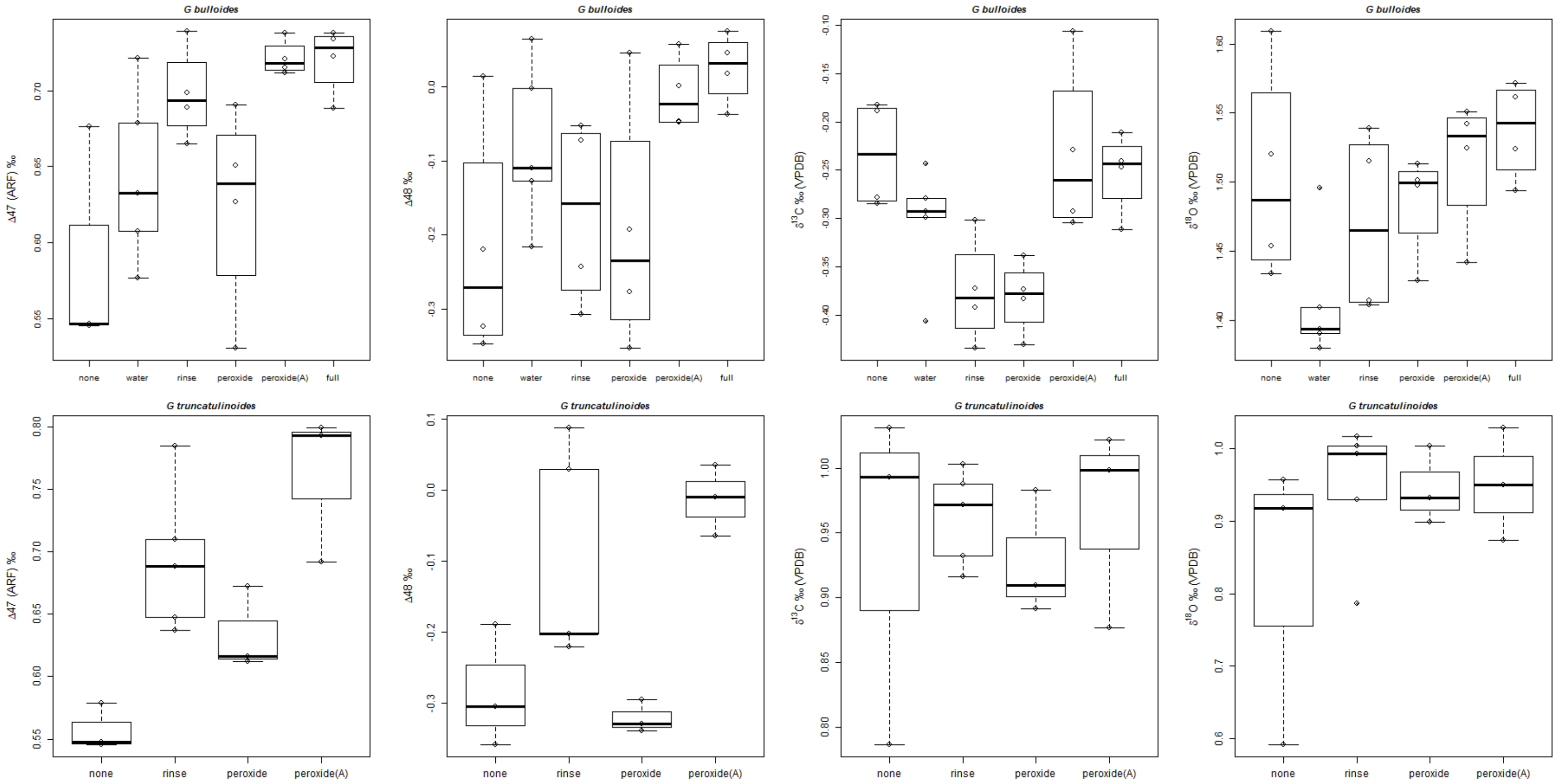

Figure 3.17 Isotopic measurements after each stage of the pre-cleaning procedure for core top *G. bulloides* (top) and G *truncatulinoides(s)* foraminifera samples (G *truncatulinoides(s)* not water covered or subjected to full treatment). Peroxide (A) is the more aggressive of the two peroxide treatments.

No difference was observed between powdered and coarse grained UEACMST samples (Figure 3.16). Rinsing and the weaker peroxide treatment had little impact on UEACMST stable or clumped isotopic signatures, however a shift to lower Δ47 values was observed when subjected to the more aggressive peroxide and acid treatments. Shifts from uncleaned samples were also observed for δ^{13}C for the full treatment and δ^{18}O for the aggressive peroxide and full treatments. Since UEACMST is known to be a pure calcite, this shift was interpreted as the impact of the treatment on the calcite rather than a signature of any contaminant removal, likely arising from a fractionation in the acid digestion step.

Interpretation of the foraminifera data was hindered by the large spread in data, however the measurements were sufficient to show that, as with UEACMST samples, Δ47 shifts were observed in both *G. bulloides* and *G. truncatulinoides (s)* for aggressive peroxide and full treatments. The impact of the rinsing protocol is less obvious. In *G. bulloides* samples, rinsed and uncleaned samples fall within error of each other, in contrast to *G. truncatulinoides* (s) where a significant shift in Δ47 is measured. The question then arises as to why an effect should be observed in *G. truncatulinoides* and not *G. bulloides*. The impact of contaminant removal is expected to be more apparent in the open test morphology of the latter species. It is assumed then that the offset in *G. truncatulinoides* (s) is a measurement anomaly arising from the shifting experimental setup between measurements. It is stressed however that further work is required to confirm this and with additional time, it would have been desirable to repeat some of these measurements.

Finally, Δ48 which is widely used as an indicator of contamination in clumped isotope studies, remains constant (within error) through each stage of the cleaning process. This suggests that any contaminant being removed was either unreactive in reagent acid, present only at concentrations below the instrumental detection level, or that the existing MIRA purification line was sufficient to remove products arising from acid digestion of contaminants.

With no obvious reduction in contamination of foraminifera samples gained from sample pre-cleaning and an undesirable alteration of clean standard calcite from the more aggressive treatments, it was concluded that there is no benefit to applying pre-cleaning procedure to foraminifera samples.

3.5.3 Size fraction tests

Temperature dependent proxies such as Mg/Ca ratios and stable isotopic composition are known to vary with foraminifera test size (Cleroux et al., 2008; Friedrich et al., 2012). Small juveniles tend to calcify in warm surface waters, before descending in the water column to cooler temperatures and acquiring a secondary layer of gametogenic calcite. Thus proxy measurements of larger specimens tend to be more characteristic of cooler environments and it is therefore desirable to pick samples from a tightly constrained size fraction (Friedrich et al., 2012). However, the large samples required for clumped isotope analysis (500+ tests for a single measurement) mean that it is not always possible to obtain a sufficient quantity without increasing the size fraction window.

In order to investigate the impact of test size on Δ47, size fractions 250 - 300 µm, 300 - 355 µm and 355-500 µm of *G. bulloides* core top NEAP 19B and 250 - 300 µm and 300 - 355 µm of *N. pachyderma (s)* from core U1305 (32.06 m depth) were measured in triplicate. The results are presented in Table 3.10.

Table 3.10 Δ47 (ARF) measurements for foraminifera size fraction tests. Three measurements were taken for each size fraction. Errors are 95 % confidence intervals. Δ47 reported on the ARF.

Size fraction (µm)	*G. bulloides*	**N *pachyderma(s)***
212 - 250		0.668 ± 0.01 ‰
250 - 300	0.676 ± 0.01 ‰	0.722 ± 0.01 ‰
300 - 355	0.694 ± 0.03 ‰	
355 - 500	0.683 ± 0.02 ‰	

G. bulloides exhibited little variation in Δ47 over a large range of size fractions. *N. pachyderma (s)* exhibited a shift in Δ47 between the 212 - 250 µm and 250 – 300 µm size fractions, shifting to colder values in the large size fraction. Such shifts have previously been observed in Mg/Ca measurements of interglacial *N. pachyderma (s)* samples from the same core (Hume, 2018). Effort was therefore made to pick *N. pachyderma (s)* samples from as constrained a size fraction as possible, usually the 250 – 300 µm range which captures predominantly adult specimens. *G. bulloides* samples were picked from a larger range of size fractions, although in practice size variation was minimised as much as possible.

3.6 Temperature calibration of Δ47

A Δ47 temperature calibration was constructed from the samples described in section 3.3, consisting of 25 core top planktonic foraminifera samples, a single coldwater coral specimen and three inorganic calcites: ETH3, UEATHC and a 5 °C inorganic precipitate. Additional inorganic precipitates produced for this study are not included in the calibration dataset due to evidence that they have been precipitated out of equilibrium (section 3.2.1). Calibration material is summarised in Table 3.11.

Two single measurement samples, Rapid 29-18B *N. pachyderma (s)* and MD99-2251 *N. incompta*, were omitted from the calibration dataset due to contamination (see section 2.3.5). Single repeat measurements of BOFS 31K and NEAP 20B *G. inflata* and two repeats of the 5 °C laboratory precipitate were also omitted from calculations of Δ47 averages since all showed evidence of fractionation during sample purification by comparison of their stable isotopic composition with repeat measurements.

Table 3.11 Summary of Clumped isotope calibration dataset. All temperatures (T) are in °C. N = number of clumped isotope measurement repeats. Samples in bold omitted from the final calibration due to evidence of contamination. Δ47 errors are standard errors calculated from the pooled standard deviation. Temperature errors are calculated as described in section 3.4. WOA, 1994 = World Ocean Atlas temperature, Mg/Ca = Mg/Ca temperature, δ18O = isotopic temperature. See section 3.4 for details.

Core	Species	Size fraction (µm)	N	Δ47 (ARF) ‰	T (WOA, 1994)	T (Mg/Ca)	T (δ^{18}O)
BOFS 31K	*G. ruber*	300 - 355	2	0.649 ± 0.02	23.2 ± 1.6	23.0 ± 2.5	27.5 ± 0.4
BOFS 31K	*G. sacculifer*	300 - 355	3	0.655 ± 0.02	23.3 ± 3.0	23.6 ± 1.0	26.3 ± 0.3
BOFS 31K	*G. bulloides*	300 - 355	2	0.673 ± 0.02	20.0 ± 0.5		26.9 ± 0.8
BOFS 31K	*G. ruber (w)*	300 - 355	3	0.651 ± 0.02	23.3 ± 1.5		25.5 ± 0.2
BOFS 31K	*G. inflata*	300 - 355	3	0.665 ± 0.02	13.5 ± 2.3		17.3 ±- 4.5
BOFS 31K	*N. incompta*	250 - 300	1	0.659 ± 0.04	20.9 ± 3.9		24.5 ± 1.1
MD99-2252	*G. bulloides*	300 - 355	1	0.673 ± 0.02	8.8 ± 1.0		8.8 ± 0.3
MD99-2252	***N. incompta***	**250 - 300**	**1**	**0.634 ± 0.04**	**9.4 ± 2.6**		**10.4 ± 0.5**
NEAP-04B	*G. bulloides*	300 - 355	3	0.651 ± 0.02	8.7 ± 0.9	10 ± 1.0	8.9 ± 0.2
NEAP-04B	*N. incompta*	250 - 300	1	0.675 ± 0.04	9.3 ± 2.4		10.2 ± 0.7
NEAP-16B	*G. bulloides*	300 - 355	1	0.634 ± 0.04	9.1 ± 1.1	12.8 ± 1.0	8.8 ± 0.2
NEAP-16B	*G. inflata*	300 - 355	1	0.670 ± 0.03	8.5 ± 0.8		8.8 ± 0.2
NEAP-16B	*N. incompta*	250 - 300	1	0.649 ± 0.03	9.7 ± 2.7		9.8 ± 0.5
NEAP-19B	*G. inflata*	300 - 355	3	0.705 ± 0.02	9.0 ± 0.6		9.3 ± 0.3
NEAP-19B	*N. incompta*	250 - 300	2	0.647 ± 0.02	10.5 ± 3.1		10.1 ± 0.3
NEAP-20B	*G. ruber*	250 - 300	3	0.658 ± 0.02	18.6 ± 2.4		17.7 ± 0.3
NEAP-20B	*G. ruber (w)*	300 - 355	1	0.663 ± 0.04	19.1 ± 2.1		17.8 ± 0.4
NEAP-20B	*G. sacculifer*	250 - 355	3	0.665 ± 0.02	19.2 ± 3.4	20.5 ± 2.2	17.7 ± 0.3
NEAP-20B	*G. bulloides*	300 - 355	3	0.646 ± 0.02	15.7 ± 1.5	15.9 ± 2.2	13.5 ± 0.4
NEAP-20B	*G. inflata*	300 - 355	2	0.697 ± 0.02	14.5 ± 0.3	14.1 ± 1.2	13.4 ± 0.7
NEAP-20B	*N. incompta*	250 - 300	2	0.688 ± 0.03	16.4 ± 4.3		14.9 ± 0.7
NEAP-20B	*G. truncatulinoides (s)*	300 - 355	3	0.685 ± 0.02	13.5 ± 0.5	13.4 ± 0.6	12.8 ± 0.4
Rapid26-14B	*G. bulloides*	300 - 355	3	0.664 ± 0.02	6.8 ± 1.4		7.6± 0.3
Rapid26-14B	*N. pachyderma (s)*	250 - 300	1	0.679 ± 0.02	4.4 ± 0.4	6.7 ± 4	4.3 ± 0.4
Rapid29-18B	*N. pachyderma (s)*	**250 - 300**	**1**	**0.653 ± 0.04**	**4.4 ± 0.4**		**5.9 ± 0.4**
coral			3 1	0.738 ±0.04	8.9 ± 2.1		
ETH3			9	0.628 ±0.008			
THC			9	0.605 ±0.02			
5 °C precipitate			7	0.711 ±0.04			

3.6.1 Regression fitting and evaluation methods

The York least squared method (York, 1968) has become the standard tool for regression fitting in isotope geochemistry (e.g. Bonifacie et al., 2017 ; Tripati et al., 2010). This method accounts for analytical uncertainty by applying a weighting to each datapoint based on the inverse of the measurement uncertainty in both the X and Y dimensions. However, the York regression is notoriously vulnerable to outliers and prone to giving skewed results (Sohn & Menke, 2002).

In order to investigate the impact of regression methodology, six regression types were applied to the calibration dataset for comparison. The standard York method of fitting was applied alongside ordinary least squares (OLS) and four additional 'robust' methods. Such robust fits are less susceptible to sample outliers which may skew small dataset regressions such as in this study.

Robust regression statistics have their roots in the 1960s with the introduction of Huber's Maximum likelihood (M-estimation) technique (Huber, 1964). The subsequent decades saw the introduction of alternative methods which looked to increase robustness in both the predictor and response variable (Huber's original method considered only outliers in the response variable) whilst improving computational efficiency. Yet robust regression fitting remains largely unexplored in the geosciences, perhaps because of the numerous competing methodologies or the lack of computational software developed to implement them (Stromberg, 2004).

Fortunately, many such robust regression fitting methods can now be easily implemented within the MASS package for the statistical software R. The statistical methodologies of each fitting technique go beyond the scope of this study but in general, are achieved through repeated regression fitting and re-weighting based on residuals. The four robust regression techniques explored in this study applied are:

- Huber's Maximum likelihood estimation (M-regression) (Huber, 1964)
- Tukey's Bi-square estimation
- Quantile regression
- MM-estimation (Yohai, 1986)

All data (foraminifera plus coral and inorganic calcite) and foraminifera only calibrations were produced using WOA, stable isotope, and Mg/Ca temperatures for the four robust methods, alongside York's regression method and ordinary least squares. The six methodologies were then assessed with a leave one out cross validation to determine the average percentage offset in predicted value against the measured value, alongside root mean square error. Vulnerability to outliers was assessed by iteratively removing each datapoint in the regression and calculating the percentage change in gradient from that produced by the entire dataset (Figure 3.18). Those regressions with a high vulnerability to outliers exhibited a higher average shift in gradient compared with more robust methods.

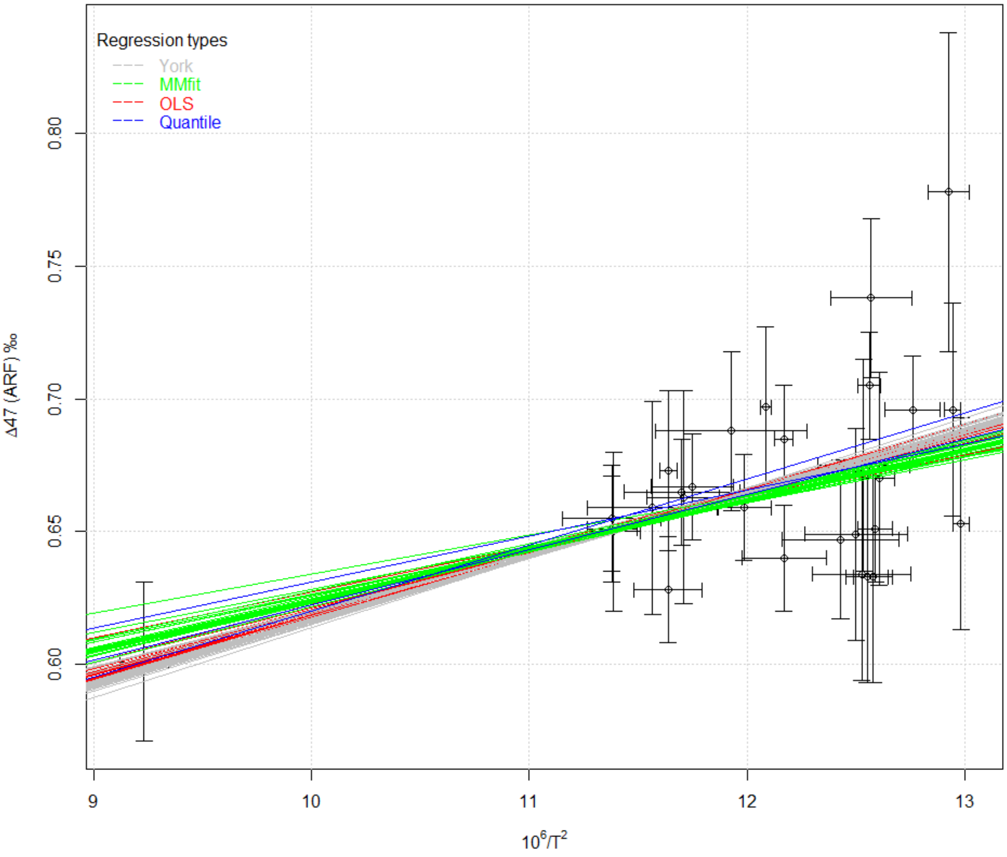

Figure 3.18 Example leave one out regression plot showing shifting gradients as each datapoint is removed and the regression recalculated. Variability in the gradient is used to assess the vulnerability of the regression to outliers. M-regression and bi-square regression not visible.

3.6.2 Calibration results

The coral sample was identified as a statistical outliers within the full dataset, lying more than 2σ from the regression (Figure 3.19). Previous studies have suggested that coldwater coral samples exhibit higher than expected Δ47 values, which have been attributed to so-called 'vital effects' – poorly understood fractionation processes in biogenic carbonate that lead to non-equilibrium precipitation (Spooner et al., 2016). Thus the coldwater coral sample was excluded from the final calibration regressions calculated below.

Calibrations were produced for full data and foraminifera only datasets for the three different methods of deriving calcification temperature (WOA, Mg/Ca and δ^{18}O temperatures), giving a total of six calibrations. Each of these six calibrations was calculated using the six regression methods outlines in section 3.6.1. These are presented in the following pages.

WOA derived calibrations are presented in Figure 3.20 and Table 3.12 on pages 115 – 116. Mg/Ca temperature derived calibrations are presented in Figure 3.21 and Table 3.13 on pages 117 – 118 and isotopic temperature derived calibrations are presented in Figure 3.22 and Table 3.14 on pages 119 – 200.

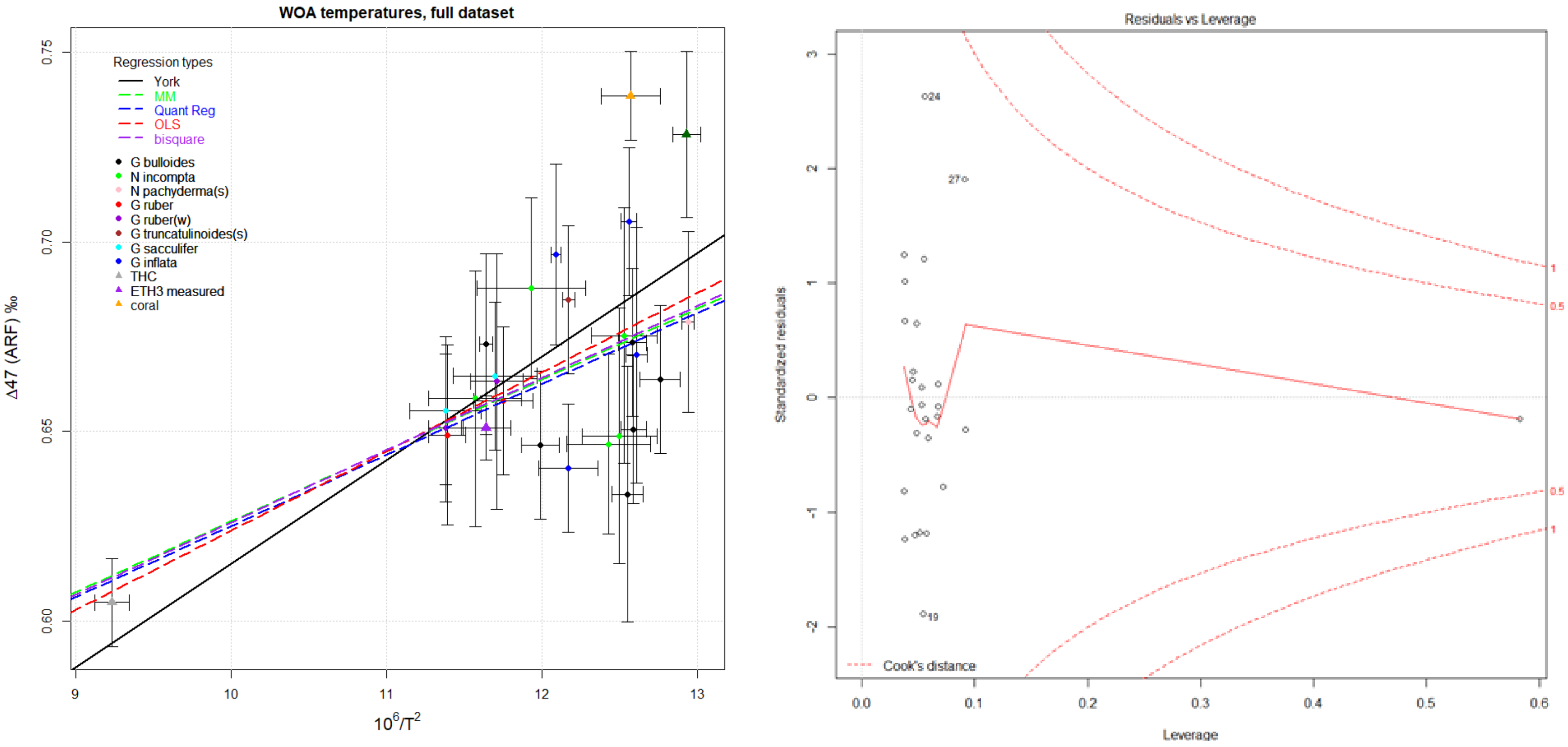

Figure 3.19 Left) Full calibration dataset including coldwater coral sample. Y-axis error bars are standard errors, x-axis error bars WOA temperature uncertainty. Right) Standardised residual vs leverage plot for Δ47 calibration produced from the full dataset of WOA temperatures. Point 24 corresponds to the coral sample with standardised residuals >2σ identifying it as an outlier.

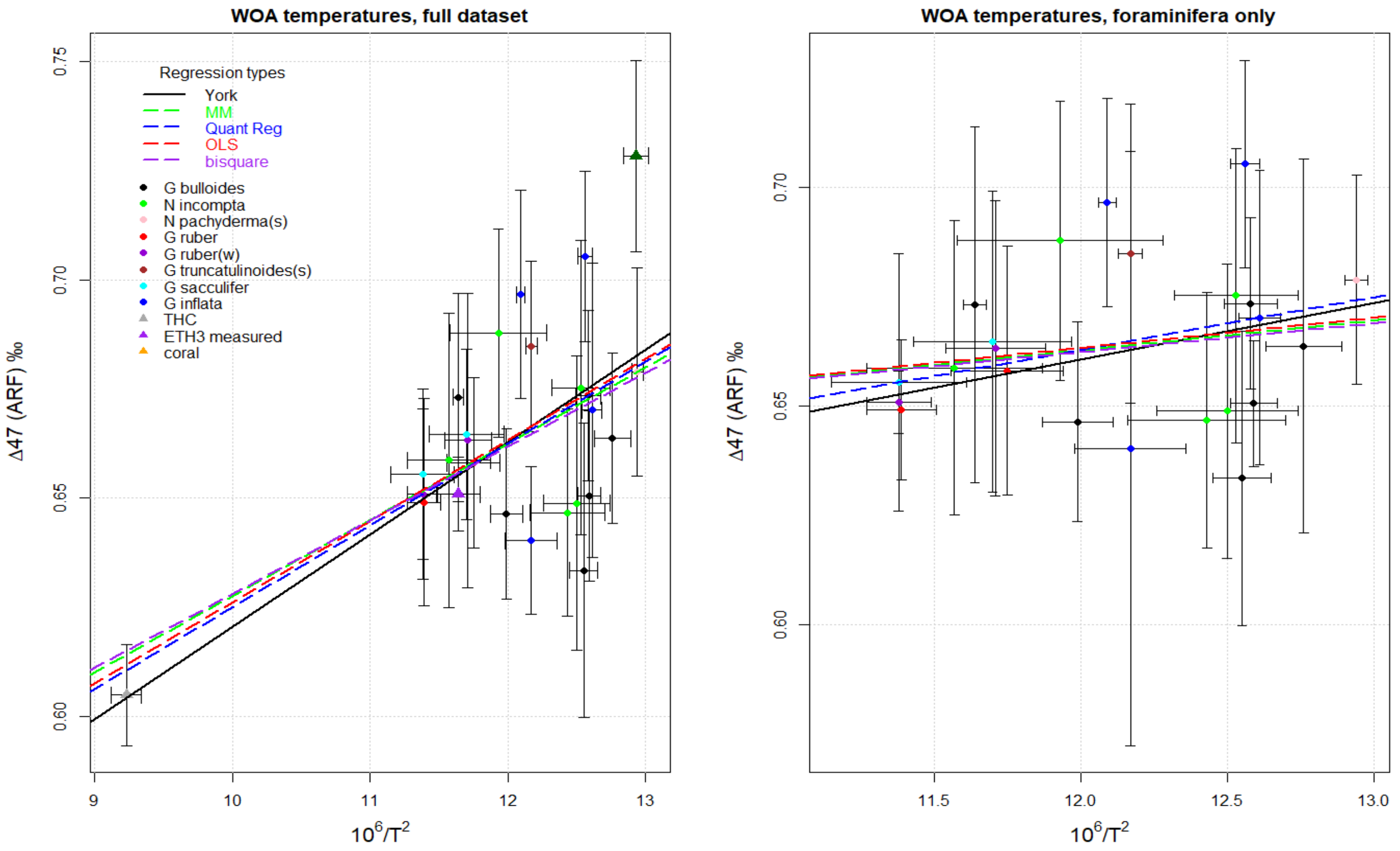

Figure 3.20 Δ47 calibration derived from WOA temperatures. Left) All data Right) foraminifera data only. Huber M-regression not plotted as indistinguishable from bi-square regression. Δ47 error bars are standard errors calculated from pooled standard deviation.

Table 3.12 Δ47 calibrations derived from WOA temperatures. Final selected calibration in bold.

Regression	Calibration	R^2	Mean leave one out % grad shift	Mean leave one % prediction error	RMSE
All data regressions					
York	$\boldsymbol{\Delta 47 = 0.0211\ (\pm 0.0039) \times \frac{10^6}{T^2} + 0.4093\ (\pm 0.0409)}$	**0.3176**	**1.62**	**2.36**	**0.0203**
Least Square	$\Delta 47 = 0.0186\ (\pm 0.0055) \times \frac{10^6}{T^2} + 0.4404\ (\pm 0.0660)$	0.3240	3.20	2.41	0.0204
Bisquare	$\Delta 47 = 0.0169\ (\pm 0.0223) \times \frac{10^6}{T^2} + 0.4533\ (\pm 0.0462)$	0.3175	4.28	2.48	0.0204
MM regression	$\Delta 47 = 0.0174\ (\pm 0.0039) \times \frac{10^6}{T^2} + 0.4533\ (\pm 0.0462)$	0.3214	4.17	2.46	0.3214
Huber maximum likelihood	$\Delta 47 = 0.0169\ (\pm 0.0055) \times \frac{10^6}{T^2} + 0.4591\ (\pm 0.0660)$	0.3175	4.28	2.48	0.3175
Quantile regression	$\Delta 47 = 0.0188\ (\pm 0.0222) \times \frac{10^6}{T^2} + 0.4375\ (\pm 0.2690)$	0.3229	2.60	3.18	0.3229
Foraminifera					
York	$\Delta 47 = 0.0106\ (\pm 0.0099) \times \frac{10^6}{T^2} + 0.5361\ (\pm 0.1201)$	0.0236	9.17	2.22	0.0181
Least Square	$\Delta 47 = 0.0069\ (\pm 0.0080) \times \frac{10^6}{T^2} + 0.5809\ (\pm 0.0977)$	0.0335	14.15	2.27	0.0180
Bisquare	$\Delta 47 = 0.0066\ (\pm 0.0109) \times \frac{10^6}{T^2} + 0.5835\ (\pm 0.1292)$	0.0302	16.42	2.27	0.0180
MM regression	$\Delta 47 = 0.0069\ (\pm 0.0099) \times \frac{10^6}{T^2} + 0.5802\ (\pm 0.1201)$	0.0326	14.31	2.28	0.0180
Huber maximum likelihood	$\Delta 47 = 0.0066\ (\pm 0.0080) \times \frac{10^6}{T^2} + 0.5835\ (\pm 0.0977)$	0.0302	16.42	2.27	0.0180
Quantile regression	$\Delta 47 = 0.0120\ (\pm 0.0109) \times \frac{10^6}{T^2} + 0.5185\ (\pm 0.1292)$	0.0144	9.27	2.11	0.0182

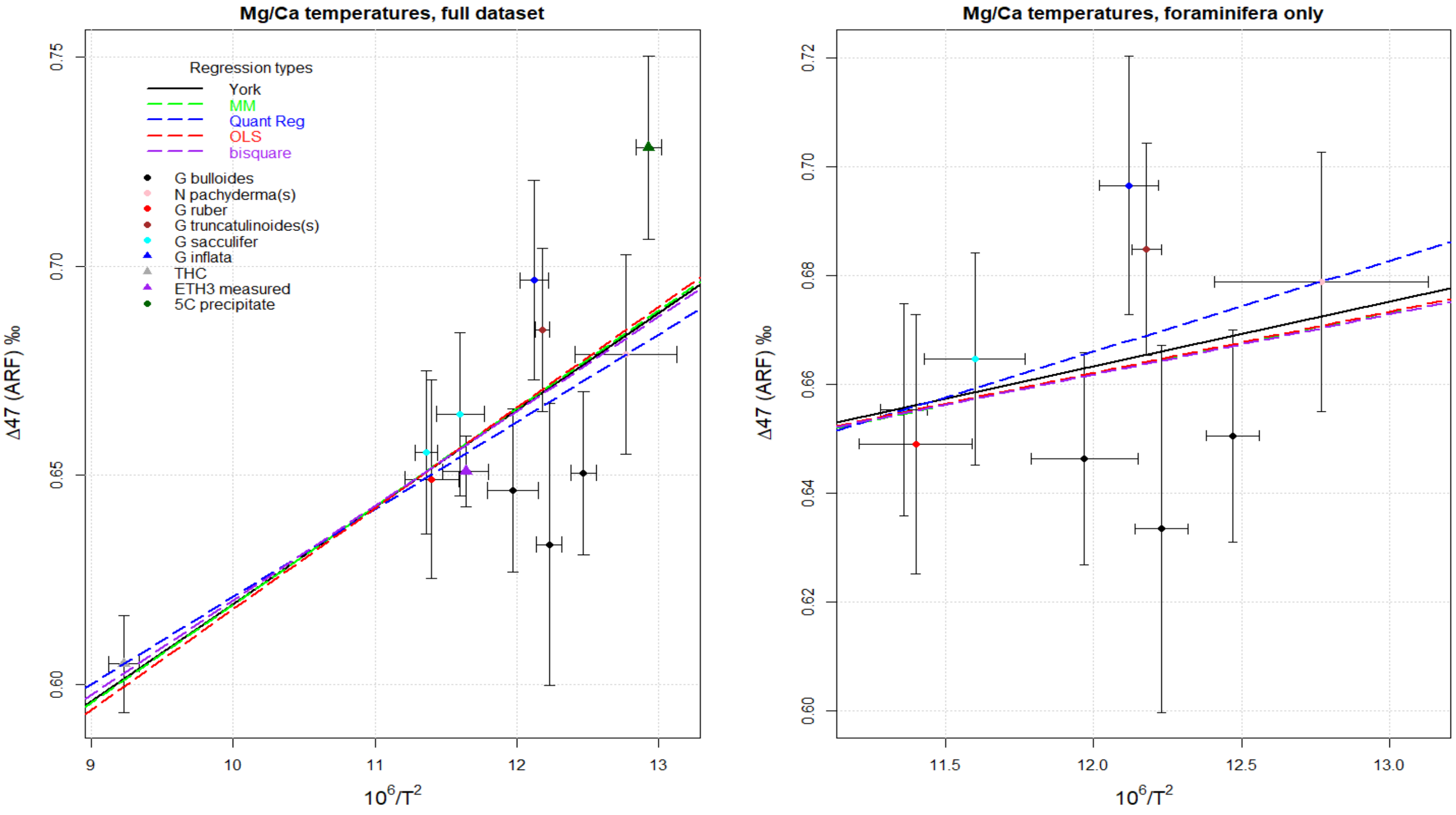

Figure 3.21 Δ47 calibrations derived from Mg/Ca temperatures. Left) All data Right) foraminifera data. Huber M-regression not plotted as indistinguishable from bi-square regression. Δ47 error bars are standard errors. Temperature error bars are calculated as described in section 3.4.

Table 3.13 Δ47 calibrations derived from Mg/Ca temperatures.

Regression	Calibration	R^2	Mean leave one out % grad shift	Mean leave one % prediction error	RMSE
All data regressions					
York	$\Delta 47 = 0.0232\ (\pm 0.0045) \times \frac{10^6}{T^2} + 0.3872\ (\pm 0.0518)$	0.5260	6.68	3.13	0.0219
Least Square	$\Delta 47 = 0.0241\ (\pm 0.0072) \times \frac{10^6}{T^2} + 0.3769\ (\pm 0.0857)$	0.5270	6.12	3.05	0.0220
Bisquare	$\Delta 47 = 0.0226\ (\pm 0.0462) \times \frac{10^6}{T^2} + 0.3940\ (\pm 0.5554)$	0.5244	7.72	3.00	0.0220
MM regression	$\Delta 47 = 0.0234\ (\pm 0.0045) \times \frac{10^6}{T^2} + 0.3845\ (\pm 0.0519)$	0.5266	6.74	3.04	0.0219
Huber maximum likelihood	$\Delta 47 = 0.0226\ (\pm 0.0072) \times \frac{10^6}{T^2} + 0.3940\ (\pm 0.0867)$	0.5244	7.72	3.00	0.0220
Quantile regression	$\Delta 47 = 0.0209\ (\pm 0.0462) \times \frac{10^6}{T^2} + 0.4120\ (\pm 0.5554)$	0.5089	2.57	4.27	0.0224
Foraminifera regressions					
York	$\Delta 47 = 0.0119\ (\pm 0.0160) \times \frac{10^6}{T^2} + 0.5211\ (\pm 0.1918)$	0.0636	24.21	2.79	0.0200
Least Square	$\Delta 47 = 0.01123\ (\pm 0.0157) \times \frac{10^6}{T^2} + 0.5274\ (\pm 0.1885)$	0.0682	25.30	2.83	0.0199
Bisquare	$\Delta 47 = 0.0111\ (\pm 0.0187) \times \frac{10^6}{T^2} + 0.5284\ (\pm 0.2138)$	0.0680	30.63	2.99	0.0199
MM regression	$\Delta 47 = 0.01141\ (\pm 0.0160) \times \frac{10^6}{T^2} + 0.5251\ (\pm 0.1918)$	0.0681	26.81	2.89	0.0199
Huber maximum likelihood	$\Delta 47 = 0.0111\ (\pm 0.0157) \times \frac{10^6}{T^2} + 0.5283\ (\pm 0.1885)$	0.0680	30.63	2.99	0.0199
Quantile regression	$\Delta 47 = 0.0167\ (\pm 0.0187) \times \frac{10^6}{T^2} + 0.4661\ (\pm 0.2138)$	0.0092	48.76	2.32	0.0205

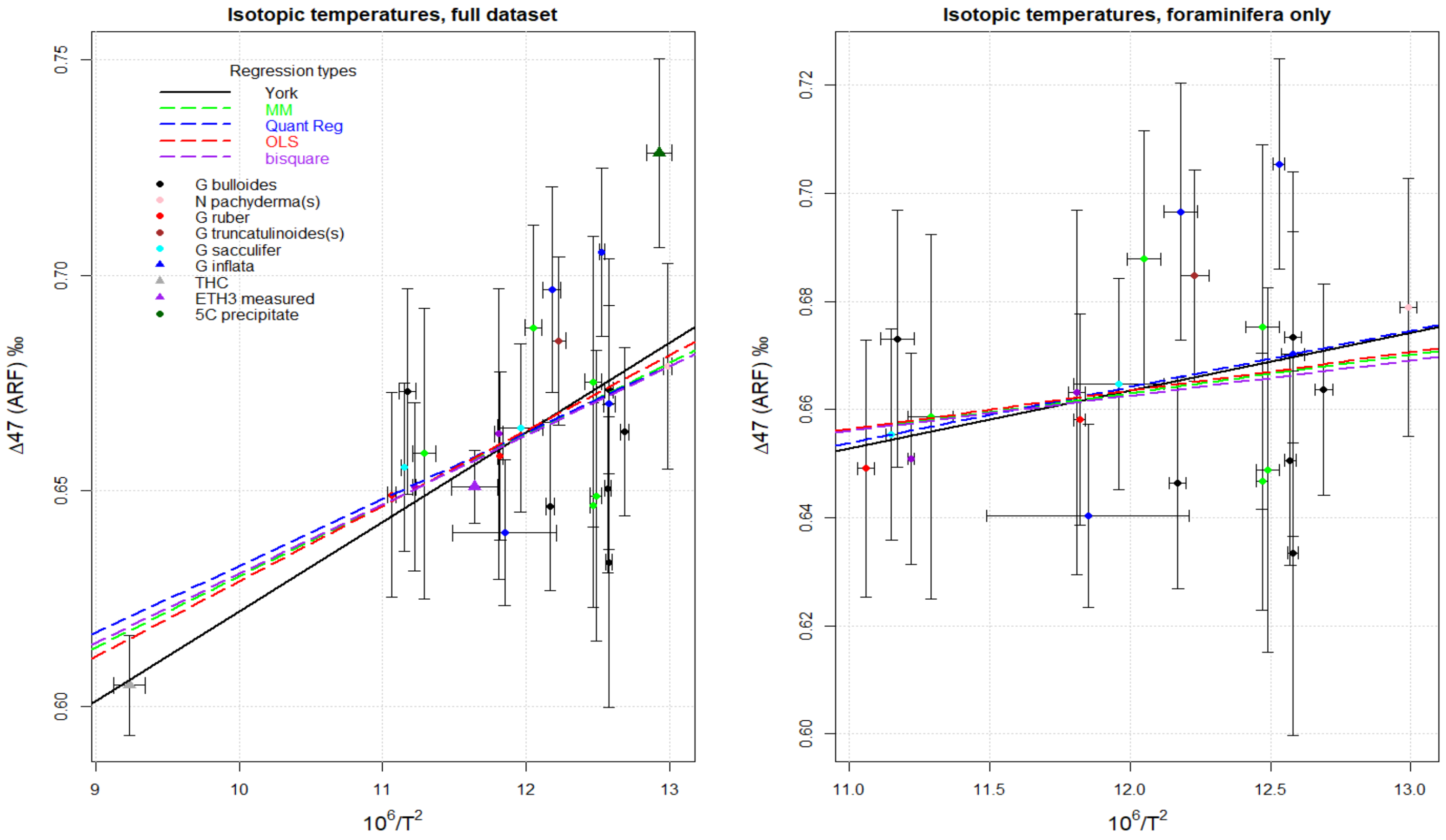

Figure 3.22 Δ47 calibration derived from isotopic temperatures. Left) All data Right) foraminifera data. Huber M-regression not plotted as indistinguishable from bi-square regression. Δ47 error bars are standard errors calculated from pooled standard deviation. Temperature error bars are calculated as described in section 3.4.

Table 3.14 Δ47 calibrations derived from isotopic temperatures.

Regression	Calibration	R^2	Mean leave one out % grad shift	Mean leave one % prediction error	RMSE
All data regressions					
York	$\Delta 47 = 0.0207\ (\pm 0.0038) \times \frac{10^6}{T^2} + 0.4147\ (\pm 0.0452)$	0.3089	1.86	2.46	0.0203
Least Square	$\Delta 47 = 0.0174\ (\pm 0.0052) \times \frac{10^6}{T^2} + 0.4549\ (\pm 0.0622)$	0.3209	3.68	2.45	0.0205
Bisquare	$\Delta 47 = 0.0160\ (\pm 0.0151) \times \frac{10^6}{T^2} + 0.4711\ (\pm 0.1808)$	0.3165	4.63	2.49	0.0204
MM regression	$\Delta 47 = 0.0165\ (\pm 0.0038) \times \frac{10^6}{T^2} + 0.4658\ (\pm 0.0415)$	0.3188	4.71	2.48	0.0203
Huber maximum likelihood	$\Delta 47 = 0.0160\ (\pm 0.0052) \times \frac{10^6}{T^2} + 0.4711\ (\pm 0.0629)$	0.3165	4.63	2.49	0.0204
Quantile regression	$\Delta 47 = 0.0154\ (\pm 0.0151) \times \frac{10^6}{T^2} + 0.4783\ (\pm 0.1808)$	0.3164	2.16	3.17	0.0204
Foraminifera regressions					
York	$\Delta 47 = 0.0107\ (\pm 0.0084) \times \frac{10^6}{T^2} + 0.5351\ (\pm 0.1019)$	0.0356	7.92	2.18	0.0180
Least Square	$\Delta 47 = 0.00707\ (\pm 0.0068) \times \frac{10^6}{T^2} + 0.5787\ (\pm 0.0823)$	0.0488	11.45	2.21	0.0179
Bisquare	$\Delta 47 = 0.0065\ (\pm 0.0087) \times \frac{10^6}{T^2} + 0.5842\ (\pm 0.1025)$	0.0450	14.05	2.23	0.0179
MM regression	$\Delta 47 = 0.0070\ (\pm 0.0084) \times \frac{10^6}{T^2} + 0.5791\ (\pm 0.1019)$	0.0481	12.09	2.23	0.0179
Huber maximum likelihood	$\Delta 47 = 0.0065\ (\pm 0.0068) \times \frac{10^6}{T^2} + 0.5842\ (\pm 0.0823)$	0.0450	14.05	2.23	0.0179
Quantile regression	$\Delta 47 = 0.0104\ (\pm 0.0087) \times \frac{10^6}{T^2} + 0.5400\ (\pm 0.1025)$	0.0358	5.87	2.04	0.0180

3.6.3 Δ47 calibration: Discussion

In all calibration methods, the model fit to the data was improved (higher coefficient of determination) with the inclusion of the non-foraminifera samples, ETH3, 5 °C precipitate and UEATHC. In these 'multicarbonate' calibrations, UEATHC and the 5 °C precipitate hold considerable leverage over the regression, forcing the gradient to higher values than in purely foraminiferal regressions. It would be beneficial to obtain additional datapoints in the 25 – 50 °C temperature range to provide greater confidence in the calibration at these relatively higher temperatures, and it is unfortunate that the other laboratory precipitates were unsuccessful as they could have been used to bridge this temperature gap.

Regressions derived from the Mg/Ca dataset exhibit the highest R^2 values, although model fits are relatively poor for all datasets given the considerable noise within the data. In all dataset regressions, robust fits offer little advantage over the traditional York regression. In nearly all regressions, leave-one-out analysis and RMSE calculations suggest poorer temperature prediction from robust fits. Similarly, leave one out gradient shifts are larger for robust fits, suggesting that they offer little advantage over the York or ordinary least square regressions in terms of robustness to outliers. This may be a symptom of the dataset which, once the coral is removed, has no obvious outliers – thus removing the advantage that robust fits hold over York and least squared regressions. In a dataset with less noise, robust regressions may yet be found to be advantageous since outliers will likely be more pronounced from the temperature driven signal.

The York regression of World Ocean Atlas temperatures offers both the lowest percentage error of prediction and gradient shift in leave one out analysis whilst exhibiting an R^2 and RMSE comparable to other regressions. Thus it is used for comparison against other calibrations.

$$\Delta 47 = 0.0211\ (\pm 0.0039) \times \frac{10^6}{T^2} + 0.4093\ (\pm 0.0409) \qquad R^2 = 0.318 \qquad (3.1)$$

A first test of the calibration (3.1) is to use it to derive core top temperatures from the calibration dataset. This exercise reveals considerable offset, averaging 8.2°C, between inferred temperatures and WOA temperatures (Figure 3.23). Further refinement is required to bring the clumped isotope calibration down to levels of certainty obtained from existing palaeo-temperature proxies such as Mg/Ca ratios, where uncertainties are generally quoted to within one or two degrees (e.g. Elderfield & Ganssen, 2000: Barker & Elderfield 2002).

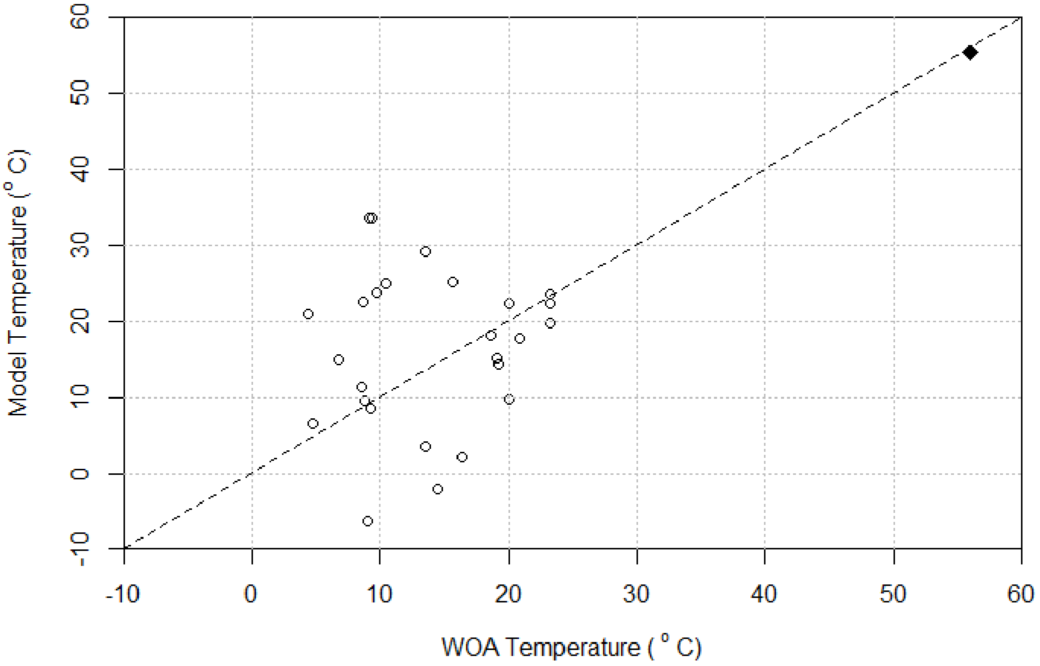

Figure 3.23 Calibration inferred temperatures derived from UEA foraminifera calibration (equation 3.1) and plotted against WOA temperatures. Dashed line is 1:1 line. Filled diamond is UEATHC sample.

Comparison with previous studies

A summary of recent clumped isotope calibrations is given in Table 3.15. The most obvious comparison for this study is with recent calibrations of Breitenbach et al. (2018) and Meinicke et al. (2020), to date the only published absolute reference frame calibrations derived solely from planktonic foraminifera. This study derives a shallower gradient and greater intercept than both these studies — falling within error of the Breitenbach et al. (2018) calibration, yet exhibiting a significant difference from Meinicke et al. (2020).

The most obvious cause of the discrepancy between this and the Breitenbach et al. (2018) study comes from the large degree of variability in Δ47 measurements in both studies. Relatively low coefficients of determination (3.1 in Breitenbach et al. (2018) and 3.2 in this study) suggest that much of the variability in Δ47 arises from sources other than foraminifera calcification temperature - the likely culprit being measurement noise. Repeat measurements may act to reduce calibration uncertainty and bring the two calibrations more in line with each other.

Additional discrepancy between this study, and the two aforementioned, may arise from the different species of foraminifera used to derive each calibration. Multiple studies have suggested foraminifera exhibit species-specific 'vital offsets' in stable isotopic composition as they precipitate out of equilibrium (e.g. Nyland et al., 2006; Pados et al., 2015). Furthermore, different species are known to exhibit varying sensitivities to other temperature proxies such as Mg/Ca incorporation (see section 3.4.2). Thus similar species specific offsets may also impact Δ47 temperature sensitivity, but as yet, the extent remains largely unexplored.

Of the 14 species in their calibration, Meinicke et al. (2020) suggest that only *G. ruber* deviates from their calculated foraminifera Δ47 calibration. However, this species is included in the calibration of this study, alongside *N. incompta* – which is not present in the Meinicke et al. (2020) calibration. Thus inclusion of these species in this study may act to increase offset between the calibrations.

Furthermore, the different methods used to project laboratory measured Δ47 onto the absolute reference frame (ARF) in each study will also give rise to calibration offsets. All studies utilise carbonate derived ARF transfer functions, but use different absolute ARF values for their 'known' standards. This study uses ARF values of 0.280 ‰ and 0.662 ‰ for ETH1 and ETH3 standards respectively - derived from repeated measurements of the two standards against laboratory equilibrated heated gases. Breitenbach et al. (2018) and Meinicke et al. (2020) use values of 0.258 and 0.691 ‰, taken from Bernasconi et al. (2018). Additionally, a larger acid fractionation factor of 0.062, calculated from Defliese & Lohmann (2016), is used to project measurements from the 70 °C reaction temperature to 25 °C compared with the same value (0.062, calculated from (Guo et al., 2009)) used to project from 87 °C in this study.

To assess the impact of the different data processing methods, this study's dataset has been recalculated by projecting Δ47 onto the absolute reference using the Bernasconi et al. (2018) Δ47 values for ETH1 and ETH3, and an acid fractionation factor calculated from Defliese & Lohmann (2016), replicating the methods of Breitenbach et al*. (*2018). Using this methodology, the following calibration is obtained:

$$\Delta 47 = 0.0319\ (\pm 0.0042) \times \frac{10^6}{T^2} + 0.3115\ (\pm 0.0513) \qquad R^2 = 0.3994 \qquad (3.2)$$

This adjusted calibration shows much closer agreement with the Breitenbach et al. (2018) study. An additional improvement in R^2 in is also observed, albeit with slightly greater percentage gradient shift and prediction error from leave one out analysis (2.35 and 3.01 respectively). Model predicted temperatures also exhibit a reduced offset from WOA values using the Breitenbach et al. (2018) Δ47 calculation method (Figure 3.24) with a mean offset of 6.9 °C, compared with 8.2 °C using the UEA methodology.

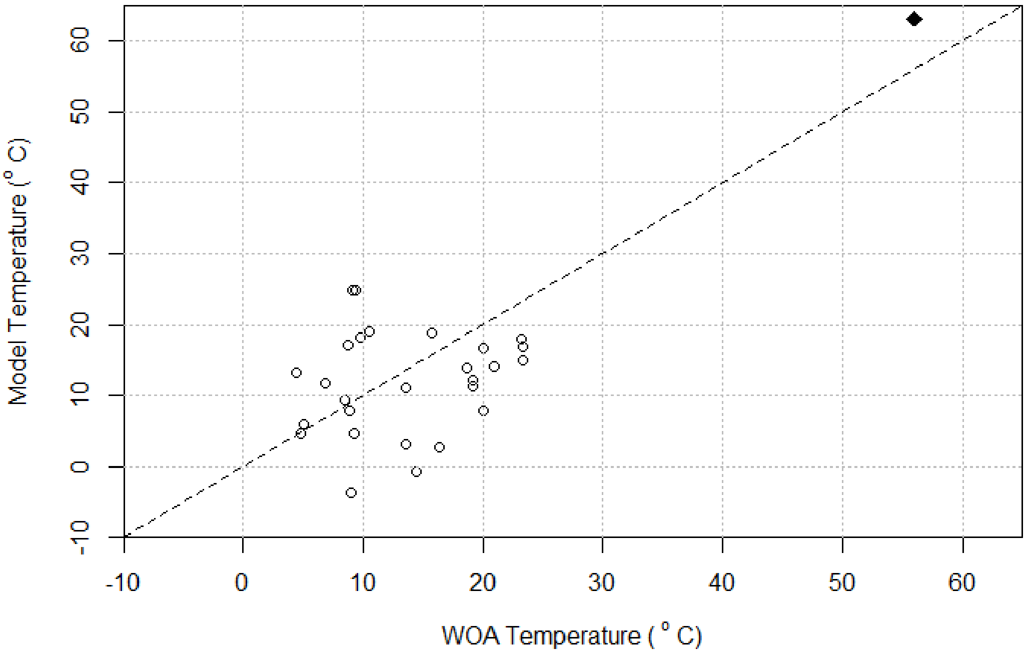

Figure 3.24 Calibration inferred temperatures derived from equation using Breitenbach et al. (2018) Δ47 calculation method (equation 3.2) and plotted against WOA temperatures. Δ47 values for ETH 1 and ETH3 are obtained from Bernasconi et al. (2018) and an acid fractionation factor calculated from Defliese & Lohmann (2016). Dashed line is 1:1 line. Filled diamond is UEATHC sample.

Table 3.15 Comparison of clumped isotope calibration (this study) with previous foraminifera calibrations and other relevant studies

Calibration	**Reference**	**Carbonate**	**Temperature range (°C)**
$\Delta 47 = 0.0211\ (\pm 0.0039) \times \frac{10^6}{T^2} + 0.4093\ (\pm 0.0409)$	This study	Foraminifera, ETH3, inorganic precipitates	5.5 – 56.0
$\Delta 47 = 0.0319\ (\pm 0.0042) \times \frac{10^6}{T^2} + 0.3115\ (\pm 0.0513)$	This study, Bernasconi (2018) ETH standard values, Muller (2016) fractionation factor	Foraminifera, ETH3, inorganic precipitates	5.5 – 56.0
$\Delta 47 = 0.0315\ (\pm 0.008) \times \frac{10^6}{T^2} + 0.313\ (\pm 0.1)$	(Breitenbach et al., 2018)	Planktonic foraminifera	2 - 27
$\Delta 47 = 0.0537\ \times \frac{10^6}{T^2} + 0.092$	(Evans et al., 2017)	Slope derived from laboratory inorganic precipitates (Zaarur et al., 2013), offset from modern day benthic foraminifera	5 - 65
$\Delta 47 = 0.0506\ (\pm 0.0007) \times \frac{10^6}{T^2} + 0.0807\ (\pm 0.0079)$	(Grauel et al., 2013)	Foraminifera, coccoliths, otoliths, inorganic carbonate, deep sea coral, enamel biopatite	2 - 28
$\Delta 47 = 0.0375\ \times \frac{10^6}{T^2} + 0.210$	(Guo et al., 2009)	Theoretical calibration	
$\Delta 47 = 0.0435\ (\pm 0.0004) \times \frac{10^6}{T^2} + 0.118\ (\pm 0.0042)$	(Jautzy et al., 2020)	Laboratory precipitates	5 - 726
$\Delta 47 = 0.0397\ (\pm 0.0021) \times \frac{10^6}{T^2} + 0.2259\ (\pm 0.0255)$	(Meinicke et al., 2020)	Planktonic foraminifera	0 - 28
$\Delta 47 = 0.044\ (\pm 0.005) \times \frac{10^6}{T^2} + 0.159\ (\pm 0.064)$	(Piasecki et al., 2019)	Benthic foraminifera	1.4 – 18.5
$\Delta 47 = 0.0416\ (\pm 0.84)\ \times \frac{10^6}{T^2} + 0.206$	(Peral et al., 2018)	Benthic and Planktonic foraminifera	23 - 250
$\Delta 47 = 0.0587\ (\pm 0.013) \times \frac{10^6}{T^2} + 0.014\ (\pm 0.138)$	(Tripati et al., 2010)	Foraminifera, otoliths, Laboratory precipitated carbonate	0.9 – 29.9
$\Delta 47 = 0.0350\ (\pm 0.004) \times \frac{10^6}{T^2} + 0.2416(\pm 0.041)$	UEA laboratory calibration (Kirk, 2017)	Modern brachiopods Inorganic precipitates	0.3 – 600
$\Delta 47 = 0.0327\ (\pm 0.0026) \times \frac{10^6}{T^2} + 0.3030\ (\pm 0.0308)$	(Wacker et al., 2014)	Foraminifera, ostrich egg shell, tropical bivalves, brachiopod, cold seep carbonate	9 - 38

This exercise suggests that adoption of universal data processing procedures, as advocated by Bernasconi et al. (2018), may reduce a lot of the discrepancies seen between calibrations. It is interesting, however, that the recent foraminifera derived calibrations of Evans et al. (2017) and Piasecki et al. (2019) show significantly higher gradients and lower intercepts despite adopting the same data processing protocols (Figure 3.25 and Table 3.15). Both these calibrations are derived from benthic specimens and it is possible that the calibration offsets reflect species-specific temperature sensitivities. The fact that the gradient and intercepts of Peral et al. (2018), derived from a mixture of benthic and planktonic specimens, falls between these benthic derived calibrations and the planktonic derived calibrations of Breitenbach et al. (2018) and this study, adds further weight to this argument. Piasecki et al. (2019) consider species-specific calibrations but suggest that there is no offset between different benthic species. There are no existing studies that consider benthic and planktonic calibrations derived from the same experimental setup.

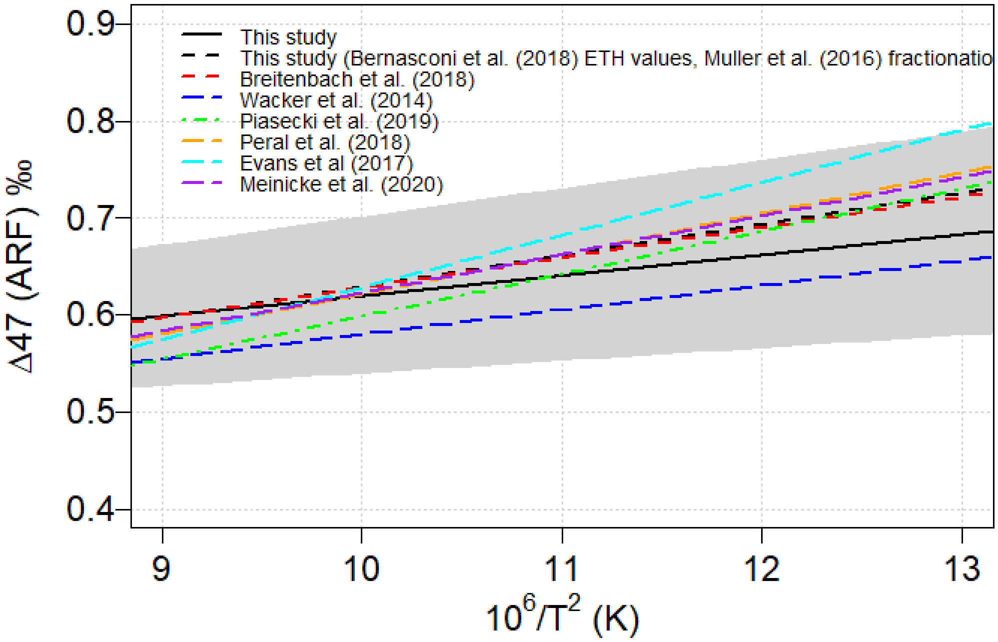

Figure 3.25 UEA foraminifera calibration (this study) calculated with laboratory best practice (equation 3.1) and Breitenbach et al. (2018) ARF projection methodologies (equation 3.2) compared with existing foraminifera calibrations. Grey shaded area is the 95 % confidence interval of the UEA projection methodology slope.

Vital effects may offer some explanation for the offset between the foraminifera calibration derived here and that of the existing UEA calibration which is largely derived from brachiopod samples (Kirk, 2017) (Table 3.15). It's also worth noting that the Kirk (2017) calibration was derived over a much larger temperature range and it is possible that temperature sensitivity varies at higher temperatures.

However, it is difficult to compare the two calibrations directly since experimental procedure has changed considerably since this first calibration was produced. Notably, the methodology by which samples are projected onto the ARF has changed from using heated gases (Kirk, 2017) to carbonate standards. Unfortunately, it is not possible to project the foraminifera data from this study onto the ARF using the Kirk (2017) methodology since no heated gases were measured during the experimental window. In addition, the reaction procedure has moved away from 25 ^{o}C reactions in individual vessels to an 87 ^{o}C common acid bath and the Porapak trap setup has undergone several iterations. Just as the pioneering calibrations from Caltech (Ghosh et al., 2007) have been updated over time (Eagle et al., 2015), so too should the UEA laboratory calibrations, particularly whilst the experimental setup is evolving.

Finally, all recent calibrations derived from inorganic calcites (Kele et al., 2015; Kelson et al., 2017; Kluge et al., 2015; Tang et al., 2014) show much steeper gradients and reduced intercepts, more in line with those derived from benthic foraminifera than those derived in this study. This suggests that planktonic foraminifera exhibit reduced Δ47 temperature sensitivity compared with inorganic samples. Further work is required to confirm the existence of foraminiferal vital effects, as well as their amplitude and inter-species variations.

3.6.4 Combining data from multiple studies to produce a 'universal' foraminifera calibration

It has already been discussed that an undesirably high level of measurement noise likely led to a reduced model fit to the data in this study. An obvious way to reduce this uncertainty is through additional data collection to improve counting statistics. Since this was not possible within the timeframe of this study, an initial first step to improve counting statistics is to combine datasets from the existing foraminifera clumped isotope studies detailed in section 3.6.3.

Only the Breitenbach et al. (2018) and Wacker et al. (2014) datasets are considered here, since Grauel et al. (2013) and Tripati et al. (2010) data is reported on a localised laboratory reference frame. It is not possible to project these to the ARF without access to temperature equilibrated gas data. The other studies are derived from benthic foraminifera and, as discussed, appear to show vital offsets from the planktonic samples explored in this study.

In order to combine the datasets from these three studies, it is first necessary to ensure that all data is projected onto the ARF in the same manner to eliminate data processing discrepancies. As discussed in section 3.6.3, Breitenbach et al. (2018) used a carbonate derived transfer function, using the 'accepted' values of Bernasconi et al. (2018) for ETH1 and ETH3. Again, without access to laboratory standard data used in the transfer function projection, it is not possible to correct the Breitenbach et al. (2018) dataset to the same methodology employed in this study. Instead the data from this study was aligned to that of Breitenbach et al. (2018), using their ARF projection methodology. Bernasconi et al. (2018) values of ETH1 and ETH3 and an acid fractionation factor of 0.079 ‰, derived from Defliese & Lohmann (2016), were used to correct the data from this study onto the Breitenbach ARF dataframe.

Similarly data from Wacker et al. (2014) was updated with a greater acid fractionation factor of 0.082 ‰, derived from Defliese & Lohmann (2016), as opposed to the 0.069 ‰, derived from Guo et al. (2009) which is used in their study. The regression was produced against World Ocean Atlas temperatures for all datasets. Results are presented in 0Table 3.16 and Figure 3.27. Note that WOA temperature uncertainty was unknown for the Breitenbach et al. (2018) study and thus York regression weighting was only applicable to the Y-dimension.

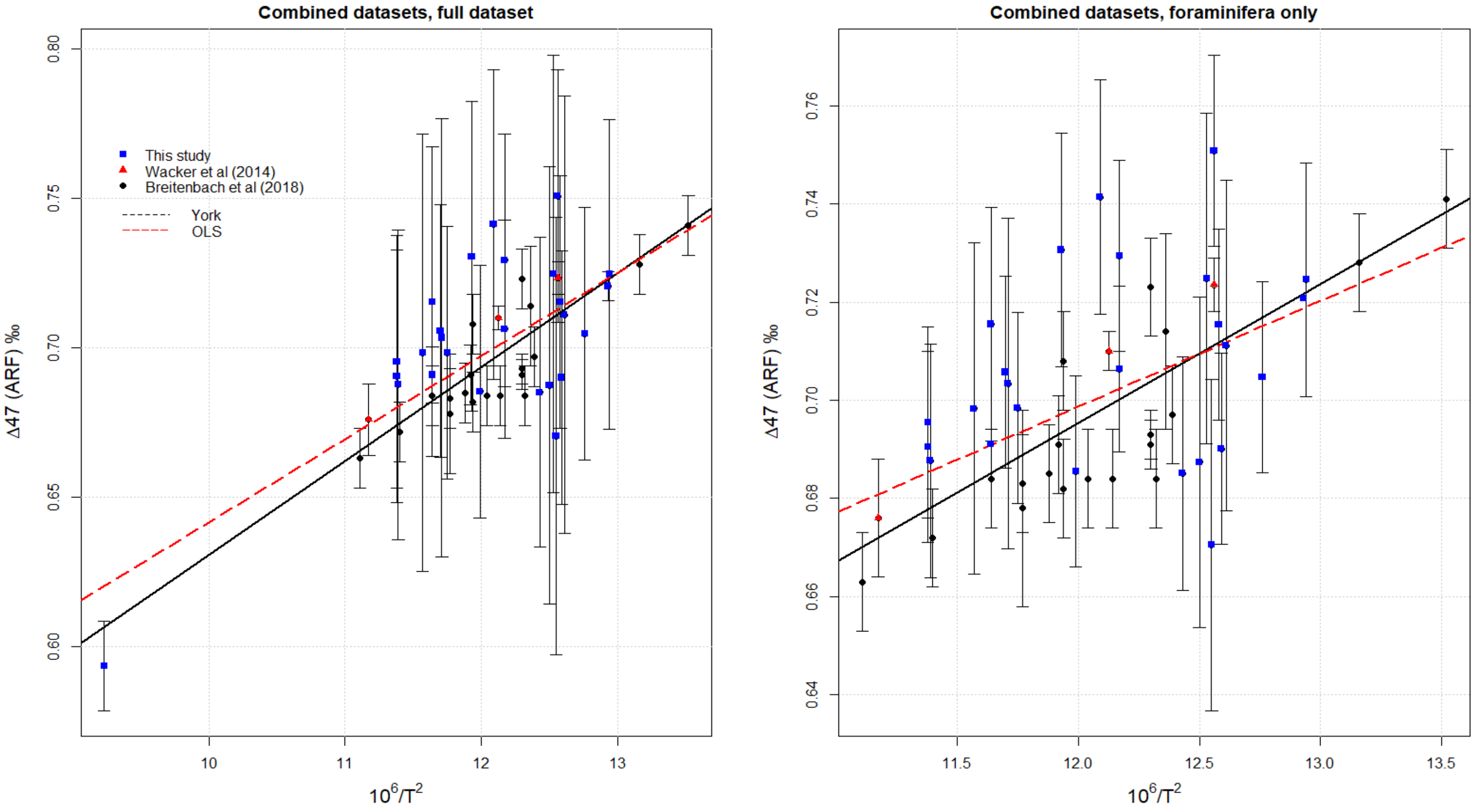

Figure 3.26 ‘Universal’ calibration produced from combining foraminifera data from this study, Breitenbach et al. *(*2018) and Wacker et al. *(*2014). Robust regressions not shown as they are indistinguishable from OLS fit. Left, all data from this study combined with additional foraminifera only data from Wacker et al. *(*2014) and Breitenbach et al. *(*2018). Right, foraminifera only data from all three studies.

Table 3.16 Δ47 calibrations derived from combined data from this study, Breitenbach et al. (2018) and Wacker et al. (2014)

Regression	Calibration	R^2	Mean leave one out % grad shift	Mean leave one % prediction error	RMSE
All data					
York	$\Delta 47 = 0.0314\ (\pm 0.0027) \times \frac{10^6}{T^2} + 0.3171\ (\pm 0.0332)$	0.4951	0.57	2.09	0.0177
Least Square	$\Delta 47 = 0.0278\ (\pm 0.0039) \times \frac{10^6}{T^2} + 0.3637\ (\pm 0.0472)$	0.5238	1.28	2.12	0.0179
Bisquare	$\Delta 47 = 0.0277\ (\pm 0.0056) \times \frac{10^6}{T^2} + 0.3642\ (\pm 0.0685)$	0.5230	1.63	2.14	0.0177
MM regression	$\Delta 47 = 0.0277\ (\pm 0.0026) \times \frac{10^6}{T^2} + 0.3648\ (\pm 0.0323)$	0.5235	1.39	2.13	0.0177
Huber maximum likelihood	$\Delta 47 = 0.0277\ (\pm 0.0039) \times \frac{10^6}{T^2} + 0.3642\ (\pm 0.0472)$	0.5230	1.63	2.14	0.0177
Quantile regression	$\Delta 47 = 0.0262\ (\pm 0.0056) \times \frac{10^6}{T^2} + 0.3833\ (\pm 0.0684)$	0.5219	7.10	3.81	0.0177
Foraminifera data					
York	$\Delta 47 = 0.0283\ (\pm 0.0036) \times \frac{10^6}{T^2} + 0.3552\ (\pm 0.0437)$	0.2454	1.14	2.11	0.0181
Least Square	$\Delta 47 = 0.02161\ (\pm 0.0052) \times \frac{10^6}{T^2} + 0.4393\ (\pm 0.0624)$	0.2906	2.10	2.12	0.0175
Bisquare	$\Delta 47 = 0.0218\ (\pm 0.0071) \times \frac{10^6}{T^2} + 0.4364\ (\pm 0.0860)$	0.2890	2.02	2.13	0.0175
MM regression	$\Delta 47 = 0.02203\ (\pm 0.0036) \times \frac{10^6}{T^2} + 0.4337\ (\pm 0.0437)$	0.2898	2.11	2.13	0.0175
Huber maximum likelihood	$\Delta 47 = 0.0218\ (\pm 0.0052) \times \frac{10^6}{T^2} + 0.4364\ (\pm 0.0624)$	0.2890	2.02	2.13	0.0175
Quantile regression	$\Delta 47 = 0.0262\ (\pm 0.0071) \times \frac{10^6}{T^2} + 0.3834\ (\pm 0.0860)$	0.2769	5.26	2.02	0.0177

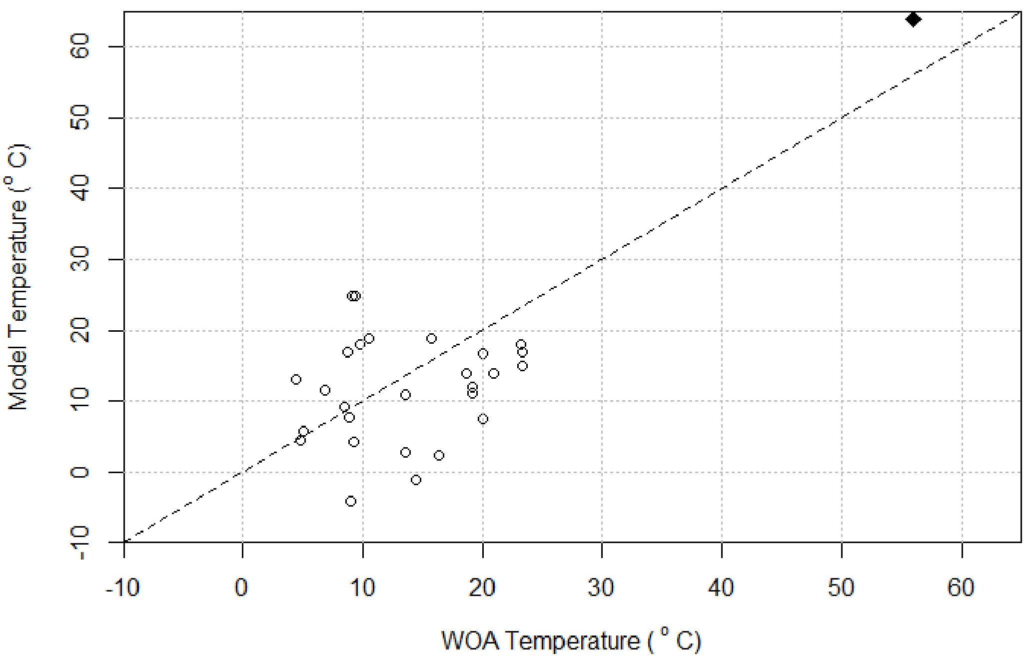

Figure 3.27 Inferred temperatures from the clumped isotope calibration dataset using the combined data from Breitenbach et al. (2018) and Wacker et al. (2014) (equation 3.3) plotted against WOA temperatures. Dashed line is 1:1 line. Filled diamond is UEATHC sample.

Of the six regression types, York offers enhanced robustness to outliers and better prediction, alongside the smallest RMSE (Table 3.16). The derived temperature calibration is:

$$\Delta 47 = 0.0314\ (\pm 0.0027) \times \frac{10^6}{T^2} + 0.3171\ (\pm 0.0332) \qquad R^2 = 0.495 \qquad (3.3)$$

The average offset between inferred temperatures using equation 3.3 and WOA temperatures of the calibration dataset is 7.1 °C (Figure 3.27). This regression lies within error of the Breitenbach et al. *(*2018), Wacker et al. (2014) and the Bernasconi ETH value adjusted calibration produced in this study (equation 3.2), however it exhibits significant offsets from the calibration produced using UEA internal standards (equation 3.1). The five regressions are summarised in Table 3.17.

Table 3.17 Summary of finalised calibrations

Calibration	R^2	Mean leave one out % grad shift	Mean leave one % prediction error	RMSE (‰)	Mean model temp vs WOA offset (°C)	Reference
$\Delta47 = 0.0211\ (\pm0.0039) \times \frac{10^6}{T^2} + 0.4093\ (\pm0.0409)$	0.32	1.62	2.36	0.020	8.2	This study, UEA internal ETH values, Guo et al. (2009) acid fractionation factor
$\Delta47 = 0.0319\ (\pm0.0042) \times \frac{10^6}{T^2} + 0.3115\ (\pm0.0513)$	0.49	2.35	3.01	0.021	6.9	This study, Bernasconi et al. *(*2018) ETH values, Defliese & Lohmann (2016) acid fractionation factor.
$\Delta47 = 0.0315\ (\pm0.008) \times \frac{10^6}{T^2} + 0.313\ (\pm0.1)$	0.31					Breitenbach et al. (2018)
$\Delta47 = 0.0327\ (\pm0.0026) \times \frac{10^6}{T^2} + 0.3030\ (\pm0.0308)$	0.99					Wacker et al. (2014)
$\Delta47 = 0.0314\ (\pm0.0027) \times \frac{10^6}{T^2} + 0.3171\ (\pm0.0332)$	0.50	0.57	2.09	0.018	7.1	This study, combining data from Breitenbach et al. (2018) and Wacker et al. (2014)

3.6.5 Testing calibrations with palaeo samples

The three calibrations produced in this study (equations 3.1 – 3.3) were used to produce palaeo-temperature estimates from three North Atlantic cores: U1305, NEAP 18K and MD99-2251 at selected depths between marine isotope stages 6 – 3. Temperature estimates are compared with those from established methodologies such as Mg/Ca ratios (Barker & Elderfield, 2002; Kozdon et al., 2009) and the modern analogue technique (Pflaumann et al., 1996). Experimental methodologies are detailed in chapter 5. Results are summarised in Table 3.18.

All Δ47 temperature reconstructions, across the three calibrations, exhibit sizeable offsets from Mg/Ca values, ranging between 5.2 and 8.9 °C. Better performance is observed at low temperatures, reflective of the *N. pachyderma (s)* samples than at warmer *G. bulloides* dominated temperatures. The combined dataset calibration (equation 3.3) exhibits the best performance with an average offset of 5.2 °C across all samples. This, and the fact that the calibration exhibits the lowest RMSE, alongside the highest R^2 and robustness to outliers, demonstrates that it outperforms the other calibrations and is recommended for future use in inferring palaeo-temperatures in foraminifera cores.

Table 3.18 Temperature estimates from palaeo-samples using the three calibrations derived in this study. Δ47 uncertainty is standard error calculated from pooled deviation. Clumped temperature uncertainties are inferred from Δ47 uncertainty. Mg/Ca temperature uncertainty calculated from calibration uncertainty. Bracketed numbers are the temperature offset from Mg/Ca temperature estimates (where available) and assemblage estimates otherwise.

Core	Depth (m)	Species	Size fraction	Δ47 ‰ (UEA stds)	Δ47 ‰ (Bern stds)	T (°C) Equation 3.1	T (°C) Equation 3.2	T (°C) equation 3.3	T Mg/Ca (°C)	T (°C) Assemblage
U1305	26.06	*N. pachyderma (s)*	212-300	0.680±0.022	0.730±0.042	**5.9±11.9** (0.7)	**2.8±15.1** (3.8)	**9.2±15.5** (2.6)	6.6 ± 4.5	
	27.91	*N. pachyderma (s)*	212-300	0.687±0.026	0.737 0.052	**2.5±13.8** (4.9)	**0.5±18.3** (6.8)	**6.9±18.9** (0.5)	7.4 ± 4.8	
	32.06	*N. pachyderma (s)*	212-300	0.697±0.015	0.756±0.030	**-2.3±7.5** (4.6)	**-5.3±9.5** (7.5)	**0.9±9.8** (1.3)	2.3 ± 2.7	
	32.11	*N. pachyderma (s)*	250-300	0.702±0.019	0.768±0.033	**-4.7±9.1** (7.2)	**-8.8±10.0** (11.4)	**-2.7±10.3** (5.3)	2.6 ± 2.9	
	32.21	*N. pachyderma (s)*	250-300	0.706±0.022	0.748±0.037	**-6.5±10.4** (8.9)	**-2.8±12.1** (5.2)	**3.4±12.5** (1.0)	2.4 ± 2.8	
	32.26	*N. pachyderma (s)*	250-300	0.684±0.022	0.738±0.042	**4.0±11.7** (1.7)	**0.3±14.6** (1.9)	**6.7±15.1** (4.4)	2.3 ± 2.7	
NEAP18K	600	*G. bulloides*	300-355	0.672±0.019	0.719±0.037	**10.3±10.8** (5.5)	**6.6±13.4** (9.1)	**13.2±6.9** (2.6)		15.8
	632	*G. bulloides*	300-355	0.69±0.022	0.735±0.042	**1.0±11.3** (13.3)	**1.3±14.8** (13.1)	**7.7±7.6** (6.7)		14.4
	660	*G. bulloides*	300-355	0.686±0.019	0.734±0.037	**3.0±9.9** (11.7)	**1.6±12.7** (13.1)	**8.0±6.5** (6.7)		14.7
MD99-2251	1612	*G. bulloides*	300-355	0.637±0.024	0.682±0.052	**31.1±17.3** (21.4)	**20.2±23.0** (10.4)	**27.1±23.6** (17.4)	9.8 ± 1	12.1
	1698	*N. pachyderma (s)*	250-300	0.668±0.019	0.716±0.042	**12.6±11.4** (8.3)	**7.6±15.8** (3.2)	**14.1±16.4** (9.8)	4.3 ± 3.7	5.1
	1824	*G. bulloides*	250-355	0.651±0.034	0.698±0.073	**22.3±23.0** (12.4)	**14.2±31.7** (4.4)	**21.0±32.8** (11.1)	9.9 ± 1	11.8
	1892	*N. pachyderma (s)*	250-300	0.726±0.024	0.781±0.052	**-14.9±10.3**(17.6)	**-12.5±15.8**(15.2)	**-6.5±16.1** (9.3)	2.8 ± 3.1	4.7
	1962	*G. bulloides*	300-355	0.657±0.024	0.704±0.052	**18.8±15.2** (7.2)	**11.9±21.0** (0.3)	**18.5±21.5** (7.0)	11.6 ± 1	9.6
	1972	*N. pachyderma (s)*	250-300	0.676±0.024	0.726±0.052	**8.0±13.5** (3.2)	**4.3±19.2** (0.5)	**10.8±19.7** (5.9)	4.8 ± 3.9	5.3
	2100	*N. pachyderma (s)*	250-300	0.707±0.024	0.754±0.052	**-7.1±11.3** (12.3)	**-4.8±17.3** (10.0)	**1.4±17.7** (3.8)	5.2 ± 4.1	6.3
	2139	*G. bulloides*	300-355	0.696±0.024	0.745±0.052	**-1.8±12.0** (12.2)	**-1.7±17.9** (12.2)	**4.5±18.4** (5.9)	10.4 ± 1	9.5
	2180	*N. pachyderma (s)*	250-300	0.711±0.024	0.762±0.052	**-8.9±11.1** (12.8)	**-7.1±16.8** (10.9)	**-0.9±17.2** (4.8)	3.9 ± 3.5	2.9
	2212	*G. bulloides*	300-355	0.692±0.017	0.741±0.037	**-0.2±8.5** (10.8)	**-0.6±12.6** (11.2)	**5.7±12.8** (4.9)	10.6 ± 1	10.0
	2274	*G. bulloides*	300-355	0.682±0.024	0.730±0.052	**4.9±13.0** (5.5)	**3.1±19.0** (7.3)	**9.5±19.4** (0.9)	10.4 ± 1	15.8
	2300	*N. pachyderma (s)*	250-300	0.700±0.017	0.750±0.037	**-3.9±8.2** (9.0)	**-3.3±12.2** (8.5)	**2.9±12.4** (2.3)	5.2 ± 4.1	7.0
	2348	*G. bulloides*	300-355	0.685±0.024	0.733±0.052	**3.4±12.8** (5.4)	**2.0±18.7** (6.8)	**8.4±19.2** (0.4)	8.8	11.1
			Average offset (all species)			8.9	7.9	5.2		
			Average offset (*N. pachyderma (s)*)			7.6	7.1	4.3		
			Average offset (*G. bulloides*)			10.5	8.6	6.4		

3.6.6 Using Δ47 temperatures to infer salinity

Since the clumped isotope thermometer gives rise to temperature estimates that are independent of the isotopic composition of precipitation waters, it is theoretically possible to use clumped temperatures to infer $\delta^{18}O$ of seawater using the Shackleton equation.

$$T = 16.8 - 4.38 \times \left(\delta^{18}O_{foraminifera} - \delta^{18}O_{seawater}\right) + 0.1 \times \left(\delta^{18}O_{foraminifera} - \delta^{18}O_{seawater}\right)^2$$

Using paired clumped and stable measurements of fossilised foraminifera reduces the unknowns within the equation to one, thus allowing it to be solved for $\delta^{18}O_{seawater}$. High resolution stable isotopic temperatures can then be recalculated with better constrained $\delta^{18}O$ of palaeo-waters. Furthermore, $\delta^{18}O$ of palaeo-waters ($\delta^{18}O_{SW}$) can in turn be used to calculate palaeosalinity, according to the relationship derived by Cleroux et al. *(*2008):

$$\delta^{18}O_{sw}(vsmow) = -19.264 + 0.558 \times salinity$$

To test the validity of using clumped isotope measurements for such a study, $\delta^{18}O$ and salinity of seawater was calculated for the calibration dataset using paired clumped and stable isotopic measurements and compared to those derived from the WOA dataset ($\delta^{18}O$ calculated from salinity using Cleroux relationship). Results are presented in Table 3.19.

A maximum offset of 4.4 ‰ is observed between Δ47 inferred and WOA calculated $\delta^{18}O_{SW}$ with an average offset of 1.9 ‰. For comparison, in the modern day, the offset between the most depleted parts of the surface Arctic Ocean and enriched parts of the surface Atlantic is around 5 – 5.5 ‰ (Legrande & Schmidt, 2006). Global average change in seawater between glacial/interglacial episodes is estimated to be around 1 ‰ (Schrag et al., 2002).

Table 3.19 Comparison of $\delta^{18}O$ of seawater ($\delta^{18}O_{SW}$), salinity and isotopic temperatures (Tiso) calculated from paired Δ47 and $\delta^{18}O$ foraminifera measurements and WOA salinity data for the calibration dataset. Δ47 temperature is calculated using the combined calibration derived in section 3.6.4. $\delta^{18}O$ reported in VPDB ‰, salinity in PSU. $\delta^{18}O_F$ is the average measured $\delta^{18}O$ of foraminifera.

Core	Species	Δ47 T (°C)	$\delta^{18}O_F$	Δ47 $\delta^{18}O_{SW}$	$\delta^{18}O_{SW}$ WOA	$\delta^{18}O_{SW}$ offset	Δ47 salinity	WOA salinity	Salinity offset	Tiso (Δ47 $\delta^{18}O_{SW()}$	Tiso (WOA $\delta^{18}O_{SW}$)	Tiso offset
NEAP-20B	*G. bulloides*	18.9	0.481	0.925	-0.281	1.2	36.18	34.02	2.2	18.9	13.5	5.3
NEAP-20B	G. truncatulinoides	3.0	1.007	-2.184	0.065	2.2	30.61	34.64	4.0	3.9	12.8	8.8
NEAP-20B	*G. inflata*	-1.0	0.924	-3.255	0.138	3.4	28.69	34.77	6.1	0.3	13.4	13.1
NEAP-20B	G. sacculifer	11.2	0.289	-0.991	0.104	1.1	32.75	34.71	2.0	11.5	16.0	4.5
NEAP-20B	G. ruber	14.0	-0.115	-0.779	0.099	0.9	33.13	34.7	1.6	14.0	17.7	3.7
NEAP-20B	G. ruber (w)	12.1	-0.130	-1.242	0.099	1.3	32.30	34.7	2.4	12.2	17.8	5.7
Rapid 26-14B	*G. bulloides*	11.6	1.943	0.616	-0.281	0.9	35.63	34.02	1.6	11.3	7.6	3.7
Rapid 26-14B	G. pachyderma	4.6	2.888	-0.082	-0.192	0.1	34.38	34.18	0.2	4.8	4.3	0.5
Rapid 29-18B	G. pachyderma	13.3	2.411	1.296	-0.231	1.5	36.85	34.11	2.7	12.1	5.9	6.2
BOFS 31K	G. sacculifer	15.1	-0.740	-1.221	1.326	2.5	32.33	36.9	4.6	14.8	26.3	11.5
BOFS 31K	G. ruber	18.1	-0.992	-0.773	1.326	2.1	33.14	36.9	3.8	17.9	27.5	9.6
BOFS 31K	G. ruber (w)	17.0	-1.019	-1.078	0.874	2.0	32.59	36.09	3.5	16.6	25.4	8.8
BOFS 31K	G. incompta	14.0	-0.367	-1.052	1.326	2.4	32.64	36.9	4.3	13.9	24.5	10.6
BOFS 31K	*G. inflata*	11.0	0.303	-1.028	0.545	1.6	32.68	35.5	2.8	11.2	17.3	6.1
BOFS 31K	*G. bulloides*	7.8	-0.577	-2.922	1.432	4.4	29.29	37.09	7.8	7.2	26.0	18.8
NEAP-20B	G. incompta	2.6	0.560	-2.806	0.121	2.9	29.50	34.77	5.3	3.3	15.1	11.8
MD99-2252	*G. bulloides*	7.8	1.587	-0.500	-0.325	0.2	33.63	33.94	0.3	8.2	8.8	0.6
MD99-2252	G. incompta	25.0	1.265	2.770	-0.259	3.0	39.49	34.06	5.4	23.7	10.4	13.4
NEAP-4B	*G. bulloides*	17.1	1.581	1.446	-0.314	1.8	37.11	33.96	3.2	16.3	8.9	7.5
NEAP-4B	G. incompta	4.5	1.354	-1.450	-0.253	1.2	31.92	34.07	2.1	5.4	10.0	4.6
NEAP-16B	*G. bulloides*	25.1	1.608	3.009	-0.292	3.3	39.92	34	5.9	23.2	8.8	14.4
NEAP-16B	G. incompta	18.2	1.400	1.526	-0.264	1.8	37.26	34.05	3.2	17.5	9.8	7.7
NEAP-16B	*G. inflata*	9.3	1.666	-0.099	-0.242	0.1	34.35	34.09	0.3	9.5	8.8	0.7
NEAP-19B	G. incompta	19.1	1.279	1.616	-0.314	1.9	37.42	33.96	3.5	18.4	10.1	8.3
NEAP-19B	*G. inflata*	-3.9	1.474	-3.336	-0.303	3.0	28.55	33.98	5.4	-1.9	9.3	11.2

The major contribution to this isotopic offset is from uncertainty in the Δ47 temperature. It is noticeable that the largest isotopic differences arise in those samples where the Δ47 derived and WOA temperature offset is also the greatest. The offset between Δ47 and WOA calculated $\delta^{18}O_{SW}$ gives rise to similarly large offsets between calculated Δ47 salinities and WOA values, with an average of 3.4 PSU and maximum of 7.4.

These results suggest that, given the uncertainty in Δ47 measurements using the current UEA setup, it is not possible to make reliable inferences of $\delta^{18}O$ of palaeowaters. Since $\delta^{18}O_{SW}$ is in turn used to infer palaeo-salinity and isotopic temperatures, further refinement of the methodology will be required to reduce uncertainty in Δ47 before additional information about oceanic conditions, or high resolution isotopic temperatures, can be deduced. Some suggestions are explored in the following section.

3.7 Δ47 calibration – conclusions and further work

This study has provided a proof of concept that palaeotemperatures can be successfully inferred from foraminifera samples using the UEA clumped isotope facilities. Measurement uncertainty remains undesirably high however, typically giving rise to temperature uncertainties of ± 10 – 15 °C, and further methodological refinement will be required to bring the uncertainty in line with those of established proxies.

The majority of measurement noise is known to arise within the sample purification line. An automated line, currently under construction, will go some way towards ensuring more uniform treatment across samples and thus improve reproducibility. Further work is also required to overcome the sample size effect — discussed in detail in chapter 2 — which acts to increase variability between samples of differing volumes. Although this is corrected for during data processing, it introduces another layer of uncertainty and its removal is desirable. Should the sample size effect be resolved, it would allow measurement of samples as low as 1.5 mg, compared with the current 4 mg mass samples. A sample which is currently measured in triplicate could theoretically be measured 8 times. Assuming no reduction in measurement precision for smaller samples, this would vastly improve counting statistics, reducing standard error from 0.019 ‰ in a triplicate measurement, to 0.01 ‰. Additional benefits could also be found in reduced sample picking time and the possibility of higher resolution studies.

This is only the fourth clumped isotope calibration that employs planktonic foraminifera to report on the absolute reference frame. It is reassuring that much of the discrepancy seen between laboratories in the pioneering studies of Grauel et al. (2013) and Tripati et al. (2010) appear to be being resolved as the slopes and intercepts of more recent planktonic foraminifera studies (Breitenbach et al., 2018; Peral et al., 2018; This study; Wacker et al., 2014) falling within error of each other when projected onto the ARF.

The importance of consistent data processing is further highlighted in section 3.6.3, where adopting the data processing methodology of Breitenbach et al. (2018) to project data from this study onto the ARF results in the two calibrations becoming almost identical. In order for data processing methodologies to be brought in line, universal agreement is required over the ARF values of international standards. Major advances have been made towards this over recent years in the inter-laboratory comparision studies of Bernasconi et al. (2018) and Petersen et al. (2019), and it was unfortunate that UEA were unable to participate in these studies. It may be necessary for us to reassess our internal accepted values of the ETH standards so that our data can be readily compared and combined with that from other laboratories.

The alignment of the four ARF planktonic foraminifera studies suggest that a universal planktonic foraminifera clumped isotope calibration is within reach. Foraminifera studies to date have focussed largely on developing laboratory specific calibrations that require vast resources before palaeo-reconstructions can be considered. The benefits therefore of establishing a universal calibration are obvious as increasing numbers of clumped laboratories come online and wish to produce palaeo data with relative ease.

This study has demonstrated the advantages of combining datasets from multiple laboratories in reducing calibration uncertainty (section 3.6.3). A multi laboratory calibration gives rise to reduced RMSE, enhanced R^2 and improved prediction compared to using only data produced in this study. In the immediate future, clumped isotope measurements, particularly of foraminifera, remain time consuming and sample quantity limited. Thus it is suggested that such a ‘multi-laboratory’ approach may be the most efficient means by which to establish more robust calibrations that can produce temperature estimates with uncertainty comparable to established proxies.

It is worth noting that this study did not consider species-specific calibrations as data was insufficient to identify species-specific offsets. It may be that individual foraminifera species exhibit their own Δ47 'vital effects' and that as laboratory protocols and instrumentation improves these will start to become apparent, just as has occurred with Mg/Ca calibrations (Barker & Elderfield, 2002; Elderfield & Ganssen, 2000; Ganssen & Kroon, 2000).

Chapter 4. Quaternary North Atlantic oceanography

The remainder of this thesis will focus on the palaeoclimate of the North Atlantic. In the modern day, the North Atlantic plays a major role in distributing heat from the equator to the high latitudes via the global thermohaline circulation.

The thermohaline circulation arises from the natural latitudinal temperature gradient across the Earth's surface. Solar irradiance declines from the equator to the poles with the increasingly large angle of incidence. Yet long wave radiative heat loss remains relatively uniform, acting like a blackbody across the entire surface of the globe. This results in a net gain of energy at latitudes below 35° and a net loss for those above. Thus to maintain the heat balance of the Earth, vast quantities of energy must be transported poleward from the equator, estimated at 5.5 PW globally (Bryden & Imawaki, 2001). Whether the ocean or the atmosphere is the dominant vehicle for heat movement remains uncertain (Bryden, 1993) — however the larger heat capacity of water compared with air suggests of the oceans must play a major role.

The largest of the thermohaline heat fluxes is found in the North Atlantic (McCarthy et al., 2017). Study of the North Atlantic region intensified with the suggestion that this global heat conveyor may slow, or even shut down, in the future due to anthropogenic forcings — with dramatic impacts on the global climate (Meehl et al., 2007). Indeed sea surface temperature data suggests the thermohaline circulation may already have slowed by up to 15 % since the mid twentieth century (Caesar et al., 2018; Rahmstorf et al., 2015). By looking to the past we can gain insight into the mechanisms which drive changes in the thermohaline circulation and the climatic impact that such changes might have.

This chapter reviews the scientific literature looking at the modern day configuration of the Atlantic thermohaline circulation (4.1) and both long (4.2) and short (4.3) term fluctuations throughout the Quaternary.

4.1 The modern day North Atlantic

4.1.1 The Atlantic Meridional Overturning Circulation

Of particular interest to this work is the Atlantic Meridional Overturning Circulation (AMOC), the North Atlantic branch of the thermohaline circulation (Figure 4.1) which transports an estimated 1.3 PW of energy from the tropics to the northern latitudes (Ganachaud & Wunsch, 2000). This results in annual mean air temperatures off Scandinavia exceeding the zonal average by more than 10 °C (Rahmstorf & Ganopolski, 1999) and the relatively mild climate enjoyed by Western Europe. For example the mean winter temperature of Dublin is 4.3 °C warmer than Seattle, a city of both similar latitude and oceanic proximity (McCarthy et al., 2015).

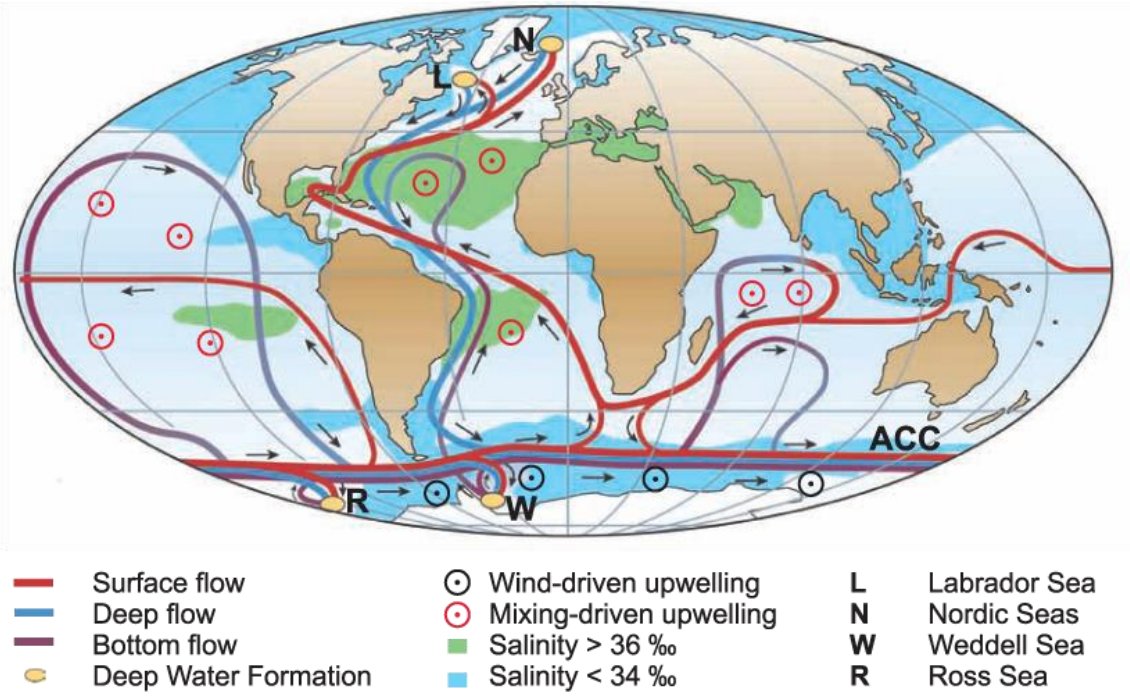

Figure 4.1 Schematic of the global thermohaline circulation. The Atlantic Meridional Overturning Circulation (AMOC) is the north Atlantic component shown above travelling as surface waters from the Gulf of Mexico to the Labrador and Nordic Seas where it sinks to the abyss, forming the southerly flowing North Atlantic Deep Water (NADW) (Source: Schmittner et al. (2013), adapted from Rahmstorf (2002)).

The AMOC is characterised by the northerly flow of warm, saline surface waters from the Gulf of Mexico across the North Atlantic and into the Nordic and Labrador Seas. It originates in the Gulf Stream which curves north around the southeast Newfoundland Rise to form the North

Atlantic Current (NAC) (Rossby, 1996). The NAC travels northward as a western boundary current before turning east at 51°N and traversing the Atlantic (Rossby, 1996). This current splits at 26W - southwest of Iceland - with a branch travelling west as the Irminger Current, before eventually joining the East Greenland current and meandering into the Labrador Sea. The remainder continues northward into the Nordic Seas (Figure 4.2) (Bower & Richardson, 2002; Brambilla & Talley, 2008; Farmer et al., 2011; Lavender et al., 2005). This latter branch splits further with one branch travelling into the Arctic Ocean through the Fram Strait and the other to the Barents Sea (Schauer, 1997).

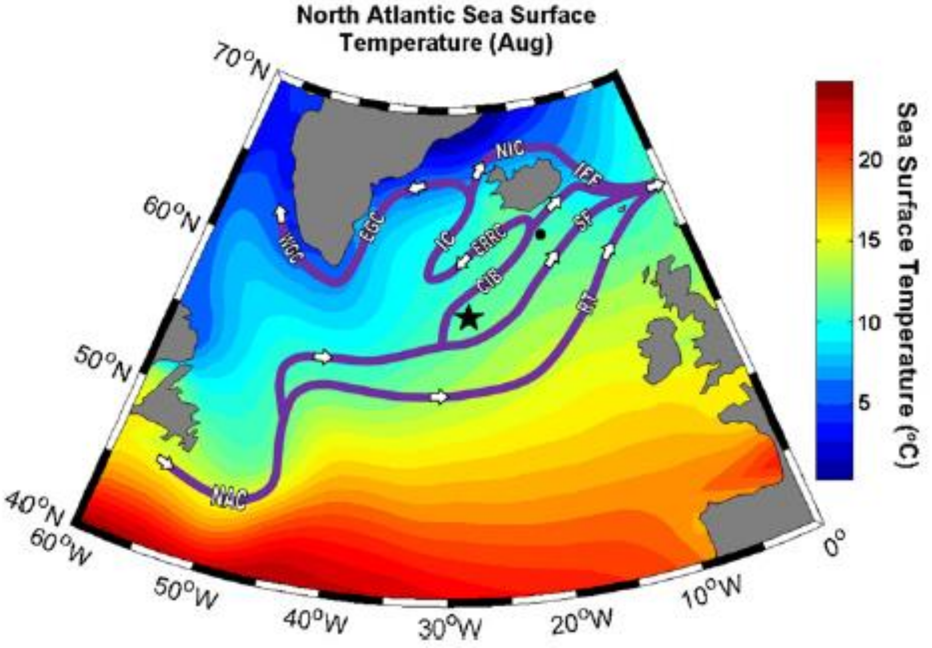

Figure 4.2 A map of North Atlantic surface currents. NAC = North Atlantic Current, CIB = Central Iceland Basin, RT= Rockall Trough branch of the NAC, SF = Subarctic Front, ERRC = East Reykjanes Ridge Current, IC = Irminger current, NIC = North Iceland current, IFF = Iceland Faroe Current, EGC = East Greenland Current, WGC = West Greenland Current. (Source: Farmer et al. (2011))

At these high latitudes, water is cooled by contact with cool ambient air, sourced from the Canadian Arctic (Broeker, 1991). At the same time, ice formation and brine rejection acts to increase salinity and accordingly, density. Newly cooled, dense waters sink at multiple downwelling sites before travelling south. Fram Strait Water forms the densest and deepest of these southerly flowing branches, entering the North Atlantic as Denmark-Strait Overflow Water (DSOW) (Raymo et al., 2004) (Figure 4.3). Water originating from the Barents Sea forms Iceland-Scotland Overflow Water (ISOW). A small proportion of this arm – Wyville Thomson

Ridge Overflow (WTRO) – flows into the North Atlantic through the Rockall Trough at intermediate depths (Johnson et al., 2010).

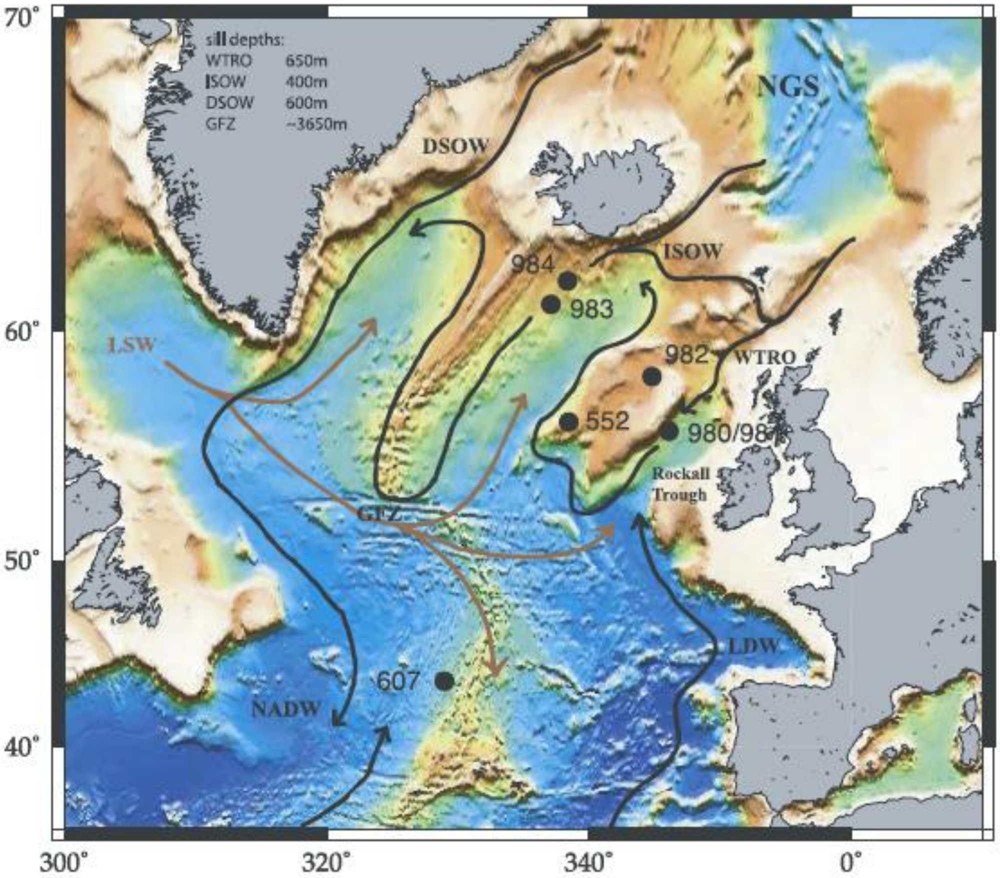

Figure 4.3 Map of North Atlantic Deepwater currents. DSOW = Denmark Scotland Overflow Water, ISOW = Iceland Scotland Overflow Water, WTRO = Wyville Thomson Ridge Overflow, LSW = Labrador Sea Water, NADW = North Atlantic Deepwater (source: Raymo et al. (2004))

In the Labrador Sea, surface stratification forms a layer of warm surface water sitting atop cold, fresh abyssal waters during the summer months. The majority of surface downwelling is induced in the winter when surface contact with cold airflows enhances turbulence and creates a convectively mixed layer (De Jong et al., 2012; Lazier et al., 2002). In severe winters, downwelling is sufficient to enable convection throughout the following summer, creating Labrador Sea Water (LAW). The depth of LAW depends upon the severity of the winter. In mild winters, no LAW may be formed and severe winters may lead to convection depths down to 2000 m (Lazier et al., 2002).

ISOW and DSW mix at depth to form the Deep Western Boundary Current (DWBC) which travels around the southern tip of Greenland, eventually mixing with LSW (Holliday, 2009) where it continues its journey south, forming the primary component of North Atlantic Deep Water (NADW).

4.1.2 Drivers of the AMOC

Two theories have been proposed as the driving mechanism behind the AMOC. The traditional view, first proposed by Sandström (1916), is that the formation of deepwater in the northern latitudes is sufficient to drive the AMOC alone. Deepwater formation is driven by wind driven turbulent mixing in the North Atlantic, allowing light water masses to rise and heavy water masses to sink (Munk & Wunsch, 1998). This creates a latitudinal density gradient across the North Atlantic which results in the northerly advection of surface waters (Kuhlbrodt et al., 2007).

Broecker et al. (1985) argued that deepwater formation occurred predominantly in the Atlantic because of its heightened salinity in comparison to the other major oceans. Exchange of high salinity waters of the Mediterranean with the lower salinity Atlantic leads to the loss of freshwater from the Atlantic basin whilst an excess of evaporation over precipitation in the Northern Atlantic acts to further heighten salinity. It is this heightened salinity that enables North Atlantic water masses to sink.

An opposing view, put forward by Toggweiler & Samuels (1998) asserts that mass driven convection alone cannot account for the continual mixing observed, since overturning would cease once the vertical mixing gradient approached zero. Thus an external energy source is required, which Wunsch (2002) attributes to wind and tidal forcing.

4.1.3 Anthropogenic climate change and the North Atlantic

With the onset of anthropogenic climate change, an increase of both precipitation and atmospheric temperature is projected over the northerly latitudes (Meehl et al., 2007). Both these effects will act to reduce the density of surface waters and supress the formation of NADW that drives the AMOC. Furthermore, increased freshwater input into downwelling sites from enhanced Greenland Ice Sheet runoff may act to further reduce surface density and supress NADW formation (Hu et al., 2009; Jungclaus et al., 2006).

The sensitivity of the AMOC to enhanced precipitation, Arctic warming and Greenland Ice sheet melt remains highly uncertain. Best estimates from the Coupled Model Intercomparison Project (CMIP5) suggest a reduction in strength of between 22 – 40 % depending on the future emissions scenario (Weaver et al., 2012). Yet confidence in the AMOC response remains low (Collins et al., 2013). Modelling studies suggest the response will depend upon an interplay between freshwater input from meltwater and increased salinity at NADW formation sites, caused by enhanced Atlantic evaporation (Drijfhout et al., 2011). These two poorly constrained effects act to decrease, and increase flux into downwelling sites respectively.

Palaeo-oceanographic studies have shown that the AMOC has been subjected to similar forcings throughout the last glacial cycle. There is evidence to suggest that freshwater input during mass iceberg discharge (Heinrich) events or land based meltwater input (Younger Dryas) lead to a weakening of AMOC strength (Adkins, 1998; Elliot et al., 2002; Kroon et al., 1997; Lynch-Stieglitz et al., 2014). Similarly it has been suggested that the reduction in ambient air temperature at NADW formation sites during glacial episodes suppressed ocean/atmosphere heat exchange, inhibiting the downwelling of cold NADW (Manabe & Broccoli, 1985; Wary et al., 2015). These events are explored in further detail in the following sections.

4.2 The AMOC during the Quaternary glacial cycles

As far back as 1906, Chamberlin first suggested that changes to the deep ocean circulation could have played a role in driving the Earth’s glacial episodes. AMOC fluctuations are an obvious driver of the late Quaternary northern hemisphere glaciations because of the role of the AMOC in transporting heat and moisture to higher latitudes (Johnson & McClure, 1976; Rooth, 1982). It’s large volume, high inertia and heat capacity mean it is able to sustain long term climate change over hundreds of thousands of years (Maslin et al., 2001). Modelling suggests that AMOC alteration during the last glacial maximum (LGM) could act to enhance global cooling by up to 30 % (Ganopolski et al., 1998). The majority of proxy data focuses on AMOC configuration and support the hypothesis that it existed in an altered state during glacial periods.

Biological proxies have provided the dominant means for inferring changes in the AMOC. In the modern ocean, primary production discriminates against ^{13}C, leading to heavy isotope enrichment in the top 1km of surface waters. The δ^{13}C gradient of the modern ocean can therefore be used as a tracer for the source regions of water masses. This isotopic signature is preserved in the tests of foraminifera deposited in oceanic sediment and can provide a historical record of changes in water mass source regions.

Studies have suggested that during the Last Glacial Maximum the Nordic seas ceased to be the dominant region of NADW formation as it is today, with downwelling sites moving south into the North Atlantic (Duplessy et al., 1988). The isotopic signature of NADW, which can be traced to the Southern Ocean in the modern day, was reduced in both its southerly penetration, and depth (Curry, 1988), operating in a suppressed state referred to as Glacial North Atlantic Intermediate Water (GNAIW) at depths of approximately 1500 m (Curry & Oppo, 2005; Marchitto & Broecker, 2006). Below this, cold southern sourced water penetrated as far north as 60^{o}N (Curry & Oppo, 2005). See summary Figure 4.4.

Results from the Palaeoclimate Modelling Intercomparison Project (PMIP) suggest that enhanced sea ice coverage over the Nordic and Labrador Seas during glacial episodes acted to suppress ocean/atmosphere heat exchange in these regions, driving NADW formation sites further south (Otto-Bliesner, 2007). At the same time, enhanced sea ice formation and brine rejection in the Southern hemisphere leads to the enhanced AABW formation apparent in the proxy record (Keigwin, 2004). This hypothesis is supported by chloride measurements of sediment pore fluid inclusions which suggest the salinity of the glacial Southern Ocean was enhanced significantly during the last glacial, reversing the modern day north-south Atlantic salinity gradient (Adkins et al., 2002) which in part drives the AMOC.

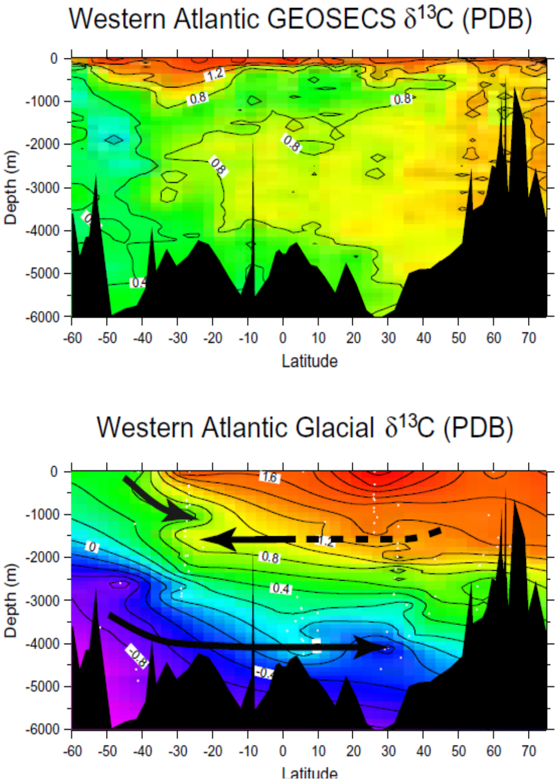

Figure 4.4 Left: Modern day Atlantic $\delta^{13}C$ distributions (From Kroopnick, 1985). The NADW ‘tongue’ with $\delta^{13}C$ values of ~0.8 %o can be seen penetrating from the high northern regions as far as 30°S. Below: $\delta^{13}C$ during the LGM (Curry & Oppo, 2005). The dark arrows show direction travel of the three dominant water masses. *(Source: Curry & Oppo, 2005).*

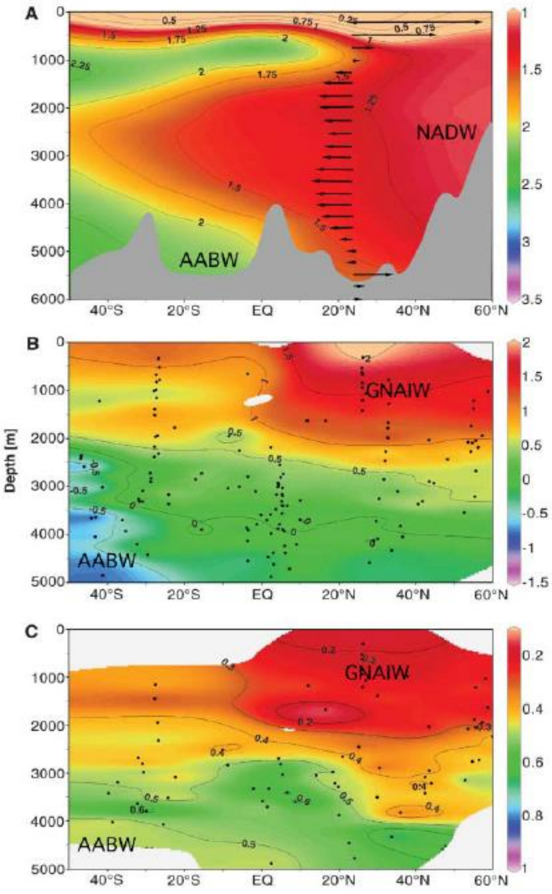

Right: A: The modern distribution of dissolved phosphate in µmol L^{-1} (a biological nutrient removed in surface waters and replenished at depth) in the Western Atlantic (Conkright et al., 2002). Arrows represent the Northerly flow of surface waters and AABW and Southerly flow of NADW. B: $\delta^{13}C$ of the glacial Western Atlantic from the shells of benthic foraminifera (VPDB) (Wefer & Mulitza., 2004 and Curry & Oppo, 2005). The depth and southerly penetration of biologically active waters (red) is much reduced when compared to the modern day. C: Estimates of the Cd in nmol Kg^{-1} (a biological nutrient, removed in surface waters and replenished at depth) concentration of the glacial Western Atlantic from the shells of benthic foraminifera (Marchitto & Broecker, 2006). Figure compiled by Lynch-Stieglitz et al. *(*2007).

4.3 Millennial scale north Atlantic climate fluctuations

4.3.1 Heinrich events and Greenland Stadial/Interstadials

The concentration of ice rafted debris (IRD) – lithic grains transported from land to the open ocean via iceberg movement – in North Atlantic sediments has long been known to increase during glacial intervals. Ruddiman (1977) showed that IRD concentrations increased dramatically during the last glacial, commencing at ~75ka and continuing until the onset of the Holocene, with extended penetration of icebergs both south and east, further from the major land based ice sheets.

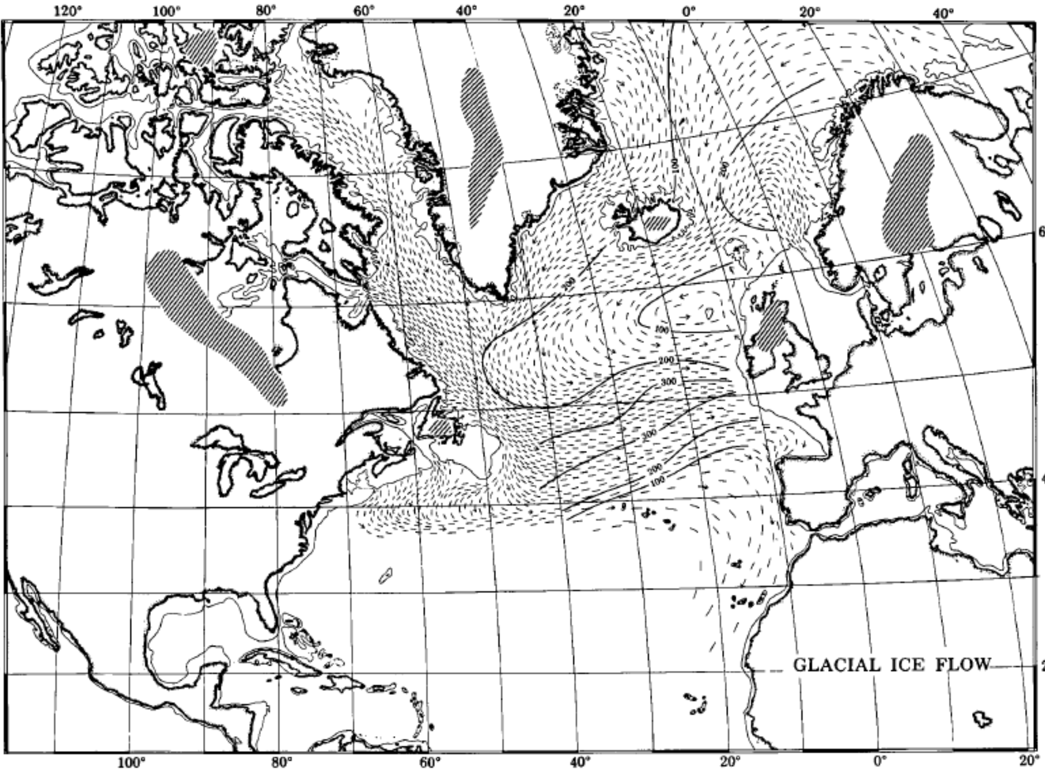

Figure 4.5 Inferred mean free paths distribution of IRD during glacial intervals. Numbers are mean depositional rates of ice rafted sand (mgcm^{-2}yr^{-1}). (adapted from Ruddiman, 1977).

Latter studies suggest that the appearance of IRD within the sediment record was quasi-periodic, occurring every 10 – 11 ka (Broecker et al., 1992; Heinrich, 1988) as distinct events, known as Heinrich events. The isotopic signature of the IRD indicated that the majority had a Laurentide, or Western Greenland origin, with icebergs discharged through the Hudson straight along a channel spanning east-west between 40 – 55°N (Grousset et al., 1993) (Figure

4.5). A Hudson source is supported by the decreasing thickness of detrital carbonate layers with distance from the Hudson Bay (Naafs et al., 2013).

Whilst the appearance of Heinrich events is unequivocal in IRD belt sediments (Figure 4.5), their presence in the wider Atlantic is less certain. Rafting events have been identified in cores north of the IRD belt from the Rockall Plateau and East Greenland Coast (Elliot et al., 2002), The Voring Plateau in the Nordic Seas (Fronval et al., 1995), and the Reykjanes Ridge (Rasmussen et al., 2016). However, whilst in IRD belt sediments the Heinrich layers appear as distinct peaks, the record further north suggests more modest peaks with similar patterns to the peaks observed in other Greenland stadials (Hemming, 2004; Naafs et al., 2013).

The climatic impact of these events appears global, with responses observed as far away as South American glacial systems (Lowell et al., 1995), the North Pacific (Kotilainen & Shackleton, 1995) and in the response of the East Asian monsoon obtained from the South China Sea (Wang et al., 1999).

The cause of Heinrich events remains speculative, yet their temporal evolution within the unstable northern hemisphere climate of the last glacial offers some clues. With the first Greenland ice core analysis came the discovery that the North Atlantic region had undergone short lived temperate excursions, or interstadials, every 500 – 2000 years throughout the last glacial period (Dansgaard et al., 1993; Johnsen et al., 1992). Later analysis gave a periodicity of 1470 ± 500 years (Bond, 1997). The signature of these ice core $\delta^{18}O$ excursions, or Dansgaard-Oeschger cycles, was soon identified in North Atlantic sediment records as increased concentrations of (IRD) during cold Greenland stadial events (Bond & Lotti, 1995; Bond et al., 1993). Furthermore, their signature could be traced back in time beyond the last glacial cycle (Oppo et al., 1998) and into the Holocene (Bond, 1997), with the interglacial equivalent being known as bond events.

Bond et al. (1993) showed that when Heinrich events were superimposed onto oceanic temperature and the GRIP ice core records it could be seen that Heinrich events occurred at quasi-regular intervals, every 3-4 Greenland stadial/interstadial cycles (Figure 4.6). Thus Greenland stadial/interstadial transitions and Heinrich events likely have similar triggers. Whilst Heinrich events coincided with the most extreme temperature declines of 3 – 6 ^{o}C below the already cold glacial climate (Bond et al., 1993; Dansgaard et al., 1993), subsequent studies have shown that ice rafting occurs during most, if not all, Greenland Stadial periods (Chapman & Shackleton, 1999; Rasmussen et al., 2016) albeit with lower intensity than the more extreme Heinrich events.

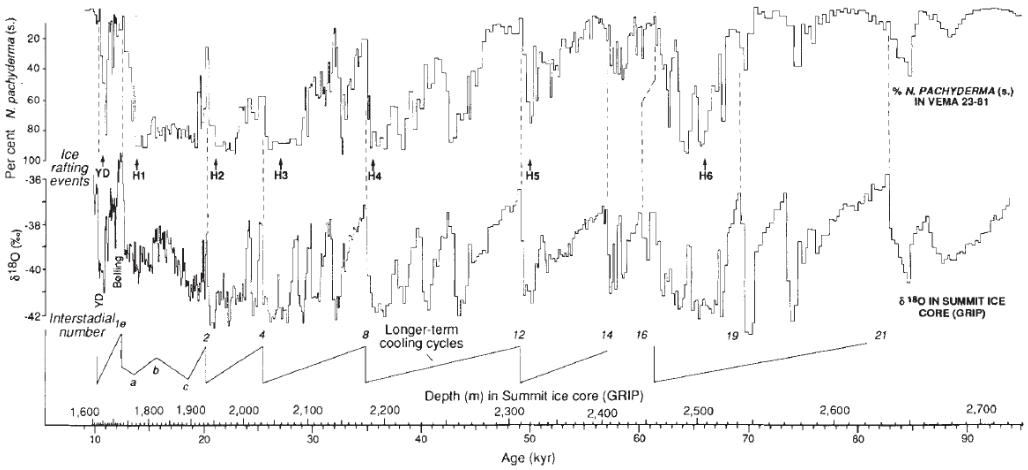

Figure 4.6 Overlain records of percentage abundance of *N. Pachyderma* at North Atlantic core site V23-81 (top) and δ^{18}O from the GRIP ice core (middle). The ~1.5ky cycles of D-O events are clearly apparent within larger Heinrich event signals (Marked H*) which occur every 3 – 4 stadial/interstadial cycles. Longer term saw tooth temperature cycles, known as bond cycles, are bookended by Heinrich events (*Source: Bond* et al*. (1993)*)

Heinrich's original 1988 paper suggested that these major rafting events, coincided with periods of winter minimum/summer maximum insolation every half processional cycle. Indeed processional harmonics have been shown to exhibit 11 – 12 ka periodicity in North Atlantic sites (Hagelberg et al., 1994). These insolation minima could have allowed the northern hemisphere ice sheets to cool and expand to sufficient size to eject large volumes of icebergs into the north Atlantic. The coincident global cooling observed in other proxy records, discussed above, supports the idea of such a globally driven forcing. However, later analysis has suggested asynchronous cooling in the Northern and Southern hemisphere (Blunier et al., 1998) such that an external insolation forcing could not be the cause.

An alternative theory proposed by MacAyeal (1993a, 1993b) suggests that instability in the Laurentide ice sheet drove the mass rafting events. Slow mass build-up of the ice sheet acted to trap geothermal heat which built up over time, eventually becoming sufficient to melt ice in contact with the bedrock and cause a high volume of basal sliding. A numerical model of the process suggested a 7 ka oscillation for this binge/purge model – in line with the observed cyclicity between Heinrich events (MacAyeal, 1993a).

Van Kreveld et al. (2000) used high resolution records of the North Atlantic to conclude that small amounts of iceberg rafting in the Nordic Seas preceded Heinrich rafting. They proposed that these initial ice rafting events caused sufficient sea level rise to undercut the ground based Laurentide ice sheet and subsequently cause the large scale rafting events through the Hudson Strait. This theory is supported by Sr-Nd isotopic analysis of IRD from the European margin which shows ice rafting from the European Ice Sheets preceded those from the Laurentide ice sheet (Grousset et al., 2000). This scenario suggests that sea level rise was sufficient to undercut the Laurentide ice sheet every 3 – 4 stadial/interstadial cycles (Maslin et al., 2001). However, the question still remains as to what causes stadial/interstadial cycles in the first place.

An additional theory put forward by Johnson & Lauritzen (1995) proposes the existence of a glacial lake, dammed by the Laurentide Ice Sheet. Heinrich events were triggered by repeated jökulhlaups – massive glacial lake outpourings – that occurred when the glacial dam at the mouth of the Hudson Strait failed. Meltwater delivery would account for the high concentration of fine grained material found in the sediment immediately prior to Heinrich events (Hesse & Khodabakhsh, 1998). However, whilst it’s possible that a glacial lake may have existed during the latter stages of MIS 5 and possibly MIS 3, it seems unlikely that the cold glacial climate could have allowed the existence of a glacial lake for prolonged periods (Hemming, 2004).

The ice shelf hypothesis proposed by Hulbe (1997) postulates the existence of an ice dome over the Hudson Bay that formed an ice shelf over the Labrador Sea. Such a configuration could transport large quantities of lithic material to the ice shelf because of the steep basal topography. The ice shelf would only operate during extreme cold periods, consistent with the observation that Heinrich events occur during the most intense cold intervals (Bond et al., 1993). However, in such a model extreme ‘Heinrich like’ rafting are expected for all cold intervals and this is not observed.

Seidov & Maslin (2001) provided a conceptual model to propose that Heinrich Events and stadial/interstadial cycles were the consequence of a natural heat exchange between the north and south hemispheres, driven by the thermohaline circulation. Their model is based on the discovery that the two hemispheres experience out of phase warming (Blunier et al., 1998). They suggest that iceberg discharge into the North Atlantic during Heinrich events and northern hemisphere stadials acts to suppress NADW formation, reducing the northerly flow of surface waters and the penetration of NADW into the Southern Ocean.

With no equivalent event in the southern hemisphere, Antarctic bottom water (AABW - deepwater formed in the Southern Ocean) formation begins to dominate over NADW formation. As AABW sinks, warm equatorial waters are drawn to replace it, leading to a reversal in the AMOC, warming the southern hemisphere and further cooling the northern. This configuration stops only once northern hemisphere ice sheets have sufficiently stabilised to have 'flushed' all icebergs and begin to regrow. At this point freshwater input into the North Atlantic is reduced and allows the AMOC to return to its 'usual' configuration.

4.3.2 Glacial Terminations

After the slow glacial build-up of northern hemisphere ice sheets over 80 – 120 ka, the transition into interglacial conditions is marked by a rapid warming, or termination (Broecker & van Donk, 1970). The majority of literature focuses on the most recent termination, Termination I and its occurrence within the radiocarbon dating range also give it the best constrained chronology. As such this section will give an overview of Termination I, against which other termination events can be compared.

Between the start of the last termination at 18 - 20 ka (Denton et al., 1981) and the disappearance of the Laurentide ice sheet at 7ka (Dyke et al., 1987), sea level rose approximately 120 m (Thompson & Goldstein, 2006) and atmospheric CO_2 concentration increased by around 90 ppm (Monnin et al., 2001). This geologically rapid transition was punctuated by periods of rapid warming and cold reversals in which the response of the AMOC is thought to have played a driving roll.

A moderate $\delta^{18}O$ increase is observed in the GRIP and GISP II Greenland records subsequent to 24ka (Sowers & Bender, 1995). This short lived excursion is interpreted as a temporary transition out of full glacial conditions however a return to near LGM values is observed by

16ka (Sowers & Bender, 1995). Atmospheric CO2 concentrations begin to rise shortly after at 17.5 ± 1 ka (Monnin et al., 2001).

The first dramatic shift in Greenland temperatures is observed at 14.7 ka at the start of the Bolling Warm Interval (Figure 4.7), marking the definitive transition out of full glacial conditions (Sowers & Bender, 1995). Atlantic sea surface temperatures increased (Kroon, et al., 1997) and land based temperature proxies suggest coincident warming in Europe (Renssen & Isarin, 2001) and North America (Shuman et al., 2004). Radiocarbon ages show an increase in North Atlantic ventilation (Adkins, 1998), alongside increasing benthic $\delta^{13}C$ showing increasing NADW formation (Piotrowski et al., 2005; Clark et al., 2012). Foraminifera derived temperatures and salinity show an influx of warm, saline waters into the North Atlantic (Kroon, et al., 1997) suggesting that the AMOC operated in a heightened state during the Bolling warm period.

The Bolling warm period is accompanied by a dramatic 10 – 20 m rise in sea level over an approximately 700 year period (Figure 4.7) (Clark et al., 2012; Peltier & Fairbanks, 2006; Fairbanks, 1989). A coincident marine $\delta^{18}O$ spike, suggests the rise was accompanied by surface water freshening, likely caused by a dramatic influx of water from land based sources, referred to as Meltwater Pulse 1a (McManus et al., 2004). The timing of Meltwater Pulse 1a remains contentious but best estimates put it around 14ka (Bard et al., 1996; Fairbanks, 1989).

The source of the freshwater has generally been attributed to the draining of glacial Lake Agassiz, triggered by the retreat of Laurentide glacial dams (Broecker et al., 1989; Rooth, 1982). Supporting evidence is provided by $\delta^{18}O$ measurements in the Gulf of Mexico that suggest a coincident increase in salinity as drainage routes were diverted from the Mississippi to the St Lawrence River (Flower et al., 2004), and a drop in Lake Agassiz levels (Thorleifson and Teller, 1982). The exact route of the flood remains contested with counter arguments suggesting that the Laurentide Ice Sheet had not retreated sufficiently by 14ka to allow the freshwater outburst (Lowell et al., 2009) and $\delta^{18}O$ records of the St Lawrence River outlet failing to identify the expected reduction in salinity from such a large amount of freshwater input (de Vernal et al., 1996).

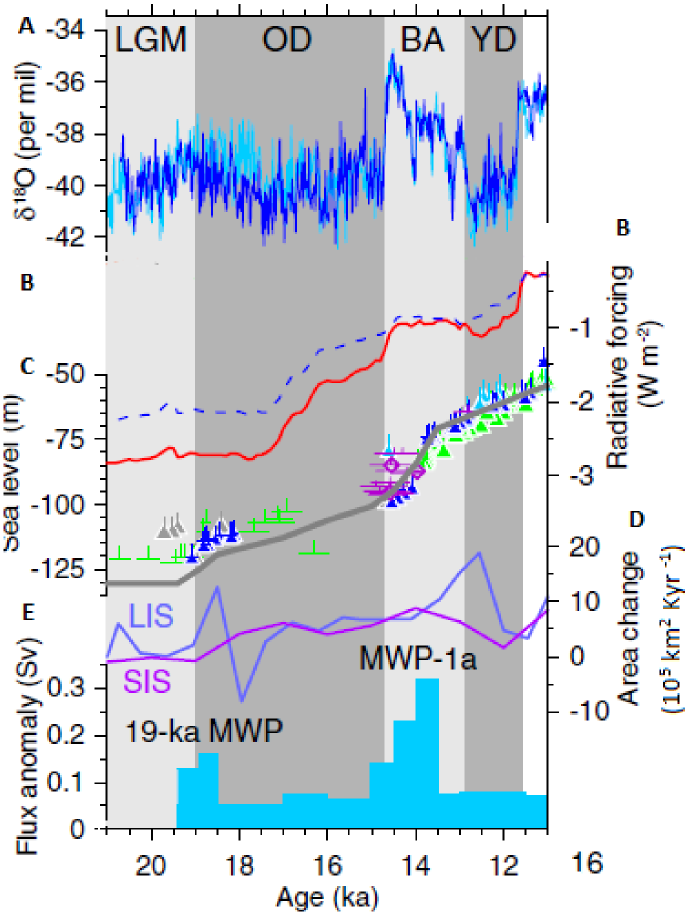

Figure 4.7 A) GISP 2 (dark blue) (Meese et al., 1997) and NGRIP (light blue) (Johnsen et al., 2001) $\delta^{18}O$ records. B) Combined radiative forcing (red line) and CO_2 only (dashed blue line) (Monnin et al., 2001, on Greenland Ice Core Chronology 05 (GICC05) timescale (Lemieux-Dudon et al., 2010)) relative to preindustrial levels. See Clark et al. (2012) for details on conversion to radiative forcing. C) Relative sea level from Bonaparte Gulf (green crosses) (Yokoyama et al., 2000), Barbados (grey and dark-blue triangles) (Peltier & Fairbanks, 2006), New Guinea (light-blue triangles) (Edwards et al., 1993), Sunda Shelf (purple crosses) (Hanebuth et al., 2000), and Tahiti (green triangles) (Bard, Bard, Hamelin, & Delanghe-sabatier, 2012). Also shown is eustatic sea level (grey line) (Peter U. Clark et al., 2009). D) Area loss from the Laurentide Ice Sheet (Dyke, 2004) and the Scandinavian Ice Sheet (Peter U. Clark et al., 2012). E) Freshwater flux to the global oceans derived from eustatic sea level in C (Peter U. Clark et al., 2012). Grey vertical shading shows timing of climatic intervals (OD = Older Dryas, BA = Bolling-Allerod, YD = Younger Dryas). (Adapted from (Peter U. Clark et al., 2012)).

Shortly after Meltwater Pulse 1a, a $\delta^{18}O$ spike is observed in the Greenland ice cores at 12.9 ka (Rasmussen et al., 2014), accompanied by a steep decline in atmospheric greenhouse gas concentrations (Clark et al., 2012) associated with the Younger Dryas cold event. Temperature drops of up to 10 °C are observed across northern Europe (Atkinson et al., 1987; Brooks & Birks, 2000), with wider climatic impacts observed as far as China (Huang et al., 2012) and Malawi (Castañeda et al., 2007).

Benthic $\delta^{13}C$ declines in north Atlantic cores (Zahn et al., 1997) and atmospheric radiocarbon spikes (Singarayer et al., 2008) suggest a reduction in North Atlantic ventilation, consistent with North Atlantic freshening from meltwater pulse 1a suppressing NADW formation (Broecker et al., 1989).

Temperatures and Greenhouse forcing remained supressed for approximately 1.2 ka (Clark et al., 2012) until a sharp increase in $\delta^{18}O$ at 11.7 ka is observed in the Greenland Ice cores (Rasmussen et al., 2014) alongside a global temperatures increase, signifying the onset of the Holocene (Clark et al., 2012).

Chapter 5. Core processing and geochemistry methodology

5.1 Core preparation

Samples were obtained from two 1.5 m sections of core MD99-2251 spanning depths 20.28 m – 23.26 m. Each section was extensively photographed prior to processing with changes in visual appearance noted. The outer 1 mm of sediment was removed prior to photographing as this may have undergone some discolouration during oxidation from contact with the air.

Figure 5.1 Close up of the upper portion of section XVI of core MD99-2251 showing uniform appearance.

The core was sliced into 1 cm segments with a craft knife, taking care to leave a thin (~0.5 cm) outer ring of sediment behind on the core housing. This outer coating is prone to sediment perturbation in the coring process and contains a high concentration of plastic contamination from the core housing. Alternate 1 cm samples were removed and bagged for storage. The remaining samples were weighed and submerged in distilled water before being placed onto a mixing table for a minimum of 48 hours to disaggregate the sediment. In denser samples, additional mixing time was sometimes required alongside physical breaking of sediment using pressurised distilled water. After disagregation, samples were sieved at 150 µm, a size fraction shown to isolate adult foraminifera tests, mineral and rock grains (Mcmanus et al., 1996), before being dried overnight at 50 °C in a drying oven. Both coarse (>150 µm) and fine (<150 µm) dry weights were recorded.

5.2 Foraminifera assemblage and IRD counts

5.2.1 Foraminifera assemblage counts

A micro-splitter was used to randomly divide the coarse size fraction (>150 µm) in half multiple times until ~300 speciments remained. The remaining specimens were tipped onto a counting slide for analysis with a binocular stage microscope.

The number of specimens counted represents a compromise between counting efficiency and accuracy. Although there is some debate as to whether 300 specimens is sufficient to accurately capture assemblage diversity (Patterson & Fishbein, 1989), it has become the standard number over which assemblages are surveyed (e.g Pflaumann, et al., 1996; Mcmanus et al., 1996). Fatela & Taborda (2002) demonstrate from analysis of 4 benthic foraminifera assemblages that 300 specimens is sufficient to provide a accurate representation of the full population. They calculate that the probability of losing species present at 5 % of the population falls to 3×10^{-5} % for counts of 300 and greater. The average number of specimens counted per assemblage in this study was 448. Specimens were identified down to the species level with unrecognisably damaged or malformed specimens counted as ‘unknown’.

Errors were estimated with eight recounts. Recounted samples chosen to represent a large range in represented species. The weighted average percentage offset between orginal and re-counts was 5.5 % for species representing >5 % abundance.

5.2.2 Ice rafted debris counts

Ice rafted debris (IRD) counts were conducted concurrently to assemblage counts. Distinction of IRD petrographic type enables the source to be identified, giving information about ice sheet dynamics and oceanic currents. In mid Atlantic cores VM29-191 and VM23-181, situated of the West of Ireland, black basaltic glass has been shown to derive from southerly migrating Iceland or Jan Mayan sourced icebergs and heamatite stained quartz from those derived on the Eastern Greenland coast and Svarlbard (Bond, 1997). Detrital carbonates from cores in the Labrador Sea have been traced to icebergs carved from the South and West Greenland Margin (Bond et al., 2001). Similarlty volcanic tephras provide geological timestamps of major volcanic eruptions which allow accurate dating of such events and cross correlation between cores (Davies et al., 2014).

For this study IRD types were split into six categories: clear quartz, stained quartz (pink, brown), glass, volcanics, carbonates and others – encompassing erratic grains that didn’t fall into the other nine categories. IRD counts were quantified as percentages of total entities (Heinrich, 1988) and as a concentration – grains per gram of dry sediment. The former method overcomes biases arising from large IRD specimens such as dropstones — a single large entity of which may skew the results by causing an erroneous increase in sediment mass (Grobe, 1987). However, this method is vulnerable to false spikes in IRD that might arise from a fall in carbonate material rather than an absolute increase in IRD material. Thus the two methods used in conjunction allow such biases to be identified.

5.2.3 Stratigraphic zoning with foraminifera assemblages

Constrained hierarchical clustering of foraminifera assemblages into stratigraphic zones was performed using the Rioja package written for the programming language R (Juggins, 2017). The package applies an incremental sum of squares method (Ward, 1963), minimising the total within cluster dispersion. The method draws upon the CONISS algorithm, originally written in FORTRAN and applied to pollen stratigraphic zoning (Grimm, 1987). CONISS applies incremental sum of squares such that only stratigraphically adjacent samples are considered for clustering.

The total number of statistically significant stratigraphic zones was obtained by comparison to the broken stick model (Bennett, 1995). This divides the total variance of the dataset into N equal zones, the length of which corresponds to the proportion of total variance that would be present in each level of zonation if the sequence consisted of samples with no stratigraphic structure. Stratigraphic zones are then assigned by comparison to this model. If the variance in each zone exceeds that expected from the broken stick model – the zone accounts for more variance that would be expected if the samples were arranged at random and can be considered significant (Bennett, 1995).

Figure 5.2 shows an example dataset from Bennett (1995) with the smooth line showing the proportion of variance with number of zones in the broken stick model and the variable line showing the same for an example palaeontological dataset. The proportion of variance for the example dataset falls below the broken stick model once 18 zones have been drawn. Thus these 18 zones are considered significant as they contain variance that differs from other zones in some way. When the dataset is further subdivided, the difference between zones are simply the result of random variance (Bennett, 1995).

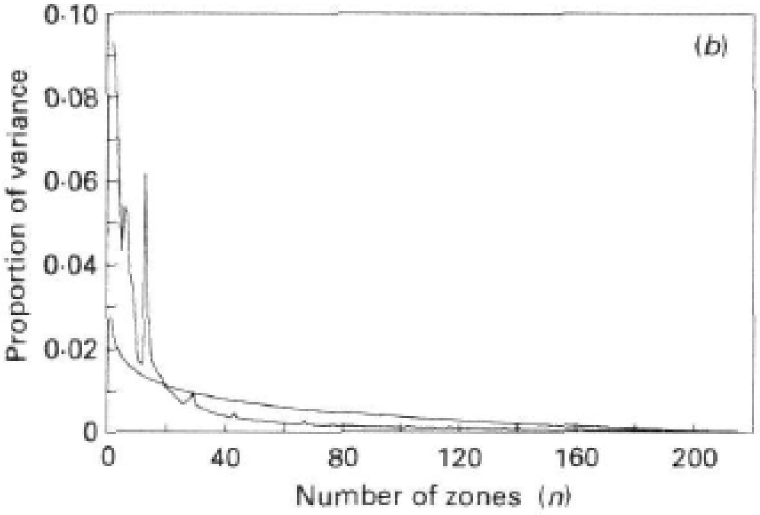

Figure 5.2 Demonstrating the use of broken stick model to assess significance of stratigraphic zoning. Once the proportion of variance of the broken sticks model (smooth line) exceeds that of the palaeontological dataset (variable line), additional zoning is not significant (Source: Bennett, 1995).

5.2.4 Temperature reconstructions from foraminifera assemblages

Methods for reconstructing palaeo-environmental conditions from micropalaeontological proxy data fall into one of two broad categories: Calibration or similarity studies. Both methods rely on three basic assumptions: (1) That the environmental variable being studied is the cause of the changes in the chosen biological proxy; (2) That the relationship between the species and environmental variable being studied has not changed over time and (3) that the modern observations contain all the data required to interpret the fossil data (Guiot, 2011).

Calibration methods generally use modern day training datasets to derive mathematical relationships between the species present in an assemblage and an environmental variable.

The earliest such example is the seminal study of Imbrie & Kipp (1971) in which principal component analysis is used to form clusters of core top assemblages associated with different environmental regimes. Each assemblage is associated with a small number of species components which are then regressed against environmental variables. These regressions can now be applied to fossil assemblages to infer palaeo-environmental conditions. This approach was also employed in the well known CLIMAP project (Climap Project Members, 1976). In the years since, various calibration approaches have been developed which vary in their mathematical methodology. These are summarised in Table 5.1.

Table 5.1 A summary of calibration methods used to infer palaeoenvironmental conditions from micropalaeontological proxy data (adapted from Guiot, 2011)

Approach	Family	Method	Example
Calibration	Ordination techniques	Principal component analysis	(Imbrie & Kipp, 1971)
		Partial Least Square	(ter Braak et al.,1993)
		Correspondence Analysis	(Roux, 1979a)
	Generalised linear models	Logistic regression	(ter Braak & Looman, 1986)
	Non-parametic methods	Artificial Neural networks	(Malmgren & Nordlund, 1996)
Similarity	Presence/Absence	Mutual climatic range method	(Sinka and Atkinson, 1999)
		Use of indicator species	(Iversen, 1944)
	Abundances	Modern Analogue technique (MAT)	(Hutson, 1980)
		MAT geographically constrained	(Pflaumann et al., 1996)
		Revised analogue method (RAM)	(Waelbroeck et al., 1998)

Rather than rely on deducing mathematical relationships between taxa and environmental variables, similarity methods compare fossil assemblages to modern day data. The modern analogue technique (MAT) was first introduced by Hutson (1980). His technique matched fossil assemblages to over 150 modern core top assemblages to obtain a subset of the most closely related modern samples (or analogues). Sea surface temperature and salinities for fossil assemblages were then inferred by averaging those variables across the subset of modern analogues.

Subsequent advances have sought to further constrain the choice of analogues either geographically (e.g. Pflaumann et al., 1996) or through the creation of 'virtual' analogues, derived from interpolation between core tops in environmental space and using these as matches for the fossil assemblage (RAM technique) (Waelbroeck et al., 1998).

This study applied the modern analogue technique (MAT) to infer temperature from 182 fossil assemblage counts of core MD99-2251 conducted for this study, as well as an additional 434 counts conducted previously by Mark Chapman, Leila Hulme and Christopher Ellison. This gave a total of 616 fossil assemblages, covering a depth range between 9.44 m and 35.74 m. *N. pachyderma* (s) percentage abundance data between 9.44 m and ~16.5 m has been published previously (Ellison et al., 2006).

MAT analysis was conducted using the aforementioned Rioja package, produced by Steve Juggins, for the statistical analysis software 'R' (Juggins, 2017). 947 Atlantic core top assemblages, compiled as part of the Glacial Atlantic Ocean Mapping (GLAMAP) project (Pflaumann, 2003) were used as modern analogues. Similarity to the modern analogues was assessed by minimising the squared chord distance between the sample and analogue. The squared chord distance was calculated by summing the square roots of each species percentage abundance in the fossil assemblage minus the square root of the species percentage abundance in the analogue.

$$Square\ chord\ distance = \sqrt{\sum_{i=1}^{n} ({q_i}^{1/2} - {p_i}^{1/2})^2}$$

Where q = species population percentage of fossil assemblage and p = species population percentage of analogue assemblage.

The inferred temperature was then calculated by averaging the temperature across the modern subset, with weighting applied to each analogue dependent on its similarity to the fossil assemblage.

The number of modern analogues (defined as K and commonly referred to as the number of "nearest neighbours" given their similarity to the sample assemblage) to include within a temperature calculation will vary depending upon the characteristics of the subset. A smaller, less variable subset could be considered more reliable than a large highly variable one, however too few analogues in the subset renders it vulnerable to outliers and biases.

The impact of the chosen K value was investigated by first applying the MAT to the 947 cores of the training dataset to derive summer SST for a value of k varying between 1 and 12. The average RMSE from the known core top temperature was then calculated for each value of k. Results are plotted in Figure 5.3. A minimum RMSE of 1.19 °C is achieved at k = 8 and thus this value was adopted for palaeotemperatures calculations for the 616 fossil assemblages of MD99-2251.

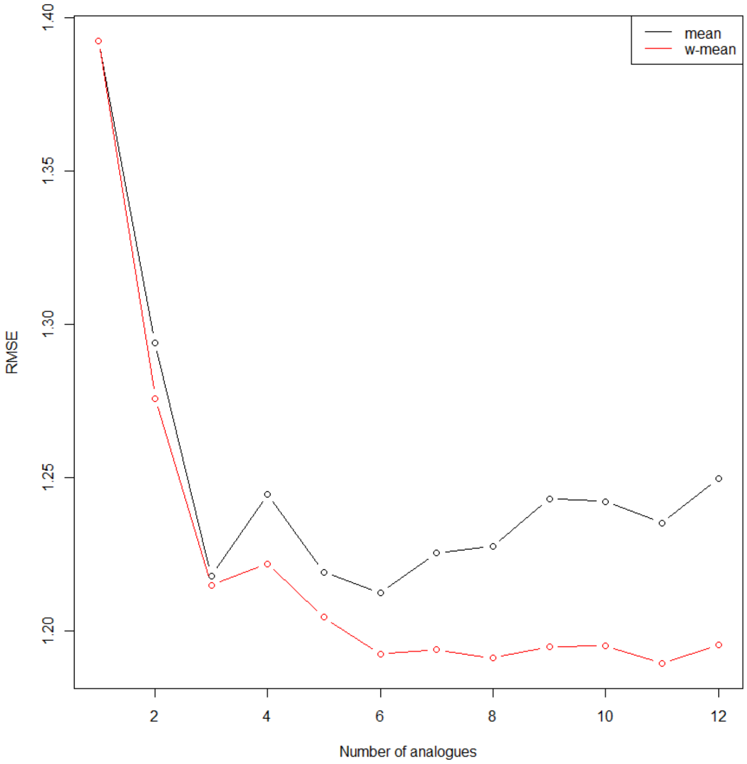

Figure 5.3 Average RMSE for predicted temperature using the 947 coretop training dataset with a given number of analogues. Minimum weighted mean RMSE is achieved with 8 analogues.

MAT performance was estimated using cross-validation bootstrapping on the 947 cores from the SIMMAX database (Figure 5.4). The technique clearly performs better at higher temperatures which are better represented within the SIMMAX dataset (Table 5.2).

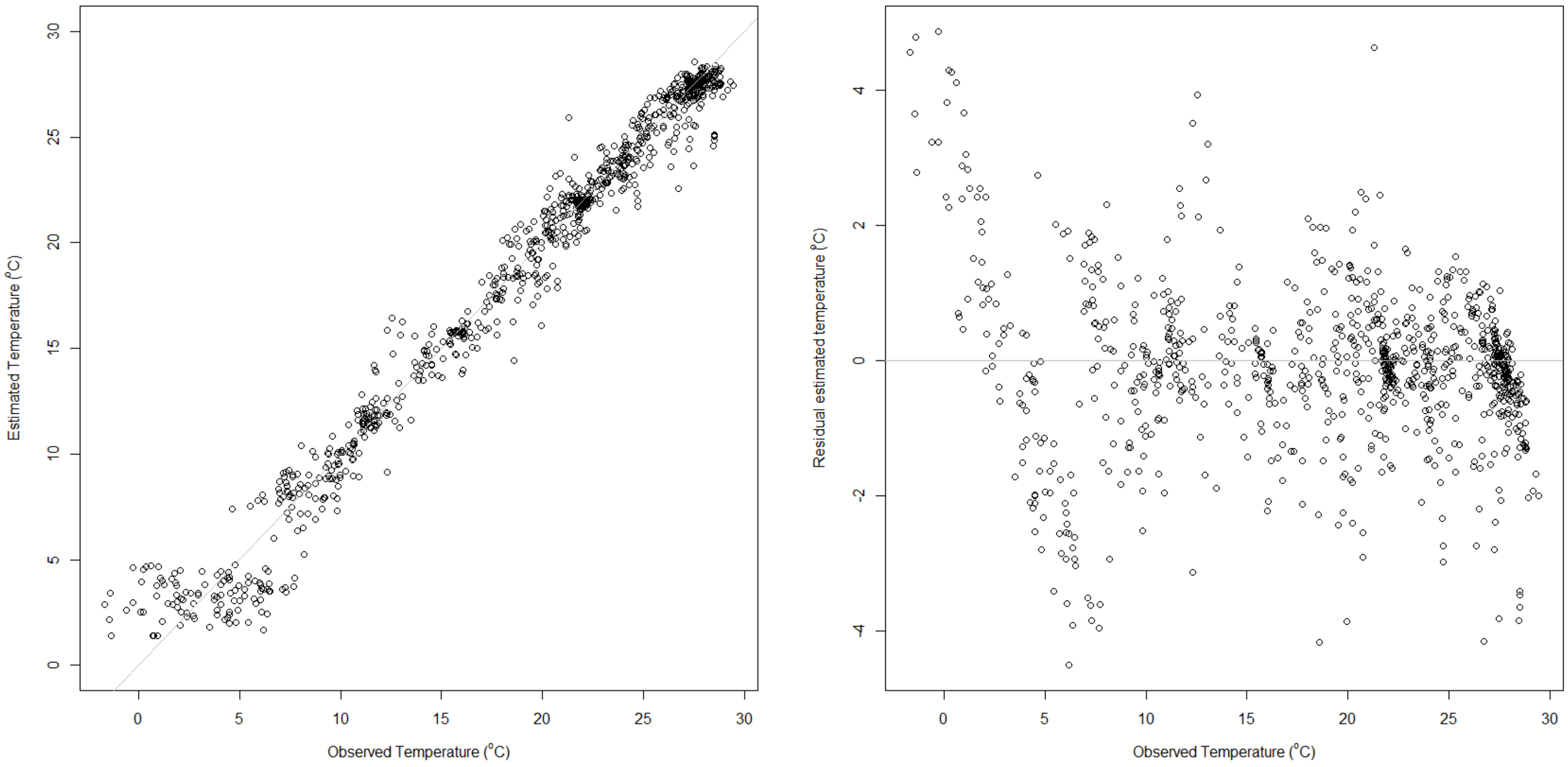

Figure 5.4 Results of bootstrapping cross validation for the 947 SIMMAX core tops using k = 8. Left shows estimated vs observed temperature and right the residuals. The method clearly performs better at higher temperatures.

The MAT was subsequently applied to the 616 fossil assemblages, with modern analogues sourced from the 947 core tops SIMMAX database. Summer SST was calculated from the weighted average across the eight most closely matching analogues. Errors were estimated from residual magnitudes in the SIMMAX cross validation at 5 °C temperature intervals (0).

Table 5.2 Summary statistics for MAT cross validated with SIMMAX 947 core top dataset (k = 8).

Temperature range (°C)	Average residual magnitude (°C)	Number of core tops in SIMMAX dataset	Estimated error of palaeo-samples (°C)
<5	1.66	80	1.8
5-10	1.46	105	1.5
10-15	0.71	109	0.8
15-20	0.77	124	0.8
20-25	0.62	258	0.7
25-30	0.63	271	0.7

5.3 Sample preparation for Mg/Ca analysis

Mg/Ca temperatures were inferred at alternate 1 cm intervals along the 3 m section of core MD99-2251 (section 5.1), with an additional six measurements at key climatic intervals selected from the entire length of the core.

Foraminifera specimens were obtained by dry sieving the coarse fraction sediment to the desired size fraction, scattering onto a gridded picking tray and manually selecting tests using a binocular microscope and fine paintbrush. Only whole tests were selected with care taken to ensure samples were pristine with no visible sign of discolouration or staining.

N. pachyderma (s) and *G. bulloides* were selected as the most abundant species, thus providing sufficient measurement material. 60 *N. pachyderma (s)* and 80 *G. bulloides* specimens were picked for each analysis in the 250 – 300 µm and 300 – 355 µm size fractions respectively.

5.3.1 Sample cleaning for Mg/Ca analysis

Samples were cleaned according to a method modified from Barker et al. *(*2003), described in detail in section 3.5.2. Briefly: samples are crushed and chamber detrital material removed under the microscope before being transferred to a 500 µL micro-centrifuge tube. Finer grained sediment was then removed through repeated ultrasonication in ultrapure water and methanol, before boiling for 15 minutes in NaOH buffered 1 % hydrogen peroxide solution to remove organic material. A final 0.001 m nitric acid leach is used to remove secondary calcite overgrowths before rinsing in ultrapure water and drying overnight in a drying oven.

5.3.2 Mg/Ca ICP-AES analysis

Immediately prior to ICP-AES analysis, samples were dissolved in 300 µL of 0.075 m nitric acid, aided by ultrasonication where necessary. Samples were inspected under the microscope to ensure full dissolution prior to being centrifuged at 5000 rpm for five minutes to remove any remaining solids. The top 250 µL was then removed and transferred to clean micro-centrifuge tubes, ready for analysis. Five-fold dilutions of each sample were then prepared by removing 50 µL from the 250 µL batch and diluting with 200 µL of ultrapure water.

Mg/Ca ratios were measured on the Varian Vista Inductively Coupled Plasma Atomic Emissions Spectographer (ICP-AES) at the University of East Anglia. Prior to analysis, the instrument was stabilised by running through 0.075 m nitric acid for a minimum of 30 minutes. Ca and Mg calibrations were produced from regressions of intensity against concentration derived from five laboratory standards with Ca concentrations of 10, 20, 40, 80 and 120 ppm, held at constant Mg/Ca ratio of 5 mmol/mol. Similar regressions were used to produce calibrations for contaminants Al, Ba, Fe, K, Mn, Na, Si, Ti and Zn using six laboratory standards.

Background contamination was assessed with measurement of six vial blanks prior to analysis. This was subtracted from final measurements. The sample five-fold dilutions were then measured and used to calculate the Ca concentration within the bulk sample. This allowed dilution of the bulk sample to a standardised concentration of either 20, 40, 60 or 100 ppm – the final choice dependent on the amount of calcium in the bulk solution. 60 ppm was generally preferred as it was found to be most accurate.

Final Mg/Ca ratios were calculated according to the method of de Villiers et al*. (*2002). Conventional ratio calculations regress element line intensities against element concentrations to estimate absolute concentration before then calculating elemental ratios. This is problematic at higher elemental concentrations where intensity calibrations have been shown to be vulnerable to curvature (Figure 5.5) – consistent with the effect expected from elemental self-absorption (Ramsey et al., 1987).

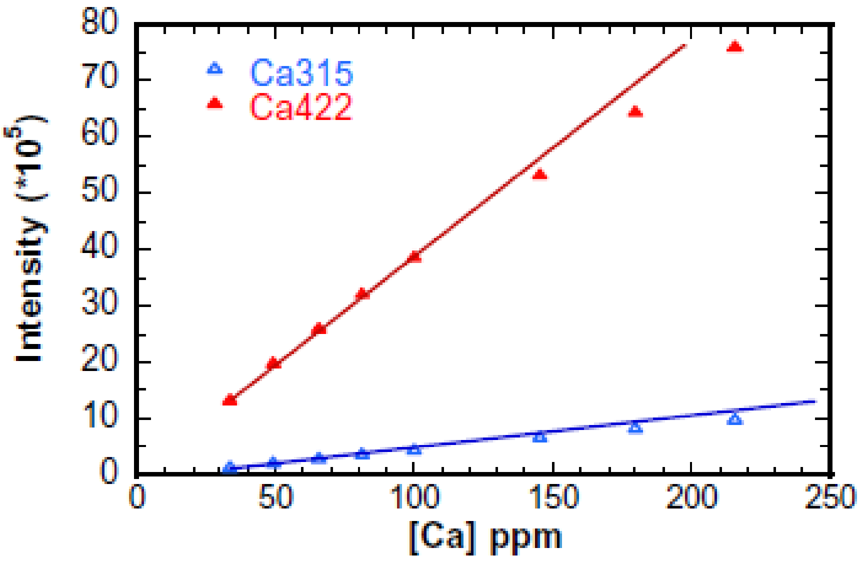

Figure 5.5 Intensity vs concentration plots from ICP-AES analysis. Lines show linear relationships with a reduction in predicted intensity at higher concentrations caused by matrix effects. Note that the effect is less apparent in the Ca315 line. (source: de Villiers et al., 2002)

Instead of regressing intensity directly with concentration, the de Villiers et al. (2002) method first produces a calibration of standards with identical calcium, but variable magnesium, concentrations. This requires measurement of six laboratory standards with Ca concentrations identical to those of the diluted sample concentrations (either 20, 40, 60 or 100 ppm). The raw intensity ratios (Mg285/Ca315) of the samples are then regressed against the Mg/Ca content of the standard solutions. Mg285 and Ca315 emissions lines were used as these exhibit the smallest matrix effects (Figure 5.5).

Instrumental drift and precision were monitored with analysis of three laboratory standards of Ca concentration 60, 70 and 100 ppm, a minimum of six times throughout the experimental run. Average relative standard deviation in Mg/Ca across the three standards was 0.048 mm/mol.

5.3.3 Mg/Ca contamination screening

A substantial proportion of marine sediment consists of mineral clays — predominantly kaolinite, illite, chlorite and montmorillonite (Barker et al., 2003) — which, since they contain elements of interest, must be removed prior to analysis. Barker et al. (2003) calculate that just 0.1 µg of mineral rich clay is sufficient to significantly increase uncertainty in Mg/Ca measurements, highlighting the need for a robust cleaning protocol and contaminant screening process.

Both Fe and Al are strong indicators of elevated clay mineral content. The co-variation of Al and Si in foraminifera samples was first noted in the pioneering studies of Emiliani (1955) who concluded that Al must therefore arise from silicate contamination. Similarly Fe has been shown to co-vary with Al and Mg content (Barker et al., 2003) and therefore can also be used as an indicator of clay contamination. Thus samples with elevated Al/Ca and Fe/Ca, above a 0.4 mmol/mol threshold or Fe/Mg above 0.2 mmol/mol were highlighted for additional scrutiny.

Ferromanganese nodules, small concretions often found within sediment or adhered to foraminifera tests, pose an additional source of contamination. Chemical analysis suggests they contain significant concentrations of Mg (de Lange et al., 1992). Thus elevated Mn was also used as an indicator of contamination and such samples were subjected to additional scrutiny. Of the 246 total measurements, 13 were discarded as contaminated and re-sampled.

During the cleaning protocol, 76 samples were impacted by a malfunctioning water purifying unit such that they were exposed to potentially contaminated water. Subsequent analysis of water outputted from this unit showed Ca present at 12 ppm and Mg at 5 ppm. For comparison, sample blanks consisting of ultrapure acid made from a dilution of ultrapure water from the same unit generally measure below the instrument detection limit and local tap water is measured as having 93 ppm Ca and 5.4 ppm Mg. The start time of the malfunction was unknown, and with samples left under a thin layer of water for storage between cleaning and analysis, it was possible that measurable levels of secondary carbonate, sourced from contaminated water, had been deposited onto the sample.

To ensure the removal of any secondary calcite arising from the malfunction the 76 samples were subjected to two additional leaches in 0.075 m nitric acid to remove surface carbonate which may have precipitated out of contaminated water. Eight of the samples were re-picked and re-cleaned for comparison with potentially contaminated samples. Re-measured sampled showed good agreement with potentially contaminated samples with an average offset in Mg/Ca of 0.10 mmol/mol. Subsequent measurement of the 76 contaminated samples revealed no evidence of additional contamination from other trace metals nor anomalous offsets from adjacent samples. Thus is was concluded that the malfunction either did not impact the measurements or the additional acid leach was sufficient to negate its effect.

5.3.4 Mg/Ca size fraction tests

Several species of foraminifera have been shown to exhibit variations in Mg/Ca with size fraction (Cleroux et al., 2008; Friedrich et al., 2012) as small juveniles descend in the water column and acquire a secondary layer of cooler, subsurface calcite later in their lifecycle. These findings are corroborated here with triplicate measurements of *N. pachyderma* (s) from the 212 – 250 µm and 250 – 300 µm size fractions giving rise to Mg/Ca ratios of 0.735 ± 0.02 and 0.853 ± 0.006 respectively. Thus all samples in this study were taken from as constrained a size fraction as possible that still allowed for sufficient sample to be acquired. For *G. bulloides,* the 300 – 355 µm size fraction is selected, and *N. pachyderma* (s), the 250 – 300 µm fraction.

5.3.5 Choice of Mg/Ca temperature calibration

As understanding of the Mg/Ca proxy has evolved, it has become apparent that foraminifera exhibit species-specific temperature sensitivities, giving rise to species-specific calibrations (Anand et al.,2003; Cleroux et al., 2008; Elderfield & Ganssen, 2000). For common species such as *G. bulloides*, numerous temperature calibrations now exist. Farmer et al. (2011) showed that the choice of calibration can result in inferred temperature discrepancies of several degrees in modern day North Atlantic core MD99-2251. This is further emphasised in section 3.4.2 of this study where the choice of calibration used to infer temperatures of core top samples is shown to result in temperature offsets exceeding 12 ^{o}C for the same sample.

Both this study and Farmer et al. (2011) demonstrated that the closest temperature estimates to modern day WOA values were derived from nearby cores. To this end the calibrations of Barker & Elderfield (2002) and Kozdon et al. (2009) were chosen for *G. bulloides* and *N. pachyderma* (s) respectively in core MD99-2251.

5.4 Stable isotope methodology

$\delta^{13}C$ and $\delta^{18}O$ were measured for three species, *G. bulloides* and *N. pachyderma* (s) and *G. quinqueloba*, at alternate 1 cm intervals along the 3 m section of core MD99-2251 between 20.28 m – 23.26 m. *G. bulloides* (Duplessy et al., 1993; Marchant et al., 1999) and *N. pachyderma* (s) (Obrochta et al., 2014; Simstich et al., 2003) have been widely utilised in palaeoceanography studies and are known to exhibit strong isotopic responses to environmental conditions. However, climatic extremes saw their abundances drop to near zero in core MD99-2251. In such instances it is probable that the few specimens that are present could have migrated from sites with climatic regimes wholly different to those at the core site. *G. quinqueloba* was therefore also measured as the species remained present throughout the entire 3 m section of core. The species is less widely utilised, presumably because the small size of individuals make it a time consuming species to isolate and measure, yet a limited number of studies have shown it exhibits an isotopic response to climatic variability (Simstich et al., 2003).

Table 5.3 No of species and size fractions for stable isotopic measurements in this study

Species	Size fraction (µm)	No. of specimens
G. bulloides	300 – 355	30
G. inflata	300 – 355	20
N. pachyderma (s)	250 - 300	20
N. incompta	250 - 300	30
G. quinqueloba	150+	100
Uvigerina peregrina	150+	5

Alongside MD99-2251, an additional 238 samples from core U1302 were also measured, including *N. incompta* and *G. inflata* species. Size fractions and sample sizes are given in **Table 5.3**0. To minimise potential influence off migratory planktonic species, a minimum of 20 – 30 specimens were picked and homogenised prior to measurement of large species *G. bulloides* *N. pachyderma* (s), *G. inflata*, and *N. incompta*, and a minimum of 60 for the smaller *G. quinqueloba*.

5.4.1 Sample cleaning for stable isotope analysis

There exists a huge degree of variability over how samples are prepared for stable isotope analysis. Published cleaning procedures include high temperature heating (Shackleton, 1974), chemical treatment with hydrogen peroxide and acetone washes (Shackleton et al., 1995) and ultrasonication in distilled water (Berger et al., 1993; Imbrie et al., 1973), with many studies detailing no prior cleaning at all (e.g. Marchitto et al., 2014; Wary et al., 2015).

In order to investigate the efficacy of different cleaning procedures on stable isotope measurements, the impact of two cleaning methodologies on *G. bulloides* were investigated — a rinsing protocol and Mg/Ca cleaning protocol (5.3.1). *G. bulloides* was chosen as a suitable species as its open test morphology is susceptible to capturing a high degree of sediment contamination. The two methods are described in detail below and compared against each other.

1. Rinsing protocol

Samples were gently crushed between two glass plates to break open test chambers and enable the removal of large contaminant grains under the microscope. They were then subjected to repeated ultrasonication in ultrapure water (3 x 10s) and methanol (2 x 10s). After each ultrasonication the sample was covered in ultrapure water and allowed to settle for 30s. Surfactant was then removed, along with any contaminants left in suspension. After five rinses, samples were inspected under the microscope for visual evidence of contamination and repeat rinses conducted if necessary.

The efficacy of the procedure was tested with measurement of six fossil *G. bulloides* samples from cores MD99-2251 and NEAP-18K, subjected to each stage of the rinsing protocol. Measurement variance was reduced with each additional stage of the protocol (Table 5.4), with no measureable impact on mean values.

Table 5.4 Stable isotope measurements of *G. bulloides* subjected to each stage of the stable isotope rinsing protocol. Full treatment is both the ultrapure water and methanol rinses. Uncertainties are 95 % confidence intervals.

Core	Depth (cm)	n	Treatment	$\delta^{13}C$ (‰, VPDB)	σ $\delta^{13}C$	$\delta^{18}O$ (‰, VPDB)	σ $\delta^{18}O$
MD99-2251	131	2	None	-0.35 ± 0.54	0.06	1.37 ± 0.07	0.01
		2	H2O rinse only	-0.24 ± 0.04	0.00	1.59 ± 0.53	0.06
		2	Full treatment	-0.19 ± 0.06	0.01	1.40 ± 0.44	0.05
	196	2	None	-0.26 ± 0.45	0.05	1.27 ± 0.10	0.01
		2	H2O rinse only	-0.38 ± 0.16	0.02	1.34 ± 0.29	0.03
		2	Full treatment	-0.41 ± 0.70	0.08	1.45 ± 0.12	0.01
	260	2	None	-0.39 ± 2.12	0.24	1.19 ± 1.91	0.21
		2	H2O rinse only	-0.62 ± 0.39	0.04	1.37 ± 0.45	0.05
		1	Full treatment	-0.35 ± 0.1		1.48 ± 0.1	
NEAP 18K	600	2	None	-0.55 ± 0.12	0.01	1.37 ± 0.51	0.06
		2	H2O rinse only	-0.66 ± 1.71	0.19	1.22 ± 0.65	0.07
		2	Full treatment	-0.81 ± 0.07	0.01	1.24 ± 0.16	0.02
	632	2	None	-0.57 ± 0.32	0.04	1.43 ± 0.25	0.03
		2	H2O rinse only	-0.71 ± 1.14	0.13	1.47 ± 0.18	0.02
		2	Full treatment	-0.85 ± 0.19	0.02	1.28 ± 0.36	0.04
	660	2	None	-1.23 ± 0.35	0.04	0.96 ± 0.51	0.06
		2	H2O rinse only	-1.03 ± 1.09	0.12	0.89 ± 0.56	0.06
		2	Full treatment	-1.03 ± 1.30	0.15	0.95 ± 0.70	0.08
			Average σ, no treatment		**0.07**		**0.06**
			Average σ, H2O rinse only		**0.08**		**0.05**
			Average σ, full treatment		**0.05**		**0.04**

2. Mg/Ca cleaning protocol

A second treatment investigated the use of the Mg/Ca cleaning procedure. Detailed methodology is outlined in section 3.5.2. 57 *G. bulloides* and 48 *N. pachyderma* (s) were prepared in such a fashion for Mg/Ca analysis prior to a small quantity being removed and dried overnight for stable isotope analysis. The same samples were cleaned using the rinsing protocol and both sets measured for comparison. Results are presented in Figure 5.6.

Considerable offset is seen in $\delta^{18}O$ between the two methodologies, with erroneously high values obtained from the Mg/Ca protocol. This finding is in contrast to those of Skinner & Elderfield (2005) who measured no offset between the two methodologies. It is possible that sample fractionation may arise during the dilute acid leach involved in the Mg/Ca cleaning protocol. However, any fractionation would have to be considerable to cause such dramatic shifts $\delta^{18}O$, and this seems unlikely given the short (60 seconds) contact time between acid and sample, and the weak acid concentration (0.075 m).

More likely, the offset arises from a contaminant derived from the Mg/Ca cleaning protocol. Trace nitric acid appears the most likely candidate, being used in small quantities in the acid leach stage of the cleaning protocol and for pipette tip cleaning. Should nitric acid enter the mass spectrometer source, it is likely to form NO_2, predominantly of mass 46 – which would be observed as a sizeable increase in the $\delta^{18}O$ measurement. A considerable memory effect observed between the Mg/Ca cleaned samples, further supports the notion of a contaminant remaining within the mass spectrometer system between samples.

In light of the erroneous $\delta^{18}O$ values measured in samples subjected to the Mg/Ca cleaning protocol, and the reduced variability of samples subjected to the rinsing protocol, the decision was taken to adopt the latter method for use in this study. All *N. pachyderma* (s) and *G. bulloides* samples from core MD99-2251 were pre-cleaned for stable isotope analysis using this procedure. Less robust *G. quinqueloba* samples were subjected to a single 5s rinse each of ultrapure water and methanol to minimise sample loss from fragmentation of the thinner walled species. U1302 samples are analysed as infills to complement a previously produced stable isotope record (Hillaire-marcel et al., 2011; Hume, 2018) in which samples were cleaned via heating to 250 ^{o}C under vacuum prior to stable isotope analysis. In the absence of facilities to conduct this protocol, no prior treatment was applied to the U1302 samples.

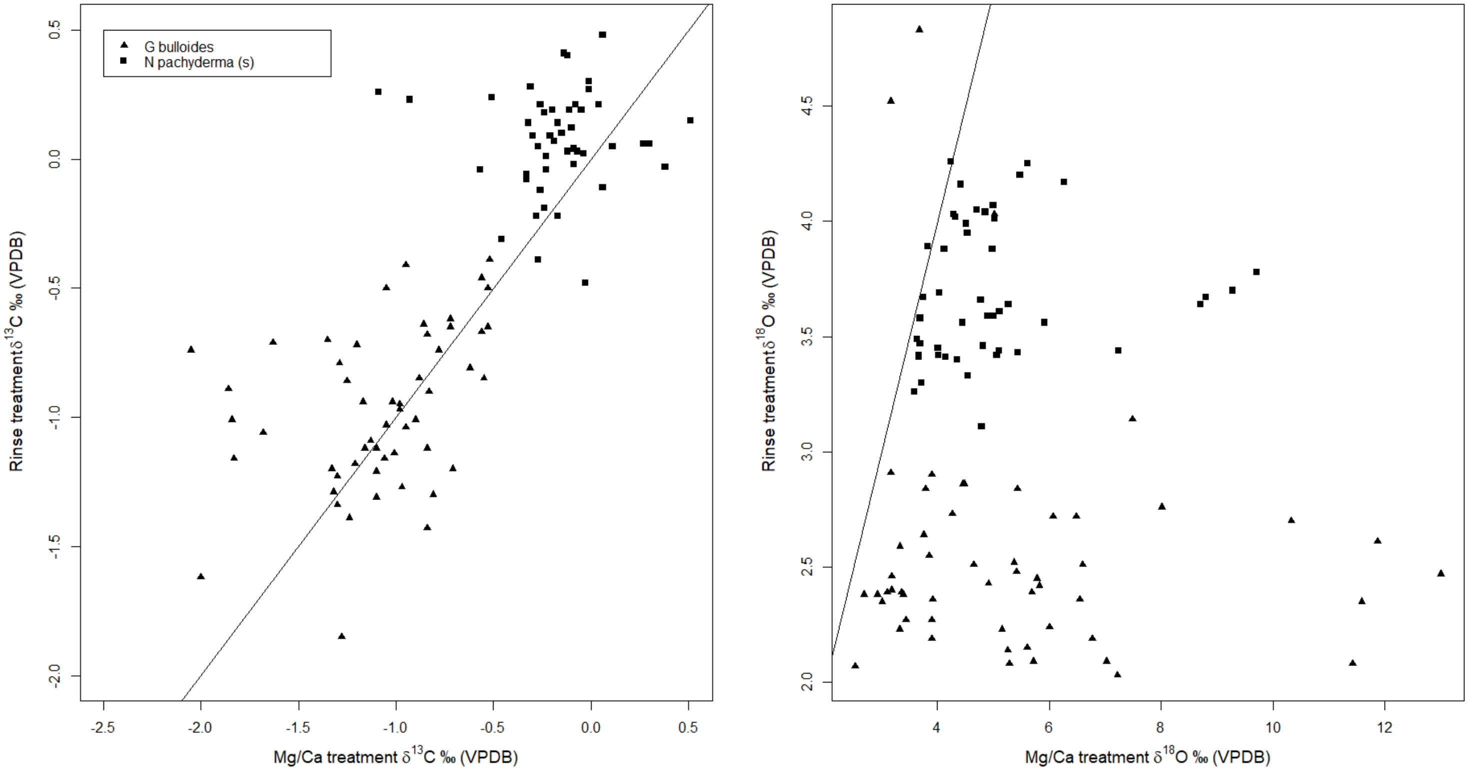

Figure 5.6 Left) δ^{13}C comparison of samples prepared using the rinse method and Mg/Ca method. Right) δ^{18}O comparison of samples prepared using the rinse method and Mg/Ca method. Solid line is 1:1 line

5.4.2 Stable isotope IRMS analysis

Stable isotope measurements were conducted on the VG SIRA Series II isotope-ratio-mass-spectrometer in the Stable Isotope Laboratory at the University of East Anglia. The instrument is fitted with a Europa instruments pinta-bloc micro duel-inlet system. 60-80 µg samples are reacted in a common 102 % phosphoric acid bath. Each instrumental cycle of 47 samples contained 7 UEACMST standards with a long term standard deviation of 0.08 ‰ for both $\delta^{13}C$ and $\delta^{18}O$.

Chapter 6. A high resolution multiproxy glacial record of core MD99-2251 from the Gardar Drift

6.1 Introduction and background

6.1.1 MD99-2251 site description

Core MD99-2251 (57°26.87’N, 27°54.47’W, 2620 m depth) was obtained from the southern extent of the Gardar Drift – a 1100km long sedimentary body running NE-SW from the Icelandic Margin to the Charles Gibbs Fracture Zone (Bianchi & McCave, 2000). The surrounding North Atlantic region plays a major role in driving the global thermohaline circulation through formation of North Atlantic Deep Water (NADW). The thermohaline circulation is known to have fluctuated with both the millennial-scale climatic fluctuations of the Greenland stadials (Boyle, 2000; Wary et al., 2015) and the glacial cycles of the Pleistocene (Hodell et al., 2009; Lynch-Stieglitz et al., 2007) (See chapter 4 for a detailed overview). Yet much uncertainty remains as to its strength and configuration compared with the modern day and whether the oceans acted as a driver of global climatic change or simply responded to the wider climatic conditions. Further study of the region can help answer such questions and inform future climate projections as a melting Arctic, and changes in high latitude precipitation patterns, inject freshwater into deepwater formation zones with uncertain consequences.

Surface ocean circulation in the region is dominated by convection of warm, saline North Atlantic Current (NAC) waters from the Subpolar Gyre northeast through the Icelandic Basin and into the Nordic Seas. The NAC branches into the Subarctic Front and Central Iceland Basin Current as it moves northward (Brambilla & Talley, 2008) and it is the latter of these which influences the MD99-2251 site as it travels on the Eastern Flank of the Reykjanes Ridge (Farmer et al., 2011). This current splits again, at 26W — south of Iceland — with a portion travelling west as the East Reykjanes Ridge Current, where it eventually joins the Irminger Current, and the remainder continuing northward to join other branches of the NAC (Bower & Richardson, 2002; Brambilla & Talley, 2008; Farmer et al., 2011; Lavender et al., 2005) (Figure 6.1).

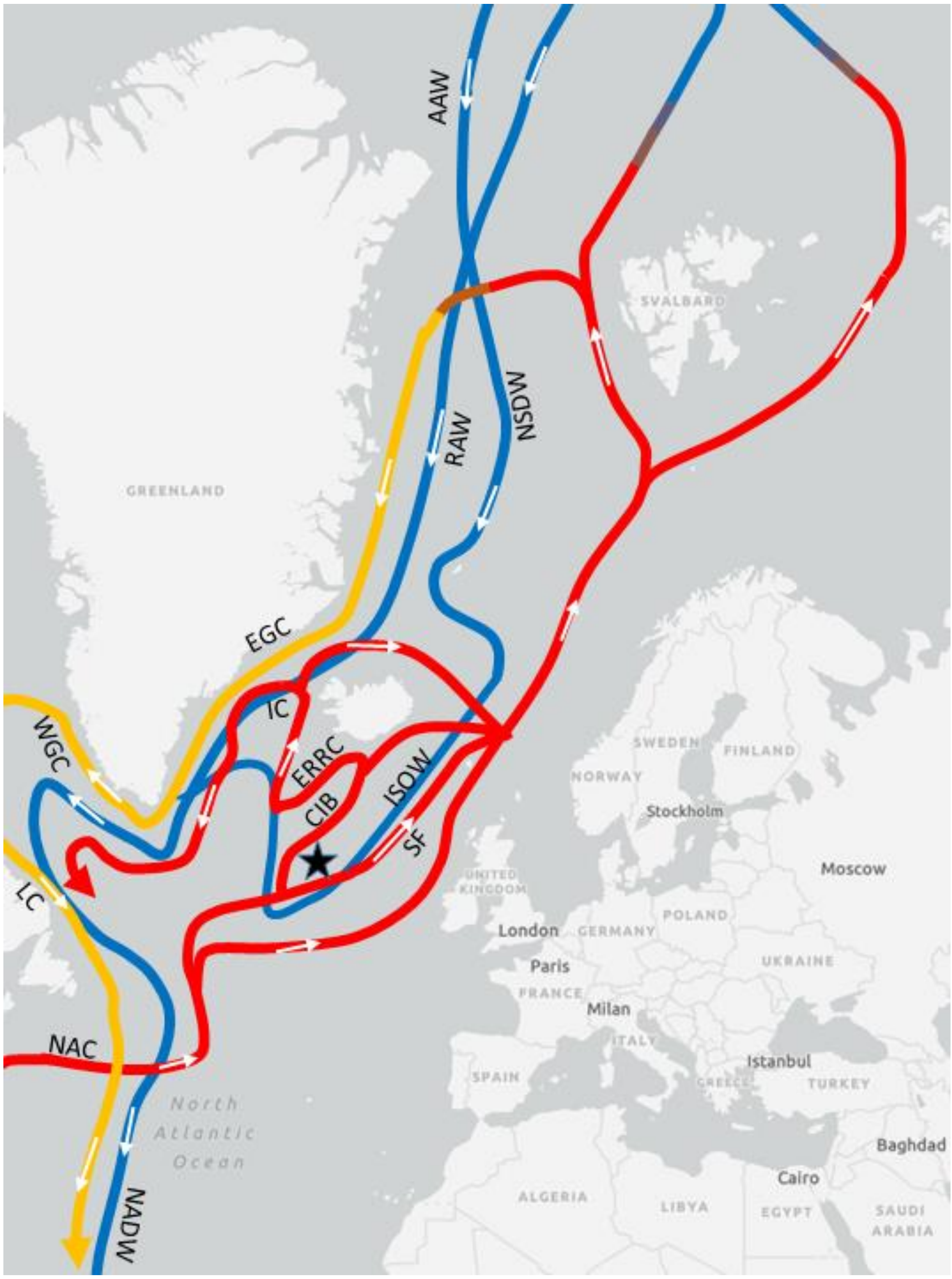

Figure 6.1 Major currents of the modern day North Atlantic. The star marks the MD99-2251 coring site. Warm surface currents are in red, deep water currents in blue. North Atlantic Current (NAC), Central Iceland Basin Current (CIB), Subarctic front (SF), East Reykjanes Ridge Current (ERRC,) Irminger Current (IC,) Norwegian Sea Deep Water (NSDW), Arctic Atlantic Water (AAW), Return Atlantic Water (RAW), Iceland-Scotland Overflow Water (ISOW), East/West Greenland Current (EGC/WGC), LC (Labrador Current), North Atlantic Deep Water (NADW).

As it continues north the current again branches into three with one branch travelling north-east through the Barents Sea, a second entering the Arctic Ocean and a third flowing west through the Fram Strait (Mauritzen, 1996). The latter of these currents remains largely unperturbed as it retroflects and travels south with the East Greenland Current (Mauritzen, 1996). The other two water masses continue north, gaining density through heat exchange with the atmosphere and downwell before returning south. The Arctic water mass passes along the Greenland margin as Arctic Atlantic Water, the deepest component of the East Greenland Current. The final branch subducts under polar waters in the Arctic Ocean and travels south as Norwegian Deep Sea water (Mauritzen, 1996). Following mixing with other water masses as it crosses the Scotland-Iceland Ridge, Norwegian Deep Sea Water becomes Iceland-Scotland-Overflow Water (ISOW) (Bianchi & Mccave, 2000; Mauritzen, 1996; Van-Aken & Becker, 1997) and passes directly over the Gardar Drift on its southerly journey.

6.1.2 The North Atlantic during glaciations

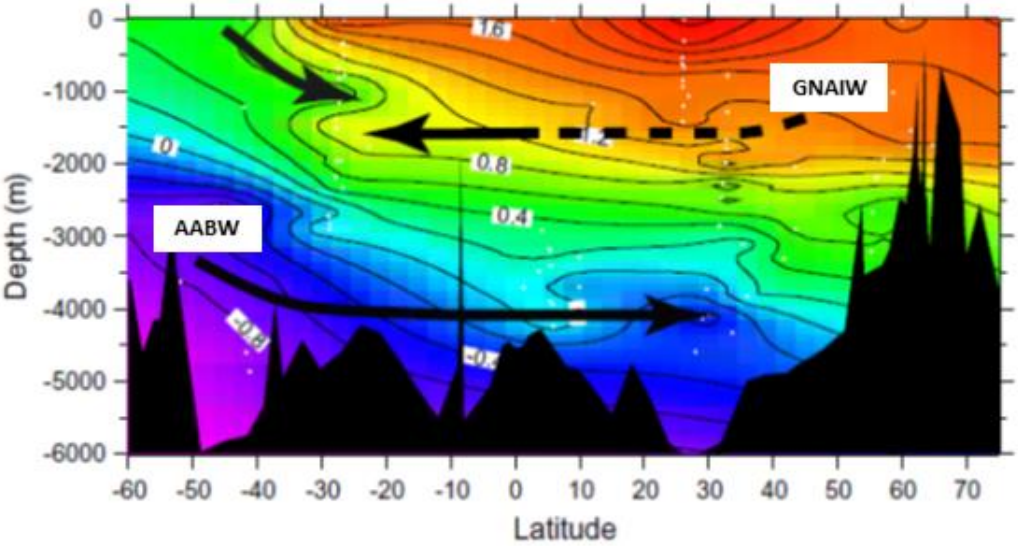

Figure 6.2 West North Atlantic Water masses at the last glacial maximum. Numbers are average $\delta^{13}C$ compositions in ‰ VPBD. (Adapted from Curry & Oppo (2005))

$\delta^{13}C$ reconstructions from the Last Glacial Maximum (LGM) suggest that the AMOC underwent significant reconfiguration during the last glacial (see section 4.2 for further detail). The Norwegian Sea ceased to be the dominant region of North Atlantic Deepwater (NADW) formation as it is today, with downwelling sites moving south of the Greenland-Scotland Ridge (Duplessy et al., 1988). Rapid $\delta^{13}C$ reduction with depth suggests that the North Atlantic was highly stratified (Oppo & Lehman, 1993). NADW was replaced by the shallower Glacial North Atlantic Intermediate Water (GNAIW) above 2000 m. Below this southerly sourced Antarctic

Bottom Water penetrated as far north as 60 +°N (Curry & Oppo, 2005; Lynch-Stieglitz et al., 2006) (Figure 6.2).

6.1.3 Justification for the study

MD99-2251 sits between the main IRD belt (Ruddiman, 1977) and Greenland-Scotland Ridge, a region recently highlighted by Rasmussen et al. (2016) as worthy of further investigation given its proximity to the glacial ice sheet extent whilst still representing open ocean (Figure 6.3). The region sits close to the boundary between Greenland and Antarctic influenced glacial climatic regions (Rasmussen et al., 2016). North of MD99-2251, in the Nordic Seas, abrupt warming and gradual cooling is observed in phase with the Greenland ice cores (Bond et al., 1993; Rasmussen et al., 1996). South of the core site, in the mid latitudes, more ‘gradual’ responses are observed, similar to the changes seen in the Antarctic ice cores (Charles et al., 1996; Sachs & Lehman, 1999).

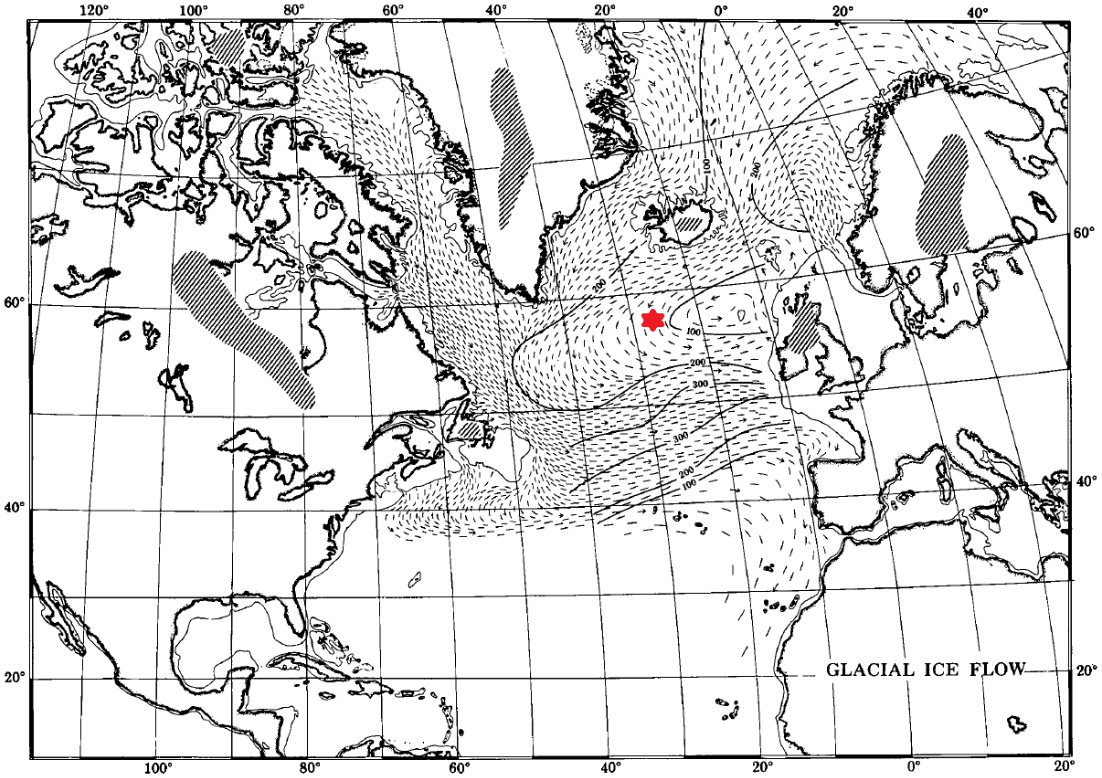

Figure 6.3 Inferred mean free paths of distribution of IRD during glacial intervals. Numbers are mean depositional rates of ice rafted sand (mgcm^{-2}yr^{-1}). Red star marks the position of MD99-2251 (adapted from Ruddiman, 1977).

The offsets between Nordic Sea and mid-latitude cores are generally attributed to changes in the AMOC and the resultant impact on heat transfer. However, the causal mechanism of the alteration, and the nature of the various operational states, remains debated. Hypotheses include changes in current strength (Bond et al., 1993; Shackleton et al., 2000), changes in sea-ice extent (Li et al., 2010), shifts in deep-water formation location (Bohm et al., 2015), variations in continental ice sheet height (Zhang et al., 2014) and meltwater discharge (Menviel et al., 2014).

The MD99-2251 site is influenced by both the warm surface North Atlantic current components and the cool subsurface ISOW return flow. Better understanding of the region during glacial episodes can help improve understanding of the response of the AMOC over long periods and during short lived D/O cycles.

6.2 Core description

MD99-2251 is a calypso core collected in 1999 aboard the Marion Dufresre during the Images V cruise (Gherardi & Labeyrie, 1999). The site had previously been identified during Charles Darwin Cruise 88 as a potential target for a thick Holocene sedimentary layer (McCave, 1994). Interaction of Iceland-Scotland Overflow Water (ISOW) — which transports large volumes of sediment from Iceland and the northwest European landmass (Revel et al., 1996) — with seafloor topology, results in exceptionally high sedimentation rates. Thus when the Images V cruise returned five years later with the aim of acquiring cores capable of inferring changes in the Gulf Stream at a resolution comparable to the instrumental record (Gherardi & Labeyrie, 1999), the site was an obvious target.

Physical properties (p-wave velocity, bulk density and magnetic susceptibility) were recorded at 2 cm intervals on ship. Spectrographic data was recorded every 5 cm. The 36.58 m long core consists of silty clay of uniform grain size, shifting from an olive grey at the core-top to brown at the base (Szeremeta et al., 2004) and spanning a period from MIS 5c to the late Holocene (Miller et al., 2011). Mean accumulation of 110 cm ky^{-1} in some Holocene sections (Ellison et al., 2006) is more than sufficient to recover decadal resolution.

6.3 Context with previous MD99-2251 work

Much analysis has been conducted upon MD99-2251 with *N. pachyderma* (s) abundance, stable isotope, sortable silt size (Ellison et al., 2006), Mg/Ca (Farmer et al., 2008; Farmer et al., 2011b) and IRD (Miller et al., 2011) data published for Holocene sections of the core. This data is not considered as part of this study. Tephra layers, identified during IRD counts of MD99-2251, have been previously published as part of a chronostratigraphic framework (Abbott et al., 2018), some of which are used in this study to aid with dating.

Table 6.1 Summary of pre-Holocene data for core MD99-2251

	Number of samples	**Total coverage (m)**	**Resolution**	**Depths (m)**
Assemblage counts	This study 182	9.44 – 35.74	10 cm	9.44 – 14.94
	Additional 434		2 cm	14.96 – 23.37
	Total 616		5 – 10 cm	23.47 – 35.74
IRD counts	This study 182	15.34 – 35.74	10 cm	15.34 – 16.34
	Additional 316		2 cm	16.34 – 23.27
	Total 500		5-10 cm	23.47 - 35.74
Mg/Ca	This study 218 **Total 218**	14.44 – 23.26	six measurements at key transitions	15.44 – 20.20
			2 cm (multiple species at single depth)	20.20 – 23.26
Stable isotopes	This study 376	15.18 – 20.20	2 cm	15.18 – 16.24
	Additional 130		10 cm	16.28 – 20.20
	Total 506		2 cm (multiple species at single depth)	20.20 – 23.26
Clumped isotope measurements	This study 13 **Total 13**	15.86 – 22.82	samples at key transitions	15.86 – 22.82

A new multiproxy (assemblages, IRD, Mg/Ca, stable/clumped isotope) analysis of a ~3 m section of the core between depths 20.20 m and 23.36 m is presented here. An additional 32 assemblage and IRD counts were conducted to fill gaps in the existing full core record as well as six Mg/Ca measurements and 13 clumped isotope measurements at key climatic intervals. This new data is presented alongside additional unpublished foraminifera assemblage and IRD counts, as well as stable isotope data conducted by Mark Chapman, Leila Hume and Christopher Ellison at the University of East Anglia. A summary of new and existing data used in this study is found in Table 6.1.

6.4 Foraminifera assemblages and stratigraphic zoning

Downcore percentage abundances for major species (abundance > 5 %) are presented in Figure 6.5. Cluster analysis identified 29 statistically significant stratigraphic zones within the sequence. For ease of interpretation, this number was reduced with a dispersion threshold (See section 5.2.3 for methodology). Figure 6.4 shows the MD99-2251 downcore dendogram that illustrates the hierarchical relationship between samples. 12 major clusters were created using a height cut off of 90. When plotted onto the downcore percentage abundances, this encapsulates the dominant stratigraphic transitions. Six primary zones were identified, with zone 5 subdivided a further seven times (5a – 5g). The zones represent major climatic regimes. Transitions between the zones were aligned with chronologically constrained records such as NGRIP to infer a reliable age model for the core (section 6.5.1).

Palaeotemperatures were inferred via the modern analogue technique (section 5.2.4) for all 616 downcore assemblages. Results are presented alongside assemblages in Figure 6.5.

Zone 1 (3754 (base of analysed section) to 2982 cm)

Zone 1 is characterised by a gradual shift from assemblages dominated by temperate-dwelling species (*G. bulloides*, *G. quinqueloba* and G. *glutinata*) towards an increasing prevalence of colder dwelling *N. pachyderma* (s). MAT-derived temperatures remain relatively constant throughout with an average of 9.1 ^{o}C – a few degrees cooler than the modern day SST.

The zone exhibits a high degree of variability, switching between *G. bulloides*, *N. pachyderma* (s) and *G. quinqueloba* as the dominant species. Three relatively short-lived cold excursions are observed at 4484 – 3474 cm, 3354 cm and 3205 – 3195 cm; signified by a rapid switch to *N. pachyderma* (s) dominated regimes. These excursions are reflected in the MAT-derived temperature, which drops below 4.5 °C during each excursion.

Table 6.2 MD99-2251 stratigraphic clusters. See section 6.5 for age model details.

Zone	Start depth (cm)
6	1569
5g	1721
5f	1769
5e	1837
5d	1901
5c	1949
5b	2005
5a	2133
4	2425
3	2750
2	2982
1	3574 (base of analysis)

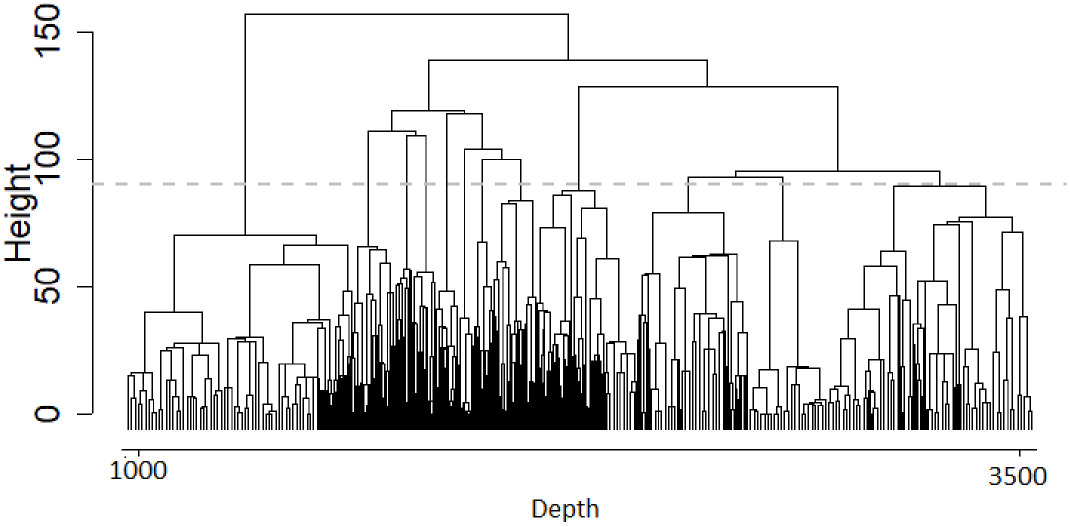

Figure 6.4 Dendogram for MD99-2251 downcore assemblage counts. Horizontal dashed line shows a dispersion threshold of 90. Observations that are joined together below this line are grouped into 12 clusters.

Zone 2 (2982 cm – 2750 cm)

Zone two exhibits a gradual increase in *N. pachyderma* (s) from around 60 % abundance to a near total-dominance at 2796 cm (94.5 %). This is reflected in MAT temperatures which reach a minimum of 3.3 °C. The top of the zone is marked by a sudden and dramatic decline in *N. pachyderma* (s) as the assemblages transition from cold to temperate dominated species.

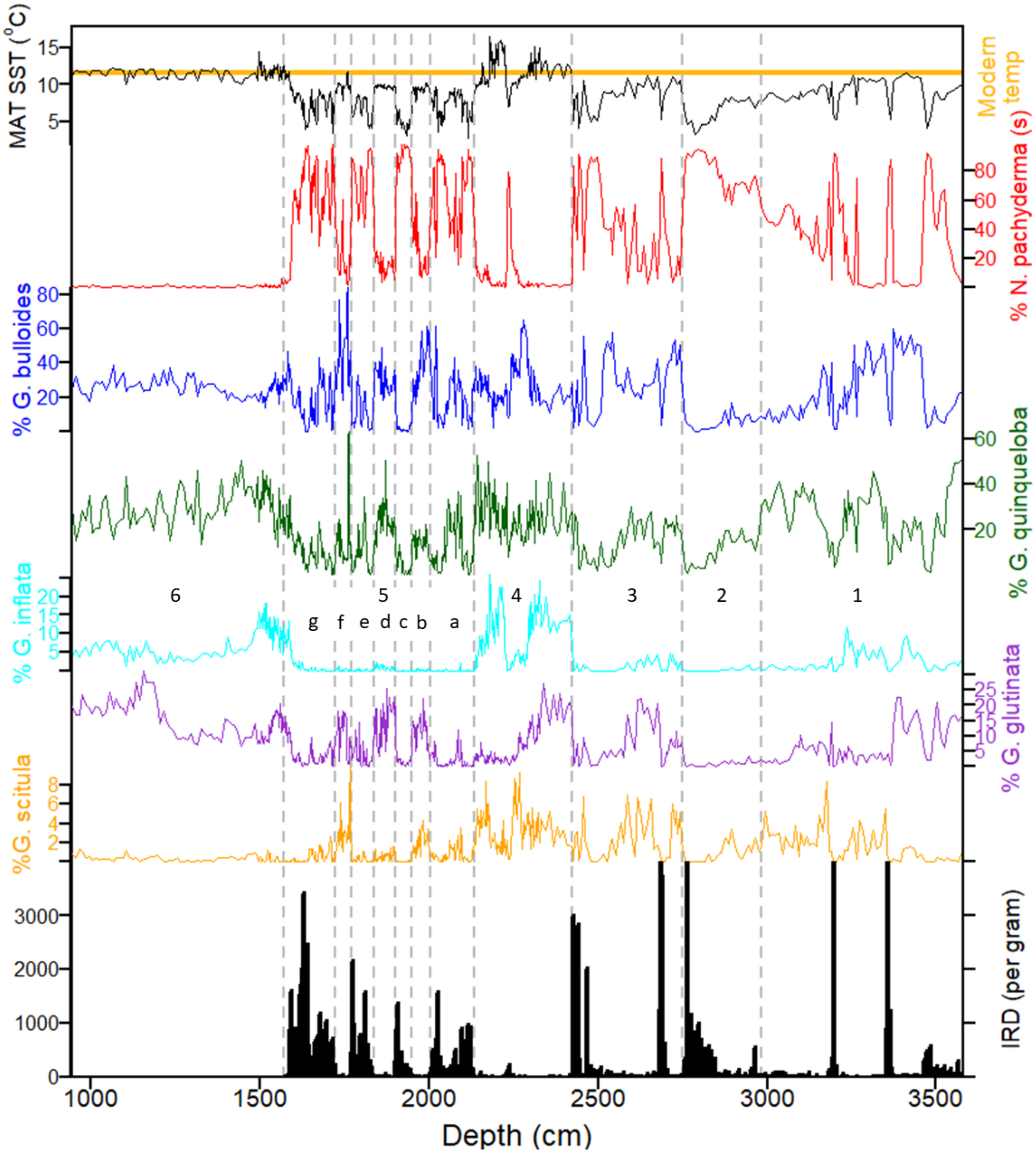

Figure 6.5 MAT-derived temperature and percentage abundances of major species (>5 %) for core MD99-2251. Vertical hyphenated grey lines are boundaries between stratigraphic zonation.

Zone 3 (2750 cm – 2425 cm)

A high degree of variability is observed in zone 3 with the dominant species switching between *G. bulloides* and *N. pachyderma* (s) on three occasions. *G. bulloides* abundance fluctuates inversely with *N. pachyderma* (s) between 3 % – 55 % and *N. pachyderma* (s) between 3 % and 90 %. *N. pachyderma* (s) peaks occur at 2691 – 2686 cm, 2507 – 2467 cm and 2452 – 2442 cm, dropping to MAT SST temperatures below 5.5 ^{o}C on each occasion, down from the zonal average of 9.6 ^{o}C (excluding periods of cold excursion). G. *glutinata* and *G. quinqueloba* both decrease from 20 – 30 % abundance at the base of the zone to below 10 % at the top.

The transition into zone four is marked by a sudden decrease in *N. pachyderma* (s) from 83.2 % abundance at the top of zone 3 to just 2 % at the base of zone 4.

Zone 4 (2425 cm – 2133 cm)

Zone 4 is characterised by near-zero abundance of *N. pachyderma* (s) throughout, aside from a relatively short-lived cold excursion between 2244 and 2232 cm, where abundances peak at 79 %. At the start of the zone *G. bulloides*, *G. quinqueloba*, *G. inflata* and *G. glutinata* are all present in roughly equal proportions between approximately 15 – 20 %. Levels of *G. bulloides*, *G. inflata* and G. *glutinata* drop dramatically during the cold excursion with *G. inflata* and *G. bulloides* quickly recovering thereafter, but *G. glutinata* levels remain suppressed. The transition into zone 5 is again marked by a sharp shift in *N. pachyderma* (s) from ~13 % at the top of zone 4 to 89 % at the base of zone 5.

Zone 5 (2133 cm – 1569 cm)

Zone 5 is characterised by a high degree of variability with seven subdivisions (5a – 5g) representing the dramatic switching in *N. pachyderma* (s) between approximately 5 % and 80 % abundance. *G. bulloides*, *G. glutinata* and *G. quinqueloba* show a similar level of variability, fluctuating between 0 – 60 %, 0 – 20 % and 0 – 40 % respectively between the cold and temperate extremes. *G. inflata* abundances remain low throughout. MAT temperatures fluctuate between 4.5 ^{o}C – 9 ^{o}C in the cold and warm extremes.

Zone 6 (1569 – 994 cm (top of analysed section))

Zone 6 marks the transition into relative stability toward the top of the core. *N. pachyderma* (s) abundance declines to near-zero with temperate species *G. bulloides*, *G. quinqueloba* and *G. inflata* present at stable abundances between 40 – 60 %, 20 – 50 % and 5 – 15 % respectively. *G. glutinata* increases from ~ 10 % at the base of the section to ~ 20 % at 1564 cm.

6.5 Age model

6.5.1 MD99-2251 chronology

An age model for the upper ~15 m of core has been established previously with 23 accelerator mass spectrometer ^{14}C dates (Ellison et al., 2006) and converted to calendar ages using the CALIB program (Stuiver et al., 1998). The dates that fall within the section of core analysed in this study were reanalysed by Mark Chapman using the Bchron calibration package available in the statistical software R. Bchron performs calibration of radiocarbon dates and age-depth modelling by utilising the algorithm of Haslett & Parnell (2008).

For archives extending beyond the radiometric timeframe, establishing reliable chronological models is hindered by a lack of suitable dating techniques. In marine archives this is generally overcome with orbital tuning approaches (*e.g.* Berger & Jansen, 1994; Imbrie et al., 1984). The LR04 benthic stack (Lisiecki & Raymo, 2005) — a collection of 57 globally distributed stable isotope records from benthic foraminifera, chronologically aligned using a mathematical model of global ice volume driven by insolation forcing — has become the standard against which new marine chronologies are aligned. This record has recently been updated by Lisiecki & Stern (2016) to form the LS16 record, expanding the library of cores to 263 and deriving regional, as well as global, reference chronologies.

Since the MD99-2251 record comprises predominantly of planktonic foraminifera derived proxies, alignment with the North Greenland Ice Core Project (NGRIP) record (Rasmussen et al., 2014) was considered a more suitable approach, overcoming lag issues which might arise from alignment of the MD99-2251 surface record with the LS16 benthic record. In addition, the LS16 record lacked the sampling resolution to elucidate many of the centennial scale climatic fluctuations apparent in the MD99-2251 record. Using major climatic transitions as tie points to the Greenland ice core record is a widely applied technique for dating marine records (e.g. Austin et al., 2012; Shackleton et al., 2000). Whilst the relatively close geographical proximity of MD99-2251 to Greenland suggest that lag effects between the two sites will be minimal, it should be noted the method eliminates possible insights into lag times and climatic inertia between the sites that might arise from comparison of independently dated records.

The foraminifera assemblage zones outlined in section 6.4 were assumed to mark distinctive climatic regimes at the MD99-2251 site and thus the transitions between zones were aligned with major transitions in the NGRIP 50 year average $\delta^{18}O$ record (Rasmussen et al., 2014). The chronology was further fine-tuned using the MD99-2251 *N. pachyderma* (s) percentage abundance record which was aligned with high-magnitude fluctuations in the NGRIP record. A further tie point was obtained from a tephra layer at 2014 cm which was attributed to North Atlantic Ash Zone II (Svensson et al., 2008). Such layers are becoming increasingly utilised to provide chronological time stamps by alignment to their appearance in the Greenland ice core record (Davies et al., 2014b). A final tie point was used at the MIS 3/4 transition at 59 ka (Siddall et al., 2008), creating a total of 33 tie points. Ages between tie points were calculated by applying a linear interpolation, assuming constant sedimentation rate. A summary is given in Table 6.3.

Table 6.3 Tie points used to create the MD99-2251 chronology. NGRIP data taken from Rasmussen et al. (2014), Ash Zone II from Svensson et al. (2008) and MIS 3/4 transition from Siddall et al. (2008) and ^{14}C date recalibrated from Ellison et al. (2006). All dates are corrected to a baseline of 1950. GI = Greenland interstadial, GS = Greenland stadial.

Assemblage zone	Zone depth	Tie point depth (cm)	Reference tie point	Calendar Age (ka)	Error (yrs)
		944	Recalibrated existing 14C date	5.75	
		1034	Recalibrated existing 14C date	6.8	
		1094	Recalibrated existing 14C date	7.1	
		1224	Recalibrated existing 14C date	8.29	
		1284	Recalibrated existing 14C date	9.07	
		1364	Recalibrated existing 14C date	9.5	
		1474	Recalibrated existing 14C date	10.2	
		1534	Recalibrated existing 14C date	10.63	
6	1569 -	1594	NGRIP End of Younger Dryas/ start of the Holocene	11.65	100
		1622	Start of GI 1e	14.8	200
		1634	GS 2.2	23.1	600
		1674	GI 4	28.65	900
		1706	GI 5.2	32.3	1150
5g	1721 - 1569	1738	Start of GI 7c	35.4	1350
5f	1769 - 1721	1766	Start of GI 8c	38.2	1500
		1790	Start of GS 10	41	1650
		1812	Start of GI11	43.35	1750
5e	1837 -1769	1836	Start of GS12	44.38	1800
5d	1901 - 1837	1898	Start of GI12C	46.86	1950
5c	1949 - 1901	1950	Start of GS 13	48.4	2000
5b	2005 - 1949	1996	GI 14c	53.9	2300
		2014	North Atlantic Ash zone II	55.33	1190
		2022	MIS 3/4 transition	59	
5a	2133 - 2005	2132	Start of GS 19.2	70.35	
		2226	Start of GI 19.2	72.3	
		2260	Start of GS 20	74.05	
4	2425 - 2133	2422	Start of GS 20c	76.4	
		2507	Start of GS 21.1	77.7	
		2681	Start of GI 21.1e	84.76	
		3185	Start of GI 23.1	103.95	
		3454	Start of GI 24.2	108.26	
		3544	Start of GS 25	110.64	

6.5.2 Sedimentation

Sedimentation rates were calculated at 2 cm intervals down the core and are presented in Figure 6.6. Extremely high rates, in excess of 50 cm ka^{-1} at the end of MIS 5, were comparable to those found in nearby core U1304 (~40 cm ka^{-1}) (Hodell et al., 2009) — situated on the southerly extent of the Gardar drift, some 600 km southwest of the MD99-2251 site (Figure 6.14). This incredibly high sedimentation rate allowed proxy reconstructions on centennial timescales. Sedimentation remains relatively high (between 20 – 40 cm ka^{-1}) until the transition into MIS 4. In the highest sampled region, between 80 – 70 ka, decadal resolution was achieved. Sedimentation declines dramatically to below 10 cm ka^{-1} between MIS 4 – 2. Similar rates, between 9 – 12 cm ka^{-1}, are found at ODP site 983, 400km northeast of MD99-2251 during the same interval (Channell et al., 1997).

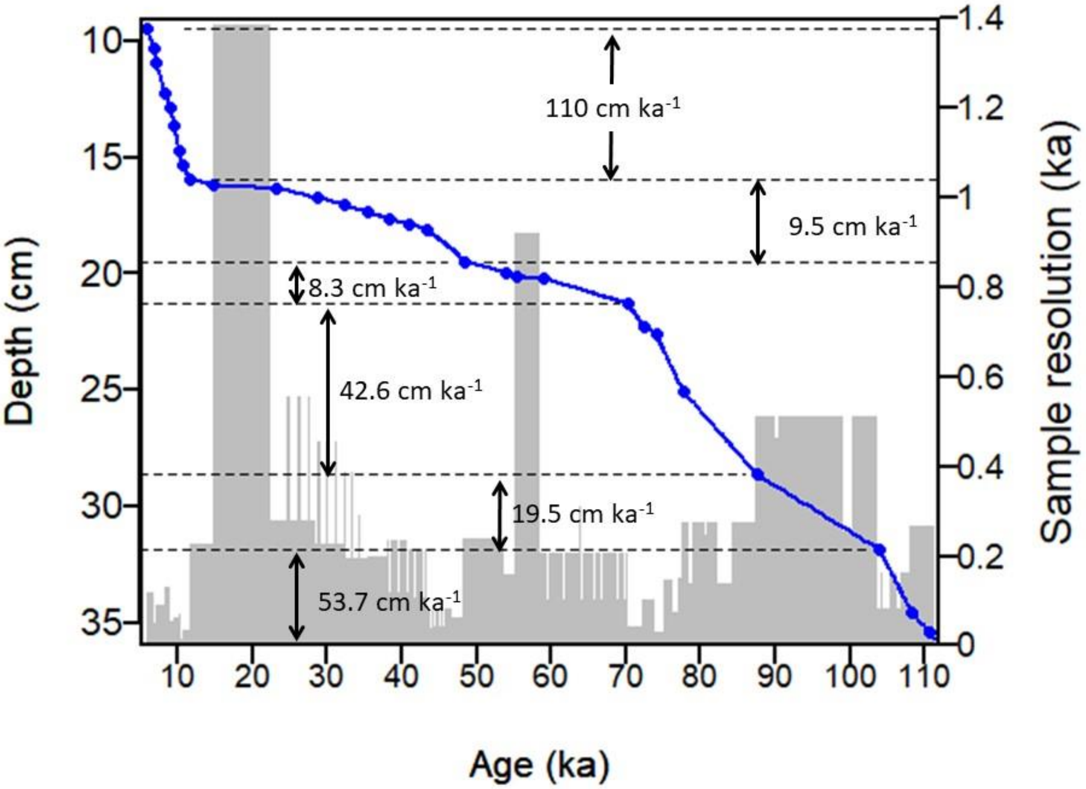

Figure 6.6 Sedimentation rate in core MD99-2251. Sample resolution is shown by the grey histogram.

A sedimentation minimum of just 1.4 cm ka^{-1} is reached at 23.1 ka, which continues through the LGM until 14.8 ka. At such low sedimentation rates, only millennial-scale sampling resolution was achievable. From the start of the Holocene at 11.65 ka (Rasmussen et al., 2014), the sedimentation rate increases dramatically, fluctuating between 60 and 130 cm ka^{-1}. For the highest deposition rate period between 11.65 – 10.63 ka, sampling resolution as frequent as every 15 years was achieved, comparable with the most high-resolution North Atlantic core studies (Bond et al., 2001) and is sufficient to allow detailed study of centennial scale climatic fluctuations.

6.5.3 Comparison with NGRIP and MD95-2042 records

The MD99-2251 *N. pachyderma* (s) percentage abundance record is presented alongside δ^{18}O records from NGRIP (Rasmussen et al., 2014) and core MD95-2042 from the Iberian margin (Shackleton et al., 2004) in Figure 6.7. *N. pachyderma* (s) percentage abundance was used in preference to δ^{18}O since it offers the highest resolution and most continuous proxy record within the MD99-2251 archive. MD95-2042 offers exceptionally high resolution and a well constrained age model, obtained from multiple radiocarbon dates in the recent past, and correlation to independently dated speleothem records further back in time (Shackleton et al., 2004). As such it has become a standard against which many sedimentary records are correlated (Hodell et al., 2008) and compared (Tzedakis et al., 2002). The MD95-2042 chronology was aligned with MD99-2251 for this study by Mark Chapman by tying the MD95-2042 *G. bulloides* δ^{18}O record to NGRIP. This allows direct comparison between the two cores.

The peak and trough pattern of the Greenland stadial (GS) and interstadial (GI) events can clearly be seen in the MD99-2251 record with the majority of fluctuations apparent (Figure 6.7). Alignment of numerous δ^{18}O excursions in both the Greenland and MD99-2251 record in-between tie points, such as GS 14 and GS 24.2, gives additional confidence in the age model. However, the MD99-2251 record lacks the resolution to identify many of the decadal scale excursions seen within the ice cores, such as GS 3 and interstadial events between GI 15.2 and GI 20a. Many of the more recent GI spikes that are missing in MD99-2251 are apparent in the higher resolution MD95-2042 record, suggesting that their absence in MD99-2251 is the result of insufficient resolution rather than the event being localised to Greenland.

It is interesting then that the earlier GI events between GI15.2 and GI 20a are less pronounced in the MD95-2042 record. However, because these events are very short lived (decadal in timeframe), it is uncertain whether their absence is a result of insufficient resolution or a suppressed climatic signal in the North Atlantic. Certainly climatic transitions appear less abrupt in the oceanic record compared with the ice core, as is most evident in the transitions between GS 19.1 and GS 18. GI 19.1 is observed as a short lived-spike between relatively stable stadial episodes in the Greenland record. A much more prolonged event is observed in the sediment.

Isotopic fluctuations within the MD95-2042 benthic record exhibit a more muted response than the planktonic records. Shackleton et al. (2000) contrasted the ‘square-wave’ like response observed in the planktonic record with the ‘triangular’ benthic form and suggested the dissimilarity arose because the benthic record reflected changes in ice volume compared with a Greenland temperature response in the planktonic. The benthic record was found to closely resemble the surface temperature record over Antarctica, likely a driver of global ice volume.

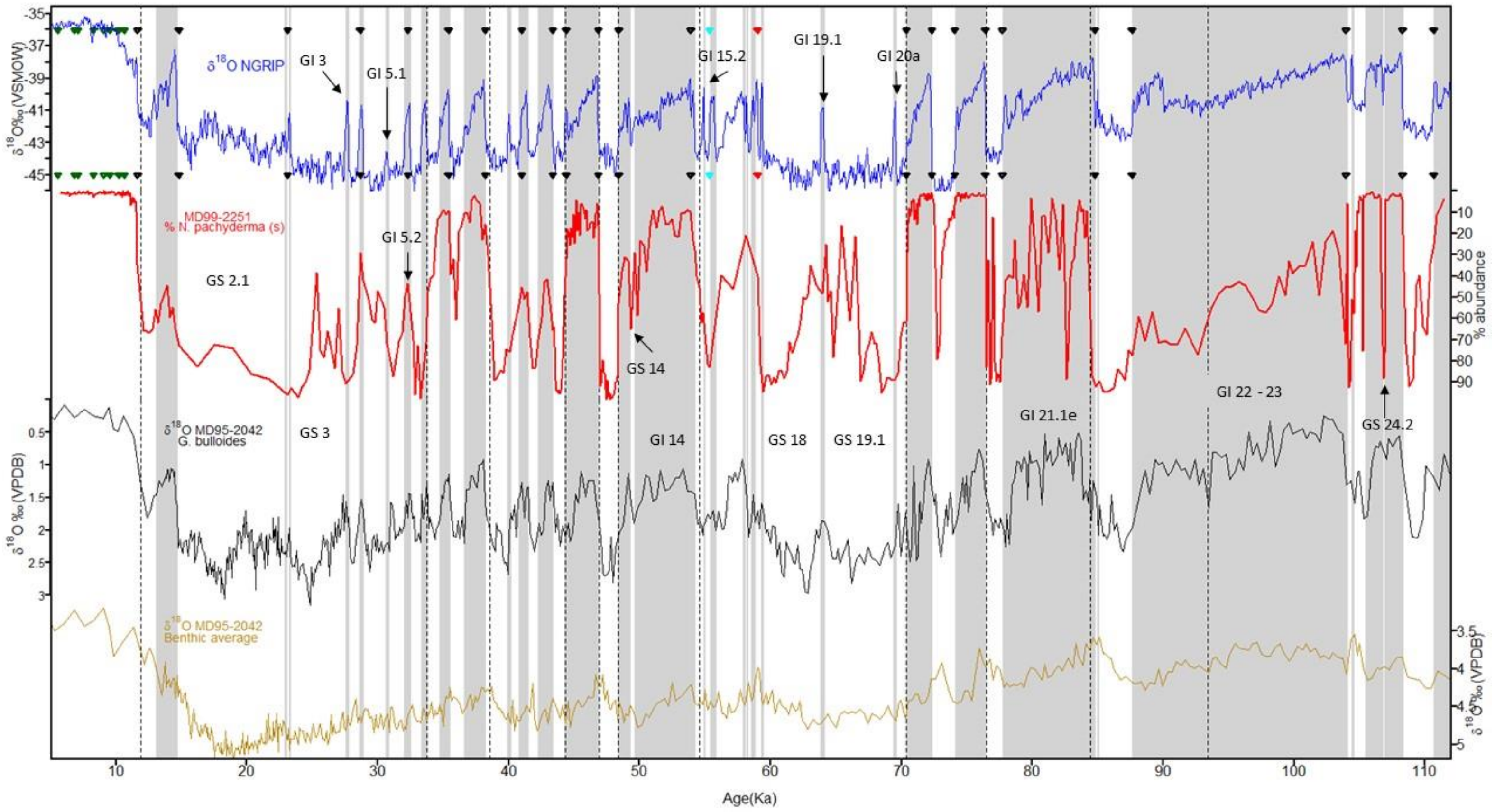

Figure 6.7 MD99-2251 % *N. pachyderma* (s) abundance aligned with NGRIP 50-year average δ^{18}O. MD95-2042 (Shackleton et al., 2004) and LR16 North Atlantic benthic stack (Lisiecki & Stern, 2016) records are also shown for comparison. Triangular markers indicate tie points used to align the records with ^{14}C dates in green, MIS 3/4 transition in cyan (Siddall et al., 2008), NAAZ II in red (Svensson et al., 2008) and NGRIP alignments in black. Grey vertical bars are Greenland stadials (Rasmussen et al., 2014) and hyphenated lines are the transitions between foraminifera assemblage zones.

6.6 Results

6.6.1 Ice rafted debris and magnetic susceptibility

Ice rafted debris counts are presented alongside magnetic susceptibility in Figure 6.8. In cores located within Ruddiman's IRD belt — through which Laurentide ice sheet-derived icebergs are channelled — magnetic susceptibility peaks have been shown to exhibit a positive correlation with IRD content. This indicates input from continental crust (Dowdeswell et al., 1995; Grousset et al., 1993). Elevated concentrations of iron sulphides such as pyrrhotine or greigite (Poutiers, 1975), titanium-rich magnetite (Pouthier & Gonthier, 1978), goethite (Robinson, 1986), and iron rich clay minerals (Poutiers, 1975) may all lead to increased magnetic susceptibility (Grousset et al., 1993).

For cores located outside of the main IRD belt, the relationship is less straightforward. Rasmussen et al. (1996) showed that magnetic susceptibility in core ENAM93-21 from the Faroe-Shetland channel exhibited an inverse relationship with IRD, attributed to enhanced input of non-magnetic carbonate and quartz grains. However, the opposite was found in core MD95-2006, located slightly further south and east in the Bara Fan, still outside the main IRD belt (Peters et al., 2008). Noting the unpredictability in relating magnetic susceptibility to iceberg rafting events, Chapman & Shackleton (1998) proposed IRD counts as the preferable method for recording Heinrich events.

MD99-2251 exhibits an inverse relationship between IRD content and magnetic susceptibility. For the 60.7–75 ka period, where data on IRD lithology exists, it can be seen that the majority of IRD is quartz (Figure 6.9). Thus it was assumed that magnetic susceptibility minima arise from the higher concentrations of non-magnetic material during periods of high IRD influx. Although comparably detailed IRD lithology data does not exist for the entire length of core, the inverse relationship between IRD and magnetic susceptibility remains constant throughout — aside from the minor IRD peaks at 64.8 and 85.9–84.3 ka, discussed below. Thus it is reasonable to assume that the composition of IRD remains similar throughout the entire core.

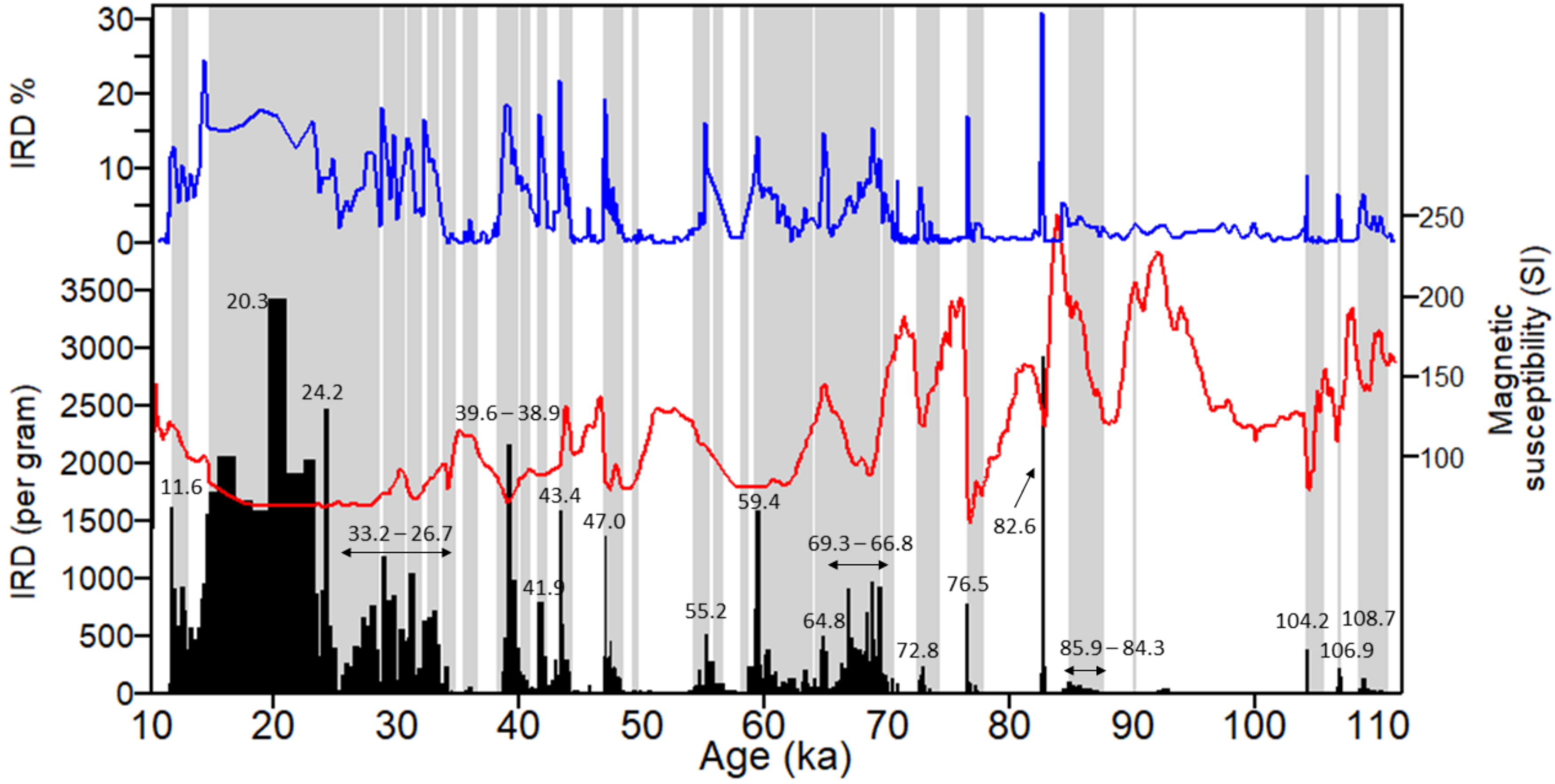

Figure 6.8 IRD data for core MD99-2251. IRD counts in the histogram, magnetic susceptibility in red and percentage IRD in blue. Numbers are ages of IRD peaks and grey bars are NGRIP stadials.

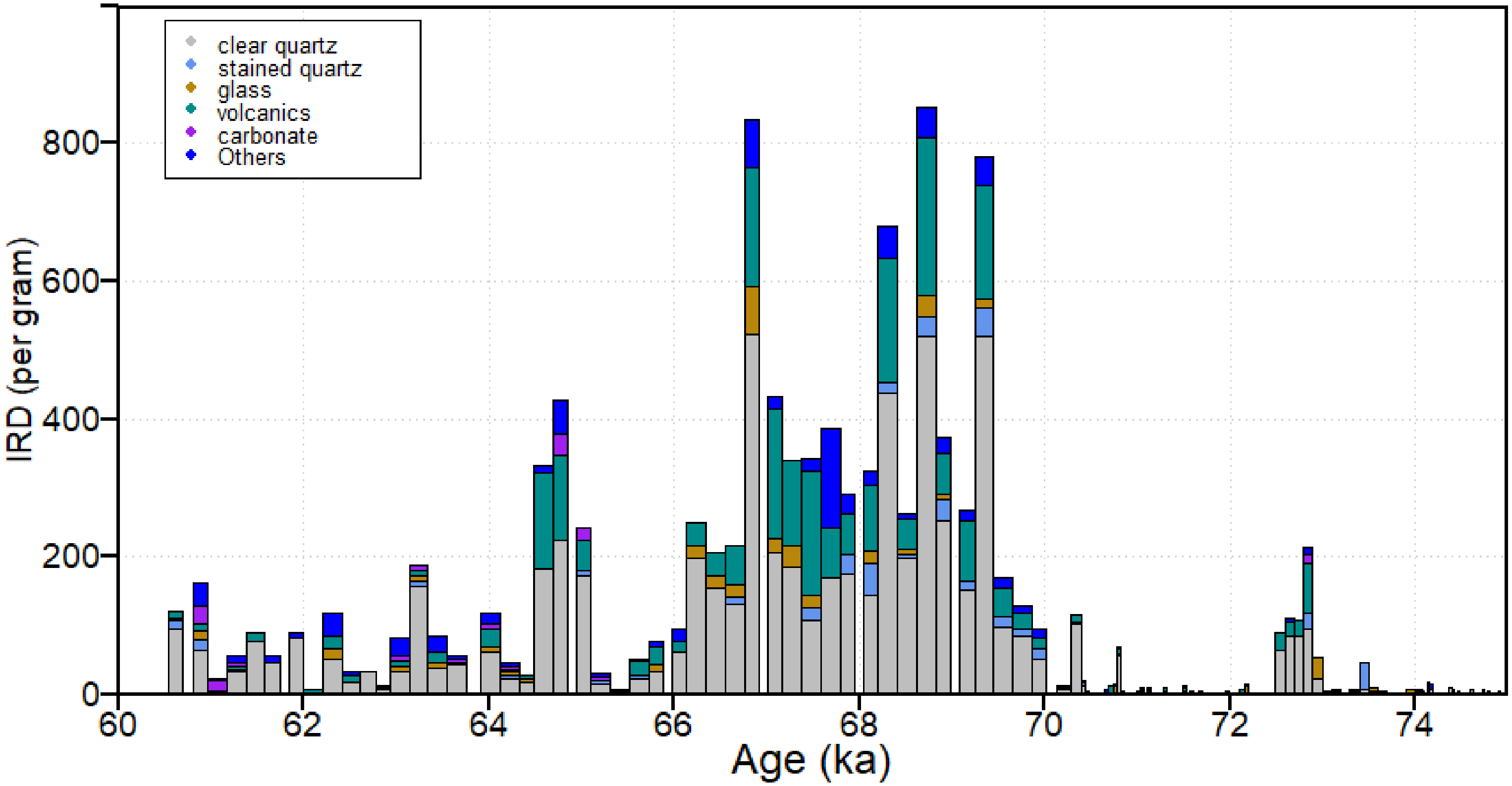

Figure 6.9 MD99-2251 IRD lithology data in the interval 60.7 – 75 ka.

As with other cores in this area, IRD tracers consisted largely of quartz with a small proportion (<10 %) of haematite stained grains, derived from red beds located on the North Eastern Greenland margin (Bond & Lotti, 1995; Bond, 1997). A small proportion of volcanic glass and black igneous grains, sourced from Iceland and Jan Mayan (Bond, 1997) persisted throughout. Carbonate content remains low during IRD peaks as with other cores situated outside of the 'IRD belt' (Ruddiman, 1977).

The inverse relationship between IRD concentration and magnetic susceptibility is contravened at 64.8 ka and 85.9–84.3 ka, where small IRD peaks are accompanied by increased magnetic susceptibility. When IRD species for the 64.8 ka event are compared alongside other IRD peaks for which IRD lithology data is available, there appears little difference in the concentration of potentially magnetic volcanic derived material, fluctuating between 20 and 40 %. However, a small number of carbonate/dolomite grains are present which may be indicative of an increasing influence from Laurentide-derived icebergs. It is also worth noting that ferromanganese grains, present throughout the core, have not been included in IRD count data due to their oceanic origin (de Lange et al., 1992). Thus the increased magnetic susceptibility during rafting events at 85.9–84.2 ka and 64.8 ka may arise from an increased concentration of such grains. Further analysis is necessary to determine the cause of these magnetic susceptibility/IRD relationship breakdowns.

In general, IRD counts increase during Greenland stadial periods, with major rafting events occurring towards the end stadials (Figure 6.8) - in line with the theory of major ice sheet collapse at the end of Greenland cold intervals (Bond et al., 1993). The only exception within the MD99-2251 record is for the cold event at 82.8–82.5 ka, attributed here to H8, which occurs during a Greenland interstadial period. Peak counts are reached at the LGM between 23.4 and 14.1 ka.

Identification of specific Heinrich and cold events was achieved through chronological alignment with existing records. There is considerable variation in the literature regarding naming convention. Much of this arises from dating uncertainty, particularly in dates beyond the reach of radiocarbon dating techniques, where uncertainty may be several thousands of years, making alignment between archives difficult. In addition, the varying number of events present within a single archive, alongside variable rafting magnitude, can lead to numbering discrepancies and disagreements as to whether an event is considered 'major'. For example, in core MD95-2024 from the Orphan Knoll, H7 is observed as a single event around 75 ka, and H8 a single event around 108 ka (Weber et al., 2001). However, in Norwegian Sea cores ENAM93-21 and MD95-2009, H7 is divided into two short-lived rafting events, H7a and H7b, and a major rafting event at 85 ka is attributed to H8 (Rasmussen et al., 2003). The event at 108 ka in these Norwegian Sea records is attributed to H10. In this study, the Heinrich event numbering system of Rasmussen et al. (2003) was used, which allows the majority of major rafting events to be identified. Less pronounced cold events have been identified from Chapman & Shackleton (1999).

IRD peaks for Heinrich events H2 – H10 (Hemming, 2004; Rasmussen et al., 2003) are all apparent (Table 6.4), including event 5a, first identified in cores from the Irminger and Icelandic Seas by Van Kreveld et al. (2000) and later found in records from the Labrador Sea and Orphan Knoll (Rashid et al., 2003). Sedimentation rate between 25 and 15 ka is insufficient to allow detailed resolution of H1; however, greater IRD influx was observed throughout this period. Additional peaks were identified as cold periods C19, C21, C24 and C25, signified by elevated IRD in core NEAP 18K, also located in the Gardar Drift (Chapman & Shackleton, 1999). A summary of IRD peaks is given in Table 6.4.

In general, each Greenland stadial is associated with a single rafting event. The only GS event without elevated levels of rafting is GS 23.1, during the relatively warm MIS 5d. Of course it is entirely possible that rafting does occur during GS 23.1 but that icebergs do not reach as far as the MD99-2251 site. This pattern of a single rafting event associated with each Greenland Stadial is contravened at the LGM, where sustained rafting occurs throughout, and during the rafting events from 69.3 – 64.8 ka, where several large IRD pulses are associated with GS19.1.

Table 6.4 Ice rafting events seen in the MD99-2251 record. Accepted HS dates (1-6, excluding 5a) from Hemming (2004). HS5a accepted age from Rashid et al. (2003). C events are cold events from Chapman & Shackleton (1999). H7 – H10 assigned according to Rasmussen et al. (2003).

Ice rafting Interval (ka)	Peak (ka)	Reference Event	Reference age (ka)	Peak count (grains/gram)	Greenland interval
11.9 – 11.5	11.6	Younger Dryas	12.9 – 11.7	1618	GS1
23.4 - 14.1	20.3-19	LGM		3426	GS2
24.8 – 23.9	24.2	H2	24	2477	GS3
28.1 – 26.7	28.1			763	GS4
29.8 – 28.9	28.9			1190	GS5.1
31.2 – 30.5	31.2	H3	31	1045	GS5.2
33.4 – 32.3	33.1			719	GS6
39.6 - 38.9	39.1	H4	38	2158	GS9
41.9 – 41.6	41.9			800	GS11
44.1 – 43.4	43.4			1585	GS12
47.0	47.0	H5	45	1367	GS13
56.2 – 54.5	55.2	H5a	53-52	514	GS15.2
60.2 – 59	59.4	H6	60	1582	GS17.2
65.0 – 64.6	64.8			503	GS19.1
69.3 – 66.8	69.3	H7a/C19		930	GS19.1
	68.7			969	GS19.1
	66.9			904	GS19.1
72.9 – 72.5	72.8	C20		227	GS20
76.5	76.5	H7b		776	GS21.1
82.8 – 82.5	82.6	H8		2924	GI21.1
85.9 – 84.3	84.8	C21		101	GS21.2
104.2	104.2	H10		385	GS23.2
106.9–106.7	106.7	C24		213	GI 24.1
108.8	108.8	C25		130	GS25

6.6.2 Magnesium/calcium ratios

Mg/Ca ratios were measured for *N. pachyderma* (s) and *G. bulloides* along a 3 m section of MD99-2251 spanning 75 to 58.1 ka. Farmer et al. (2011) showed using Holocene samples from MD99-2251 that the choice of calibration used to derive temperature estimates can give rise to temperature discrepancies of up to 4 ^{o}C. Thus before attempting to infer palaeotemperatures, it is useful to compare raw Mg/Ca values.

The analysis technique outlined by Skinner & Elderfield (2005) was followed by assuming an Mg/Ca temperature sensitivity of 10 % per 1 ^{o}C, common to all species. The two species exhibit an average offset of approximately 1 mmol/mol over the experimental interval, with an average Mg/Ca of 2.0 mmol/mol in *G. bulloides* and 1.0 mmol/mol in *N. pachyderma* (s). This equates to a temperature difference of 5 – 6 ^{o}C using the Skinner & Elderfield (2005) methodology. The difference probably arises from differing calcification depths, although there is also likely a species-specific 'vital effect' giving rise to differing Mg/Ca temperature sensitivities.

Farmer et al. (2011) used the same methodology to infer a 5 ^{o}C offset between the calcification temperatures of *G. bulloides* and *G. inflata* for MD99-2251 Holocene samples (Figure 6.10**Error! Reference source not found.**). *G. inflata* and *N. pachyderma* (s) are both thought to calcify between 75 and 100 m depth (Cleroux et al., 2007; Jonkers et al., 2010) suggesting that the temperature gradient in the top 100 m was similar during late MIS 5/early MIS 4 as for the Holocene.

Offset between the two species exhibits a gradual decline over the 17 ka window, declining from an average of 1.16 ± 0.1 mmol/mol from 75 – 70 ka to 0.92 ± 0.1 mmol/mol between 63 and 58 ka. This suggests a slight reduction in the temperature gradient in the top 100 m with the onset of increasingly glacial conditions. This supports the findings of Farmer et al. (2011) who showed an increasing offset in Mg/Ca between the species as the record progressed from the cold conditions of the Younger Dryas into the Holocene. However, the offset between the species observed by Farmer et al. (2011) is driven largely by surface temperature changes, with increasing Mg/Ca ratios observed in *G. bulloides* whilst *G. inflata* ratios remain largely constant. The opposite is true in the MIS 5 – 4 record produced for this study, where the *G. bulloides* Mg/Ca ratio exhibits very little variation over the entire record (gradient =

0.01 mmol/mol/ka) and step-like increases in the thermocline dwelling *N. pachyderma* (s) at 66.7 and 63.7 ka drive the reduction in offset. It should also be noted that the effect is far less pronounced in the MIS 5 – 4 record produced in this study, perhaps due to the glacial conditions of MIS 4 being largely established at the start of the 17 ka record. As such, it is difficult to draw firm conclusions, although the record appears to support the findings of Farmer et al. (2011) that the temperature gradient within the mixing layer is reduced during glacial conditions. It would be interesting to extend the record back further in order to assess how the offset changes under the full interglacial conditions of the MIS 5e plateau.

The only notable fluctuation within the *G. bulloides* record is a peak in Mg/Ca during Greenland Stadial 20. *N. pachyderma* (s) appears to exhibit a similar warm excursion within GS 20, but the record does not cover the full period, and it is unknown whether this is an excursion from a lower baseline or a continuation of a long term reduction.

Figure 6.11 shows paired measurements for the two records, normalised to their mean to aid comparison. Both species show considerable short-term variability with little evidence of covariation. The Pearson correlation coefficient was calculated downcore between paired samples over a 1000 year rolling window and is presented in the lower half of the figure. It rarely exceeds ± 0.6 suggesting that the two records are largely driven by different forcings.

This is reinforced when comparing the direction of change in the two records. The grey hatched bars on Figure 6.11 indicate regions where the direction of change is the same (i.e. both exhibit an increase/decrease from the previous sample). Out of 63 paired measurements, 30 show variation in the same direction. The majority of these occur in the period post 66.7 ka, subsequent to the increase in *N. pachyderma* (s) Mg/Ca ratio that reduces offset between the species. Of the paired measurements after 66.7 ka, 60 % (21/35) show a similar direction of change compared with just 32 % (9/28) before. This hints towards a coupling of the surface and thermocline with the onset of intensifying glacial conditions, but the relationship is too weak to derive any firm conclusions.

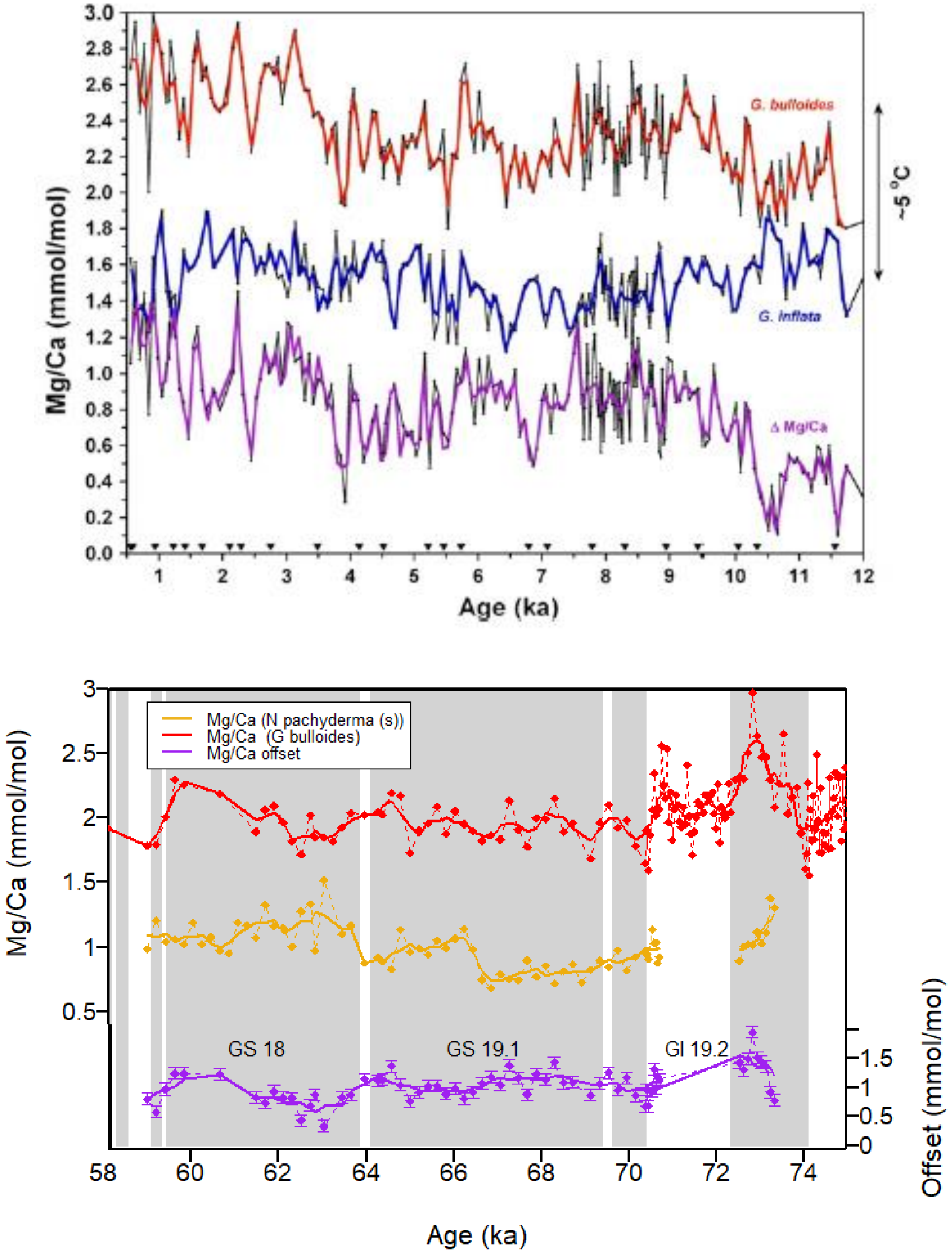

Figure 6.10 Mg/Ca ratios for core MD 99-2251. Top: Holocene (Farmer et al., 2011). Black lines show the mean data and coloured lines the 200 year Gaussian smoothed data. Species offset in purple. Below: 75 – 58.1 ka (This study). Solid lines are the 1000 year running mean and dashed lines raw data. The purple lines are the offset between the two species. Grey vertical bars mark Greenland stadials.

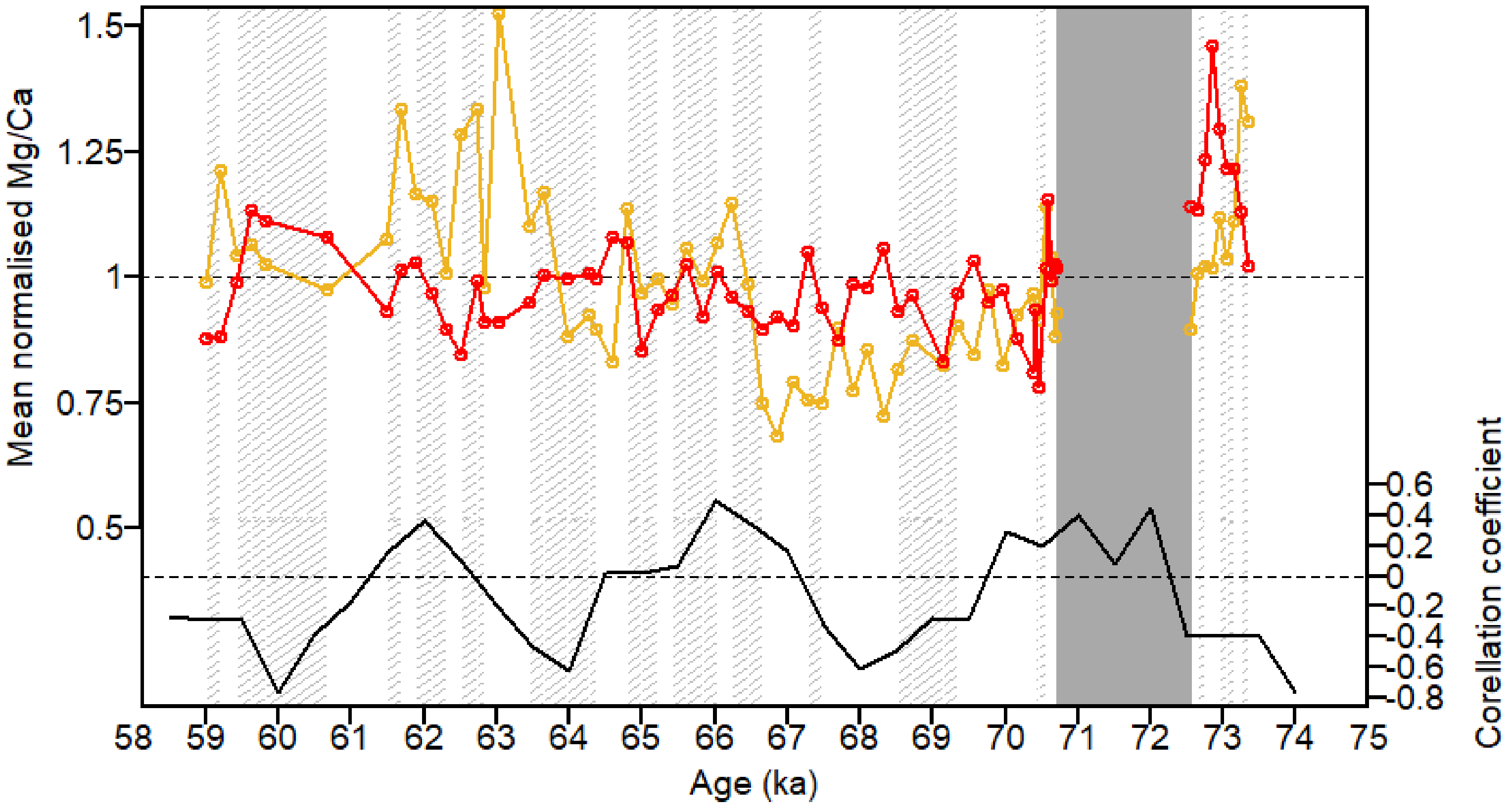

Figure 6.11 Top: Paired mean normalised Mg/Ca ratios for *N. pachyderma* (s) (yellow) and *G. bulloides* (red). Bottom: Pearson correlation coefficient between paired measurements calculated over a 1000 year rolling window. Grey hatched bars indicate regions where the direction of change in paired measurements is the same. Solid grey bar denotes absent data

Mg/Ca inferred temperatures exhibit remarkably little fluctuation between stadial and interstadial periods throughout the 17 ka section (Table 6.5). In comparison, MAT temperatures show a much greater differential between stadial and interstadial intervals over the same period (Table 6.5 and Figure 6.12). The suppressed range in Mg/Ca temperatures may be a result of species migration both within the water column and geographically. MAT temperatures suggest a high degree of temperature variability during this period, and it is reasonable that dominant species would migrate in and out of the MD99-2251 vicinity with fluctuating temperatures. Thus the Mg/Ca inferred temperatures may in fact reflect an average of short-lived warm or cold intervals within the sampling window. This illustrates a disadvantage of using Mg/Ca ratios for temperature inference compared with the MAT. MAT inferred temperatures generally fall between Mg/Ca temperatures inferred from surface dwelling *G. bulloides* and cool, subsurface *N. pachyderma*(s).

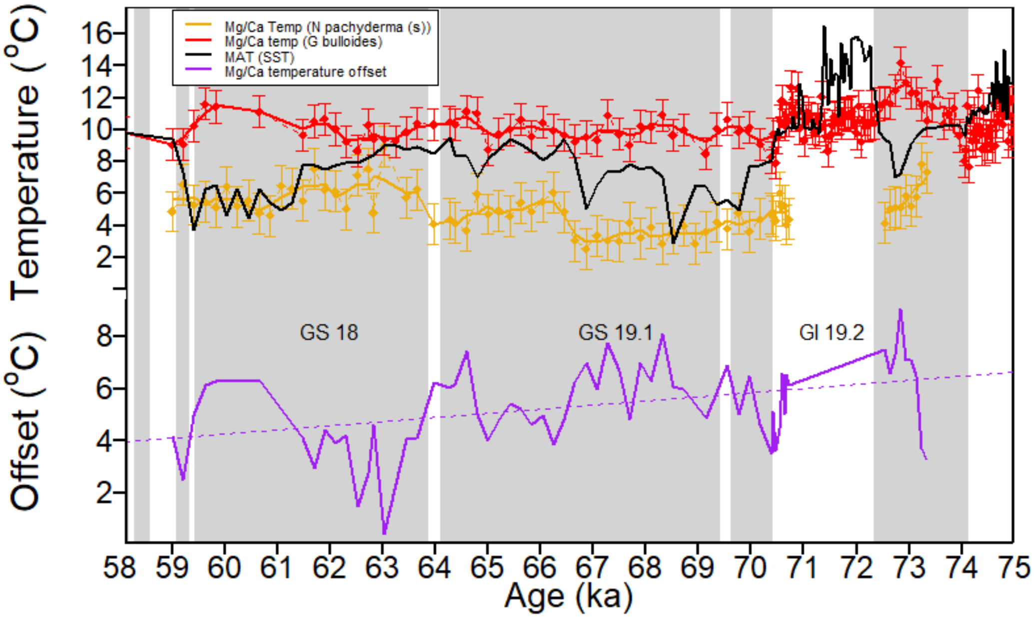

Figure 6.12 Mg/Ca inferred temperatures for core MD99-2251. Solid lines are the 500 year running mean and dashed lines the raw data. Bottom plot (in purple) is the offset between the two species with a linear trend (dashed line) through the points.

The increase in Mg/Ca ratio of *G. bulloides* during Greenland Stadial 20 (GS 20) is reflected in the inferred temperature, which rises to a maximum of 14.2 ± 1.2 °C at 72.8 ka, compared with an average of 10.4 ± 1.1 °C across the 1.5 m section of core. This is in contrast to both MAT and *N. pachyderma* (s) Mg/Ca temperatures which appear to show a coincident decline from 10.1 ± 0.8 °C to 7.0 ± 1.5 °C in MAT, and 7.9 ± 1.3 °C to 4.1 ± 1.3 °C in *N. pachyderma* (s) Mg/Ca temperatures.

Table 6.5 Summary of temperature calculations for Mg/Ca and MAT methods over the interval 75 – 58.1 ka. Errors are standard deviations.

	Temp range (°C)	**Stadial average (°C)**	**Interstadial average (°C)**
MAT	13.6	8.9 ± 2.4	9.9 ± 2.5
Mg/Ca *N. pachyderma(s)*	6.4	5.1 ± 1.4	4.7 ± 0.7
Mg/Ca *G. bulloides*	6.5	10.3 ± 1.2	10.4 ± 1.0

The question then arises as to what drives the discrepancies between the MAT and *N. pachyderma* (s) temperatures and those of *G. bulloides.* The shifts exceed measurement uncertainty and are expressed in over ten samples, suggesting that they are real and not simply an artefact of measurement noise.

The increased offset between species could arise from a disparity between temperature trends in the surface and thermocline waters, with a warming surface and cooling thermocline. This seems unlikely however. The event occurs within a Greenland Stadial event, when surface temperatures would be expected to cool. Furthermore, this is contradicted by the decline in MAT temperatures, which are generally assumed to be a proxy for surface temperatures.

Alternatively, such a discrepancy could arise from a shift in seasonality. In modern-day core studies, *G. bulloides* has been found to calcify with the northerly migrating spring bloom (Ganssen & Kroon, 2000). A shift to a later, warmer spring bloom may go some way to explaining the warmer temperatures observed in *G. bulloides* whilst MAT temperatures, a reflection of summer surface temperatures, decline. These observations suggest a warming spring and cooling summer in the region. Recent single test studies of *G. bulloides* in North Atlantic core T88-3P have supported the idea of a later spring bloom during glacial intervals

(Brummer et al., 2019). However, since the increased *G. bulloides* temperatures are not maintained throughout GS 19.1 or GS 18, it seems unlikely that such a high-magnitude shift could occur over such an isolated time frame.

G. bulloides abundance is noticeably low during this interval, fluctuating between 5 – 15 % compared with an average of 25 % across the 17 ka record. It may be that at such low abundances, *G. bulloides* are migratory, representing specimens from a remote formation site. Alternatively, specimens may represent a relatively short time window – below the sampling resolution – in which conditions were warm enough for temperate dwelling species to flourish. Indeed, a similar shift is observed throughout part of GS 18, between 62 and 59 ka. Again, *G. bulloides* abundance drops to 5 – 10 % and inferred temperatures increase whilst MAT and *N. pachyderma* (s) Mg/Ca temperatures decrease.

This highlights the limitations of Mg/Ca temperature reconstructions for species with low percentage abundances and the advantages of using multiple temperature proxies. In particular, the MAT inferred temperature offers advantages over Mg/Ca temperatures in such cases with the overall assemblage acting to reduce the temperature signal derived from minor represented species.

6.6.3 Stable isotope results

Stable isotope ratios were measured for *N. pachyderma* (s) and *G. bulloides* along an approximately 8 m section of MD99-2251 spanning ages 75 – 10.4 ka. High resolution records were constructed between 75 – 58.1 ka for both the aforementioned species, as well as *G. quinqueloba*. This latter species proliferated throughout the entire ~17 ka window and thereby offers a continuous record. Results are presented in Figure 6.13.

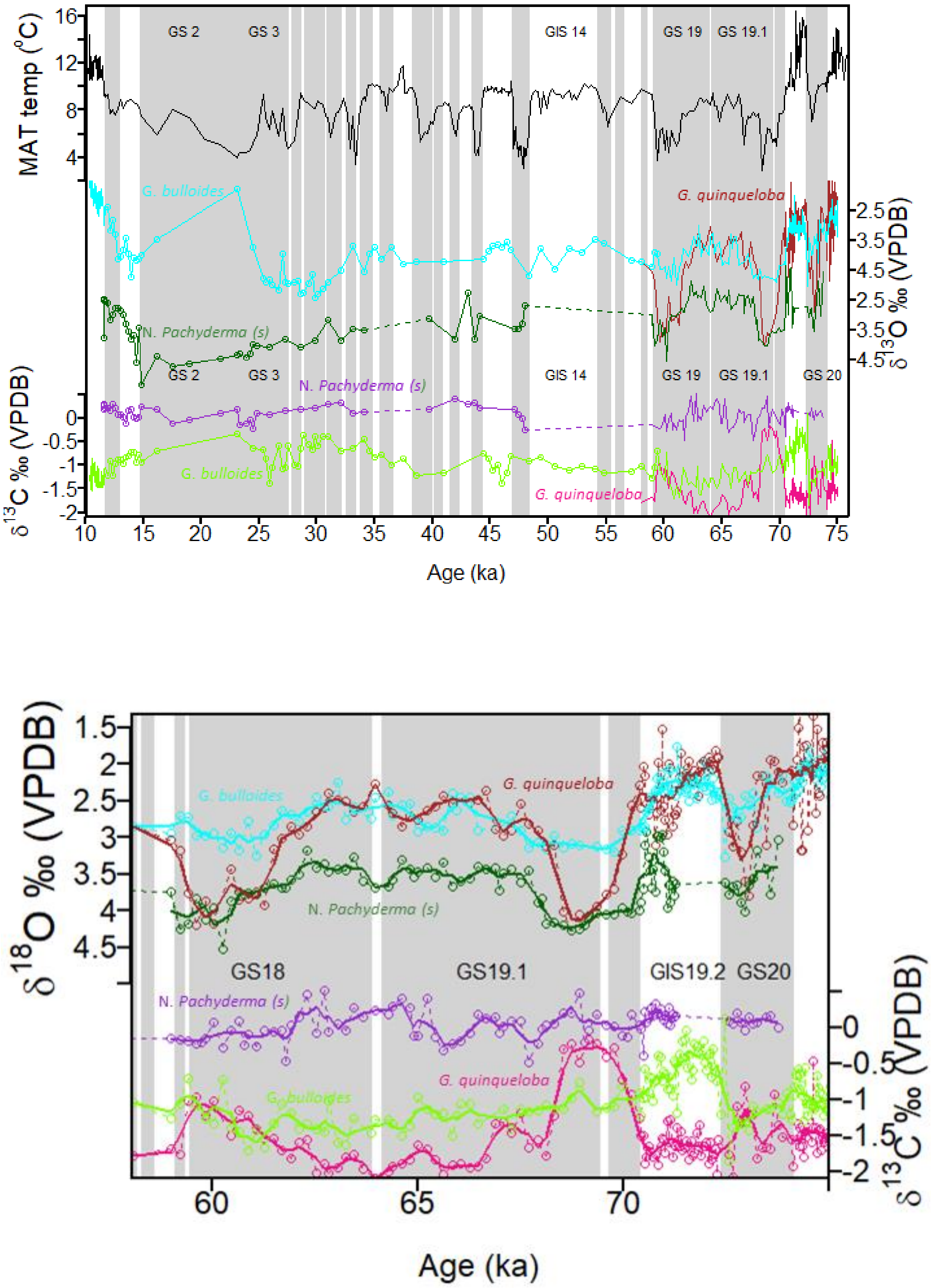

Figure 6.13 Stable isotope record for MD99-2251, Above) Full record. Below) Magnified high resolution period between 75 – 58.1 ka. Dashed line = raw data, solid line = 500 year smoothing.

The oxygen isotope curves follow the standard saw-tooth shape of recent glacial cycles (Broecker & van Donk, 1970), gradually declining from MIS 5 to MIS 2, before rapidly increasing at the start of the Holocene. Species variability of approximately 1 ‰ during glacial periods is in line with previous North Atlantic studies (McManus et al., 1996). *N. pachyderma* (s) δ^{18}O values fluctuate between 3 and 4.5 ‰ for the majority of the record, representing typical values for the glacial North Atlantic (Hillaire-Marcel et al., 2011; Vidal et al., 1997). A δ^{18}O peak of 4.55 ‰ is reached at 19.0 ka with elevated values, above 4.0 ‰, observed from 29.8 -13.7 ka. *G. bulloides* δ^{18}O values are offset by ~1 ‰ to higher values, likely a reflection of differing calcification habitats and variable degrees of fractionation in species-specific 'vital effects'. These findings are in line with those of Duplessy et al. (1991) who first suggested an offset of ~0.75 ‰ between *N. pachyderma* (s) and surface dwelling species such as *G. bulloides*.

G. quinqueloba remains less well studied within the literature. Jonkers et al. (2010) used sediment trap data from the Irminger Sea to suggest that *G. quinqueloba* calcification occurs as a single pulse in the summer, reflecting temperatures at the base of the thermocline. Since *N. pachyderma* (s) was found to calcify during spring at the same depth, the authors suggest using the offset in δ^{18}O between these species in the fossil record as an indication of seasonal temperature differences. However, these findings are contradicted by studies from the Nordic Seas where δ^{18}O signatures of *G. quinqueloba* reflect shallower depths between 25 – 75 m, within the mixing layer, and *N. pachyderma* (s) between 70 – 130 m, near the base of the pycnocline (Simstich et al., 2003).

From the record produced here *G. quinqueloba* δ^{18}O has a similar pattern with both the *G. bulloides* and *N. pachyderma (s)* records (Figure 6.13 and Table 6.6), although is closer in magnitude to *G. bulloides*. Average δ^{18}O over the high resolution 3 m section of core is 3.7 ‰, 2.5 ‰ and 2.6 ‰ for *N. pachyderma* (s), *G. bulloides* and *G. quinqueloba* respectively. The correlations between *G. quinqueloba* and the other two species suggests a habitat in between the surface dwelling *G. bulloides* and the base of the mixing layer, occupied by *N. pachyderma* (s).

Table 6.6 Correlation coefficients between isotopic records in the 3 m high resolution section of MD99-2251.

Species	$\delta^{18}O$	$\delta^{13}C$
N. pachyderma (s) – *G. bulloides*	0.47	0.14
G. bulloides – *G. quinqueloba*	0.66	0.34
N. pachyderma (s) - *G. quinqueloba*	0.63	-0.01

G. quinqueloba $\delta^{18}O$ exhibits a greater stadial/interstadial range than the other species — with an average offset of 0.74 ‰ compared with 0.26 ‰ and 0.43 ‰ in *N. pachyderma* (s) and *G. bulloides* respectively (Table 6.7). Furthermore, *G. quinqueloba* $\delta^{18}O$ fluctuations exhibit a clear correlation with MAT-derived temperature (Figure 6.13). The wide geographical distribution of the species suggest it is tolerant to a wide range of environmental conditions and therefore may be less likely to migrate during more extreme temperature excursions. *G. quinqueloba* remains a relatively underutilised species in isotopic studies, likely due to its small size which makes it time consuming to isolate and measure. However, this study suggests that if these time barriers are overcome, its strong isotopic response to temperature forcings make it a suitable species for further study.

Table 6.7 Stable isotope averages for stadial and interstadial samples across the three species. Excludes Holocene samples

	$\delta^{18}O$		$\delta^{13}C$	
	Stadial	**Interstadial**	**Stadial**	**Interstadial**
N. pachyderma (s)	3.80 ‰	3.54 ‰	0.05 ‰	0.16 ‰
G. bulloides	2.78 ‰	2.35 ‰	-1.06 ‰	-0.79 ‰
G. quinqueloba	2.95 ‰	2.21 ‰	-1.48 ‰	-1.56 ‰

The isotopic record between 75–58 ka provides sufficient resolution to identify $\delta^{18}O$ peaks during GIS 19.2 and GIS 20 in both the *G. bulloides* and *G. quinqueloba* records, as well as reductions during Interstadial events. All three species exhibit an increase in $\delta^{18}O$ at the MIS 5/4 boundary, commencing around 70.8 ka. Both *G. bulloides* and *N. pachyderma* (s) exhibit approximately 1 ‰ increases, with *N. pachyderma* (s) settling to higher values slightly earlier (70.2 ka) than *G. bulloides* (69.8 ka). The *G. quinqueloba* response is more dramatic, roughly 1.5 ‰, and prolonged — reaching values as high as 4.3 ‰ by 69.1 ka. After an initial peak, *G.*

quinqueloba $\delta^{18}O$ decreases slightly by 67 ka, setting into new stadial values ~0.5 ‰ higher than interstadial values. Similar shifts of about 1 ‰ at the MIS 5/4 boundary have been recorded previously in North Atlantic core SU90-03 (Chapman & Shackleton, 1998).

Carbon isotopes have been widely utilised as a proxy for oceanic ventilation and end member variation in benthic species (Boyle & Keigwin, 1982, Hillaire-Marcel et al., 2011; McManus et al., 1996). Yet relatively few studies have made use of $\delta^{13}C$ in planktonic species. In MD99-2251, the covariation of *G. quinqueloba* $\delta^{13}C$ with both $\delta^{18}O$, and MAT temperature is striking and suggests that it may be of use as an environmental proxy. In cores from the Southern Ocean (Mulitza et al., 1999) and Arabian Sea (Steens et al., 1992), elevated planktonic $\delta^{13}C$ has been used as a proxy for nutrient enrichments. Reduced ocean/atmosphere exchange of CO_2 due to enhanced stratification has also been postulated as a driver of increased $\delta^{13}C$ in planktonic species (Mulitza et al., 1999).

Little fluctuation is seen across the entire *N. pachyderma* (s) $\delta^{13}C$ record; however *G. bulloides* $\delta^{13}C$ exhibits a complex and varying relationship with $\delta^{18}O$. Two negative excursions in *G. bulloides* $\delta^{13}C$ are observed at 46.8–45.2 ka and 26.7 – 25.3 ka. Throughout both these excursions little variation in $\delta^{18}O$ is observed. As the record moves out of peak glacial conditions and into the Holocene, a gradual decline is observed in both in $\delta^{13}C$ and $\delta^{18}O$. The drivers of these fluctuations is considered further in section 6.7.

6.7 Discussion: North Atlantic ice rafting

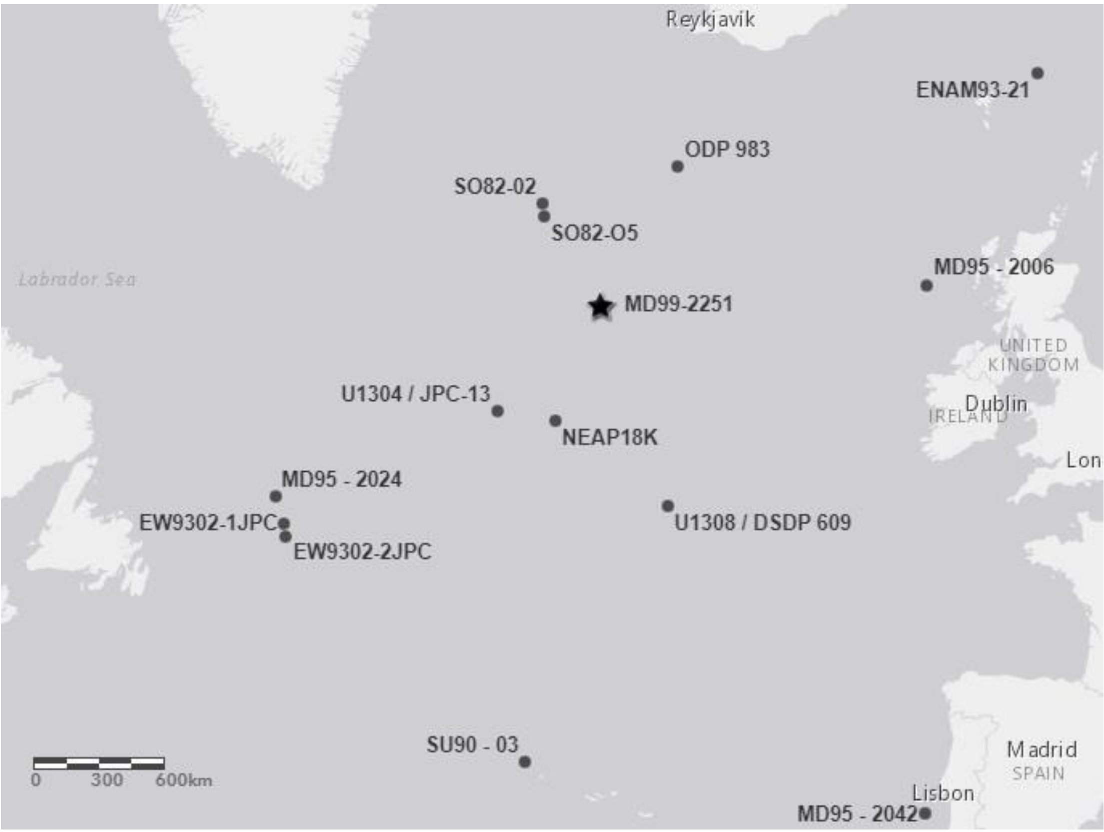

Figure 6.14 Locations of cores considered in the MD99-2251 analysis.

The MD99-2251 record offers a high resolution, well dated record of North Atlantic ice rafting over the last glacial cycle from which a comprehensive chronology can be constructed. Figure 6.15 shows IRD proxy records for a further four North Atlantic sites, coincident with the MD99-2251 record. The sites have been chosen to provide a cross section of the North Atlantic and are presented from East to West. Sites U1308 (Channell et al., 2008; Age model Obrochta et al., 2014) and DSDP 609 (Obrochta et al., 2012) are derived from the same location but are both used here. Use of the U1308 record extends the archive over the entire MD99-2251 time interval, however since this record is of magnetic susceptibility, inclusion of the DSDP IRD count record ensures magnetically inert events can be identified. Heinrich events identified by the original paper authors are in black. Additional events have been identified by alignment to the MD99-2251 record and are listed in red.

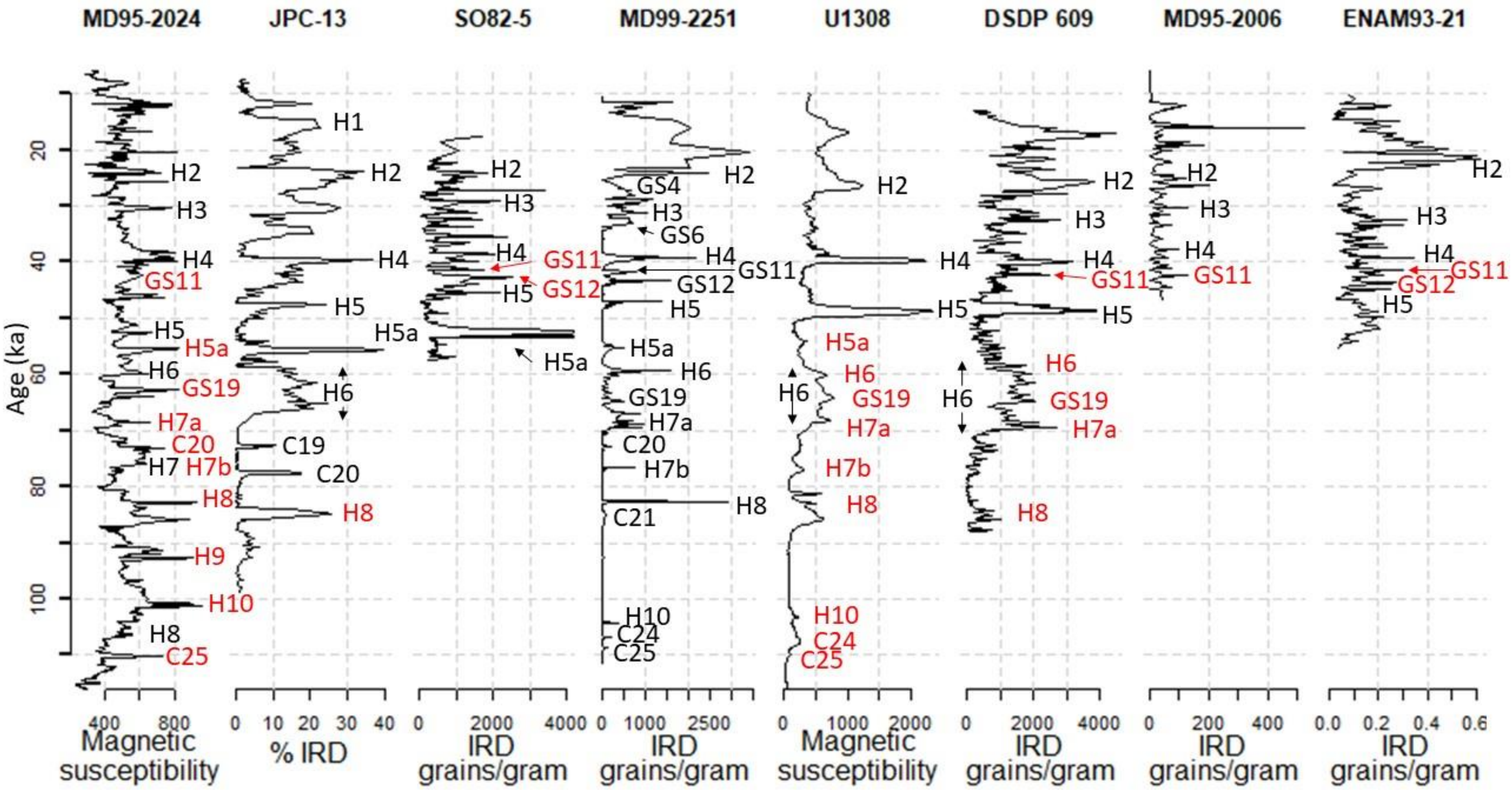

Figure 6.15 IRD records from six North Atlantic cores presented from East to West (left to right). MD95-2024 (Weber et al., 2001), JPC-13 (Hodell et al., 2010), SO82-5 (Van Kreveld et al., 2000), U1308 (Channell et al., 2008; Age model: Obrochta et al., 2014), DSDP 609 (Obrochta et al., 2012), MD95-2006 (Knutz et al., 2001), ENAM93-21 (Rasmussen, 1996; Age model Waelbroeck et al., 2019). Events identified by original paper authors in black, additional events identified in this study in red.

This study adopts the Heinrich Event naming convention of Rasmussen et al. (2003) which identifies separate events for H5a, H7a and H7b. Less prominent rafting events, associated with cold intervals, are named according to the cold events in Chapman & Shackleton (1999) whereby naming is derived from the associated Greenland stadial number.

The rafting events during GS11, GS12 and GS19, identified within the MD99-2251 record, can be observed across multiple sites — suggesting that these are large-scale, non-localised events. Rasmussen et al. (2016) showed that IRD peaks can be associated with each of the Greenland Stadial intervals in core SO82-02 from the Reykjanes Ridge back to H6. With the discovery of seven additional rafting events between 130 – 70 ka in core NEAP 18K (Chapman & Shackleton, 1999) associated with the Greenland stadials it is now unequivocal that the quantity of rafting events over the last glacial cycle extends beyond those originally identified by Heinrich (1988) and can be associated with each Greenland stadial cooling.

The recently identified Heinrich events of H5a (Rashid et al., 2003; Van Kreveld et al., 2000) and H7a and H7b (Rasmussen et al., 2003) do not appear unusual in their magnitude or extent compared with other stadial rafting episodes, both in the MD99-2251 record and those presented in Figure 6.15. It remains unclear whether these should be referred to as 'true' Heinrich events. This study suggests that beyond the prominent H1 – H6 events (excluding H5a) additional rafting episodes should be identified by their association to the coincident Greenland stadial.

6.7.1 Timing of ice rafting events

All ice rafting events, aside from H8, coincide with cold episodes - generally occurring at the end of GS events (Figure 6.16 and Figure 6.17). This supports the notion of ice sheet build up and collapse described in MacAyeal's (1993) binge–purge model. In this model, accumulation over stadial intervals causes ice sheets to increase to an unstable size such that they collapse — causing the massive iceberg discharges of Heinrich events. Geothermal heat accumulation (MacAyeal, 1993), boundary layer friction build up (Verbitsky & Saltzman, 1995), and sea-level oscillations (Maslin et al., 2001) have all been suggested as triggers for collapse. The MD99-2251 record cannot offer further insight into the likely trigger.

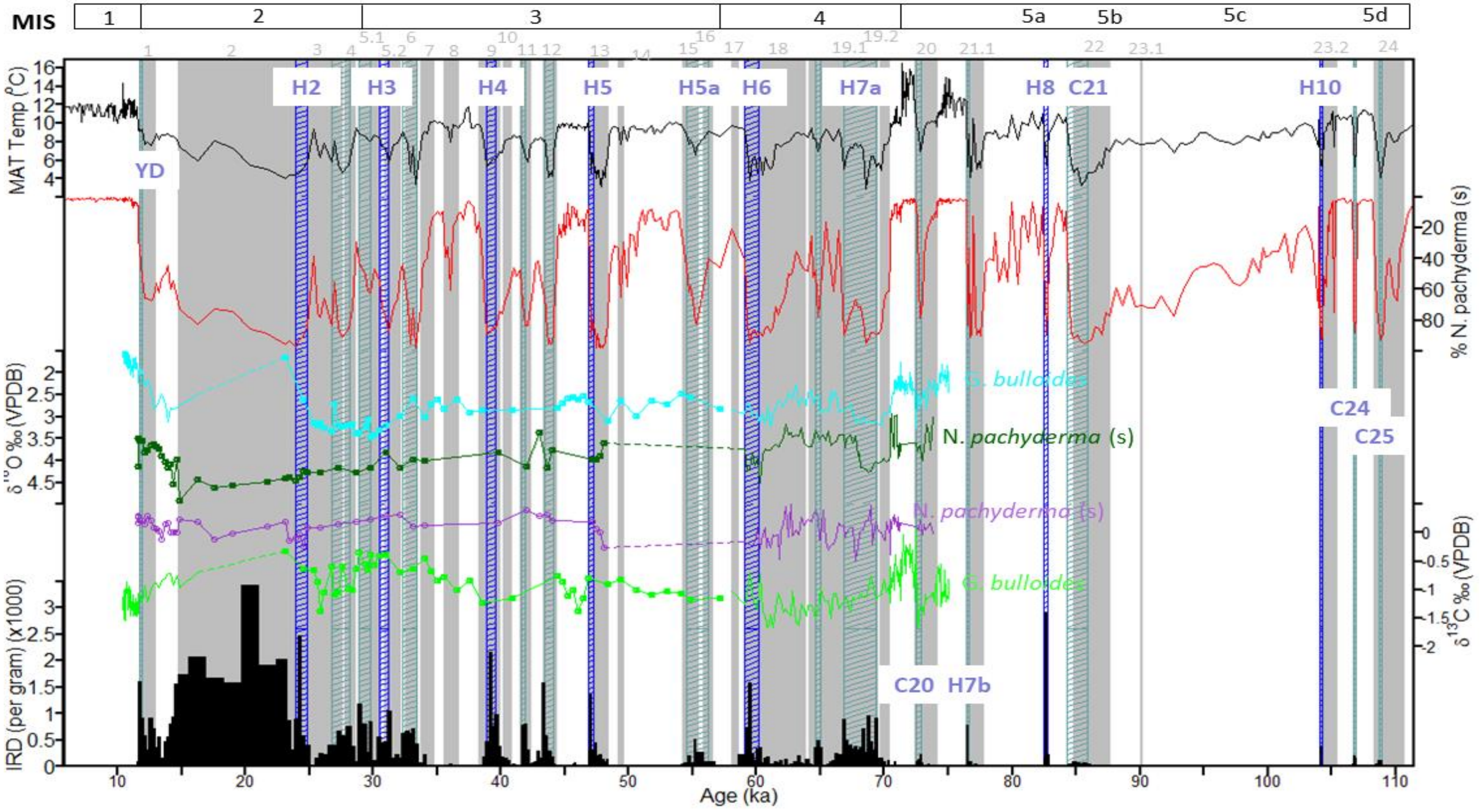

Figure 6.16 Multiproxy downcore plot from core MD99-2251. Top to bottom: MAT inferred temperature, *N. pachyderma* (s) percentage abundance, $\delta^{18}O$ of planktonic species, $\delta^{13}C$ of planktonic species, IRD per gram. Grey shades bars show Greenland Stadials. Dark blue hatched bars are Heinrich Events and light blue hatched bars are minor rafting events. Grey numbering above indicates GS episode(Rasmussen et al., 2014). Marine isotope stage transitions from Lisiecki & Raymo (2005), 5a – 5d are positions of isotopic peaks.

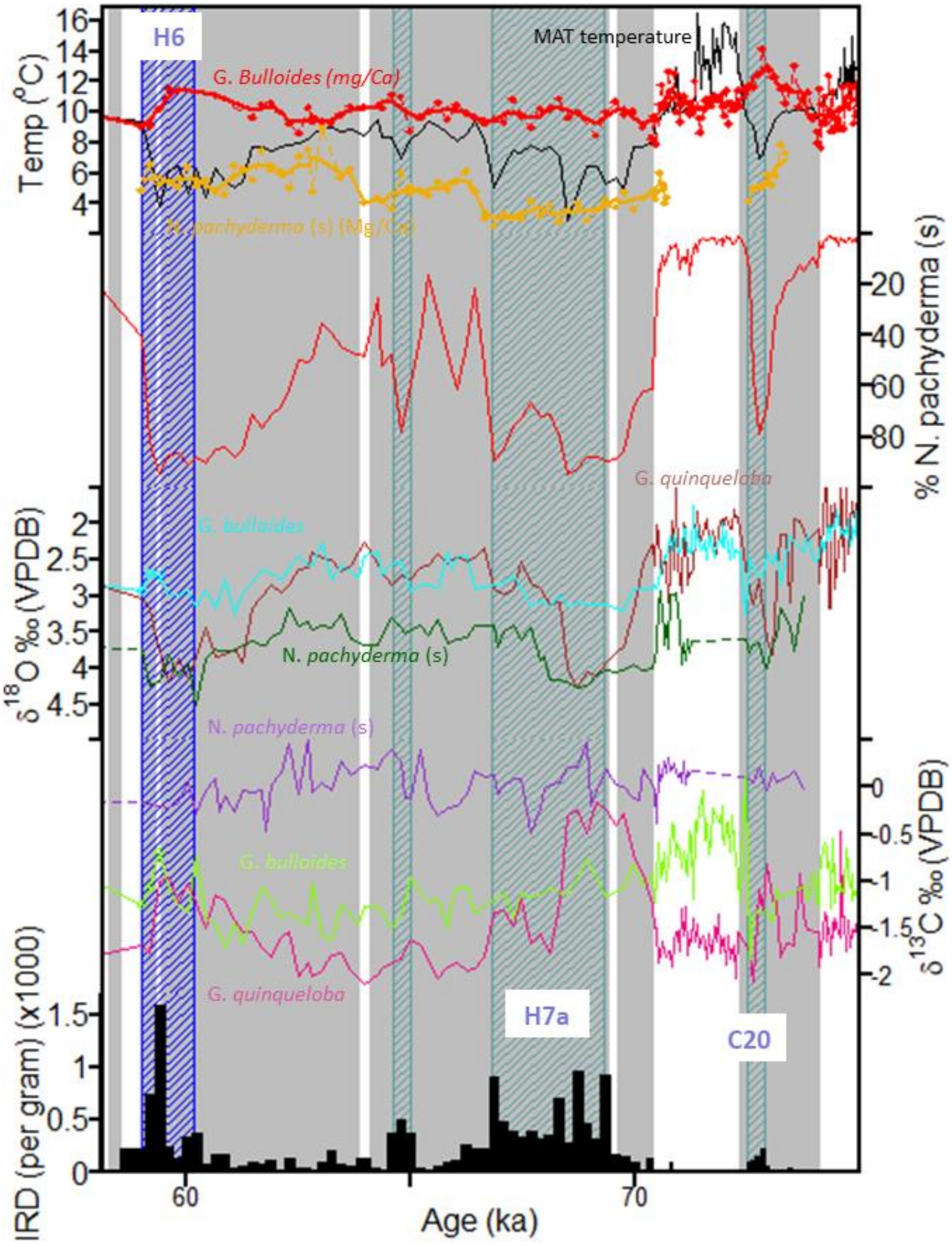

Figure 6.17 Multiproxy downcore plot from the high resolutions section of core MD99-2251. Top to bottom: MAT and Mg/Ca inferred temperatures, *N. pachyderma* (s) percentage abundance, $\delta^{18}O$ of planktonic species, $\delta^{13}C$ of planktonic species, IRD per gram. Grey shaded bars show Greenland Stadials. Dark blue hatched bars are Heinrich Events and light blue are minor rafting events.

A key aspect of the binge-purge model is a 7–8 ka cycle between major purge events which has been attributed to both Greenland climatic cycles (Bond et al., 1992) and the surpassing of basal heating thresholds (Alley & MacAyeal, 1994). If H7 is subdivided into H7a and H7b, as in Rasmussen et al. (2003), this periodicity generally holds true throughout Marine isotope stages 5b – 1 but as the record stretches back into MIS5d, rafting events become much less frequent. The periodicity also breaks down between H6 and H5 with a 15 ka gap observed between the two events. It was this prolonged gap that first led to the proposal of an additional event, H5a, which divided the period of absent rafting in two (Rashid et al., 2003). However, the event attributed to H5a in MD99-2251 occurs some 2 ka prior to the assigned date within the existing literature (Rashid et al., 2003). Thus the existence of H5a does little to resolve the lack of periodicity in MD99-2251 between H6 and H5.

6.7.2 Heinrich events and their relation to Greenland cooling

The association between temperature minima and enhanced iceberg rafting has long been established (Bond & Lotti, 1995) and can be clearly observed throughout the MD99-2251 record (Figure 6.16 and Figure 6.17). This relationship has led to several modelling studies which have used freshwater forcing from increased iceberg rafting to infer reductions in the Atlantic Meridional Overturning Circulation (Ganopolski et al., 1998; Vellinga & Wood, 2002). The resulting decrease in heat transport to the higher latitudes has been postulated as a driver of the stadial events observed in the Greenland ice cores (Seidov & Maslin; 2001) (See section 4.3.1 for further detail).

However, numerous proxy studies have observed a lag between the onset of Greenland stadial events and increased incidence of ice rafting — leading to the conclusion that ice rafting events are a result of high latitude cooling, rather than a cause (Barker et al., 2015; Shaffer et al., 2004; Van Kreveld et al., 2000).

To investigate this further, the MD99-2251 record was analysed using the algorithm developed by Barker et al. (2015) for objectively assessing the temporal offsets between temperature fluctuations and the arrival/departure of IRD. Briefly, the algorithm, written in Matlab, applied a smoothing to the IRD and temperature record by calculating a 0.5 ka running mean, before differentiating with respect to time. Abrupt transitions in *N. pachyderma* (s) percentage abundance and IRD concentration were then identified when their derivatives exceed a set threshold. In this instance, the change in % concentration of *N. pachyderma* (s) with respect to time was set to 40 and the rate of change in IRD to 100 grains per gram. These values were found to capture the major transitions within the record.

Under these parameters, 20 cooling events were identified, 17 of which had associated rafting events. The onset of stadial cooling was found to occur on average 600 years prior to the appearance of IRD. These lag times are slightly longer than those recorded by Barker et al. (2015) who found a lag time of around 200 years from Northeast Atlantic core ODP983. IRD peaks tend to occur towards the end of IRD intervals and thus the average lag between the onset of temperature decline and IRD peak is slightly longer, at 700 years.

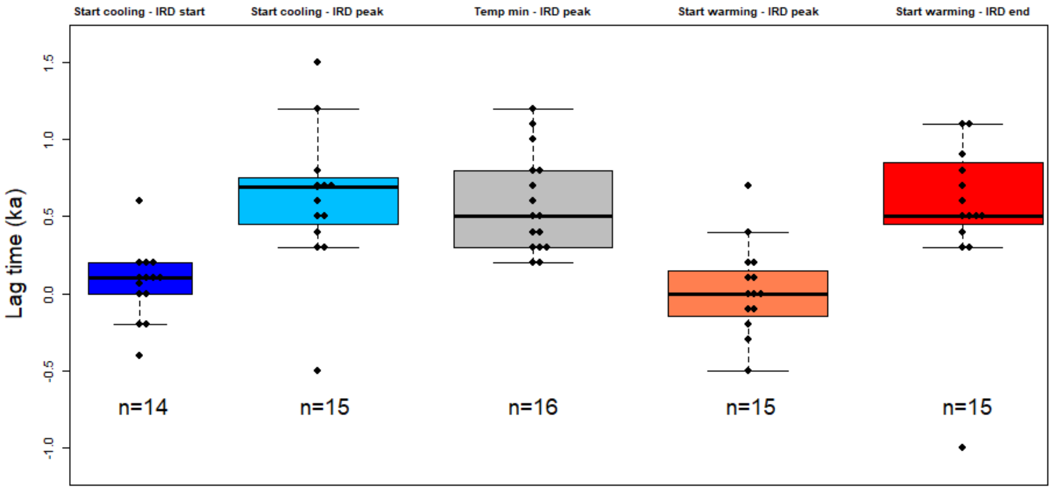

Figure 6.18 Lag times between temperature and IRD transitions. A positive lag time means the temperature transition occurred before the IRD response and negative vice-versa. Box is the interquartile range and minimum/maximum values shown by the bars.

17 of the MD99-2251 cold events exhibit subsequent warming, 15 of which also have associated IRD events. In the majority of instances (11/15) IRD peaks prior to the subsequent warming. The average gap between warming onset and IRD peak is negligible (10 yrs), however, there is considerable variability with the onset of warming ranging from 1.8 ka prior to the IRD peak to 700 years after. On average, warming commences some 600 years before IRD counts decline to background levels. This is in contrast to Barker et al. (2015), who found a closer alignment between warming and the disappearance of IRD. In the MD99-2251 record, the onset of warming is largely coincident with IRD peaks rather than IRD disappearance.

The ~600-year average lag between cooling events and the subsequent arrival of IRD supports the findings of the aforementioned proxy studies and their conclusion that iceberg rafting from Northern Hemisphere ice sheets cannot be the initial driver of Greenland Stadial events. Several modelling studies have suggested that freshwater input into the North Atlantic may act to prolong stadial events (Alvarez-Solas et al., 2013; Clark et al., 2013) and this effect cannot be ruled out.

These findings also counter Johnson & Lauritzen's (1995) proposal that Heinrich Events were triggered by repeated glacial lake flooding after Laurentide ice dam failure. Rather than drive ice sheet melting and destabilisation of ice dams, cooling prior to the rafting episodes would be expected to have the opposite effect.

6.7.3 Heinrich events H3 and H6

The prolonged and less pronounced nature of H3 and H6 within the sedimentary record (Hemming, 2004) led Gwiazda et al. (1996) to suggest that these events might be incidences of low foraminifera abundance, rather than absolute increases in IRD flux. In this study, both events have been defined as short lived pulses of similar duration to the other Heinrich events (1.2 ka for H6, and 0.7 ka for H3). However, their position amongst extended Greenland stadials (GS18 for H6, and GS6 to GS4 for H3) mean that they are situated within extended periods of ice rafting which may offer some insight into their longevity within other records. Both events appear as prominent IRD spikes and there’s little to suggest these arise simply from a decrease in foraminifera abundance. Both are preceded by a reduction in temperature, as with other Heinrich stadials (Figure 6.16) and show no evidence of reduced foraminifera abundance.

Wary et al. (2015) termed HS3 a three-phase event. Their magnetic susceptibility record from Southwest of the Faroe Islands indicated two peaks at 30.5 and 29.5 (H3a and H3b) which were thought to have triggered two NADW formation reductions, interspersed with a short lived recovery. The MD99-2251 record supports these findings with IRD spikes recorded either side of 30 ka — thought to correspond to H3a and H3b in Wary et al. (2015). However, the MD99-2251 record suggests the presence of two additional rafting events at 33.1 ka and 28.1 ka such that H3 can either be viewed as a single pulse, surrounded by additional rafting events or a single event consisting of four IRD pulses, interspersed with low level continuous rafting. In this study the pulse at 31 ka has been defined as H3, as defined by Hemming (2004), with the surrounding IRD peaks associated with GS 6, GS 5.1 and GS 4.

Similarly a distinct IRD peak is observed at 64.8 ka before IRD declines to negligible levels at 62 ka (Figure 6.8). As such this event appears distinct from the IRD peak at 59.4 ka which is attributed to H6. The timing of H6 is poorly constrained, with best estimates putting it at 5 ka either side of at 60 ka (Hemming, 2004). In magnetic susceptibility measurements from core U1308 from the mid North Atlantic (Hodell et al., 2008) and IRD counts in core NEAP 18K (Chapman & Shackleton, 1999) from the Gardar Drift, H6 exhibits a prolonged signal, commencing around 65 ka and incorporating the event seen at 64.8 ka.

It is suggested here that the exceptionally high sampling resolution in the MD99-2251 record compared with that of NEAP 18K (in the order of every 200 yrs) allows the 64.8 ka event to be resolved from the more pronounced H6 peak. As previously mentioned, IRD compositional analysis for the 64.8 ka event shows a small concentration of carbonate grains that are not seen in the larger H6 event. This further supports the assertion that the event is distinct from H6 which has been shown to be largely void of a carbonate signature in North East Atlantic cores (Bond et al., 1992).

6.7.4 Heinrich events 7a and 7b and the MIS 5/4 transition

The events attributed to Heinrich event 7 in this study were first subdivided into H7a and H7b by Rasmussen et al. (2003) in core EW9302-2JPC from the Newfoundland coast. The events were characterised by high detrital carbonate content and a $\delta^{18}O$ spike in *N. pachyderma* (s). However, the events are not observed in core EW9302-1JPC, situated just 50 km north of EW9302-2JPC, nor in cores from the Reykjanes Ridge (Rasmussen et al., 2003).

Only a relatively minor H7b spike is recorded in core MD95-2024 from the Orphan Knoll which Weber et al. (2001) attributed to a single H7 event (Figure 6.15). In additional records from the Orphan Knoll (Channell et al., 2011) and in other North Atlantic records (Figure 6.15), the event remains largely unreported (although H7 has been attributed to rafting at ~130 ka by Van Kreveld et al. (1996), this is not considered here as it is clearly a separate event).

Both events 7a and 7b are recorded in the MD99-2251 record as relatively minor IRD spikes (Figure 6.16 and Figure 6.17). Their presence in the aforementioned core records, as well as site U1308 suggest that they are non-localised events. However, both events appear as relatively minor spikes across all records (Figure 6.15), suggesting that they could be considered as standard glacial rafting episodes rather than major rafting events. Certainly the low concentration of carbonate material within these rafting events does not suggest a Laurentide origin as observed in the majority of the last six Heinrich events (Naafs et al., 2013).

H7b is a short lived (<100 yrs) event occurring at 76.5 ka, towards the end of GS 21. H7a is characterised as a prolonged rafting episode between 69.3–66.8 ka. It occurs in close temporal proximity to additional rafting events C19 and H6. It is suggested that the prolonged nature of H6 and poor constraint over its timing (Hemming, 2004) may arise when both C19 and H7a cannot be resolved from H6, and are therefore considered all considered as a single event.

H7a is unusual in that it occurs relatively early within a Greenland Stadial event, in this case GS19.1. However, the short timeframe between GS19.2 and GS19.1 mean that temperatures begin to decline some 1.2 ka prior to the initial IRD spike and remain low with only a short lived interstadial between. Viewed in this manner, H7a can be considered to have occurred mid-way through GS 19, but it is unusual in that it is not associated with subsequent warming — as are the majority of rafting events.

The high sampling resolution of MD99-2251 allows identification of three distinct peaks within H7a at 69.3, 68.7 and 66.9 ka. The last of these, at 66.9 ka was first identified by Chapman & Shackleton (1999) as the C19 cold event in core NEAP18K and later assigned the name H7a by Rasmussen et al. (2003). Despite a relatively high sampling resolution in NEAP18K, in the order of every 300 yrs during this interval, the event is identified as a single, prolonged peak of ~1500 years. The event is not identified in core U1308, situated to the south of MD99-2251, in the centre of the Ruddiman's IRD belt (Hodell et al., 2008) but occurs at the beginning of a prolonged period of rafting attributed to H6.

The identification of distinct H7a IRD peaks in the MD99-2251 record may be the result of improved sampling resolution. However, resolution in U1308 and NEAP 18K remains relatively high over this period and should be sufficient to identify these events. Thus it is suggested that the presence of multiple peaks may arise from the higher latitude location of MD99-2251. These are relatively minor rafting events, with lithology data suggesting an Icelandic/Jan Mayan source. Thus it is possible that sufficient iceberg penetration did not reach far enough south to allow peak resolution within these other cores.

6.7.5 What happened to Heinrich event 9?

One clear feature of the MD99-2251 record is the conspicuous absence of rafting events between 104–86 ka. The largest recorded event within this interval is the IRD peak between ~95–90 ka — identified in core EW9302-2JPC (Rasmussen et al., 2003) from the Newfoundland Coast and attributed to H9. The event is characterised by a high abundance of detrital carbonate, combined with reduced planktonic $\delta^{18}O$. A coincident IRD spike is observed in core MD95-2024 (Figure 6.15), although the authors do not directly attribute it to H9 (Weber et al., 2001).

Whilst the event is prominent in these two Newfoundland Coast records, it is largely absent from both U1308 and MD99-2251, and appears as a minor, prolonged spike in JPC-13 (Figure 6.15). It coincides with cold event C22 in NEAP 18K (Chapman & Shackleton, 1999), although in this record it is signified by a relatively minor, short lived peak. The high carbonate content observed in EW9302-2JPC indicates a Laurentide Ice Sheet derived event, and its absence from the MD99-2251 and U1308 records suggests limited penetration of icebergs into the north east Atlantic.

6.8 The North Atlantic during the last glacial

The MD99-2251 multiproxy record is presented in Figure 6.16 and compared alongside nearby cores KN166-14-JPC-13 (hereafter JPC-13) (Hodell et al., 2010), MD95-2042 (Shackleton et al., 2004) and NEAP18K (Chapman & Shackleton, 1999) in Figure 6.19 and Figure 6.20. MD95-2042 and NEAP18K have been aligned with the NGRIP record by Mark Chapman as part of this study. The JPC-13 record is plotted on the age model constructed by Hodell et al. (2010) with alignment to the MD95-2042 record of Shackleton et al. (2004) up to 80 ka, and the Lisiecki & Raymo (2005) benthic stack thereafter. The differing timescales on which the JPC-13 and MD99-2251 records are presented make it difficult to compare temporal offsets between the two sites; however, inclusion of the JPC-13 gives information of the spatial extent of North Atlantic events and wider environmental trends.

Comparison with the benthic $\delta^{13}C$ records from these three additional core allows inferences about the rate of oceanic ventilation to be made. $\delta^{13}C$ has long been established as a means to infer oceanic ventilation rates (Keigwin, 2004; McManus et al., 2004) with the enhanced downwelling of high productivity surface waters leading to elevated $\delta^{13}C$ in the lower ocean.

However, ventilation is not the sole control on $\delta^{13}C$, with variation in end member location and atmospheric CO_2 fluctuations also driving changes in the palaeorecord (Curry, 1988; McManus, 1999). These competing influences make it difficult to derive absolute ventilation changes (LeGrande & Wunsch, 1995) yet the $\delta^{13}C$ record still provides a useful indicator of large scale ventilation variability.

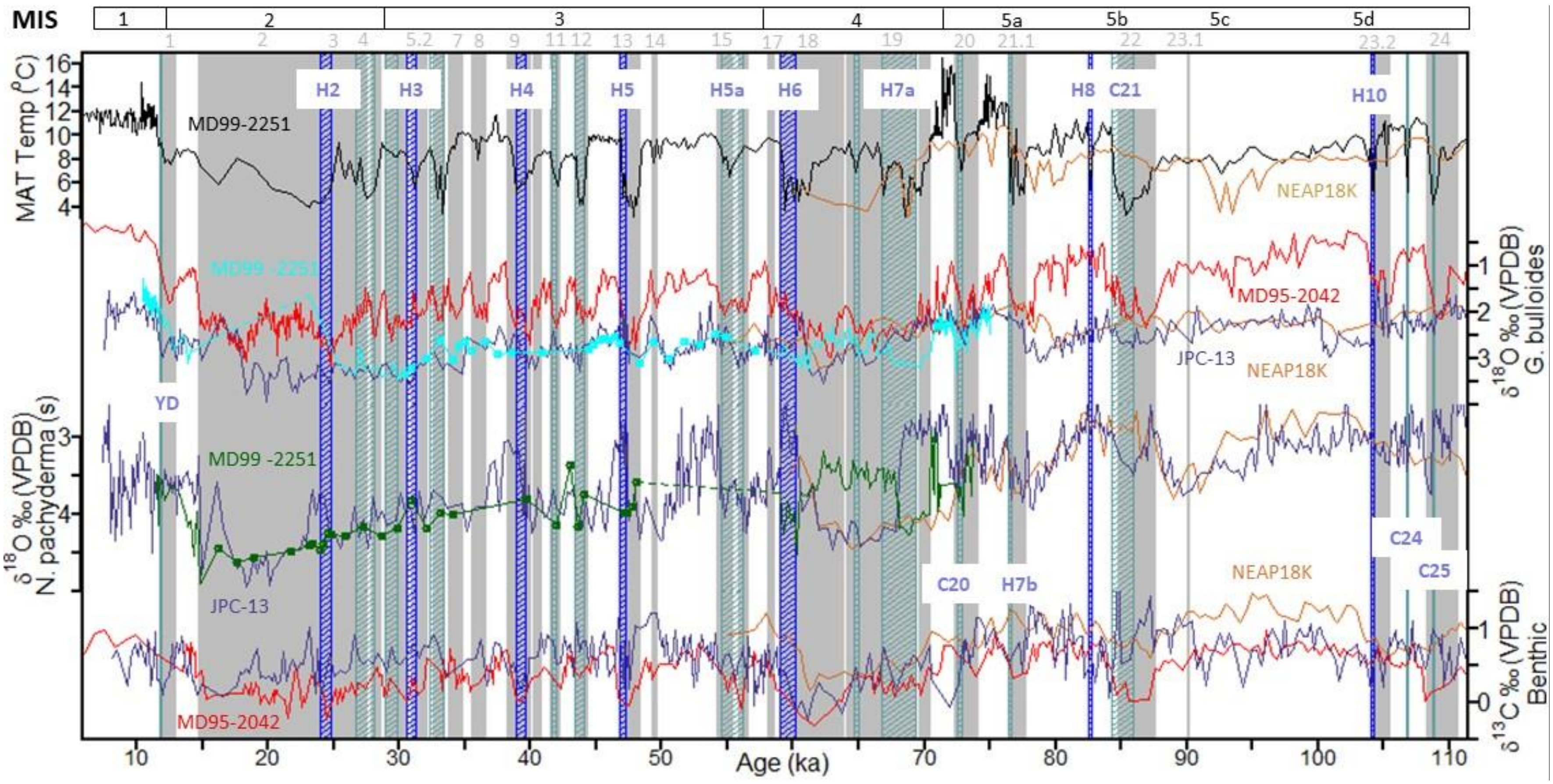

Figure 6.19 MD99-2251 temperature and isotope comparisons with local core records. Top to bottom: MAT inferred temperatures from MD99-2251 (black) and NEAP 18K (brown); *G. bulloides* δ^{18}O records from MD99-2251 (cyan), MD95-2045 (red), NEAP 18K (brown) and JPC-13 (blue); *N. pachyderma* (s) δ^{18}O records from MD99- 2251 (green), NEAP 18K (brown) and JPC-13 (blue); benthic δ^{13}C records from MD95-2042 (red), JPC-13 (blue), and NEAP 18K (brown). MD95-2042 (Shackleton et al., 2004), JPC-13 (Hodell et al., 2010), NEAP 18K (Chapman & Shackleton, 1999). Grey numbering indicates GS episode (Rasmussen et al., 2014). Marine isotope stage transitions from Lisiecki & Raymo (2005), 5a – 5d are positions of isotopic peaks.

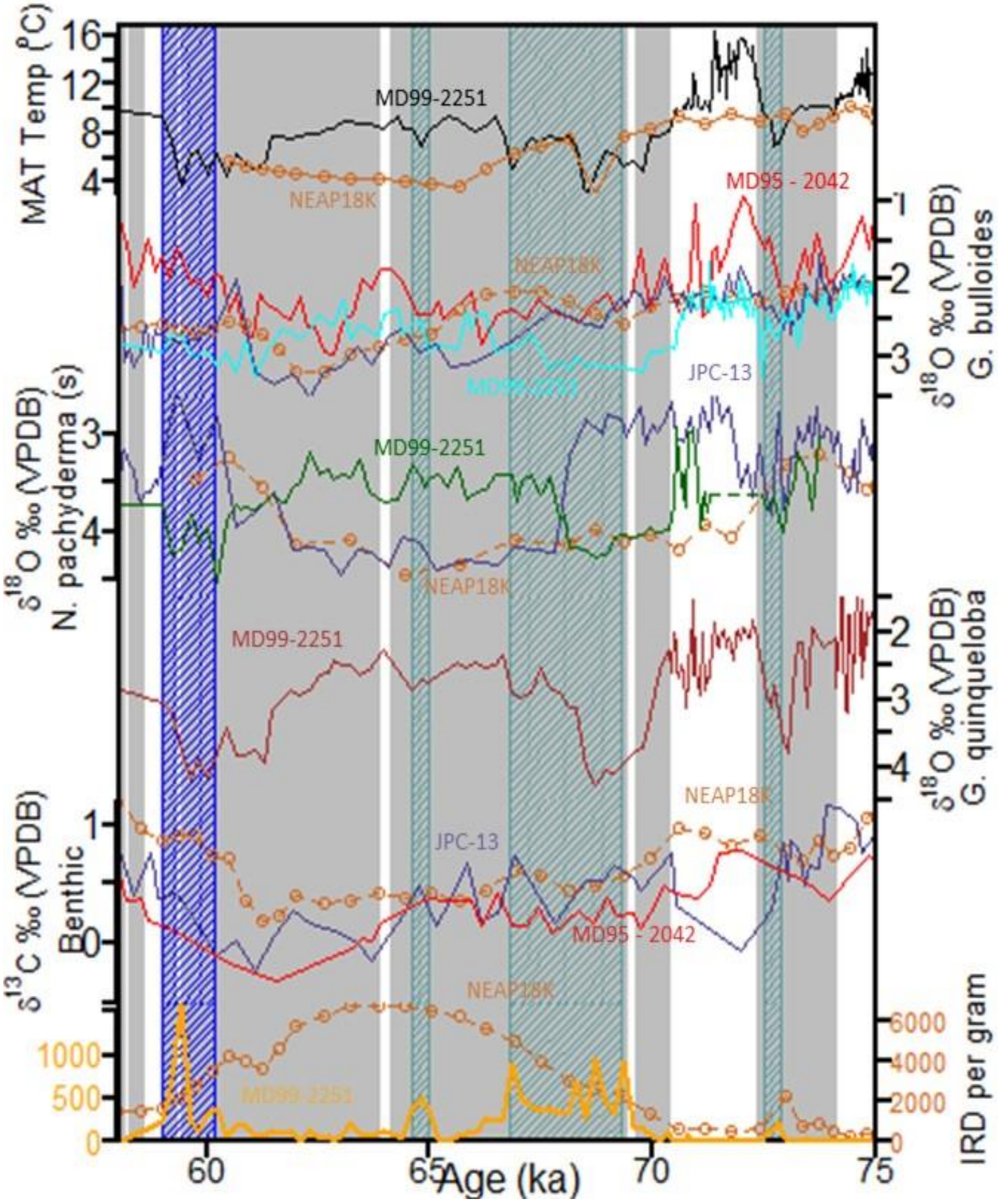

Figure 6.20 MD99-2251 MAT temperature and $\delta^{18}O$ comparisons with local core records for the high resolution section of the core. From top to bottom: MAT inferred temperature: MD99-2251 (black) and NEAP18K (brown); *G. bulloides* $\delta^{18}O$ records: MD99-2251 (cyan), NEAP 18K (brown), MD95-2042 (red), and JPC-13 (blue); *N. pachyderma* (s) $\delta^{18}O$ records: MD99-2251 (green), NEAP18K (brown), and JPC-13 (blue); *G. quinqueloba* $\delta^{18}O$ record from MD99-2251; benthic $\delta^{13}C$ records from NEAP 18K (brown), JPC-13 (blue), MD95-2042 (brown); IRD concentration from MD99-2251 (orange) and NEAP 18K (brown). Note the offset in the y-axes. NEAK18K (Chapman & Shackleton, 1999), MD95-2042 (Shackleton et al., 2004), JPC-13 (Hodell et al., 2010)

6.8.1 MIS 5

MAT-derived SSTs gradually decline throughout MIS 5 as the record progresses towards full glacial conditions (Figure 6.19). Temperatures during MIS 5 average 9.9 ± 1.5 °C, some 1.5 °C lower than both the modern day and early Holocene MAT temperature of 11.5 ± 0.8 °C. Chapman & Shackleton (1999) consider cold event C25 to mark the transition into glacial conditions after the MIS 5e warm period, and the gradual decline in their MAT-derived SSTs in NEAP 18K can be observed thereafter, prior to increasing once more during MIS 5a (Figure 6.19). Similarly, the MD99-2251 temperature shows a gradual temperature decline over the same period of approximately 1.4 ± 1.5^{0}C through MIS 5d–5b. The decline is punctuated by three short lived cold excursions of approximately -6 ± 1.5 °C of C25, C24 and H10 respectively. High δ^{13}C throughout MIS 5d–5c in all three benthic records suggest a strongly ventilated AMOC.

As the record progresses through MIS 5b, GS 22 is associated with a temperature decline of approximately 5± 1.5 °C to minima of 3.6 ± 1.5 °C. δ^{13}C reductions of approximately 0.5 ‰ in all three benthic records suggest the temperature decline is accompanied by a reduction in North Atlantic ventilation.

MIS 5a shows an average temperature increase of some 4 °C above MIS 5b, with a high degree of variability. Temperatures average 11 ± 0.8 °C with highs of up to 15 ± 0.8 °C and a minimum of 5.1 ± 1.5 °C during H7b. A coincident temperature increase is observed within the NEAP 18K record — yet temperatures average 8 – 11 °C with a maximum temperature of 10.9 °C, and reduced variability compared to the MD99-2251 record. Suppressed δ^{18}O in the MD95-2042 record during this period also suggests warmer temperatures across the North Atlantic.

The magnitude of the MD99-2251 MIS 5a MAT temperature increase is somewhat surprising, with short lived excursions up to 4.5 °C above the modern day World Ocean Atlas temperature. It is telling that these high temperatures are not mirrored in the Mg/Ca temperature reconstructions with *G. bulloides* temperatures averaging 10.6 °C and increasing above 13 °C on only two occasions (Figure 6.16). These high MAT temperature samples are unique in that they contain a high percentage of *G. inflata* specimens such that the closest modern analogue equivalents are found from coastal cores with relatively warm SSTs. Heightened *G. inflata* abundance has been used as an indicator for increased influence of the North Atlantic Current

(Staines-urías et al., 2013) and it this may also be the case during MIS 5a. Increased δ^{18}O values support the notion of an influx of warm, saline North Atlantic Waters.

With constant Mg/Ca temperatures over the interval, it is recommended that the elevated MAT inferred temperatures across MIS 5a be treated with some caution. Whilst elevated temperatures compared with the MIS 5d – 5b are likely, the magnitude of the increase is subject to a high degree of uncertainty. The discrepancies between the MAT and Mg/Ca inferred temperatures highlight a limitation of the MAT technique and further work to expand the modern analogue dataset may provide enhanced accuracy.

The MD99-2251 MAT temperature exhibits a much higher degree of variability compared to that of NEAP18K. Whilst the closer proximity of MD99-2251 to Greenland might suggest it more closely reflects stadial/interstadial temperature fluctuations, the high variability in the more Southerly MD95-2042 record, from the Iberian margin suggests that the entire North Atlantic was subject to high frequency temperature fluctuations. The relative stability observed in NEAP18K is thus more likely a result of the lower sampling frequency meaning that short lived variability is unresolved. The higher resolution MD99-2251 and MD95-2042 records suggest MIS 5a was a period of high-frequency temperature fluctuations.

6.8.2 MIS 5/4 transition

The biggest temperature shift is associated with the MIS 5/4 transition. The transition falls within the highly resolved section of the record and as such it is possible to study isotopic and IRD changes in some detail. This dramatic 7.0 ± 1.5 ^{o}C temperature transition occurs over a period of 3.2 ka from 71.3–68.1 ka. The temperature decline observed here is somewhat larger than the 2–3 ^{o}C observed in core SU90-03 (Chapman & Shackleton, 1998). This is likely in part due to the more Southerly location of SU90-03 although – as discussed in the previous section – there is a large uncertainty in the MD99-2251 MAT temperatures inferred before the transition, and thus the magnitude of the temperature drop within this record may be somewhat less.

An approximately 500-year lag is observed between the commencement of the MAT SST transition and a dramatic δ^{18}O transition of 1–1.5 ‰ which is observed across all three species in MD99-2251 between 70.8 and 69.1 ka. Whilst reduced temperatures in MIS 4 undoubtedly play a role in driving the $\delta^{18}O$ increase, the lag hints towards a delayed ice sheet growth response. Similar magnitude transitions are seen in the MD95-2042 *G. bulloides* record, as well as the JPC-13 and NEAP18K *N. pachyderma (s)* $\delta^{18}O$ records. In MD95-2042 and NEAP18K, the transitions begin earlier than in the MD99-2251 record such that no lag can be seen from the MAT record. It is interesting that an approximately 5 ka lag is seen between the isotopic shifts in MD99-2251 and JPC-13 *N. pachyderma (s)* records. This may be explained by chronological misalignment, yet the relative similarity in the *G. bulloides* records suggests the shift may arise from shifts in subsurface end members. Future work should look to investigate the cause of this lag.

Declining benthic $\delta^{13}C$ values hint towards a slow reduction in North Atlantic ventilation over this interval, however the timing differs between records. MD95-2042 exhibits a sharp decline at 72.0 ka following an elevated $\delta^{13}C$ plateau during MIS 5c and MIS 5b. The downward trend continues for some 10 ka, settling to lower values at 61.6 ka. The decline in NEAP 18K precedes that of MD95-2042, with $\delta^{13}C$ peaking at 76.6 ka and declining through the MIS 5/4 transition. The prolonged decline continues for some 15 ka, reaching a $\delta^{13}C$ minima at 60.2 ka. Benthic $\delta^{13}C$ records from core SU90-03 support these findings with a sharp reduction occurring some 5 ka prior to the MIS 5/4 transition and remaining suppressed until ~60 ka (Chapman & Shackleton, 1998).

It was suggested in section 6.6.3 that the increase in *G. quinqueloba* $\delta^{13}C$ observed during the MIS 5/4 transition and maintained some 1.5 ka thereafter may reflect increased surface pooling of high nutrient waters, driven by a slowing North Atlantic Current. However, any surface effect is not mirrored in the benthic records explored here. Whilst *G. quinqueloba* exhibits a 1.5 – 2 ‰ transition over a timespan of ~800 years, the benthic response is muted and there's no evidence to suggest a reduction in downward ventilation.

The position of the MIS 5/4 transition during a prolonged reduction in oceanic ventilation suggests that suppressed AMOC heat transport to the Northerly latitudes may have played a role in driving the temperature decline. The MIS 5/4 transition signifies a non-linear response, perhaps reached once ice sheet extent had surpassed a threshold volume. Modelling studies by Gildor & Tziperman (2003) have suggested enhanced albedo from gradual ice sheet expansion can drive non-linear responses once temperatures drop sufficiently to allow rapid sea ice formation. The dramatic $\delta^{18}O$ transitions observed shortly after the temperature decline certainly suggest extensive ice sheet expansion. It is proposed then that the onset of H7 at 69.3 ka may be the result of the ice sheets expanding beyond an instability threshold.

6.8.3 MIS 4 to the LGM

MAT-derived SSTs across MIS 4, MIS 3 and MIS 2 average 7.9 ± 1.5 °C, 8.1 ± 1.5 °C and 7.1 ± 1.5 °C respectively. The warmest temperatures throughout this interval are found immediately following H4 from 34 – 39 ka where MAT temperatures average some 9.6 ± 1.5 °C, just 2 °C colder than the early Holocene average. The period is punctuated by cold excursions – each associated with increased ice rafting – during every Greenland Stadial interval. Temperature transitions average -4 °C with some, such as during H5, as large as -7 °C.

The lowest temperature within the entire record is found at the LGM, with MAT temperatures as low as 3.9 ± 1.5 °C inferred at 23.1 ka. Planktonic $\delta^{18}O$ continues to increase throughout and beyond the LGM, peaking at 14.8 ka.

6.8.4 Bolling warm period, Younger Dryas and the onset of the Holocene

MAT inferred temperatures gradually increase from the LGM onwards, accompanied by increasing AMOC ventilation from 21.5 ka — signified by increasing $\delta^{13}C$ within the MD95-2042 record. A sharp decrease in *N. pachyderma* (s), $\delta^{18}O$, and MAT temperature at 16.1 ka marks the onset of the Bolling warm period. This timing is slightly earlier than existing estimates (Adkins, 1998) however the low sampling resolution (~1.4 ka) during this section of the core mean there is a high degree of uncertainty assigned to this age.

Shortly after the onset of the Bolling warm period, benthic $\delta^{13}C$ from MD95-2042 exhibits a step-like increase (Figure 6.19), commencing at 15.3 ka, suggestive of an upturn in oceanic ventilation. Despite the upturn in ventilation and increasing temperatures at the onset of the Bolling warm period, $\delta^{18}O$ exhibits a sharp increase (approximately 0.5 ‰) in both planktonic species, suggestive of increasing salinities. A similar response is observed at the Barra fan by Kroon et al. (1997), where the isotopic increase is due to the influx of warm, highly saline water from the subtropics and insolation-driven evaporation enhancing the salinity of water advected to high latitudes. The increased salinity enhances downwelling sufficiently such that the AMOC operated in a ‘superconveyor’ like state.

The early Bolling warm interval marks a highly variable period for the AMOC. The initial upturn in ventilation and corresponding δ^{18}O peak is short lived (approximately 200 years) with both benthic δ^{13}C records suggesting an increased, but highly variable rate of AMOC ventilation thereafter (Figure 6.19). A short lived increase in benthic δ^{13}C and a coincident ~0.6 ‰ planktonic δ^{18}O excursion at 14.4 ka suggest a second period of enhanced AMOC ventilation.

The Younger Dryas is identified by an approximately 0.5 ^{o}C drop in MAT inferred temperatures between 13 – 11.8 ka. A reduction in benthic δ^{13}C occurs shortly prior to the onset of the Younger Dryas in MD95-2042 and throughout in JPC-13, consistent with earlier findings that suggest the period marked a downturn in AMOC ventilation (Clark et al., 2001). However, after this initial reduction, increasing δ^{13}C in both benthic records suggest ventilation quickly recovers throughout the Younger Dryas, alongside increasing temperatures.

The rafting event at 11.7 ka marks the end of the Younger Dryas cold period with a ~4 ^{o}C MAT temperature increase observed over an approximately 600 year period between 12.1 and 11.5 ka. Early Holocene temperatures remain stable, averaging 11.5 ^{o}C – the same as the modern day World Ocean Atlas temperature at the site. MD95-2042 benthic isotopes suggest the AMOC enters a prolonged, intense period of stability by 10.5 ka.

6.8.5 Ventilation changes in response to Heinrich events

Comparison with the MD95-2042 benthic records suggest ventilation reductions immediately followed H10, H6, H2, and H4, with rapid recoveries observed in under 500 years. Ventilation minima have also been observed during these events by Vidal et al. (1997) and Wary et al. (2015). The latter study also found evidence of a ventilation reduction subsequent to H3. Yet the North Atlantic response to H3 remains ambiguous with conflicting studies from the Florida Straight finding no evidence of an AMOC slowdown (Lynch-Stieglitz et al., 2014a). Similarly, no reduction is observed within MD95-2042. However, a reduction is associated with the GS 5.1 rafting event and it may be this reduction, occurring in close proximity to H3, that is observed by Wary et al. (2015).

These findings appear to support the idea that enhanced iceberg rafting acted as a driver of AMOC reductions through the impact of surface freshening on downwelling rates (Seidov & Maslin, 2001b). Yet the MD95-2042 benthic record during H5, and the cold event associated with GS19.1, suggest this relationship may not be straightforward. $\delta^{13}C$ is observed to decrease some 1.7 ka prior to H5 and 200 years prior to the GS 19.1 rafting event. This may arise from dating uncertainty between the two records and it's unfortunate that the MD99-2251 core has insufficient specimens for a high resolution benthic record that would remove this uncertainty. However, the JPC-13 record, although not directly aligned to MD99-2251, also exhibits $\delta^{13}C$ reductions during numerous Greenland stadial events, prior to the onset of ice rafting. Thus it is suggested that whilst rafting generally acts to reduce ventilation, in some instances AMOC reduction may trigger rafting. Further work should look to investigate these mechanisms.

Numerous studies have used planktonic $\delta^{18}O$ as a proxy for surface freshening (Adkins et al., 2002; Ellison et al., 2006). The MD99-2251 planktonic record shows little evidence of freshening in response to ice rafting — although in most instances, the record is of insufficient resolution to deduce short lived transitions. An ~0.75 ‰ $\delta^{18}O$ increase is seen across all planktonic species during H7a, immediately following the IRD pulse at 68.7 ka (Figure 6.20), however a coincident increase in MAT temperature suggest this is largely temperature driven. This is not the case however for a ~1.5 ‰ increase in $\delta^{18}O$ of *G. bulloides* following H2 (Figure 6.19). A declining MAT temperature suggest this increase is largely driven by surface freshening. These findings are in contrast to those of both Wary et al. (2015) and Chapman & Shackleton (1998) who found little evidence of surface freshening after H2. The site of the Wary et al. (2015) study lies north of the MD99-2251 site, off the cost of the Faroe Islands, whilst the Chapman & Shackleton (1998) SU90-03 site, lies to the south. Thus it is surprising that a freshening should be observed in MD99-2251. However, H2 is thought to be largely derived from the Hudson Strait and thus the localised freshening seen in MD99-2251 may reflect the movement of icebergs through Ruddiman's IRD belt with meltwater not reaching as far as the other study sites.

6.9 Conclusions

MD99-2251 offers a multi-proxy record of the North Atlantic during the last glacial cycle. Particularly high resolution is obtained throughout MIS 4 – 3. Surface temperatures were highly variable, punctuated by numerous cold excursions, averaging 4 °C and with some as large as 7°C. The largest temperature transition is associated with the MIS 5/4 boundary between 71.3 and 68.1 ka, which is characterised by a non-linear response to a long term reduction in AMOC.

The region underwent a period of intense variability following the LGM at 23.1 ka. The Bolling warm period is characterised by intense ventilation and surface temperature fluctuations, accompanied by considerable ice rafting, which drives surface salinity changes. The relative stability of the Holocene is reached by 11.5 ka.

The MD99-2251 ice rafting chronology has provided enhanced detail on the nature and timing of specific Heinrich Stadial events, offering improved clarity on the timing and nature of H3 and H6, as well as showing that H7a and H7b (Rasmussen et al., 2003) exhibit suppressed magnitude across most North Atlantic records. Furthermore, the additional H5a event proposed by Rashid et al. (2003) shows similar magnitude to the more frequent stadial rafting events. The association of ice rafting events with each Greenland stadial show that such episodes are common. Thus beyond the well constrained events H1 – H6 (excluding H5a), this study advocates the use of a nomenclature system that links rafting events to their associated Greenland Stadial.

Analysis of the timing of ice rafting in comparison to the onset of Greenland cooling shows that rafting tends to occur towards the end of Greenland Stadial intervals, supporting the binge/purge model of gradual ice sheet expansion and collapse once stability thresholds are exceeded (MacAyeal, 1993). The onset of cooling has been shown to precede ice rafting, supporting the growing body of evidence that suggests Greenland cooling acted as a driver of ice rafting — as opposed to rafting driving cooling (Barker et al., 2015; Shaffer et al., 2004; Van Kreveld et al., 2000).

Comparison with nearby benthic $\delta^{13}C$ records has provided additional detail on the relationship between ice rafting and oceanic ventilation. The AMOC shows evidence of reduced downwelling following H10, H6 and H4. However, suppressed ventilation after intense iceberg rafting is by no means universal and AMOC reduction appears to lead rafting in some instances. The relationship between ice rafting and oceanic ventilation is by no means straightforward and may vary depending on the prevailing environmental conditions. Further study is required to better refine this relationship. A good first step would be the construction of an MD99-2251 benthic record. Unfortunately, the concentration of benthic specimens within the sediment is extremely low and it remains to be seen whether it would provide sufficient sample for isotopic measurements.

Methodologically, this study has shown the power of combining multiple temperature proxies, in this case foraminifera assemblage derived temperatures using the modern analogue technique and Mg/Ca ratio temperatures from multiple species. Not only does this provide information on palaeo-ocean temperature gradients and seasonality, it also overcomes uncertainties that might arise from use of a single reconstruction method. This was highlighted in MAT reconstructions of MIS 5a where a lack of suitable modern analogue assemblages resulted in unrealistically high temperature reconstructions. Comparison with Mg/Ca inferred temperatures provides context and allows temperature estimates to be better constrained.

Finally, this study has highlighted the use of *G. quinqueloba* as an excellent species for isotopic measurements since it exhibits a strong isotopic temperature response, of higher magnitude than highly utilised species such as *G. bulloides* and N *pachyderma* (s). Whilst the small test size makes it a time consuming species to isolate from the bulk sediment, it is suggested that if this can be overcome, it is a potentially powerful species for future studies.

Chapter 7. Termination II and MIS 5e in the outer Labrador Sea

7.1 Background and Introduction

7.1.1 Core U1302

U1302 (50°9.985’N, 45°38.271’W, 3568.6 m depth) is an advance piston core collected by the JOIDES Resolution in 2004 during the Integrated Ocean Drilling Programme’s expedition 303 (Channell, 2006). The cruise targeted strategic North Atlantic sites with the potential to generate high resolution records of Pliocene-Quaternary climate. The aim was to integrate the resulting geomagnetic intensity, stable isotope and palaeoceanographic proxy records to generate high resolution stratigraphies for the last few million years (Channell, 2006).

The U1302 site is situated in the Orphan Basin — a deepwater basin between 2000 – 3000 m in depth (Campbell, 2015), situated off the continental margin of Newfoundland. Throughout the Quaternary the region received significant proglacial sedimentary input from the local ice shelf which crossed the Grand Bank plateaus off the south eastern Newfoundland coast (Campbell, 2015), as well as from further afield — transported south in the Labrador Current (Tripsanas & Piper, 2008).

Previous cores from the Orphan Basin had shown the presence of numerous detrital layers, often rich in carbonate that have been linked with low productivity meltwater pulses (Hillaire-marcel, 1994; Hiscott et al., 2001; Stoner et al., 2000; Stoner & Hillaire-marcel, 1996). Thus the site was targeted to provide a record of instability of the Laurentide Ice Sheet going back farther than existing records, to the base of the core at MIS 17 (Channell, 2006).

Shipboard analysis of the 91.7 m core revealed the sediment contained a mixture of terrigenous and biogenic components with rich assemblages of microfossils (Channell, 2006). Mean sedimentation rate was 13.4 cm ka^{-1} over the length of the core, estimated by comparison to the geomagnetic polarity timescale (Channell et al., 2006).

7.1.2 Major oceanic currents affecting the U1302 site

Surface circulation at the U1302 site is dominated by the Labrador Current, a western boundary current which flows south along the North American Shelf (Figure 7.1). The current consists of an upper and lower regime. The upper regime lies over the continental shelf and transports cold, fresh water from Baffin Bay and the Hudson Strait down 2000 m (Cuny et al., 2002; Lazier & Wright, 1993). The deeper regime flows below the upper current over the lower continental shelf between 2000 – 3000 m (Cuny et al., 2002). As the Labrador Current water flows south it subducts below the northerly flowing Gulf Stream off the coast of Novia Scotia (Pickart & Smethie, 1993).

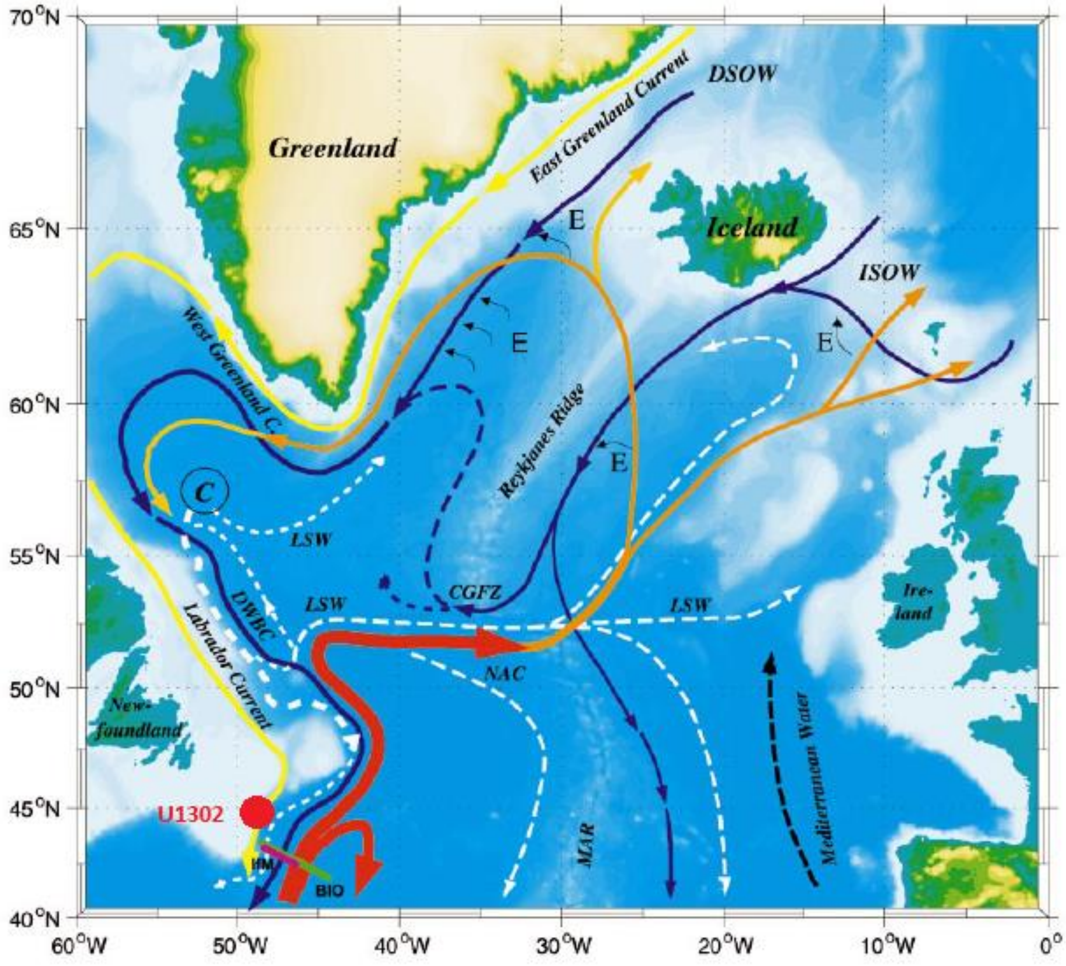

Figure 7.1 Major currents affecting the U1302 site (red circle). NAC = North Atlantic Current, LSW = Labrador Sea Water, CGFZ = Charlie Gibbs Fracture Zone, DWBC = Deep Water Boundary Current, DSOW = Denmark Strait Overflow Water. ISOW = Iceland-Scotland Overflow Water. (Adapted from Schott et al. (2004)).

Deep circulation is dominated by the Deep Western Boundary Current, which exports recently ventilated waters southward. The Deep Western Boundary Current consists predominantly of Denmark-Strait Overflow Water and Iceland-Scotland Overflow Water – formed by downwelling in the Nordic Seas – and intermediate Labrador Sea Water, formed by downwelling within the Labrador Sea itself (Pickart & Smethie, 1993; Schott et al., 2004). These waters flow south, combining with other deep water masses to form North Atlantic Deep Water.

7.1.3 Existing studies of the Orphan Knoll and surrounding region

Considerable research has been conducted in the outer Labrador Sea, including the U1302 site. ODP leg 105 provided early sedimentary records from site 647 from the nearby Southern Labrador Sea and showed the region could provide detailed chronologies of North Atlantic palaeoceanography. The regular appearance (approximately every 120 ka) of turbidite layers throughout the last 2.4 Ma at site 647 was interpreted as periods of intense meltwater input from the Laurentide ice sheet following fluctuations in the AMOC (Hiscott et al., 1989).

Hillaire-Marcel et al. (1994) compiled a record of 25 box and piston cores from the Labrador Sea which showed the presence of a vertically homogenous water mass during glacial intervals. This, they suggested, was symptomatic of suppressed NADW formation. Included within this study were the first isotopic and sedimentological records of the Orphan Knoll, obtained aboard the CSS Hudson from two cores (91-045-093 and 91-045-094), which offered detailed resolution of carbonate and Heinrich events over the last glacial cycle. Increases in coarse fraction sediment coincided with reductions in $\delta^{13}C$ and coccolithophore concentration, suggesting reduced primary productivity during ice rafting events — likely a result of elevated sea ice cover. These early piston core records were limited to the last glacial cycle, extending back approximately 100 ka (Stoner et al., 1998).

The first Images Cruise of the Marion Dufresne obtained two further cores from the Orphan Knoll, MD95-2024 and MD95-2025, which pushed the sediment record back over multiple glacial cycles. The latter core was used by Hiscott et al. (2001) to compile a ~ 340 ka ice rafting chronology of the Orphan Knoll site. 500 – 1000 ka lags between SST maxima and meltwater/IRD events were interpreted as the delayed response of ice sheets to changing oceanic currents, highlighting the region as a recorder of Laurentide ice sheet fluctuations.

Site MD95-2024 offered a somewhat shorter record, extending back approximately 110 ka (Stoner et al., 2000). Consistent Holocene isotopic offsets between epipelagic, mesopelagic and benthic foraminifera species during the Holocene in core MD95-2024 are proposed to have arisen from a highly stratified water column, indicative of thermohaline conditions (Hillaire-Marcel & Bilodeau, 2000). The increase in species offset during the last glacial was interpreted as evidence of a strong halocline, and therefore a reduction in the formation of intermediate water masses.

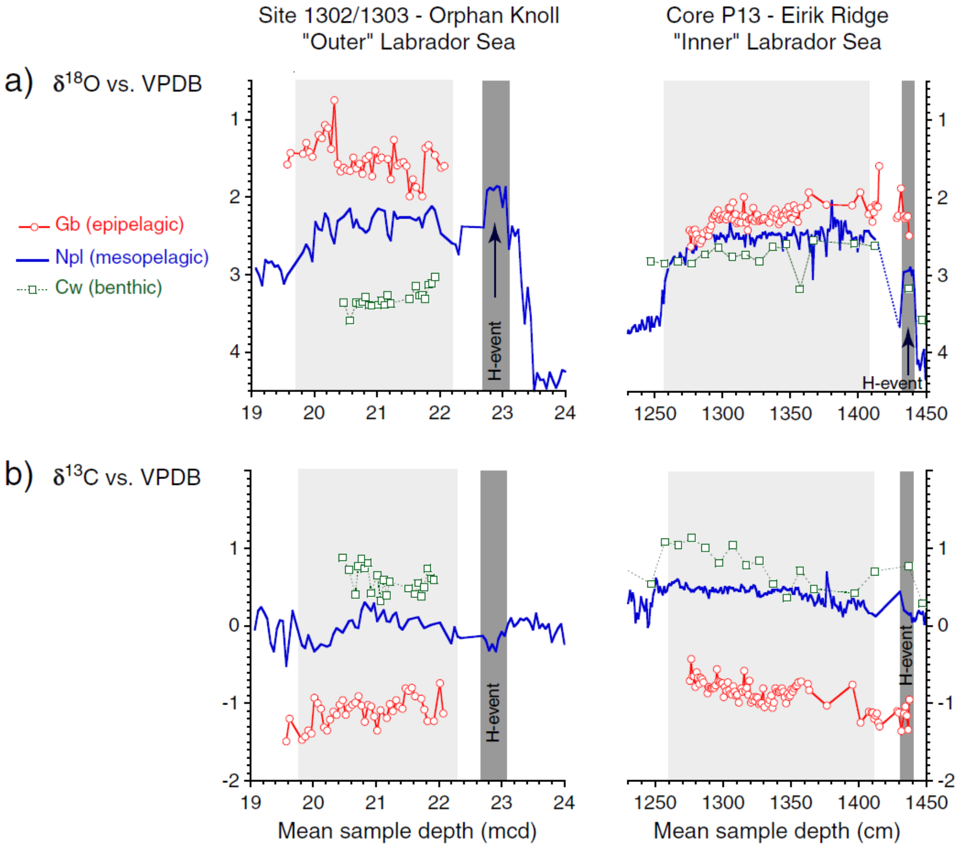

Figure 7.2 Oxygen and carbon isotopic composition of Labrador Sea cores U1302 and U1305 during the last interglacial. U1302 shows a large range of $\delta^{18}O$ values, indicative of a highly stratified water mass. Similar values across all species in U1305 suggest a single water mass across the entire water column. H-event shows H11. Light grey shading is MIS 5e plateau (Source: Hillaire-Marcel et al. 2011).

The acquisition of U1302 extended the Orphan Knoll record back to approximately 950 ka (Channell, 2006; Channell et al., 2012). Hillaire-Marcel et al. (2011) used core U1302 to produce an 800 ka high resolution $\delta^{18}O$ stratigraphy at the Orphan Knoll. This was complemented by isotopic studies detailing water mass structure during key climatic intervals.

Of relevance to this study was the production of a multispecies isotopic record across the MIS 5e plateau (Figure 7.2).

Consistent isotopic offsets between epipelagic (*G. bulloides*), mesopelagic (*N. pachyderma (s)*) and benthic (*C. wuellerstorfi*) species across the MIS 5e interval reflected those observed previously in core MD99-2024 during the Holocene (Hillaire-Marcel & Bilodeau, 2000). Thus it was concluded that MIS 5e oceanic circulation at site U1302 was similar to the modern day, with production of Labrador Sea Intermediate Water leading to a highly stratified upper ocean, and the presence of a deep NADW component sitting below it.

The U1302 record was compared to nearby core U1305 from the Eirik Ridge. At this more northerly site, isotopic offset between the three species was negligible over the MIS 5e plateau (Figure 7.2), suggesting the presence of a homogenous water mass from the surface ocean to the seafloor. δ^{18}O values at site U1305 across the three species were similar to mesopelagic values in U1302, suggesting the presence of intermediate waters throughout the water column. Significantly, heavier δ^{13}C at intermediate depths at the U1305 site, compared with U1302, suggest the presence of younger, better ventilated waters. The presence of differing deepwater masses between the two sites was further emphasised by the opposing trends in δ^{13}C of the benthic records (Figure 7.2).

Hillaire-Marcel et al. (2011) used this isotopic evidence to suggest a northerly penetration of the Western Boundary Under Current (WBUC) into the Northern Labrador Sea such that it bathes both the U1302 and U1305 sites (Figure 7.3). This is supported by earlier sedimentological data showing an active WBUC during the MIS 5e interval (Hillaire-Marcel et al., 1994). At depth, separate water masses bathe the U1302 and U1305 sites. Thus Hillaire-Marcel et al. (2011) proposed the existence of a Deep North Atlantic Water (DNAW) which passes over the more southerly U1302 site without penetrating into the Labrador Sea (Figure 7.3).

More recently Nicholl et al. (2012) used U1302 to identify a 20 cm thick layer of red detrital material deposited shortly after the transition into MIS 5e (Figure 7.4). The layer is accompanied by high Ca/Sr content and low δ^{18}O values indicating the detrital material is sourced from the Hudson Bay region of Eastern Canada (Hodell & Curtis, 2008). A similar red layer in core U1305 suggests that the detrital content arises from a massive glacial outburst event. The authors suggest the event was analogous to the flooding event at 8.4 ka, shortly after the transition into the Holocene, where glacial Lake Agassiz is thought to have drained through the Hudson Strait into the Labrador Sea (Hillaire-Marcel et al., 2007).

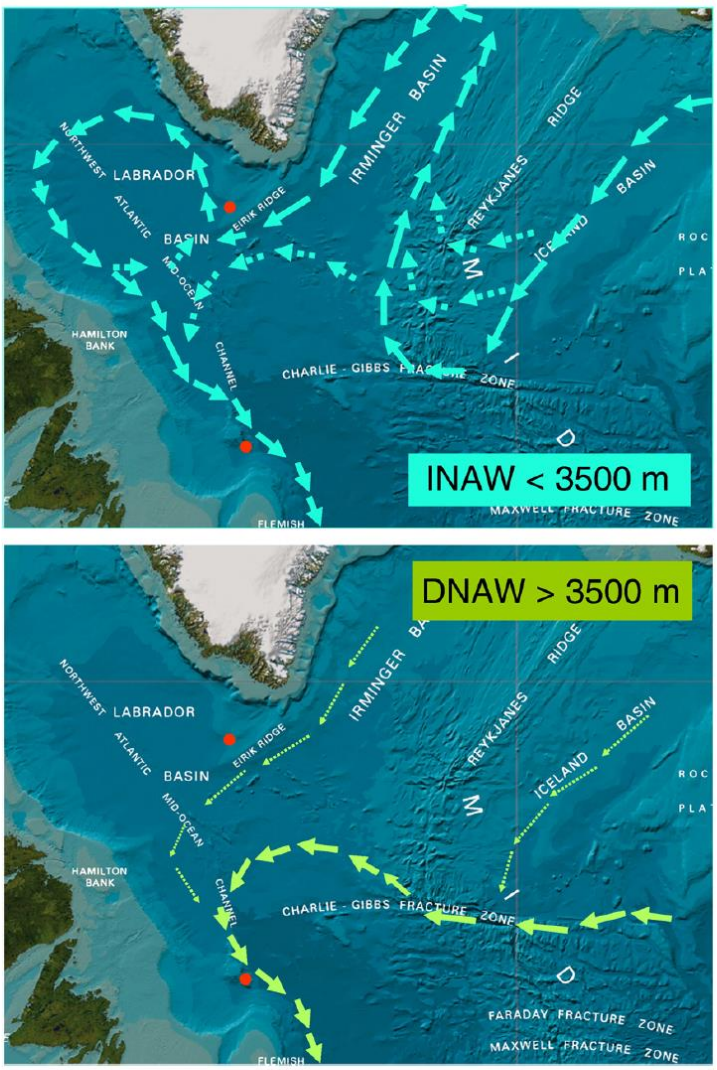

Figure 7.3 Intermediate (top) and deep water (bottom) circulation in the Labrador Sea during MIS 5e. INAW = Intermediate North Atlantic Water, DNAW = Deep North Atlantic Water (Source: Hillaire-Marcel et al., 2011)

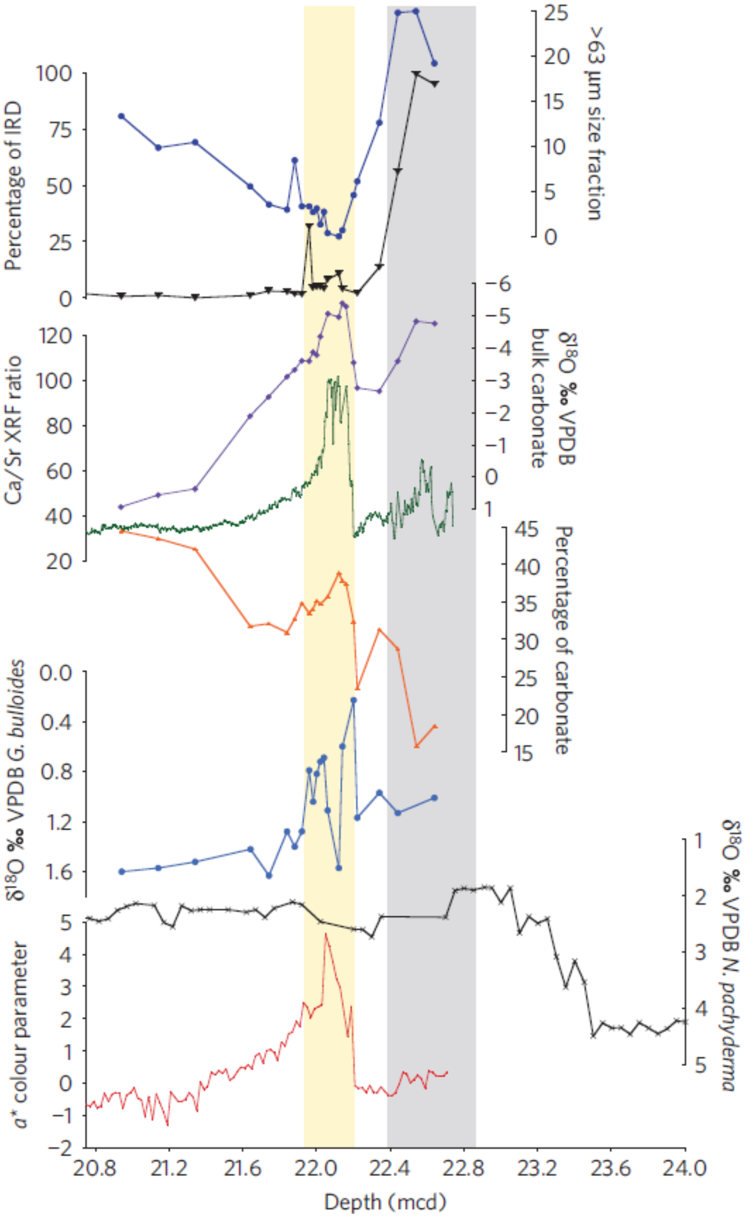

Figure 7.4 Data from core U1302 showing the position of the red layer (red banding). From top to bottom: Weight percent in the >63 µm size fraction (dark blue), % IRD (black), $\delta^{18}O$ of bulk carbonate (purple), Ca/Sr (green), weight % of carbonate in bulk sediment (orange), $\delta^{18}O$ of *G. bulloides* (blue), $\delta^{18}O$ of *N. pachyderma* (black), a* colour reflectance parameter (red). Grey vertical bar is H11. (Source: Nicholl et al., 2012).

This work has recently been expanded upon by Hume (2018), who combined the earlier Hillaire-Marcel et al. (2011) isotopic work with temperature reconstructions from fossil foraminiferal assemblages and Mg/Ca ratios, ice rafted debris counts, and Ba/Ca ratios (as a proxy for meltwater runoff) to investigate the regional responses to ice sheet dynamics. The record was extended back into MIS 6, covering Termination II and H11 which are also considered in this study.

Last interglacial temperatures at the U1302 site showed good agreement with the modern day World Ocean Atlas 1998 summer SST (Hume, 2018). Comparison of the oxygen isotopic record of U1302 with the U1305 record from the Eirik Ridge and MD95-2042 from the Iberian Margin, shows much closer agreement with the latter (Hume, 2018). This was attributed to the enhanced influence of the NAC at the U1302 and MD99-2042 site compared with U1305, reinforcing the earlier assertions of Hillaire-Marcel et al. (2011).

IRD input throughout MIS 5e remains low at U1302, with ice sheet melt ceasing after H11 at 121.1 ka (Hume, 2018). Depleted $\delta^{18}O$ throughout the early interglacial suggests reduced salinity, brought on through iceberg rafting. Depleted $\delta^{18}O$ due to warmer SSTs are ruled out because there is no indication of elevated temperatures in Mg/Ca or MAT inferred temperatures during this interval.

7.1.4 Scope of this study

This study adds two additional high resolution planktonic isotope records obtained from *G. inflata* and *N. incompta* to the U1302 archive. Both new records span the MIS 5e plateau. An additional 41 *N. pachyderma (s)*, 52 *G. bulloides*, and 10 *U. peregrina* measurements were made as part of this study to complement those from Hillaire-Marcel et al. (2011). These measurements are presented alongside an additional 7 *U. peregrina* and 24 *C. wuellerstorfi* measurements made at the University of Potsdam, Institute of Geoscience and kindly offered for inclusion in this study by Dr Stephanie Kaboth.

The new *N. pachyderma (s)* measurements fill gaps within the existing Hillaire-Marcel et al. (2011) record, giving 5 cm resolution over the MIS 5e plateau. In particular, additional clarity is obtained over the detrital red later, offering higher resolution than previously achieved – such that isotopic transitions at the pycnocline can be readily deduced. Two further planktonic isotopic records over the MIS 5e plateau allows further insight into stratification within the water column during the last interglacial. Additional benthic and *N. pachyderma (s)* measurements mean that a continuous record of the transition into the last interglacial can now be achieved at 5 cm intervals, giving sampling every ~200 years.

7.2 Results

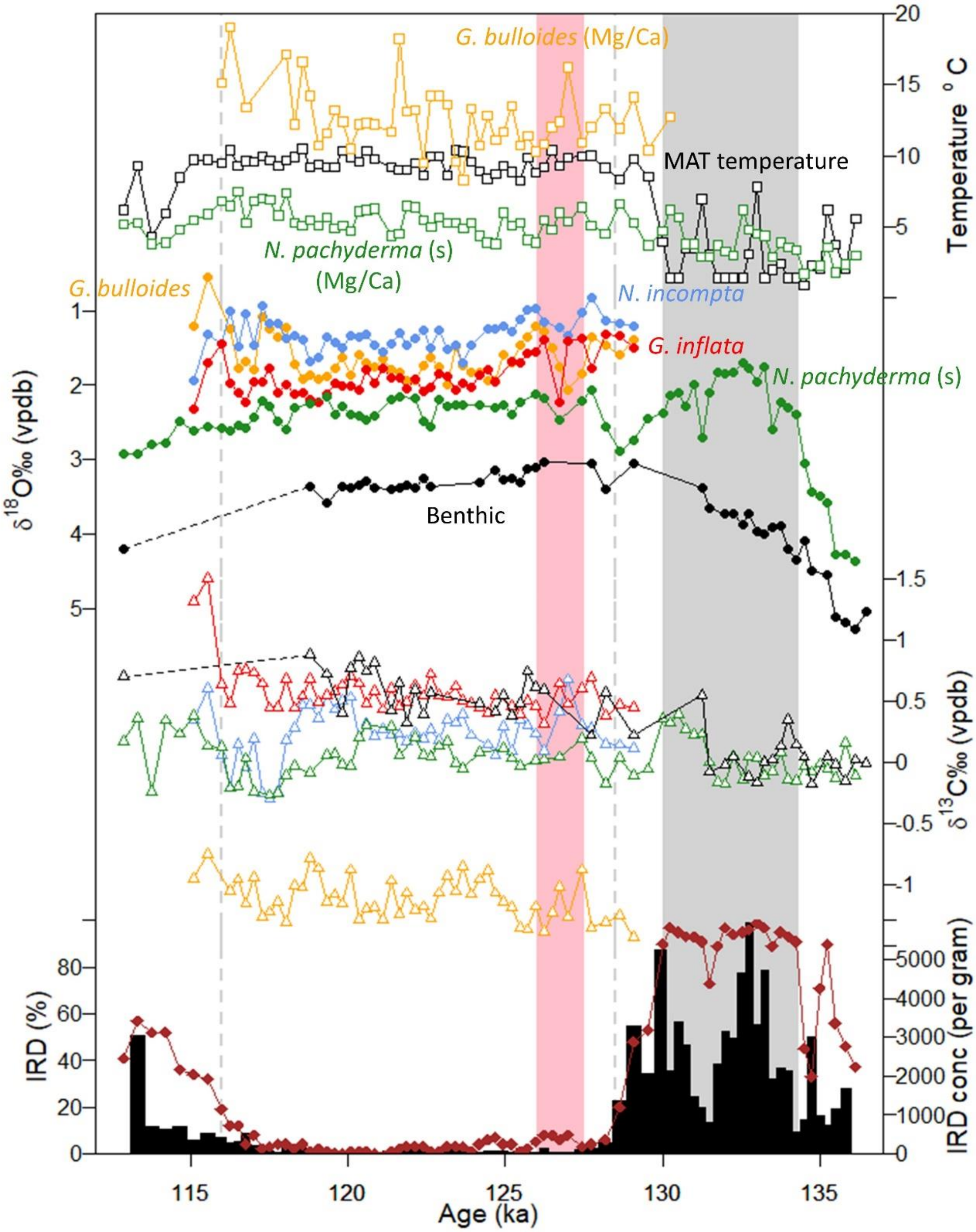

Figure 7.5 U1302 temperature (Hume, 2018), isotope and IRD (Hume, 2018) records. IRD concentration shown in the histogram and percentages in maroon points. H11 and the red layer are shown by the grey and red vertical bars respectively. MIS 5e plateau boundaries are shown by the vertical dashed lines.

The data produced in this study is presented on an updated age model developed by Hume (2018). Briefly, the age model identifies 12 isotopic events which are tied to the LR04 and LS16 reference benthic stacks (Lisiecki & Raymo, 2005; Lisiecki & Stern, 2016). In addition, the aforementioned red layer and a single IRD peak are used to provide coincident tie points with the dated record from Eirik Drift core U1305. It should be noted that whilst dates are reported to the nearest 0.1 ka in the following section, uncertainty is around ±4 ka in this section of the core (Lisiecki & Stern, 2016). All temperature and IRD data presented was produced by Hume (2018) according to the methodology outlined in Chapter 4 of this work.

The *N. pachyderma (s)* record of Hillaire-Marcel et al. (2011) has been combined with the new data from this study. A total of 30 repeat *N. pachyderma (s)* measurements were taken, showing good agreement with the original dataset, with an average offset of 0.3 ‰ in $\delta^{18}O$ and 0.4 ‰ in $\delta^{13}C$. In such cases where multiple measurements were taken at a single depth interval, average values are presented. *U. peregrina* data has been adjusted by +0.9 ‰ to allow comparison with *C. wuellerstorfi,* as is standard practice (Shackleton, 1984).

7.2.1 Termination II

Additional resolution within the *N. pachyderma (s)* and benthic isotope records allow the timing of Termination II to be reassessed. No new measurements have been obtained prior to the onset of Termination II and thus the date of 135 ka derived by Hume (2018) remains the best estimate. However, infilling of the *N. pachyderma (s)* record immediately subsequent to the Hume (2018) estimate for the end of Termination II provides additional constraint on the timing of the onset of the MIS 5e plateau.

The start of MIS 5e is often defined as the mid-point in the Termination II transition. However, Hume (2018) argued that this definition results in an erroneously cold start to the warm interglacial period, and instead defined the onset of MIS 5e as the point at which warm maxima are achieved across multiple proxies. This includes *N. pachyderma (s)* abundance, IRD, and planktonic $\delta^{18}O$ minima, alongside MAT SST maximum. In this study, this point will be defined as the start of the MIS 5e plateau, as per conventional nomenclature.

The new *N. pachyderma (s)* data provides additional resolution subsequent to H11 such that it can be shown $\delta^{18}O$ continues to decrease for some ~2 ka after IRD levels decline to near zero, reaching minimum values at 127.7 ka (Figure 7.5). Decreasing trends are also observed up to 127.7 ka in the *G. bulloides* and *N. incompta* δ^{18}O records produced for this study, albeit across a relatively limited time window due to the limited timespan of the record.

Although this updated interpretation of the planktonic isotope record suggests a later start to the MIS 5e Plateau than of Hume (2018), it is important to view this within the context of the other proxies. MAT and Mg/Ca inferred temperatures plateau by 128.5 ka, with IRD declining to negligible levels. Thus it is reasonable to assume that full interglacial conditions had been reached by this point. With steady temperatures, it can be assumed that the continued decrease in planktonic δ^{18}O between 128.6 and 127.7 ka likely arises from surface freshening. Support for this comes from elevated Ba/Ca ratios in Eirik Drift core U1305 during this period, suggesting increased runoff from terrestrial sources (Hume, 2018) — most likely the nearby Greenland Ice Sheet. Enhanced freshwater runoff has also been identified during the early part of MIS 5e in core NEAP 18K from the Gardar Drift (Hodell et al., 2009).

Increased resolution of the *N. pachyderma (s)* record over Termination II reveals the decreasing δ^{18}O trend is punctuated by two short lived enrichment excursions of +0.4 ‰ and + 0.6 ‰ at 133.5 ka and 131.3 ka respectively (Figure 7.5). A similar ‘step-like’ deglacial is observed in the planktonic isotopic records from Icelandic Sea cores (Zhuravleva et al., 2017), as well as core MD01-2444 from the Iberian Margin (Skinner & Shackleton, 2006). Recent alkenone and Mg/Ca temperature recontructions from the Iberian margin show three cold excursions during H11 (Tzedakis et al., 2018), possibly the same events.

Some clues as to the cause of these excursions can be drawn from the improved benthic δ^{13}C record, derived in this study and employed here as a proxy for oceanic ventilation. The start of Termination II signifies an upturn in ventilation with benthic δ^{13}C increasing 0.5 ‰ between 135.8 and 134 ka. The resulting heat influx is evident in a coincident downward trend in *N. pachyderma (s)* δ^{18}O.

134 ka marks the onset of enhanced ice rafting associated with H11, at which point benthic δ^{13}C begins to decline — likely caused by ice-melt induced surface freshening suppressing deepwater formation. A similar downturn in δ^{13}C is seen in core MD03-2664 from the Eirik Drift during H11 (Galaasen et al., 2014; Zhuravleva et al., 2017) suggesting this is a large scale phenomenon. The *N. pachyderma (s)* δ^{18}O spike observed some 500 years later at 133.5 ka is

coincident with a ~1 ^{o}C drop in Mg/Ca temperatures. This is interpreted as evidence of localised cooling arising from suppressed heat transport into the region. The episode is short lived, with planktonic δ^{18}O and Mg/Ca temperatures exhibiting warming some 250 years later.

Benthic δ^{13}C remains suppressed for a further 2.5 ka until 131.5 ka, at which point a dramatic ~0.6 ‰ increase is observed in approximately 250 years. This is coincident with a ~4 ^{o}C jump in MAT derived temperatures and the second *N. pachyderma (s)* δ^{18}O excursion of ~0.6 ‰. The benthic response is interpreted as enhanced oceanic ventilation as the thermohaline circulation enters an active phase. The resultant influx of Atlantic water increases local temperature and salinity resulting in the observed shifts in MAT temperature and δ^{18}O. Again, this event appears short lived with MAT temperatures and δ^{18}O returning to pre-excursion values with ~500 years.

7.2.2 The MIS 5e Plateau

The end of Termination II at 128.5 ka marks the onset of the MIS 5e Plateau. Average isotopic values are presented in **Table 7.1** and show good agreement (within 0.1 ‰) with previous estimates from U1302 (Hillaire-Marcel et al., 2011 ; Channell et al., 2012). The addition of surface dwelling *N. incompta* and mesopelagic *G. inflata* illustrate a clear δ^{18}O/depth gradient, with more enriched values seen at increasing depth.

Table 7.1 Average isotopic values over MIS 5e.

	δ^{18}O, ‰ (pdb)	δ^{13}C, ‰ (pdb)
N. incompta	1.3 ± 0.20	0.2 ± 0.2
G. bulloides	1.7 ± 0.2	-1.1 ± 0.2
G. inflata	1.9 ± 0.2	0.6 ± 0.1
N. pachyderma (s)	2.3 ± 0.2	0.02 ± 0.15
Benthic	3.3 ± 0.1	0.6 ± 0.2

Modern day measurements of planktonic foraminifera at the Orphan Knoll gave average values of 1.4 – 1.9 ‰ and 2.0 – 2.5 ‰ for *G. bulloides* and *N. pachyderma (s)* respectively (de Vernal et al., 2002). The MIS 5e values obtained in this study fall well within these boundaries, suggesting a similar surface structure to the modern day.

The most remarkable feature of the planktonic δ^{18}O records is their stability throughout the entire MIS 5e window (excluding the 'red layer', detailed in 7.2.3). This is reflected in both MAT, and *N. pachyderma (s)* Mg/Ca temperature reconstructions. Similar stability has been previously observed cores from the South of Greenland (Hillaire-Marcel et al., 2001) which has been attributed to reduced deepwater formation in the Labrador Sea leading to the presence o f single, stable, surface water mass (Hillaire-Marcel et al., 2001). This is in contrast to multiple North Atlantic reconstructions which show a gradual temperature decline over the window, punctuated by short lived cold excursion events C28 – C23 (Mokeddem et al., 2014; Tzedakis et al., 2018). In core ODP 984, south of Iceland, these excursions were linked to southerly encroachments of the Arctic Front (Mokeddem et al., 2014). Modelling studies have subsequently suggested these were driven by short lived fluctuations in the AMOC cause by enhanced freshwater runoff (Tzedakis et al., 2018).

A δ^{13}C/depth gradient is not immediately apparent and differences between species may reflect nutrient availability during the time of test formation. Similar trends in δ^{13}C across multiple planktonic species support the notion of well mixed water mass in the upper water column. The early interglacial sees an increasing trend in all species to around 118 – 120 ka. Declining values thereafter are quickly reversed at the 5e/5d boundary where a dramatic increase in δ^{13}C up to 0.9 ‰ is observed across all species. The long term increase in δ^{13}C is also observed in the benthic record, suggesting a gradual increase in oceanic ventilation over time. However, the record lacks the resolution to infer many of the short-term fluctuations seen in the planktonic record.

7.2.3 Red layer

The red layer, first identified by Nicholl et al. (2012) in core U1302, has been dated to 127.5 – 126 ka using the updated chronology of this study. Nicholl et al. (2012) identified an approximately 1 ‰ decrease in δ^{18}O across the red layer which was attributed to significant surface freshening. The high resolution record produced here appears to show a positive excursion with little difference in the δ^{18}O values either side of the layer (**Table 7.2** and Figure 7.6).

Table 7.2 Isotopic excursions in each species over the red layer. Values shown are those immediately above and below the red layer. Insufficient resolution makes it impossible to determine the magnitude of the benthic excursion.

Species	Below red layer δ^{18}O	Above red layer δ^{18}O	Magnitude of excursion
N. incompta	0.8 ‰	1.0 ‰	+ 0.4 ‰
G. bulloides	1.4 ‰	1.4 ‰	+ 0.6 ‰
G. inflata	1.8 ‰	1.6 ‰	+ 0.4 ‰
N. pachyderma (s)	2.0 ‰	2.2 ‰	+ 0.5 ‰
Benthic	3.1 ‰	3.1 ‰	-

Nicholl et al. (2012) highlighted only a negative transition in epipelagic *G. bulloides,* with no change seen in the deeper dwelling *N. pachyderma (s)*. Since input of isotopically light waters through brine intrusion is likely to impact the subsurface (Hillaire-Marcel et al., 2011) and this is not seen, the transition was instead attributed to freshwater input from land-based sources.

Here the excursion is observed in both epipelagic and mesopelagic species and thus brine input cannot be ruled out. Isotopic maxima are observed at 127.0 ka for epipelagic species and 126.7 ka for mesopelagic, although it should be noted that the lower resolution of the *N. pachyderma (s)* record means that its maximum could overlap with epipelagic species.

Relatively stable temperatures suggest this is a salinity, rather than temperature driven change. Although a ~5 °C increase is seen in *G. bulloides* Mg/Ca temperature at the initial onset of the red layer, such a shift is not seen in *N. pachyderma (s),* nor MAT inferred temperatures. It seems unlikely such an extreme, short lived, excursion would be observed in one record without being observed in the other two and since this temperature jump is represented by a single datum — it seems likely to arise from an erroneous sample, rather than a physical temperature signal.

Nicholl et al. (2012) suggest the negative *G. bulloides* δ^{18}O transition arose from surface freshening, driven by the large scale draining of Lake Agassiz, analogous to that seen at 8.2 ka (Lajeunesse & St-Onge, 2008). In the record compiled here, surface freshening may be called upon as a possible mechanism by which δ^{18}O values recover to their pre-red layer values, subsequent to reaching their maxima. Yet it cannot explain the cause of the positive excursion in the initial instance. It should be noted that whist the earlier red layer record from U1302 produced by Nicholl et al. (2012) did record an overall decrease in $\delta^{18}O$ across the red layer, a positive excursion was observed within it (Figure 7.4), but was not considered further.

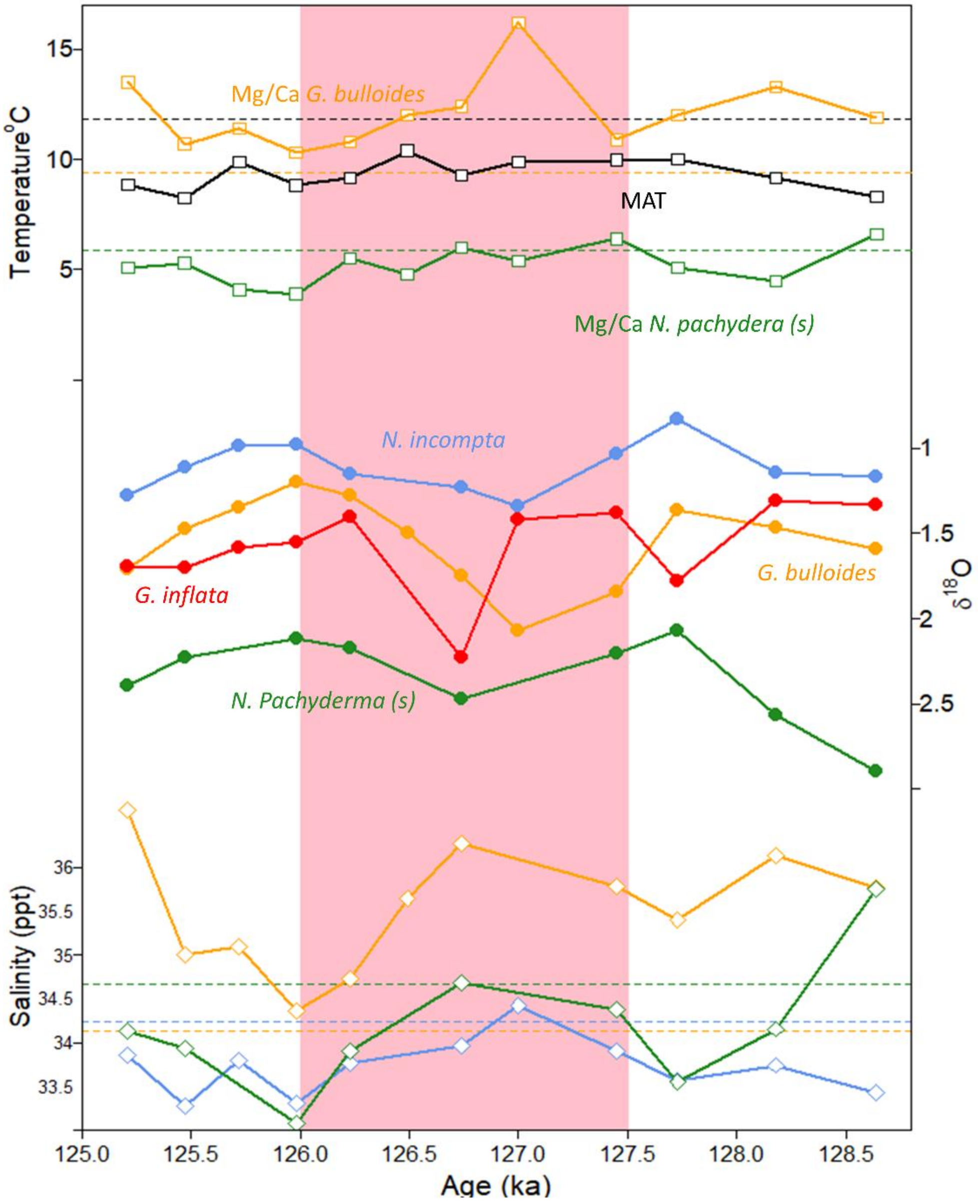

Figure 7.6 Environmental conditions across the red layer: Temperature (top), $\delta^{18}O$ (middle) and salinity (bottom). Red vertical bar marks the position of the red layer. Horizontal dashed lines are modern day values (WOA 1994).

It is postulated here that the initial increase in planktonic $\delta^{18}O$ values occurs after a prolonged increase in benthic $\delta^{13}C$, signifying a gradual upturn in oceanic ventilation. The $\delta^{18}O$ spike may represent the realisation of full interglacial AMOC conditions, as warm, saline water is transported into the Labrador Sea via the North Atlantic and Irminger Currents in the Subpolar Gyre. The increasingly saline conditions are reflected in elevated $\delta^{18}O$.

Using paired temperature (Mg/Ca for *G. bulloides* and *N. pachyderma (s)*, alongside MAT temperatures for *N. incompta*) and $\delta^{18}O$ measurements, it was possible to derive an estimate for palaeosalinity by re-arranging the isotopic temperature equation of Shackleton (1974) to obtain $\delta^{18}O$ of seawater. This was in turn inputted into the $\delta^{18}O$/salinity relationship derived by Cleroux et al*. (*2008) to derive estimates for palaeo-salinity (see section 7.3 for detailed methodology). The results of this calculation are presented in Figure 7.6. Increasing salinity is observed across all species in the early part of the red layer, providing further evidence of intruding high salinity waters.

The onset of active, interglacial AMOC and Subpolar Gyre conditions is likely to have brought enhanced heat flux into the Labrador Sea causing the breakup of the remaining Laurentide Ice Sheet, and triggering the catastrophic flooding observed within the red layer. This subsequent influx of freshwater lead to the rapid decrease in planktonic $\delta^{18}O$, and decrease in salinity, that is observed in the upper half of the red layer.

Supressed salinity values prevail for approximately 1.5 ka and for some 500 years after cessation of the red layer. Similar reductions in salinity have been observed in cores from the Eirik Drift during this interval (Irval et al., 2012). Such a prolonged episode could be explained by a transition in the dominant surface currents — from the warm, saline Irminger current to the cool, fresh West Greenland Current.

Without an increase in resolution of the benthic isotope record to infer oceanic ventilation, it’s difficult to further corroborate the role of the AMOC in triggering the Laurentide outburst seen in the red layer. Some insight can be drawn from nearby cores U1305 (Hume, 2018) and MD03-2264 (Galaasen et al., 2014), both from the Eirik Ridge in the Labrador Sea. Both records have been projected onto the U1302 chronology by Hume (2018) to allow direct comparison. These are presented alongside the benthic record of MD95-2042 record of Shackleton et al. (2002) from the Iberian Margin in Figure 7.7.

The benthic MD95-2042 record exhibits increasing $\delta^{13}C$ up until the onset of the red layer supporting the theory of enhanced heat and salinity flux into the Labrador Sea prior to the red layer. A short lived reversal observed midway through the layer indicates that the resultant freshwater pulse may have acted to the suppress oceanic ventilation, similar to the freshwater pulse shortly after Termination I (Kleiven et al., 2008).

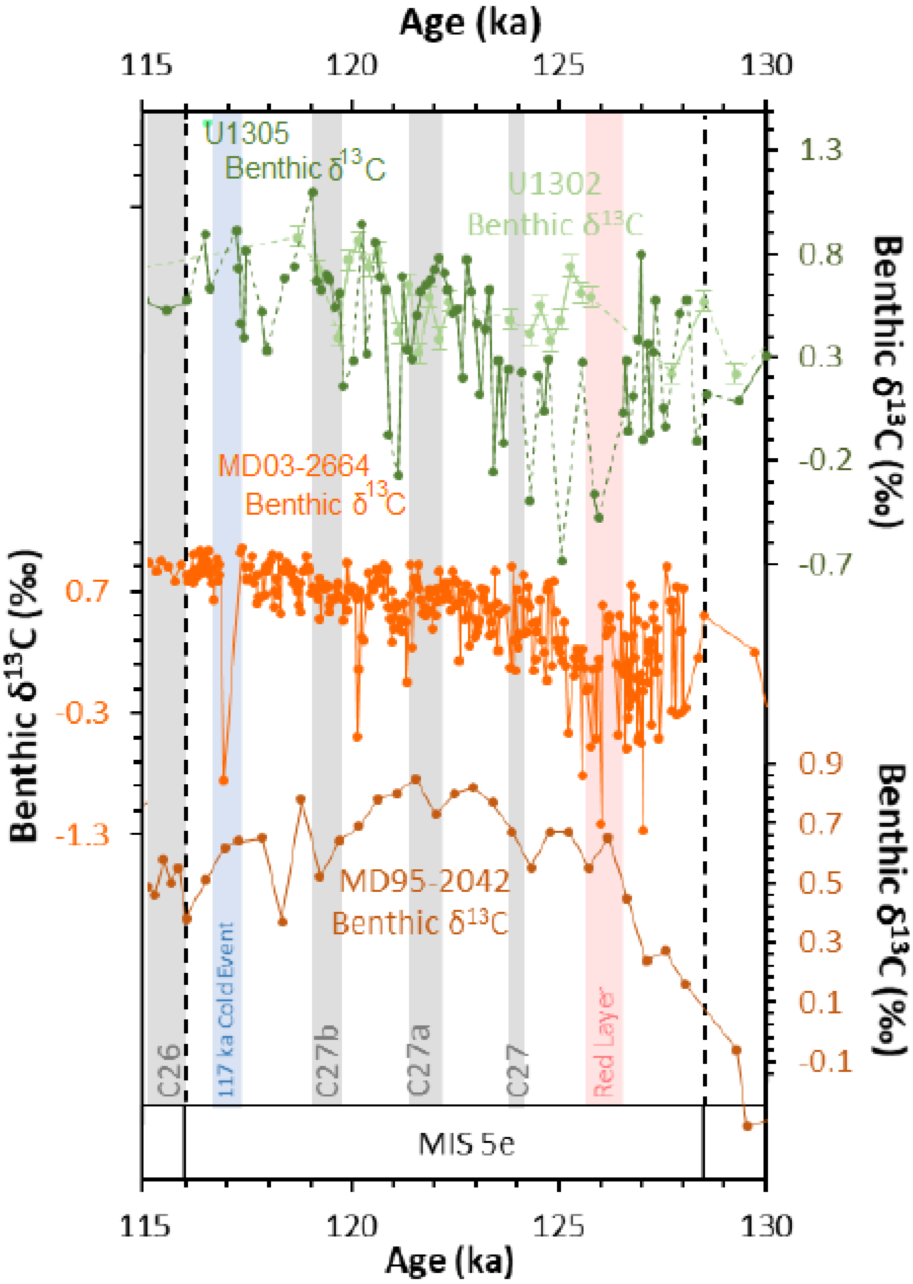

Figure 7.7 Benthic δ^{13}C records from nearby cores U1305 (Hume, 2018), MD03-2264 (Galaasen et al., 2014) and MD95-2042 (Shackleton et al., 2002), projected onto the U1302 chronology of Hume (2018). Vertical grey and red bars mark the

position of cold events and the red layer respectively. Black dashed lines bracket the MIS 5e plateau. (Adapted from Hume (2018)).

A high degree of variability in the U1305 and MD03-2264 records make it difficult to identify any discernible trends. In MD03-2264 benthic δ^{13}C values are certainly reduced towards the top of the red layer, compared with the base — supporting the notion that a suppression in ventilation arose during the red layer. U1305 benthic δ^{13}C also exhibits reduced values during the red layer however poor resolution make it difficult to identify when the transition to lower values occurs.

These findings contradict those of Carlson (2008) who suggests the meltwater pulse associated with MIS 5e occurred in such a short interval after Termination II that the AMOC had not yet achieved its full interglacial state, and as such the impact on ventilation and climate was limited. The records presented here suggest a clear reduction in ventilation during the MIS 5e meltwater pulse. Temperatures decline slightly over the interval with decreases of 1.0 °C, 0.6 °C, and 1.2 °C seen in *N. pachyderma (s)* Mg/Ca, *G. bulloides* Mg/Ca and MAT temperatures respectively, either side of the red layer. This is slightly less dramatic than the 2 °C cooling in North Atlantic SSTs during the 8.2 ka event (Came et al., 2014; Ellison et al., 2006).

7.3 δ¹⁸O of the Labrador Sea in the Last Interglacial

7.3.1 Consideration of vital offsets

The U1302 record offers paired foraminiferal calcite δ^{18}O ($\delta^{18}O_C$) measurements and temperature estimates such that it is possible to deduce the isotopic composition of seawater ($\delta^{18}O_{SW}$) using the Shackleton equation (Shackleton, 1974):

$$T = 16.9 - 4.38 \times (\delta^{18}O_C - \delta^{18}O_{SW}) + 0.1 \times (\delta^{18}O_C - \delta^{18}O_{SW})^2 \qquad (7.1)$$

Where T is the temperature of the palaeo-ocean. $\delta^{18}O_{SW}$ was converted to the PDB scale by subtracting 0.27 (Hut, 1987).

However, uncertainty is introduced by numerous studies which have suggested measured δ^{18}O of *N. pachyderma (s)* exhibits consistent offsets from those expected under precipitation of calcite in isotopic equilibrium (e.g. Nyland et al., 2006; Pados et al., 2015; Simstich et al., 2003). In modern day samples, where both seawater temperature and $\delta^{18}O$ ($\delta^{18}O_{SW}$) can be directly measured, estimated $\delta^{18}O_C$ can be calculated according to the following rearrangement of the Shackleton equation (Shackleton, 1974).

$$\delta^{18}O_C = \delta^{18}O_{SW} - 0.27 + \left[\frac{4.38-\sqrt{4.38^2-0.4(16.9-T)}}{0.2}\right] \quad (7.2)$$

Using in situ $\delta^{18}O_{SW}$ measurements dating back to 1950, alongside paired Mg/Ca and $\delta^{18}O_C$ measurements from recent sediment, Nyland et al. (2006) showed that $\delta^{18}O_C$ of *N. pachyderma (s)* exhibited measured values up to 0.6 ‰ heavier than those predicted from the Shackleton equation. However, much uncertainty surrounds this estimate. Plankton hauls in the same region suggest a much lower 'vital offset' between measured and predicted $\delta^{18}O_C$ of -0.9 – -1.0 ‰ (Simstich et al., 2003). Data from the Fram Strait predicts an offset of -1.5 ‰ (Pados et al., 2015) and similar values of -1 ‰ and -1.3 ‰ have been measured for the Nansen Basin (Bauch et al., 1997) and Laptev Sea (Volkmann, 2000) respectively. A summary of existing estimates of *N. pachyderma (s)* vital offset is presented in Table 7.3.

The effect is also observed in *G. bulloides* plankton haul samples from the Southern Ocean which exhibit an approximately 2 ‰ offset from predicted $\delta^{18}O_c$ (Prasanna et al., 2016). Interestingly however this same study found no such vital effect for samples obtained further north in the Indian Ocean, between 10 °N – 40 °S. Sediment trap studies of both *G. bulloides* and *N. incompta* from the Santa Barbara Basin have found good agreement between Mg/Ca and $\delta^{18}O$ derived temperatures, suggesting that isotopic offsets are minimal (Pak et al., 2004). This is in contrast to the 0.6 ‰ vital offset applied by Nyland et al. (2006) for *N. incompta* in the Nordic Seas. Few studies have looked at such 'vital effects' in *G. inflata*, the other species explored in this study.

The cause of such isotopic offsets remains unclear. Urey et al. (1951) first proposed that they arise from isotopic discrimination in the formation of foraminiferal tests. In core top samples, bioturbation has been suggested as a possible cause, as colder historical samples are reworked to the surface sediment (Simstich et al., 2003). However, such a mechanism fails to explain the offset observed in sediment trap and plankton tow studies, nor can it account for the apparent shift to warmer values seen in numerous studies.

Bauch et al. (1997) concluded that the variability in vital offset of *N. pachyderma (s)* could be explained by differing calcification depths. They suggested that shallower samples tended to exhibit less enriched $\delta^{18}O$ signatures by comparing samples from 50 – 100 m and 100 – 200 m depths. Furthermore, larger test sizes tended to exhibit less enriched $\delta^{18}O$ values – likely arising from their migration to greater depths later in their lifecycle, during which a secondary layer of calcite is acquired (Kohfeld et al., 1996; Simstich et al., 2003).

In modern plankton tow studies, where the sampling depth can be reasonably constrained, quantifying vital offset from varying depth habitat is relatively straightforward. However, in core top studies and palaeo-studies, calcification depth is far less well known. Core top studies often assume a calcification depth based upon that which most closely aligns the $\delta^{18}O_C$ value with that estimated from equilibrium precipitation. And further difficulty is introduced in palaeo-studies where species may migrate in the water column with shifting oceanic temperature and nutrient supply.

Table 7.3 A summary of studies into the vital offset of *N. pachyderma (s)*

Study	Type of study	Temperature inference/measurement	$\delta^{18}O_{SW}$ inference/measurement	Location	Depth	Size fraction	Vital offset
(Bauch et al., 1997)	Plankton tow	Water sampling	Water sampling	North Nansen Basin	50 - 100	160 – 250 µm	1.43 ‰
						>250 µm	1.21 ‰
				South Nansen Basin	100 -200	160 – 250 µm	0.84 ‰
						>250 µm	0.64 ‰
(Kohfeld et al., 1996)	plankton tow Core top Sediment trap	Water sampling	Calculated from in situ salinity measurements using study derived relationship	Arctic Ocean off North East Greenland	0 - 400 m	>63 µm	-0.8 ‰
(Nyland et al., 2006)	Modern downcore	Mg/Ca	Global Seawater Database (Schmidt et al., 1999)	Nordic Seas	100 m	150 – 250 µm	0.6 ‰
(Ortiz et al., 1996)	plankton tow	Water sampling	Calculated from in situ measurement of salinity using Zahn & Mix (1991)	Central North Pacific (Californian coast)	400 - 600	125 – 212 µm	-0.7 ‰
(Pados et al., 2015)	Plankton tow core top	Water sampling	Water sampling	Fram Strait	0 - 500 m	>100 µm (tows) 100 – 250 µm (core top)	-1.5 ‰
(Simstich et al., 2003)	Plankton tow sediment trap core top	Hydrobase (Lozier et al., 1995)	Calculated from Hydrobase salinity using study derived relationship	Nordic Seas and Arctic Ocean	25 - 75 m (western Arctic) 70 - 250 m (off Norway) 70 - 130 m (East Greenland Current)	125 - 250 µm	-0.9 – -1.0 ‰
(Stangeew, 2001)	plankton tow	Water sampling	Measured from in situ water sample Calculated from in situ salinity measurements using Wu & Hillaire-Marcel (1994)	Fram Straight	0 - 200 m	140 – 240 µm	0.9 ‰
				Labrador Current	0 - 200 m	140 – 240 µm	0.7 ‰
(Wu & Hillaire-Marcel, 1994)	Core top	Oceanographic Atlas of the North Atlantic Ocean	Calculated from salinity	Predominantly Labrador Sea with some Nordic Seas	0 – 500 m	unknown	0.2 –0.4 ‰ (below 8 °C)

Review of the studies in Table 7.3 suggests a high degree of variability in the δ^{18}O vital effect is introduced by locality, and the methodology by which $\delta^{18}O_{SW}$ and temperature is measured or inferred. Identical samples from the Labrador Sea and Fram Strait measured by Stangeew (2001) exhibited differing degrees of vital effect — as do similar samples measured from the Nordic Seas (Simstich et al., 2003) and Nansen Basin (Bauch et al., 1997).

Peeters et al. (2002) used plankton tow samples from the Arabian Sea to show that δ^{18}O vital effect increases with decreasing carbonate ion concentration. These studies are supported by laboratory evidence (Spero et al., 1997). As such, differing pH between study sites may go some way to explaining varying degrees of isotopic offset in samples of the same taxon from different locations.

7.3.2 Investigating the cause of variation in vital offset estimations using Nyland et al. (2006) and the clumped isotope calibration dataset

Recalculating data from Nyland et al*. (*2006)

A great degree of variability exists in the methods used to estimate calcification temperatures and $\delta^{18}O_{SW}$ values, and these cannot be ruled out as a cause of the vast differences in estimated vital offset observed between studies. To illustrate this point, the vital offsets derived in Nyland et al. (2006) were recalculated using different, widely applied methods for deriving temperature and $\delta^{18}O_{SW}$.

Mg/Ca temperatures from Nyland et al. (2006) were recalculated using alternative, widely applied calibrations for *N. pachyderma (s)*. This has been shown to alter calculated temperatures by several degrees (Farmer et al., 2011; this study, section 3.4.2). Alternative temperatures, derived from the 2018 World Ocean Atlas (Locarnini et al., 2018) were also explored. These were calculated from the decadal mean by interpolating between the 4 nearest grid points at a depth of 100 m – the assumed calcification depth in the Nyland et al. (2006) study. $\delta^{18}O_{SW}$ is calculated from the relationship between salinity and δ^{18}O described in Cleroux et al*. (*2008):

$$\delta^{18}O_{sw}(vsmow) = -19.264 + 0.558 \times salinity \tag{7.3}$$

Where salinity is obtained from the World Ocean Atlas 2018 (Zweng et al., 2018) using the same interpolation method. The recalculated vital offset values are presented in Table 7.4.

Table 7.4 Recalculated vital offset values from Nyland et al. (2006), using differing Mg/Ca temperature calibrations and $\delta^{18}O_{SW}$ values. A value of 0.3 ‰ for $\delta^{18}O_{SW}$ is adopted by Nyland et al. (2006) from (Schmidt et al., 1999). Mg/Ca temperature calibrations: E+G (2000) = Elderfield & Ganssen (2000), K (2009) = Kozdon et al*. (*2009), N (1995) = Nurnberg (1995).

	Vital offset (‰)					
$\delta^{18}O_{SW}$ source	0.3 ‰ (Nyland 2006)				WOA (2018)	
Temp source	Mg/Ca E+G (2000)	Mg/Ca K (2009)	Mg/Ca N (1995)	WOA (2018)	Mg/Ca E+G (2000)	WOA (2018)
Sample date						
1975	-0.03	0.52	0.19	0.17	0.07	0.27
1970	0.64	1.11	0.88	0.27	0.73	0.36
1965	0.59	1.05	0.83	0.18	0.68	0.27
1960	0.61	1.04	0.85	0.10	0.70	0.19
1955	0.18	0.70	0.41	0.03	0.28	0.13
1950	0.58	1.01	0.82	0.07	0.68	0.17
Average	**0.43**	**0.91**	**0.66**	**0.13**	**0.52**	**0.23**

The data presented in Table 7.4 shows that the methods used to derive temperature and $\delta^{18}O_{SW}$ estimates can have a dramatic impact on the calculated vital offset. Average $\delta^{18}O$ offset ranges between 0.13 ‰ and 0.91 ‰ with differing temperature and $\delta^{18}O_{SW}$ estimates, equivalent to an approximately 3 °C temperature difference. The biggest degree of uncertainty is introduced by the temperature estimate, in particular the choice of Mg/Ca calibration applied. Indeed, Mg/Ca temperatures inferred in Nyland et al. (2006) are some 1-2 °C lower than those measured in situ at the nearby Ocean Weather Station M (See figures within Nyland et al. (2006)). Higher oceanic temperatures, closer to those derived from WOA in the reanalysis conducted above, act to reduce vital offset to negligible levels.

Estimating vital offset using the clumped isotope calibration dataset

To date, there is relatively little published data on vital offsets in *N. incompta, G. bulloides* or *G. inflata*. Thus vital offsets were calculated for each of the 25 core top samples used to derive the clumped isotope temperature calibration in Section 3.3 (hereafter the chapter 3 calibration dataset). Core locations are shown in Figure 3.5, repeated below for reference. All temperature and salinity estimates were obtained from the 1994 World Ocean Atlas and detailed in Table 3.4. An alternative depth of 0 – 30 m is adopted for *N. incompta* for the Labrador Sea according to Bauch & Kandiano (2007). Vital effects are calculated for single species across multiple cores and for multiple species in a single core top. Results are presented in Table 7.5.

Figure 3.5 Calibration core top locations used in this study.

The magnitude of the average species vital effect appears reduced compared with previous studies, with a $\delta^{18}O$ offset of 0.16 ‰ seen in *N. pachyderma (s)*, compared with up to 1.5 ‰ observed elsewhere (Pados et al., 2015). However, these averages hide a great deal of variability between locations — vital offset values for *G. bulloides* range from -0.49 ‰ in core NEAP 20B to 1.31 ‰ in BOFS 31K.

Table 7.5 Vital effect calculations for the chapter 3 calibration dataset. $\delta^{18}O_C$ are measured values. $\delta^{18}O_{SW}$ is estimated from WOA 1994 and $\delta^{18}O_C$ est is calculated from equation 7.1. Vital effect = $\delta^{18}O_C$ est - $\delta^{18}O_C$.

Core	Species	T (°C) (WOA)	$\delta^{18}O_C$ (‰)	$\delta^{18}O_{SW}$ (‰)	$\delta^{18}O_C$ est (‰)	Vital effect (‰)
NEAP20B	*G. bulloides*	15.7	0.48	-0.28	-0.01	-0.49
	G. *truncatulinoides*	13.5	1.01	0.07	0.86	-0.15
	G. inflata	14.5	0.92	0.14	0.69	-0.23
	G. *sacculifer*	19.2	-0.11	0.10	-0.41	-0.30
	G. *ruber*	18.6	-0.11	0.10	-0.29	-0.17
	G. *ruber* (w)	19.1	-0.13	0.10	-0.40	-0.27
	N. incompta	16.4	0.59	0.12	0.24	-0.35
Rapid26-14B	*G. bulloides*	6.8	1.94	-0.28	2.16	0.22
	N. pachyderma (s)	4.8	2.89	-0.19	2.77	-0.12
Rapid29-18B	*N. pachyderma (s)*	4.4	2.41	-0.23	2.84	0.43
BOFS31K	G. *sacculifer*	23.3	-0.74	1.33	-0.09	0.65
	G. *ruber*	23.2	-0.99	1.33	-0.07	0.92
	G. *ruber* (w)	23.3	-1.02	0.87	-0.54	0.48
	N. incompta	20.9	-0.37	1.33	0.43	0.80
	G. inflata	13.5	0.42	0.55	1.34	0.91
	G. bulloides	20	-0.58	1.43	0.74	1.31
MD99-2252	*G. bulloides*	8.8	1.59	-0.33	1.61	0.02
	N. incompta	9.4	1.27	-0.26	1.53	0.26
NEAP4B	*G. bulloides*	8.7	1.58	-0.31	1.65	0.06
	N. incompta	9.3	1.35	-0.25	1.56	0.20
NEAP16B	*G. bulloides*	9.1	1.61	-0.29	1.57	-0.04
	N. incompta	9.7	1.40	-0.26	1.45	0.05
	G. inflata	8.5	1.67	-0.24	1.77	0.10
NEAP19B	*N. incompta*	10.5	1.28	-0.31	1.20	-0.08
	G. inflata	9	1.47	-0.30	1.58	0.11

BOFS 31K shows a clear offset from other cores within the dataset (Table 7.5 and Table 7.6). The site occupies a wholly different climatic regime to the other Northern Atlantic cores and sits in an area of significant upwelling and high productivity (Chapman et al., 1996). As such, carbonate ion concentration, is likely to be offset from the other cores and this may explain the differing vital effect values (Peeters et al., 2002). BOFS 31K has therefore been removed from the species average calculations (Table 7.6). Even with the removal of BOFS 31K, there is still a great deal of variability in average species vital effect and these estimates are not considered robust.

Table 7.6 Species (top) and core (bottom) vital offset averages for the chapter 3 calibration dataset

Species	n	Average vital effect (‰)	Standard deviation
G. bulloides	5	-0.04	0.26
N. incompta	5	0.25	0.34
N. pachyderma (s)	2	0.16	0.38
G. inflata	3	-0.01	0.19

Core	n	Average vital effect (‰)	Standard deviation
NEAP20B	7	-0.28	0.12
Rapid26-14B	2	0.05	0.24
Rapid29-18B	1	0.43	-
BOFS31K	6	0.85	0.28
MD99-2252	2	0.14	0.17
NEAP4B	2	0.13	0.10
NEAP16B	3	0.04	0.07
NEAP19B	2	0.01	0.13

Far less variability is observed when average vital offset is considered at specific core locations (Table 7.6). This suggests that vital offset is highly influenced by the specific water properties at the calcification site. This may go some way as to providing an explanation for the high degree of variability in observed *N. pachyderma (s)* vital effects listed in Table 7.3.

7.3.3 Results and discussion

In the absence of data from Orphan Basin in the clumped isotope calibration dataset, estimates for vital offsets of *G. bulloides* and *N. pachyderma (s)* were calculated using modern day foraminiferal $\delta^{18}O$ measurements from the Orphan Knoll by de Vernal et al. (2002). Values of 1.9 ‰ and 2.5 ‰ were used for *G. bulloides* and *N. pachyderma (s)* respectively, reflective of values from larger specimens most similar to those used in this study. Temperature and $\delta^{18}O_{SW}$ values derived from the World Ocean Atlas 1994 were used to calculate estimated $\delta^{18}O_C$ from equation 7.2. This gave calculated vital offset values of -0.73 ‰ and -0.31 ‰ for *G. bulloides* and *N. pachyderma (s)* respectively.

These vital offset values were used to calculate historical $\delta^{18}O_{SW}$ for the two species using Mg/Ca derived temperatures, inputted into equation 7.3. An additional value of $\delta^{18}O_{SW}$ was calculated for *N. pachyderma (s)* using a vital offset of 0.7 ‰ as derived by Stangeew (2001) for the Labrador Sea. Results are presented in Table 7.7. It should be noted that the calculated $\delta^{18}O_{SW}$ values assume the same vital offset during the MIS 5e plateau as during the modern day.

Table 7.7 Modern day and mean MIS 5e plateau water properties at the U1302 site calculated for two planktonic foraminifera species. Modern data is from WOA 1994 with errors representing the range of values over the calcification depths. MIS 5e plateau errors are standard deviations. Gb = *G. bulloides* and NPS = *N. pachyderma (s)*.

	Modern			MIS 5e plateau averages			
	Salinity	$\delta^{18}O_{SW}$ (‰, SMOW)	Temp (°C)	Temp (°C)	Vital effect	$\delta^{18}O_{SW}$ (‰, SMOW)	Salinity
Gb	34.1 ± 0.1	-0.21 ± 0.06	9.4 ± 2.2	12.7 ± 2.3	-0.73	0.23 ± 0.6	34.9 ± 1.05
NPS	34.7 ± 0.04	0.08 ± 0.02	5.9 ± 0.4	5.4 ± 0.9	-0.31	-0.43 ± 0.4	33.7 ± 0.6

Surface salinity estimates from *G. bulloides* are slightly higher, but within error of previous estimates derived from dynocyst assemblages for the Orphan Knoll (Hillaire-Marcel et al., 2001). However, the raw value MIS 5e Plateau salinities suggest a reversal of the salinity/depth gradient of the surface ocean that is observed in the modern day — with more saline surface waters and a fresher subsurface (Figure 7.8). This is surprising since warmer temperatures at the surface, reflected in higher Mg/Ca *G. bulloides* temperatures suggest reduced ice sheet extent and therefore lower $\delta^{18}O_{SW}$ values.

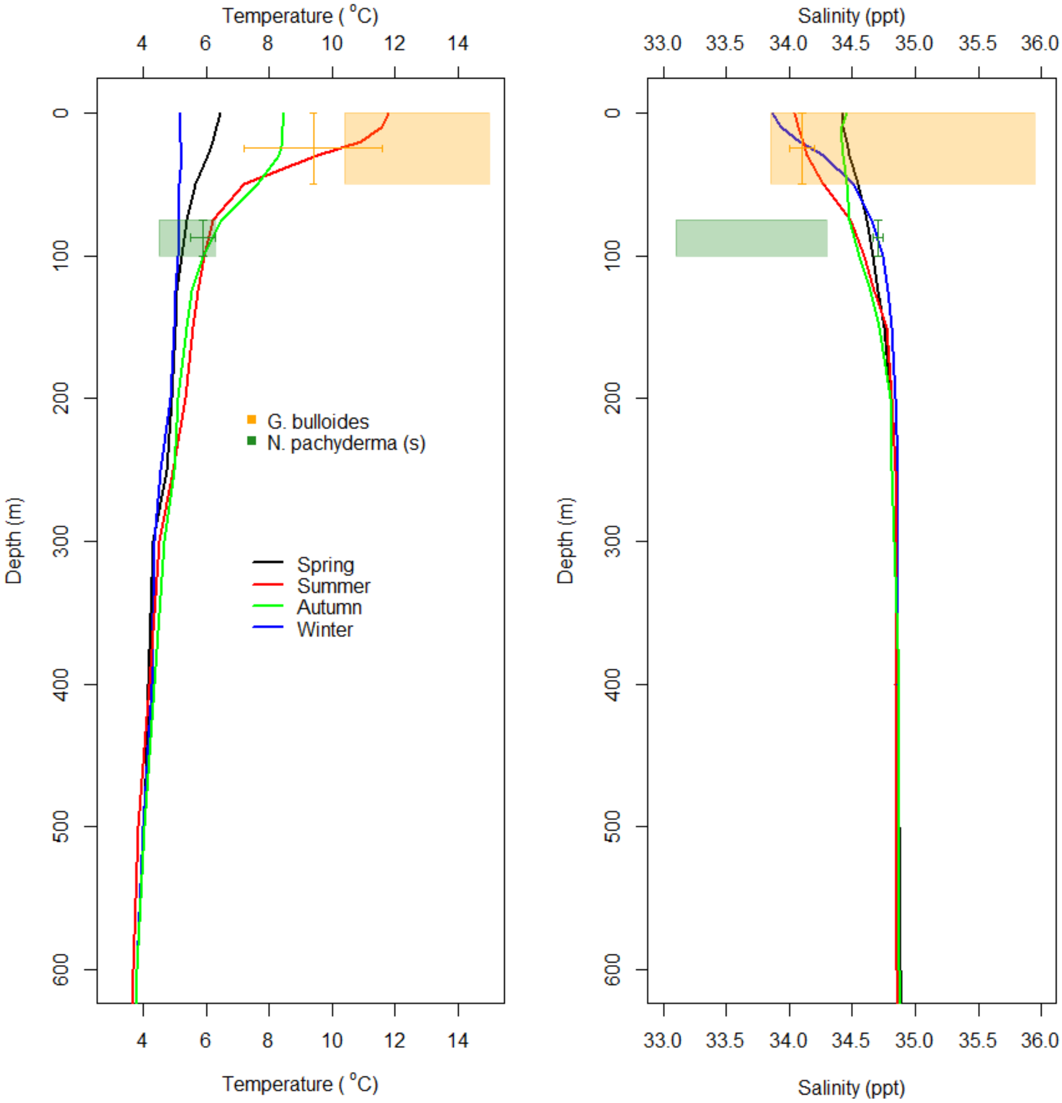

Figure 7.8 Depth profiles for the U1302 site for the modern day using WOA 1994 data. Crosses mark the calcification environments in the modern day and shaded rectangles the average environment over the MIS 5e Plateau, assuming calcification depths in line with the modern day.

It is difficult to envisage how such a realignment might physically arise. Rather it is suggested the increase in salinity observed in the *G. bulloides* record is a reflection of calcification earlier in the year. *G. bulloides* calcification is generally associated with the spring bloom when the diatoms on which the species feeds, proliferate (Ganssen & Kroon, 2000). However, in the high latitudes, calcification is often limited to the late summer.

Previous studies of the Orphan Knoll — as well as the Mg/Ca temperatures measured here — have suggested summer temperatures some 3–5 °C warmer during the last interglacial than the present day (Hillaire-Marcel et al., 2001). Such temperatures would have allowed *G. bulloides* to proliferate during a spring window when food availability is greatest. Modern day WOA estimates suggest late spring salinity is some 0.5 ppt higher at the U1302 site than in summer. Thus a shift in calcification timing could certainly account for the higher salinity observed in *G. bulloides* during the MIS 5e Plateau.

MIS 5e *N. pachyderma (s)* Mg/Ca temperatures are similar to the modern day and thus no alteration in calcification timing is thought to have occurred. As such the shift to lower salinities can be seen as a direct comparison with the modern day.

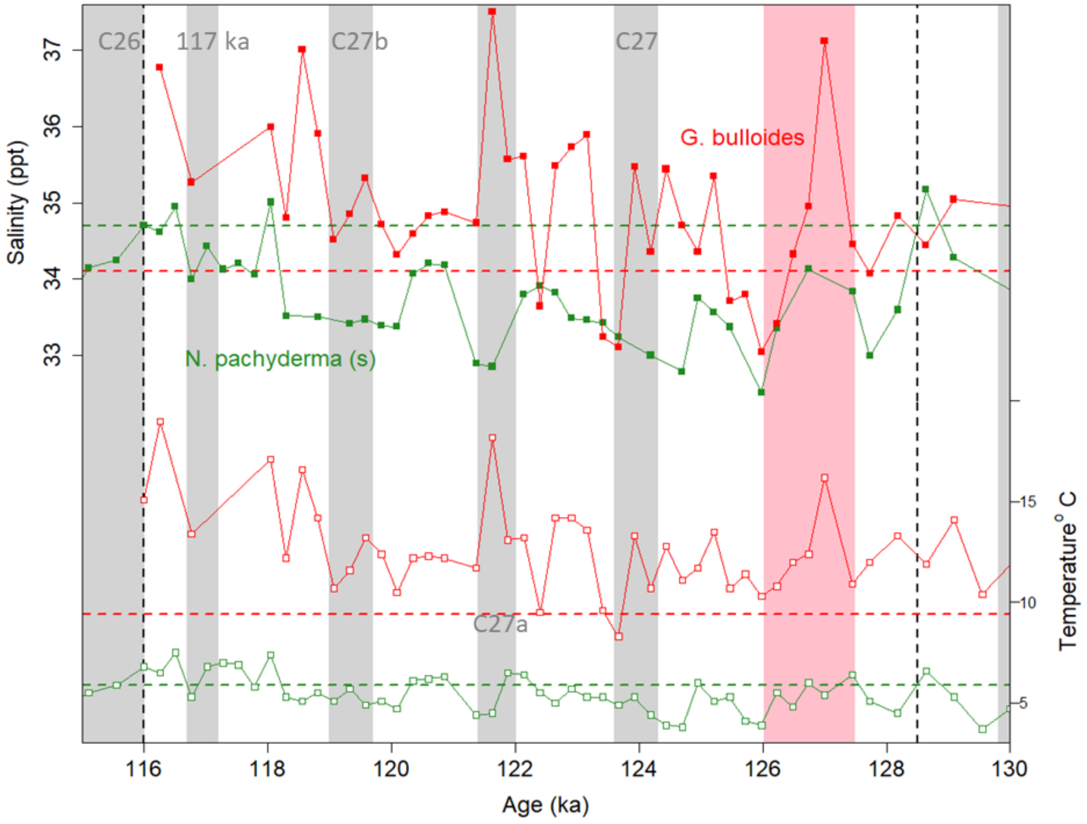

Figure 7.9 Salinity (top) and Mg/Ca temperature (bottom) for *N. pachyderma (s)* and *G. bulloides* over the MIS 5e Plateau. Grey and red horizontal bars are the positions of cold events and the red layer respectively. Vertical dashed lines bracket the MIS 5e Plateau. Dashed horizontal lines are the modern day values. Timing of cold events from Oppo et al., (2006) and 117 ka event from Irvalı et al., (2016).

Figure 7.9 shows the calculated salinity and temperature for *G. bulloides* and *N. pachyderma* (s) over the MIS 5e Plateau. Temperatures and salinities in both species show a gradual increase over the window, interpreted as the gradual influx of warm, saline waters through an increasingly active Subpolar Gyre.

The MIS 5e stability is punctuated by numerous short-term declines in salinity and temperature observed both species. These coincide with North Atlantic cold events (Oppo et al., 2006), with suppressed responses in the subsurface *N. pachyderma (s)* compared with *G. bulloides*. Such a pattern could arise from iceberg formation during cold events — with the rejection of brines causing the observed increases in salinity. However, this seems unlikely given the warm surface temperatures, rarely dipping below 10 ^{o}C even during cold intervals. More likely is short-term reductions in the transportation of warm, saline surface waters to the Labrador Sea via the Irminger current.

7.4 Conclusions

This study has added two additional high resolution planktonic isotope records for U1302 and improved the detail of the previously published *G. bulloides, N. pachyderma (s)*, and benthic records with sample infilling. This has allowed the Termination II climatic transition and MIS 5e to be studied in exceptional detail.

Termination II exhibits a 'stuttered' transition with two positive δ^{18}O excursions thought to arise from short-term 'flickering' of the AMOC heat conveyor (7.2.1). Similar 'step-like' transitions have been observed in cores from the Nordic Sea (Zhuravleva et al., 2017) and Iberian Margin (Skinner & Shackleton, 2006) — both sites that are influenced by North Atlantic Current waters. The 'flickering' observed in U1302 may be analogous to that seen during the transition into the Holocene in Termination I (Kroon et al., 1997).

Increasing foraminiferal δ^{18}O values with calcification depth during the MIS 5e Plateau suggest a highly stratified water mass, confirming previous findings from the region (Hillaire-Marcel et al., 1994; Hillaire-Marcel et al., 2011; Hume, 2018). The relative stability of the MIS 5e Plateau is interrupted by a ~1.5 ka positive δ^{18}O excursion associated with the detrital red layer between 127.5 – 126 ka. The increased resolution offered by this study allows the positive excursion to be highly resolved (7.2.3), adding further detail beyond the previously observed negative transition (Nicholl et al., 2012).

It is suggested that this positive excursion reflects an increasing influence of high salinity North Atlantic Waters at the U1302 site during the early interglacial. The resultant increase in heat flux to the regions triggered the collapse of the Laurentide Ice Sheet, leading to the mass flooding event seen in the red layer. Salinity remains suppressed for some 1.5 ka suggesting a reduction in high salinity Irminger Current waters to the Labrador Sea which are replace by lower salinity West Greenland Current waters.

$\delta^{18}O$ of surface and subsurface palaeo-waters are derived for the MIS 5e plateau, with consideration of species vital effects (7.3). It is shown that a high degree of uncertainty exists in species vital effects, with the methods chosen to infer calcification temperature and $\delta^{18}O_{SW}$ — as well as the locality of the study site — having a considerable impact on the values calculated (7.3.2). This may be a factor in the huge variability observed in species-specific vital effects within the literature. Relatively few studies have looked at vital offsets within the Labrador Sea and it is suggested that this will need to be addressed should reliable estimates of $\delta^{18}O$ of palaeo-waters be desired.

Despite the high degree of uncertainty surrounding the best estimates for MIS 5e plateau $\delta^{18}O_{SW}$, the values derived in this study are sufficient to derive general trends and fluctuations. Surface and subsurface estimates suggest a reduction in the $\delta^{18}O_{SW}$ depth-gradient observed in the modern day. Salinity gradually increases over the Plateau suggesting increasing influx of warm, saline north Atlantic waters. The stability of the MIS 5e Plateau is interrupted by several short lived salinity excursions coinciding with north Atlantic cold events. It is postulated that these intervals represent a shift in dominant current into the Labrador Sea, from the high salinity Irminger Current to the low salinity West Greenland Current.

Chapter 8. Conclusions and further work

8.1 Foraminifera clumped isotope palaeothermometer

This study has established a UEA laboratory foraminifera clumped isotope calibration, demonstrating the possibility of inferring palaeotemperatures from fossilised foraminiferal calcite. Robust experimental protocols were developed for sample cleaning and preparation, and an R based algorithm was written to correct for samples of differing volumes. In addition, investigations were made into different methodologies by which transfer functions should be constructed for projection of Δ47 values onto the absolute reference frame, from which recommendations made for optimising standard throughput.

These methodological advances were utilised to derive the following clumped isotope temperature calibration for foraminifera:

$$\Delta 47 = 0.0314\ (\pm 0.0027) \times \frac{10^6}{T^2} + 0.3171\ (\pm 0.0332)$$

It shows good agreement with existing published calibrations. By unifying data processing methodologies, it was shown that measurement discrepancies between laboratories could be dramatically reduced, allowing data to be pooled from multiple instruments for the creation of the calibration.

However, measurement precision must be improved, with uncertainty as high as 10 – 15 ^{o}C for single sample temperature estimates. This hindered attempts to infer reliable palaeotemperatures from foraminifera over the last glacial cycle in cores U1305 and MD99-2251.

The majority of Δ47 measurement scatter is introduced within the sample purification procedure. It is shown here that water — likely arising from the acid reaction vessel and adhering to glassware surfaces, is the most likely cause of the ongoing sample size effect. Therefore, improved dehydration practices are required in order to overcome this. Installation of additional water traps on the purification line have acted to reduce water contamination via the acid reaction vessel and vacuum manifold — yet further long-term investigation into their effectiveness is still required.

If water can be effectively eliminated from the sample purification line, additional refinement can be made on instrumentation to reduce sample sizes further. Currently, a minimum of approximately 1.5 mg of pure calcite is required for measurement on the MIRA instrument. This could be further decreased with a reduction in the volume of sample input bellows to maximise baseline pressure and minimise sample gas wastage. Early investigations to install mercury bellows for small samples based on the designs of Coplen (1981) fell victim to time constraints. Given further opportunity, it would be beneficial to explore this further.

For the field in general, sample sizes are limited by a failure to utilise the vast majority of ions within a given sample. MIRA ionises just one molecule in approximately 300 (Dennis et al., 2013). Advances in source design, to liberate a greater proportion of ions from a given sample, would go a significant way to reducing uncertainty associated with counting statistics. Recent studies using laser spectroscopy have shown promising advances in reducing sample sizes by an order of magnitude (Prokhorov et al., 2019).

Further efforts are required by the clumped isotope community to introduce universal data processing techniques. This study has shown (3.6.4) that much of the discrepancy seen in interlaboratory measurements arises from the differing methodologies used to project Δ47 values onto the absolute reference frame. This includes variability in the chosen acid fractionation factor and Δ47 values of ‘known’ international standards. When these methodologies are unified, measurement discrepancy between laboratories is dramatically reduced. Furthermore, unifying data processing techniques would allow calibration data from different laboratories to be combined more readily to improve counting statistics, reducing calibration uncertainties.

Finally, this study did not examine species-specific Δ47 temperature sensitivity. Just as with Mg/Ca and stable isotope studies, individual species may exhibit unique temperature responses and vital offsets. Further attempts to produce species-specific calibrations are required if reliable palaeotemperature estimates are to be obtained.

8.2 MD99-2251: The North Atlantic in the last glacial cycle

This study has produced a high-resolution, multiproxy record of the North Atlantic throughout the last glacial period. Surface temperatures were highly variable, with regular cold excursions averaging 4 °C, and some as high as 7 °C.

A detailed ice rafting record has provided detail on the timing and evolution of specific Heinrich events. In particular:

- Improved estimates of H6 timing suggest bracketing dates of 60.2 – 59 ka, reducing the existing 5ka uncertainty in timing (Hemming, 2004).
- corroborated the findings of Wary et al. (2015), suggesting that H3 exhibited three IRD peaks over a prolonged period
- Proposed Heinrich events H5a (Rashid et al., 2003), and H7a and H7b (Rasmussen et al., 2003) show similar levels of rafting to regular stadial events, and it is suggested that they are considered as such.

Comparison of the IRD record produced here with existing north Atlantic benthic records has shown the response of the AMOC to major ice rafting events is not uniform. Suppression of ventilation is observed in nearby cores after H10, H6 and H4 — but little impact is seen after other such events.

The ice rafting chronology developed in this study can inform community wide efforts to establish a definitive nomenclature system for rafting events. Further study of the North Atlantic is required to determine the magnitude of 'new' Heinrich events H5a and H7a and H7b and whether a distinction can be made between North Atlantic rafting events associated with stadial cooling and 'more extreme' Heinrich events. It may be the case that a new nomenclature system, based on Greenland stadial numbering system, proves more convenient.

Additional exploration of the MD99-2251 locality, on the boundary between Ruddiman's IRD belt and the Nordic Seas, may shed additional insight into the causes of ice rafting events and the relationship between Laurentide and Greenland/Scandinavian sourced rafting. Grousset et al. (2000) have proposed that rafting from the European Margin preceded Laurentide rafting, supporting the theory that initial iceberg discharge from Greenland and Scandinavia elevated sea levels sufficiently to undercut the Laurentide ice sheet, triggering further rafting (Van Kreveld et al., 2000). Yet evidence to support these theories remains limited. Further study of the boundary region between Laurentide and Nordic source regions may help provide further insight.

8.3 U1302: The Labrador Sea in the last interglacial

This study has provided additional clarity on the nature of Termination II, showing it exhibited a step-like transition as AMOC flickering triggered short-term reversals in the warming trend.

Additional high resolution planktonic isotope records have confirmed earlier studies that suggested the Labrador Sea was highly stratified throughout the MIS 5e plateau (Hillaire-Marcel et al., 2011). Attempts to infer δ^{18}O of seawater throughout the interglacial suggest that the δ^{18}O/depth gradient was likely similar to the modern day or slightly reduced, indicative of significant oceanic ventilation.

However, a high degree of uncertainty exists around estimates of δ^{18}O of seawater from the last interglacial, arising from ambiguity in the extent of species-specific vital offsets and Mg/Ca derived temperatures. Uncertainty could be reduced with further study into species-specific vital offsets in *G. bulloides* and *N. incompta*, where data is relatively limited — as well as localised Labrador Sea studies.

Nevertheless, the planktonic records produced here show a gradual increase in δ^{18}O and salinity over the MIS 5e plateau with the increasing influx of warm, saline Irminger current waters into the Labrador Sea. The relative stability of the last interglacial is punctuated by several short lived freshening events where a transition to a West Greenland Current dominated regime is postulated.

Increased resolution of foraminiferal δ^{18}O records over the previously identified red layer (Nicholl et al., 2012) has identified a positive excursion, reflective of an influx of warm, saline north Atlantic waters subsequent to the AMOC entering an active phase. The resultant heat flux into the region triggered the collapse of the Laurentide ice shelf and the subsequent mass flooding event.

Benthic $\delta^{13}C$ records from nearby cores support the notion that oceanic ventilation varied considerably over the red layer interval, but limited data exists at the U1302 site itself. Expanding the existing benthic record to infill data gaps, particularly over the red layer interval, could help to corroborate the assertion that the Laurentide flooding event associated with Termination II was triggered by AMOC fluctuations.

References

Abbott, P. M., Griggs, A. J., Bourne, A. J., Chapman, M. R., & Davies, S. M. (2018). Tracing marine cryptotephras in the North Atlantic during the last glacial period: Improving the North Atlantic marine tephrostratigraphic framework. *Quaternary Science Reviews*, *189*, 169–186. http://doi.org/10.1016/j.quascirev.2018.03.023

Adkins, J. F. (1998). Deep-Sea Coral Evidence for Rapid Change in Ventilation of the Deep North Atlantic 15,400 Years Ago. *Science*, *280*(5364), 725–728. http://doi.org/10.1126/science.280.5364.725

Adkins, J. F., Mcintyre, K., & Schrag, D. P. (2002). The Salinity , Temperature , and δ18 O of the Glacial Deep Ocean. *Science*, *298*(November), 1769–1773.

Affek, H. P., & Eiler, J. M. (2006). Abundance of mass 47 CO 2 in urban air , car exhaust , and human breath, *70*, 1–12. http://doi.org/10.1016/j.gca.2005.08.021

Affek, H. P., & Zaarur, S. (2014). ScienceDirect Kinetic isotope effect in CO 2 degassing : Insight from clumped and oxygen isotopes in laboratory precipitation experiments. *Geochimica et Cosmochimica Acta*, *143*, 319–330. http://doi.org/10.1016/j.gca.2014.08.005

Alley, R. B., & MacAyeal, D. R. (1994). Ice-rafted debris associated with binge/purge oscillations of the Laurentide Ice Sheet. *Paleoceanography*, *9*(4), 503–511. http://doi.org/10.1029/94PA01008

Alvarez-Solas, J., Robinson, A., Montoya, M., & Ritz, C. (2013). Iceberg discharges of the last glacial period driven by oceanic circulation changes. *Proceedings of the National Academy of Sciences of the United States of America*, *110*(41), 16350–16354. http://doi.org/10.1073/pnas.1306622110

Anand, P., Elderfield, H., & Conte, M. H. (2003). Calibration of Mg / Ca thermometry in planktonic foraminifera from a sediment trap time series, *18*(2). http://doi.org/10.1029/2002PA000846

Atkinson, T. C., Briffa, K. R., & Coope, G. R. (1987). Seasonal temperatures in Britain during the past 22,000 years, reconstructed using beetle remains. *Nature*, *325*(6105), 587–592.

Austin, W. E. N., Hibbert, F. D., Rasmussen, S. O., Peters, C., Abbott, P. M., & Bryant, C. L. (2012). The synchronization of palaeoclimatic events in the North Atlantic region during Greenland Stadial 3 (ca 27 . 5 to 23 . 3 kyr b2k). *Quaternary Science Reviews*, *36*, 154–163. http://doi.org/10.1016/j.quascirev.2010.12.014

Bandy, Frerichs, & Vincent. (1967). ORIGIN, DEVELOPMENT, AND GEOLOGIC SIGNIFICANCE OF NEOGLOBOQUADRINA BANDY, FRERICHS, AND VINCENT, GEN. NOV. *CUSHMAN FOUNDATION*, 152.

Barber, D. C., Dyke, a., Hillaire-Marcel, C., Jennings, a. E., Andrews, J. T., Kerwin, M. . W., … Gagnon, J.-M. (1999). Forcing of the cold event of 8,200 years ago by catastrophic drainage of Laurentide lakes. *Nature*, *400*(July), 344–348. http://doi.org/10.1038/22504

Bard, E., Bard, E., Hamelin, B., & Delanghe-sabatier, D. (2012). with Boreholes at Tahiti, *1235*(2010), 1235–1238. http://doi.org/10.1126/science.1180557

Bard, E., Hamelin, B., Arnold, M., Montaggioni, L., Cabiochll, G., Faure, G., & Rougerie, F. (1996). Global Meltwater Discharge, *382*(July), 241–244.

Barker, S., Chen, J., Gong, X., Jonkers, L., Knorr, G., & Thornalley, D. (2015). Icebergs not the trigger for North Atlantic cold events. *Nature*, *520*(7547), 333–336. http://doi.org/10.1038/nature14330

Barker, S., & Elderfield, H. (2002). Foraminiferal Calcification Response to Glacial-Interglacial Changes in Atmospheric CO 2, *297*(August), 833–837.

Barker, S., Greaves, M., & Elderfield, H. (2003). A study of cleaning procedures used for foraminiferal Mg/Ca paleothermometry. *Geochemistry, Geophysics, Geosystems*, *4*(9), 1–20. http://doi.org/10.1029/2003GC000559

Bauch, D., Carstens, J., & Wefer, G. (1997). Oxygen isotope composition of living Neogloboquadrina pachyderma (sin.) in the Arctic Ocean. *Earth and Planetary Science Letters*, *146*(1-2), 47–58. http://doi.org/10.1016/s0012-821x(96)00211-7

Bauch, H. A., & Kandiano, E. S. (2007a). Evidence for early warming and cooling in North Atlantic surface waters during the last interglacial, *22*(December 2005), 1–11. http://doi.org/10.1029/2005PA001252

Bauch, H. A., & Kandiano, E. S. (2007b). Evidence for early warming and cooling in North Atlantic surface waters during the last interglacial. *Paleoceanography*, *22*(1), 1–11. http://doi.org/10.1029/2005PA001252

Bell, N., & Smith, J. (1999). Coral growing on North Sea oil rigs. *Nature Communications*, *402*(December).

Bennett, B. Y. K. D. (1995). Determination of the number of zones in a biostratigraphical sequence. *New Phytologist*, *132*, 155–170.

Berger, W. H., Bickert, T., Schmidt, H., Wefer, G., & Yasuda, M. (1993). Quaternary oxygen isotope record of Pelagic foraminifers: Site 805, Ontong Java Plateau. *Proceedings of the Ocean Drilling Program, Scientific Results*, *130*, 363–379.

Berger, W. H., & Jansen, E. (1994). Mid-Pleistocene climate shift - The Nansen connection. *The Polar Oceans and Their Role in Shaping the Global Environment*, *85*, 295–311. http://doi.org/10.1029/GM085p0295

Bernasconi, S. M., Müller, I. A., Bergmann, K. D., & Breitenbach, S. F. M. (2018). Reducing Uncertainties in Carbonate Clumped Isotope Analysis Through Consistent Carbonate-Based Standardization Geochemistry , Geophysics , Geosystems, 2895–2914. http://doi.org/10.1029/2017GC007385

Bianchi, G. G., & McCave, I. N. (2000). Hydrography and sedimentation under the deep western boundary ¨ rn and Gardar Drifts , Iceland Basin current on Bjo, *165*, 137–169.

Bigeleisen, J., & Mayer, M. G. (1947). Calculation of Equilibrium Constants for Isotopic Exchange Reactions. *The Journal of Chemical Physics*, *15*(5), 261–267. http://doi.org/10.1063/1.1746492

Blunier, T., Chappellaz, J., Schwander, J., Dällenbach, a., Stauffer, B., Stocker, T. F., … Johnsen, S. J.

(1998). Asynchrony of Antarctic and Greenland climate change during the last glacial period. *Nature*, *394*, 739–743. http://doi.org/10.1038/29447

Bohm, E., Lippold, J., Gutjahr, M., Frank, M., Blaser, P., Antz, B., … Deininger, M. (2015). Strong and deep Atlantic meridional overturning circulation during the last glacial cycle. *Nature*, *517*(7532), 73–76. http://doi.org/10.1038/nature14059

Boltovskoy, E. (1973). Note on the determination of absolute surface water paleotemperature by means of the foraminiferGlobigerina bulloides d'Orbigny. *Paläontologische Zeitschrift*, *47*(3), 152–155. http://doi.org/10.1007/BF02985703

Bond, G. (1997). A Pervasive Millennial-Scale Cycle in North Atlantic Holocene and Glacial Climates. *Science*, *278*(5341), 1257–1266. http://doi.org/10.1126/science.278.5341.1257

Bond, G., Broecker, W., Johnsen, S., McManus, J., Labeyrie, L., Jouzel, J., & Bonani, G. (1993). Correlations between climate records from North Atlantic sediments and Greenland ice. *Nature*, *365*(6442), 143–147. http://doi.org/10.1038/365143a0

Bond, G. C., & Lotti, R. (1995). Iceberg discharges into the North Atlantic on millennial time scales during the last glaciation. *Science*, *267*(5200), 1005–1010. http://doi.org/10.1126/science.267.5200.1005

Bond, G., Heinricht, H., Broecker, W., Labeyrie, L., Mcmanus, J., Andrews, J., … Ivy, S. (1992). Letters to nature 15, *360*(November), 1668–1672.

Bond, G., Kromer, B., Beer, J., Muscheler, R., Evans, M. N., Showers, W., … Bonani, G. (2001). Persistent solar influence on North Atlantic climate during the Holocene. *Science (New York, N.Y.)*, *294*(5549), 2130–2136. http://doi.org/10.1126/science.1065680

Bonifacie, M., Calmels, D., Eiler, J. M., Horita, J., Chaduteau, C., Vasconcelos, C., … Bourrand, J. (2017). Calibration of the dolomite clumped isotope thermometer from 25 to 350 ° C , and implications for a universal calibration for all (Ca , Mg , Fe) CO 3 carbonates. *Geochimica et Cosmochimica Acta*, *200*, 255–279. http://doi.org/10.1016/j.gca.2016.11.028

Bower, A. S., & Richardson, P. L. (2002). Directly measured mid-depth circulation in the northeastern North Atlantic Ocean, 603–607. http://doi.org/10.1038/nature01106.1.

Boyle, E. a. (2000). Is ocean thermohaline circulation linked to abrupt stadial/interstadial transitions? *Quaternary Science Reviews*, *19*(1-5), 255–272. http://doi.org/10.1016/S0277-3791(99)00065-7

Boyle, & Keigwin. (1982). Deep Circulation of the North Atlantic over the Last 200,000 Years: Geochemical Evidence. *Science*, *218*(November).

Boyle, & Keigwin. (1985). Comparison of Atlantic and Pacific paleochemical records for the last 215,000 years: changes in deep ocean circulation and chemical inventories. *Earth and Planetary Science Lett*, *76*, 135–150.

Brambilla, E., & Talley, L. D. (2008). Subpolar Mode Water in the northeastern Atlantic : 1 . Averaged properties and mean circulation, *113*(December 2006), 1–18. http://doi.org/10.1029/2006JC004062

Brand, W. A., Assonov, S. S., Coplen, T. B., & Biogeochemistry, M. (2010). Correction for the 17 O interference in δ (13 C) measurements when analyzing CO 2 with stable isotope mass spectrometry (IUPAC Technical Report)* (C) N (N (N (C) O), *82*(8), 1719–1733. http://doi.org/10.1351/PAC-REP-09-01-05

Breitenbach, S. F. M., Mleneck-vautravers, M. J., Grauel, A., Lo, L., Bernasconi, S. M., Mu, I. A., … Ga, F. (2018). ScienceDirect Coupled Mg / Ca and clumped isotope analyses of foraminifera provide consistent water temperatures. http://doi.org/10.1016/j.gca.2018.03.010

Broecker, W. et al. (1968). Milankovitch Hypothesis Supported by Precise 18, (January), 297–300.

Broecker, W., Bond, G., Klas, M., Clark, E., & McManus, J. (1992). Origin of the northern Atlantic's Heinrich events. *Climate Dynamics*, *6*(3-4), 265–273. http://doi.org/10.1007/BF00193540

Broecker, W. S., Kennett, J. P., Flower, B. P., Teller, J. T., Trumbore, S., Bonani, G., & Wolfli, W. (1989). Routing of meltwater from the Laurentide Ice Sheet during the Younger Dryas cold episode. *Nature*, *341*, 318–321. http://doi.org/10.1038/341318a0

Broecker, W. S., Peteet, D. M., & Rind, D. (1985). Does the ocean-atmosphere system have more than one stable mode of operation? *Nature*, *315*(6014), 21–26. http://doi.org/10.1038/315021a0

Broecker, W. S., & van Donk, J. (1970). Insolation Changes , Ice Volumes , and the O18 record in Deep-Sea Cores. *Reviews of Geophysics and Space Physics*, *8*(1), 169–197. http://doi.org/10.1029/RG008i001p00169

Broeker. (1991). The Great Ocean Conveyor. *Oceanography*, *4*(2), 79 – 89. http://doi.org/10.1016/s0262-4079(08)61198-7

Brooks, S. J., & Birks, H. J. B. (2000). Chironomid-inferred Late-glacial air temperatures at Whitrig Bog, Southeast Scotland. *Journal of Quaternary Science*, *15*(8), 759–764. http://doi.org/10.1002/1099-1417(200012)15:8<759::aid-jqs590>3.0.co;2-v

Brummer, G.-J. A., Metcalfe, B., Feldmeijer, W., Prins, M. A., van &apos;t Hoff, J., & Ganssen, G. M. (2019). Modal shift in North Atlantic seasonality during the last deglaciation. *Climate of the Past Discussions*, (April), 1–20. http://doi.org/10.5194/cp-2018-144

Bryden, H. L. (1993). Ocean Heat Transport Across 24 N Latitude. *GEOPHYSICAL MONOGRAPH-AMERICAN GEOPHYSICAL UNION*, *75*, 65.

Bryden, H. L., & Imawaki, S. (2001). *Ocean Circulation and Climate: Observing and Modelling the Global Ocean. Chapter 6.1: Ocean Heat Transport*. Elsevier Science & Technology.

Caesar, L., Rahmstorf, S., Robinson, A., Feulner, G., & Saba, V. (2018). Observed fingerprint of a weakening Atlantic Ocean overturning circulation. *Nature*, *556*(7700), 191–196. http://doi.org/10.1038/s41586-018-0006-5

Came, R. E., Brand, U., & Affek, H. P. (2014). Clumped isotope signatures in modern brachiopod carbonate. *Chemical Geology*, *377*, 20–30. http://doi.org/10.1016/j.chemgeo.2014.04.004

Came, R. E., Eiler, J. M., Veizer, J., Azmy, K., Brand, U., & Weidman, C. R. (2007). Coupling of surface temperatures and atmospheric CO2 concentrations during the Palaeozoic era. *Nature*, *449*(7159), 198–201. http://doi.org/10.1038/nature06085

Campbell, D. C. (2015). Geological Survey of Canada Major Quaternary mass-transport deposits in southern Orphan Basin , (February).

Carlson, A. E. (2008). Why there was not a Younger Dryas-like event during the Penultimate Deglaciation. *Quaternary Science Reviews*, *27*(9-10), 882–887. http://doi.org/10.1016/j.quascirev.2008.02.004

Carstens, J., Hebbeln, D., & Wefer, G. (1997). Distribution of planktic foraminifera at the ice margin in the Aictic (Fram Strait). *Marine Micropaleontology*, *29*(August 1985), 257–269.

Castañeda, I. S., Werne, J. P., & Johnson, T. C. (2007). Wet and arid phases in the southeast African tropics since the Last Glacial Maximum. *Geology*, *35*(9), 823–826.

Chamberlin. (1906). On a Possible Reversal of Deeap-Sea Circulations and its Influence on Geologic Climates. *Journal of Geology*, *XIV*(5).

Channell, J. E. T., Hodell, D. A., & Lehman, B. (1997). Relative geomagnetic paleointensity and δ18O at ODP Site 983 (Gardar Drift, North Atlantic) since 350 ka. *Earth and Planetary Science Letters*, *153*(1-2), 103–118. http://doi.org/10.1016/s0012-821x(97)00164-7

Channell, J. E. T., Hodell, D. A., Romero, O., Hillaire-Marcel, C., de Vernal, A., Stoner, J. S., … Röhl, U. (2012). A 750-kyr detrital-layer stratigraphy for the North Atlantic (IODP Sites U1302-U1303, Orphan Knoll, Labrador Sea). *Earth and Planetary Science Letters*, *317-318*, 218–230. http://doi.org/10.1016/j.epsl.2011.11.029

Channell, J., Hodell, D., Xuan, C., Mazaud, A., & Stoner, J. (2008). Age calibrated relative paleointensity for the last 1.5 Myr at IODP Site U1308 (North Atlantic. *Earth and Planetary Science Letters*, *274*, 59–71. http://doi.org/10.1029/2001pa000733

Channell, & Scientists, E. 303. (2006). Expedition 303 summary. *Proceedings of the Ocean Drilling Program*, *303/306*. http://doi.org/10.2204/iodp.proc.303306.101.2006

Chapman, M. R. (2000). *The response of planktonic foraminifera to the Late Pliocene intensification of Northern Hemisphere glaciation*. (S. Culver & R. Peter, Eds.)*Biotic Response to Global Change: The Last 145 Million Years*. Cambridge University Press Cambridge, UK. http://doi.org/10.5670/oceanog.2002.49

Chapman, M. R. (2010). Seasonal production patterns of planktonic foraminifera in the NE Atlantic Ocean : Implications for paleotemperature and hydrographic reconstructions. *Palaeoceanography*, *25*. http://doi.org/10.1029/2008PA001708

Chapman, M. R., & Shackleton, N. J. (1998). Millennial-scale fluctuations in North Atlantic heat flux during the last 150 000 years. *Earth and Planetary Science Letters*, *159*(1-2), 57–70. http://doi.org/10.1016/S0012-821X(98)00068-5

Chapman, M. R., & Shackleton, N. J. (1999). Global ice-volume fluctuations, North Atlantic ice-rafting events, and deep-ocean circulation changes between 130 and 70 ka. *Geology*, *27*(9), 795–798. http://doi.org/10.1130/0091-7613(1999)027<0795:GIVFNA>2.3.CO;2

Chapman, M. R., Shackleton, N. J., Zhao, M., & Eglinton, G. (1996). Faunal and alkenone reconstructions of subtropical North Atlantic surface hydrography and paleotemperature over the last 28 kyr. *Paleoceanography*, *11*(3), 343–357. http://doi.org/10.1029/96PA00041

Charles, Lynch-Stieglitz, Ninnemann, & Fairbanks. (1996). Climate connections between the hemisphere revealed by deep sea sediment core/ice correlations. *Earth and Planetary Science Letters*, *142*, 19–27.

Chave, K. E. (1954). Aspects of the Biogeochemistry of Magnesium 1. Calcareous Marine Organisms. *Journal of Geology*, *62*, 266–283.

Clark, P. U., Dyke, A. S., Shakun, J. D., Carlson, A. E., Clark, J., Wohlfarth, B., … McCabe, A. M. (2009). The Last Glacial Maximum. *Science*, *325*(5941), 710–714. http://doi.org/10.1126/science.1172873

Clark, P. U., Hostetler, S. W., Meissner, K. J., Pisias, N. G., & Schmittner, A. (2013). Mechanisms for an ~7-Kyr Climate and Sea-Level Oscillation During Marine Isotope Stage 3. *Ocean Circulation: Mechanisms and Impacts - Past and Future Changes of Meridional Overturning*, 209–246. http://doi.org/10.1029/173GM15

Clark, P. U., Marshall, S. J., Clarke, G. K., Hostetler, S. W., Licciardi, J. M., & Teller, J. T. (2001). Freshwater forcing of abrupt climate change during the last glaciation. *Science (New York, N.Y.)*, *293*(5528), 283–287. http://doi.org/10.1126/science.1062517

Clark, P. U., Shakun, J. D., Baker, P. A., Bartlein, P. J., Brewer, S., Brook, E., … Williams, J. W. (2012). Global climate evolution during the last deglaciation. *Proceedings of the National Academy of Sciences of the United States of America*, *109*(19). http://doi.org/10.1073/pnas.1116619109

Cleroux, C., Cortijo, E., Duplessy, J., Gif, F.-, Cedex, Y., & Zahn, R. (2007). Deep-dwelling foraminifera as thermocline temperature recorders. *Geochemistry Geophysics Geosystems*, *8*(4). http://doi.org/10.1029/2006GC001474

Cleroux, Cortijo, Anand, Labeyrie, Bassinot, Caillon, & Duplessy. (2008). Mg / Ca and Sr / Ca ratios in planktonic foraminifera : Proxies for upper water column temperature reconstruction. *Paleoceanography*, *23*. http://doi.org/10.1029/2007PA001505

Climap Project Members. (1976). The surface of the ice age Earth. *Science*, *191*(4232).

Collins, M., R. Knutti, J. Arblaster, J.-L. Dufresne, T. Fichefet, P. Friedlingstein, X. Gao, W.J. Gutowski, T. Johns, G., & Krinner, M. Shongwe, C. Tebaldi, A. J. W. and M. W. (2013). Long-term Climate Change: Projections, Commitments and Irreversibility. In: Climate Change 2013: The Physical Science Basis. Contribution of Working Group I to the Fifth Assessment Report of the Intergovernmental Panel on Climate Change. *Cambridge University Press, Cambridge, United Kingdom and New York, NY, USA*, *9781107057*, 1029–1136. http://doi.org/10.1017/CBO9781107415324.024

Conkright, Levitus, & Boyer. (1994). *WORLD OCEAN ATLAS 1994 VOLUME 3 : SALINITY* (Vol. 3).

Conkright, M. E., Locarnini, R. a, Garcia, H. E., O’Brien, T. D., Boyer, T. P., Stepens, C., & Antonov, J. I. (2002). World Ocean Atlas 2001: Objective analyses, data statistics, and figures CD-ROM documentation. *National Oceanographic Data Center Internal Report (NOAA Atlas NESDIS)*, *17*(September), 17. Retrieved from http://www.nodc.noaa.gov/OC5/WOA01/pr_woa01.html

Coplen, T. B. (1981). Pressure Control of a Gas by a Calculator-Operated Mercury Piston. *Analytical Chemistry*, *53*(6), 940–942. http://doi.org/10.1021/ac00229a057

Coplen, T. B. (2007). Calibration of the calcite–water oxygen-isotope geothermometer at Devils Hole, Nevada, a natural laboratory. *Geochimica et Cosmochimica Acta*, *71*(16), 3948–3957. http://doi.org/10.1016/j.gca.2007.05.028

Crowley, T. J., & Zachos, J. C. (2000). Comparison of zonal temperature profiles for past warm time periods. *Warm Climates in Earth History*, 50–76.

Cuny, J., Rhines, P. B., Niiler, P. P., & Bacon, S. (2002). Labrador Sea boundary currents and the fate of the Irminger Sea Water. *Journal of Physical Oceanography*, *32*(2), 627–647. http://doi.org/10.1175/1520-0485(2002)032<0627:LSBCAT>2.0.CO;2

Curry, W. B. (1988). Changes in the distribution of d13c of deep water zco2 between the last glaciation and the Holocene. *Paleoceanography*, *3*(3), 317–341.

Curry, W. B., & Oppo, D. W. (2005a). Glacial water mass geometry and the distribution of δ^{13}C of ΣCO$_2$ in the western Atlantic Ocean. *Paleoceanography*, *20*(1), n/a–n/a. http://doi.org/10.1029/2004PA001021

Curry, W. B., & Oppo, D. W. (2005b). Glacial water mass geometry and the distribution of δ^{13}C of ΣCO$_2$ in the western Atlantic Ocean. *Paleoceanography*, *20*(1), n/a–n/a. http://doi.org/10.1029/2004PA001021

d'Orbigny, A. D. (1826). *Annals of Natural Sciences series* (Vol. 1).

Daëron, M., Blamart, D., Peral, M., & Affek, H. P. (2016). Absolute isotopic abundance ratios and the accuracy of D 47 measurements. *Chemical Geology*, *442*, 83–96. http://doi.org/10.1016/j.chemgeo.2016.08.014

Daëron, M., Drysdale, R. N., Peral, M., Huyghe, D., Blamart, D., Coplen, T. B., … Zanchetta, G. (2019). Most Earth-surface calcites precipitate out of isotopic equilibrium. *Nature Communications*, *10*(1), 1–7. http://doi.org/10.1038/s41467-019-08336-5

Dansgaard, W., Johnsen, S. J., Clausen, H. B., Dahl-Jensen, D., Gundestrup, N. S., Hammer, C. U., … Bond, G. (1993). Evidence for general instability of past climate from a 250-kyr ice-core record. *Nature*, *364*(6434), 218–220. http://doi.org/10.1038/364218a0

Dansgaard, W., & Tauber, H. (1969). Glacier oxygen-18 content and pleistocene ocean temperatures. *Science (New York, N.Y.)*, *166*(3904), 499–502. http://doi.org/10.1126/science.166.3904.499

Darling, K. F., Kucera, M., Kroon, D., & Wade, C. M. (2006). A resolution for the coiling direction paradox in Neogloboquadrina pachyderma, *21*(May), 1–14. http://doi.org/10.1029/2005PA001189

Darling, K. F., Kucera, M., Pudsey, C. J., & Wade, C. M. (2004). Molecular evidence links cryptic diversification in polar planktonic protists to Quaternary climate dynamics, *101*(20).

Davies, A. J., Wisshak, M., Orr, J. C., & Roberts, J. M. (2008). Deep-Sea Research I Predicting suitable habitat for the cold-water coral Lophelia pertusa (Scleractinia), *55*, 1048–1062. http://doi.org/10.1016/j.dsr.2008.04.010

Davies, S. M., Abbott, P. M., Meara, R. H., Pearce, N. J. G., Austin, W. E. N., Chapman, M. R., … Farmer, E. J. (2014a). A North Atlantic tephrostratigraphical framework for 130 e 60 ka b2k :

new tephra discoveries , marine-based correlations , and future challenges. *Quaternary Science Reviews*, *106*, 101–121. http://doi.org/10.1016/j.quascirev.2014.03.024

Davies, S. M., Abbott, P. M., Meara, R. H., Pearce, N. J. G., Austin, W. E. N., Chapman, M. R., … Farmer, E. J. (2014b). Invited review A North Atlantic tephrostratigraphical framework for 130 e 60 ka b2k : new tephra discoveries , marine-based correlations , and future challenges. *Quaternary Science Reviews*, *106*, 101–121. http://doi.org/10.1016/j.quascirev.2014.03.024

De Jong, M. F., Van Aken, H. M., Våge, K., & Pickart, R. S. (2012). Convective mixing in the central Irminger Sea: 2002-2010. *Deep-Sea Research Part I: Oceanographic Research Papers*, *63*, 36–51. http://doi.org/10.1016/j.dsr.2012.01.003

de Lange, Os, V., & Poorter. (1992). Geochemical composition and inferred accretion rates of sediments and manganese nodules from a submarine hill in the Madeira Abyssal Plain , eastern North Atlantic. *Marine Geology*, *109*, 171–194.

de Villiers, S., Greaves, M., & Elderfield, H. (2002). An intensity ratio calibration method for the accurate determination of Mg/Ca and Sr/Ca of marine carbonates by ICP-AES. *Geochemistry, Geophysics, Geosystems*, *3*(1), n/a–n/a. http://doi.org/10.1029/2001gc000169

Defliese, W. F., & Lohmann, K. C. (2016). ScienceDirect Evaluation of meteoric calcite cements as a proxy material for mass-47 clumped isotope thermometry. *GEOCHIMICA ET COSMOCHIMICA ACTA*, *173*, 126–141. http://doi.org/10.1016/j.gca.2015.10.022

Delaney, M. L. (1989). Temporal changes in interstitial water chemistry and calcite recrystallization in marine sediments. *Earth and Planetary Science Letters*, *95*(1-2), 23–37. http://doi.org/10.1016/0012-821X(89)90165-9

Delaney, M. L., & Boyle, E. A. (1985). Li, Sr, Mg, and Na in foraminiferal calcite shells from laboratory culture, sediment traps, and sediment cores. *Deep Sea Research Part B. Oceanographic Literature Review*, *32*(12), 1025. http://doi.org/10.1016/0198-0254(85)93853-1

Dennis, K. J., Affek, H. P., Passey, B. H., Schrag, D. P., & Eiler, J. M. (2011). Defining an absolute reference frame for “clumped” isotope studies of CO2. *Geochimica et Cosmochimica Acta*, *75*(22), 7117–7131. http://doi.org/10.1016/j.gca.2011.09.025

Dennis, K. J., & Schrag, D. P. (2010). Clumped isotope thermometry of carbonatites as an indicator of diagenetic alteration. *Geochimica et Cosmochimica Acta*, *74*(14), 4110–4122. http://doi.org/10.1016/j.gca.2010.04.005

Dennis, P. (2014). On the cause of mass spectrometer non-linearity during clumped isotope. *Figshare*, (https://doi.org/10.6084/m9.figshare.1254807.v1), Retrieved May 09 2017.

Dennis, P. F., Myhill, D. J., Marca, A., & Kirk, R. (2019). Clumped isotope evidence for episodic , rapid flow of fluids in a mineralized fault system in the Peak District , UK, *176*, 447–461.

Dennis, P. F., Vinen, S., Marca-bell, A., & Rowe, P. J. (2013). MIRA: a new isotope ratio mass spectrometer for clumped isotope studies of CO2, 1–25.

Denton, G. H., Hughes, T. J., & others. (1981). *The last great ice sheets*. Wiley.

Dietzel, M., Gussone, N., & Eisenhauer, a. (2004). Co-precipitation of Sr2+ and Ba2+ with aragonite by membrane diffusion of CO2 between 10 and 50 °C. *Chemical Geology*, *203*(1-2), 139–151.

http://doi.org/10.1016/j.chemgeo.2003.09.008

Dietzel, M., Tang, J., Leis, A., & Köhler, S. J. (2009). Oxygen isotopic fractionation during inorganic calcite precipitation - Effects of temperature, precipitation rate and pH. *Chemical Geology*, *268*(1-2), 107–115. http://doi.org/10.1016/j.chemgeo.2009.07.015

Dowdeswell, J. A., Maslin, M. A., Andrews, J. T., & McCave, I. N. (1995). Iceberg production, debris rafting, and the extent and thickness of Heinrich layers (H-1, H-2) in North Atlantic sediments. *Geology*, *23*(4), 301–304. http://doi.org/10.1130/0091-7613(1995)023<0297:IPDRAT>2.3.CO;2

Drijfhout, S. S., Weber, S. L., & van der Swaluw, E. (2011). The stability of the MOC as diagnosed from model projections for pre-industrial, present and future climates. *Climate Dynamics*, *37*(7-8), 1575–1586. http://doi.org/10.1007/s00382-010-0930-z

Duplessy, Bard, Labeyrie, Duprat, & Moyes. (1993). Oxygen isotope records and salinity changes in the Northeastern Atlantic Ocean during the last 18,000 years. *Paleoceanography*, *8*(3), 341–350.

Duplessy, J. C., Shackleton, N. J., Fairbanks, R. G., Labeyrie, L., Oppo, D., & Kallel, N. (1988). Deepwater source variations during the last climatic cycle and their impact on the global deepwater circulation. *Paleoceanography*, *3*(3), 343. http://doi.org/10.1029/PA003i003p00343

Duplessy, J.-C., Labeyrie, L., Juillet-LeClerc, A., Maitre, F., Duprat, J., & Sarnthein, M. (1991). Surface salinity reconstruction of the North Atlantic Ocean during the last glacial maximum. *Oceanologica Acta*, *14*, 311–324.

Dyke, A. S. (2004). Quaternary Glaciations-Extent and Chronology, Part II An outline of North American deglaciation with emphasis on central and northern Canada.

Dyke, A. S., Prest, V. K., Dyke, A. S., Prest, V. K., Survey, G., Street, B., & Ka, O. (1987). LATE WISCONSINAN AND HOLOCENE HISTORY OF THE LAURENTIDE ICE SHEET. *Geographie, Physique et Quaternaire*, *41*(2).

Eagle, R. A., Eiler, J. M., Tripati, A. K., Ries, J. B., Freitas, P. S., Hiebenthal, C., … Roy, K. (2013). The influence of temperature and seawater carbonate saturation state on 13C-18O bond ordering in bivalve mollusks. *Biogeosciences*, *10*(7), 4591–4606. http://doi.org/10.5194/bg-10-4591-2013

Eagle, R. a., Enriquez, M., Grellet-Tinner, G., Pérez-Huerta, A., Hu, D., Tütken, T., … Eiler, J. M. (2015). Isotopic ordering in eggshells reflects body temperatures and suggests differing thermophysiology in two Cretaceous dinosaurs. *Nature Communications*, *6*, 8296. http://doi.org/10.1038/ncomms9296

Edgar, K. M., Pälike, H., & Wilson, P. A. (2013). Testing the impact of diagenesis on the δ18O and δ13C of benthic foraminiferal calcite from a sediment burial depth transect in the equatorial Pacific. *Paleoceanography*, *28*(3), 468–480. http://doi.org/10.1002/palo.20045

Edwards, R. L., Beck, J. W., Burr, G. S., Donahue, D. J., Chappell, J. M. A., Bloom, A. L., … Taylor, F. W. (1993). A large drop in atmospheric 14C/12C and reduced melting in the Younger Dryas, documented with 230Th ages of corals. *Science*, *260*(5110), 962–968.

http://doi.org/10.1126/science.260.5110.962

Eiler, J. M. (2007). “Clumped-isotope” geochemistry-The study of naturally-occurring, multiply-substituted isotopologues. *Earth and Planetary Science Letters*, *262*(3-4), 309–327. http://doi.org/10.1016/j.epsl.2007.08.020

Eiler, J. M., Clog, M., Magyar, P., Piasecki, A., Sessions, A., Stolper, D., … Schwieters, J. (2013). A high-resolution gas-source isotope ratio mass spectrometer. *International Journal of Mass Spectrometry*, *335*, 45–56. http://doi.org/10.1016/j.ijms.2012.10.014

Eiler, J. M., & Schauble, E. a. (2004). 18O13C16O in Earth’s atmosphere. *Geochimica Et Cosmochimica Acta*, *68*(23), 4767–4777. http://doi.org/10.1016/j.gca.2004.05.035

Elderfield, & Ganssen. (2000). Past temperature and d O of surface ocean waters inferred from foraminiferal Mg / Ca ratios. *Nature*, *405*(MAY), 25–28.

Elderfield, Vautravers, & Cooper. (2002). The relationship between shell size and Mg/Ca, Sr/Ca, D 18 O, and D 13 C of species of planktonic foraminifera. *Geochemistry Geophysics Geosystems*, *3*(8).

Elliot, M., Labeyrie, L., & Duplessy, J. C. (2002). Changes in North Atlantic deep-water formation associated with the Dansgaard - Oeschger temperature oscillations (60-10 ka). *Quaternary Science Reviews*, *21*(10), 1153–1165. http://doi.org/10.1016/S0277-3791(01)00137-8

Ellison, C. R. W., Chapman, M. R., & Hall, I. R. (2006). Surface and deep ocean interactions during the cold climate event 8200 years ago. *Science (New York, N.Y.)*, *312*(5782), 1929–1932. http://doi.org/10.1126/science.1127213

Emiliani, C. (1955). Mineralogical and chemical composition of the tests of certain pelagic foraminifera. *Micropaleontology*, 377–380.

Emiliani, C. (1966). Isotopic Paeleotemperatures. *Science*, *154*(3751), 851–857.

Emiliani, C., & Epstein, S. (1953). Temperature variations in the lower Pleistocene of southern California. *The Journal of Geology*, *61*(2), 171–181.

Emiliani, & Edwards. (1953). Tertiary Ocean Bottom Temperatures. *Nature*.

Epstein, Buschsbaum, Lowestam, & Urey. (1951). Carbonation-water isotopic temperature scale. *Bulletin of the Geological Society of America*, *62*(April), 417–426.

Ericson. (1959). Coiling Direction of Globigerina pachyderma as a Climatic Index. *Science*, *130*(3369), 1–3.

Evans, D., & Mller, W. (2012). Deep time foraminifera Mg/Ca paleothermometry: Nonlinear correction for secular change in seawater Mg/Ca. *Paleoceanography*, *27*(4), 1–11. http://doi.org/10.1029/2012PA002315

Evans, D., Sagoo, N., Renema, W., Cotton, L. J., Müller, W., & Todd, J. A. (2017). Eocene greenhouse climate revealed by coupled clumped isotope-Mg / Ca thermometry, 1–6. http://doi.org/10.1073/pnas.1714744115

Fairbanks, R. G. (1989). A 17,000-year glacio-eustatic sea level record: influence of glacial melting rates on the Younger Dryas event and deep-ocean circulation. *Nature*.

http://doi.org/10.1038/342637a0

Farmer. (2010). North Atlantic Globorotalia inflata coretop Mg / Ca calibrations and temperature reconstructions over North Atlantic Globorotalia inflata coretop Mg / Ca calibrations and temperature reconstructions over Termination I. *IOP Conf. Ser.: Earth Environ. Sci*, (9). http://doi.org/10.1088/1755-1315/9/1/012019

Farmer, E. J., Chapman, M. R., & Andrews, J. E. (2008). Centennial-scale holocene North Atlantic surface temperatures from Mg/Ca ratios in Globigerina bulloides. *Geochemistry, Geophysics, Geosystems*, *9*(12), 1–15. http://doi.org/10.1029/2008GC002199

Farmer, E. J., Chapman, M. R., & Andrews, J. E. (2011a). Holocene temperature evolution of the subpolar North Atlantic recorded in the Mg / Ca ratios of surface and thermocline dwelling planktonic foraminifers. *Global and Planetary Change*, *79*(3-4), 234–243. http://doi.org/10.1016/j.gloplacha.2011.02.003

Farmer, E. J., Chapman, M. R., & Andrews, J. E. (2011b). Holocene temperature evolution of the subpolar North Atlantic recorded in the Mg / Ca ratios of surface and thermocline dwelling planktonic foraminifers. *Global and Planetary Change*, *79*(3-4), 234–243. http://doi.org/10.1016/j.gloplacha.2011.02.003

Fatela, F., & Taborda, R. (2002). Confidence limits of species proportions in microfossil assemblages. *Marine Micropaleontology*, *45*, 169–174.

Fernandez, A., Tang, J., & Rosenheim, B. E. (2014). Siderite “clumped” isotope thermometry: A new paleoclimate proxy for humid continental environments. *Geochimica et Cosmochimica Acta*, *126*, 411–421. http://doi.org/10.1016/j.gca.2013.11.006

Fiebig, J., Bajnai, D., Löffler, N., Methner, K., Krsnik, E., Mulch, A., & Hofmann, S. (2019). Combined high-precision Δ48 and Δ47 analysis of carbonates. *Chemical Geology*, *522*(February), 186–191. http://doi.org/10.1016/j.chemgeo.2019.05.019

Flower, B. P., Hastings, D. W., Hill, H. W., & Quinn, T. M. (2004). Phasing of deglacial warming and Laurentide Ice Sheet meltwater in the Gulf of Mexico. *Geology*, *32*(7), 597–600. http://doi.org/10.1130/G20604.1

Frederiksen, Jensen, & Westerberg. (1992). The distribution of the Scleractinian Coral Lophelia pertusa around the Faroe Islands and the relation to internal tidal mixing. *Sarsia North Atlantic Marine Science*, (August). http://doi.org/10.1080/00364827.1992.10413502

Friedrich, O., Schiebel, R., Wilson, P. A., Weldeab, S., Beer, C. J., Cooper, M. J., & Fiebig, J. (2012). In fl uence of test size , water depth , and ecology on Mg / Ca , Sr / Ca , δ 18 O and δ 13 C in nine modern species of planktic foraminifers. *Earth and Planetary Science Letters*, *319-320*, 133–145. http://doi.org/10.1016/j.epsl.2011.12.002

Fronval, T., Jansen, E., Bloemendal, J., & Johnsen, S. (1995). Oceanic evidence for coherent fluctuations in Fennoscandian and Laurentide ice sheets on millennium timescales. *Nature*, *374*(6521), 443–446. http://doi.org/10.1038/374443a0

Galaasen, Ulysses, Ninnemann, Irvali, Helga, Kleiven, … Hodell. (2014). Rapid Reductions in North Atlantic. *Nature*, *726*(March), 722–726.

Ganachaud, A., & Wunsch, C. (2000). Improved estimates of global ocean circulation, heat transport and mixing from hydrographic data. *Nature*, *408*, 453–456.

Ganopolski, a, Rahmstorf, S., Petoukhov, V., & Claussen, M. (1998). Simulation of modern and glacial climates with a coupled global model of intermediate complexity. *Nature*, *391*(6665), 351–356. http://doi.org/10.1038/34839

Ganssen, G. M., & Kroon, D. (2000). The isotopic signature of planktonic foraminifera from NE Atlantic surface sediments : implications for the reconstruction of past oceanic conditions, *157*(1991), 693–699.

Gass, S. E., & Roberts, J. M. (2006). The occurrence of the cold-water coral Lophelia pertusa (Scleractinia) on oil and gas platforms in the North Sea : Colony growth , recruitment and environmental controls on distribution, *52*, 549–559. http://doi.org/10.1016/j.marpolbul.2005.10.002

Gherardi, J.-M., & Labeyrie, L. (1999). CAMPAGNE INTERPOLE MD99-114 / IMAGES V, Atlantic Nord et Mers Actiques. *LES RAPPORTS DE CAMPAGNE A LA MER A BORD DU MARION-DUFRESNE*.

Ghosh, P., Adkins, J., Affek, H., Balta, B., Guo, W., Schauble, E. A., … Eiler, J. M. (2006). 13C–18O bonds in carbonate minerals: A new kind of paleothermometer. *Geochimica et Cosmochimica Acta*, *70*(6), 1439–1456. http://doi.org/10.1016/j.gca.2005.11.014

Ghosh, P., Eiler, J., Campana, S. E., & Feeney, R. F. (2007). Calibration of the carbonate “clumped isotope” paleothermometer for otoliths. *Geochimica et Cosmochimica Acta*, *71*(11), 2736–2744. http://doi.org/10.1016/j.gca.2007.03.015

Gildor, H., & Tziperman, E. (2003). Sea-ice switches and abrupt climate change. *Philosophical Transactions. Series A, Mathematical, Physical, and Engineering Sciences*, *361*(1810), 1935–1942; discussion 1942–1944. http://doi.org/10.1098/rsta.2003.1244

Grauel, A.-L., Hodell, D. A., & Bernasconi, S. M. (2016). Quantitative estimates of tropical temperature change in lowland Central America during the last 42 ka. *Earth and Planetary Science Letters*, *438*, 37–46. http://doi.org/10.1016/j.epsl.2016.01.001

Grauel, A.-L., Schmid, T. W., Hu, B., Bergami, C., Capotondi, L., Zhou, L., & Bernasconi, S. M. (2013). Calibration and application of the “clumped isotope” thermometer to foraminifera for high-resolution climate reconstructions. *Geochimica et Cosmochimica Acta*, *108*, 125–140. http://doi.org/10.1016/j.gca.2012.12.049

Grimm, E. C. (1987). CONISS : A FORTRAN 77 PROGRAM FOR STRATIGRAPHICALLY CONSTRAINED CLUSTER ANALYSIS BY THE METHOD OF INCREMENTAL SUM OF SQUARES *. *Computers and Geosciences*, *13*(I), 13–35.

Grobe, B. H. (1987). A Simple Method for the Determination of Ice-Rafted Debris in Sediment Cores *. *Polarforschung*, *57*(41), 123–126.

Grousset, F. E., Labeyrie, L., SINKO, J. A., CREMER, M., Bond, G., Duprat, J., … HUON, S. (1993). Patterns of Ice-Rafted Detritus in the Glacial North-Atlantic (40-Degrees-55-Degrees-N). *Paleoceanography*, *8*(2), 175–192. Retrieved from papers3://publication/uuid/51C81CA5-0D69-4EC7-A7B9-BCABB511ACC5

Grousset, F. E., Pujol, C., Labeyrie, L., Auffret, G., & Boelaert, A. (2000). Were the North Atlantic Heinrich events triggered by the behavior of the European ice sheets? *Geology*, *28*(2), 123–126. http://doi.org/10.1130/0091-7613(2000)28<123:WTNAHE>2.0.CO;2

Guiot, J. (2011). Transfer functions. *IOP Conference Series: Earth and Environmental Science*, *14*(1). http://doi.org/10.1088/1755-1315/14/1/012008

Guo, W., & Eiler, J. M. (2007). Temperatures of aqueous alteration and evidence for methane generation on the parent bodies of the CM chondrites, *71*, 5565–5575. http://doi.org/10.1016/j.gca.2007.07.029

Guo, W., Mosenfelder, J. L., Goddard, W. A., & Eiler, J. M. (2009). Isotopic fractionations associated with phosphoric acid digestion of carbonate minerals: Insights from first-principles theoretical modeling and clumped isotope measurements. *Geochimica et Cosmochimica Acta*, *73*(24), 7203–7225. http://doi.org/10.1016/j.gca.2009.05.071

Gwiazda, R. H., Hemming, S. R., & Broecker, W. S. (1996). Provenance of icebergs during Heinrich Event 3 and the contrast to their sources during other Heinrich episodes. *Paleoceanography*, *11*(4), 371–378. http://doi.org/10.1029/96PA01022

Hagelberg, T. K., Bond, G., & deMenocal, P. (1994). Milankovitch band forcing of sub-Milankovitch climate variability during the Pleistocene. *Paleoceanography*, *9*(4), 545–558. http://doi.org/10.1029/94PA00443

Hamel, & Mercier. (2010). Influence of size and seasonal factors on the growth of the deep-sea coral Flabellum alabastrum in mesocosm, 521–525. http://doi.org/10.1007/s00338-010-0590-9

Hanebuth, T., Stattegger, K., & Grootes, P. M. (2000). Rapid flooding of the Sunda Shelf: A late-glacial sea-level record. *Science*, *288*(5468), 1033–1035. http://doi.org/10.1126/science.288.5468.1033

Haslett, J., & Parnell, A. (2008). A simple monotone process with application to radiocarbon-dated depth chronologies. *Journal of the Royal Statistical Society. Series C: Applied Statistics*, *57*(4), 399–418. http://doi.org/10.1111/j.1467-9876.2008.00623.x

Heinrich, H. (1988). Origin and consequences of cyclic ice rafting in the Northeast Atlantic Ocean during the past 130,000 years. *Quaternary Research*, *29*(2), 142–152. http://doi.org/10.1016/0033-5894(88)90057-9

Hemming, S. R. (2004). HEINRICH EVENTS : MASSIVE LATE PLEISTOCENE DETRITUS LAYERS OF THE NORTH ATLANTIC AND THEIR GLOBAL CLIMATE IMPRINT, (2003). http://doi.org/10.1029/2003RG000128.1.INTRODUCTION

Henkes, G. A., Passey, B. H., Grossman, E. L., Shenton, B. J., Yancey, T. E., & Pérez-Huerta, A. (2018). Temperature evolution and the oxygen isotope composition of Phanerozoic oceans from carbonate clumped isotope thermometry. *Earth and Planetary Science Letters*, *490*, 40–50. http://doi.org/10.1016/j.epsl.2018.02.001

Hesse, R., & Khodabakhsh, S. (1998). Depositional facies of late Pleistocene Heinrich events in the Labrador Sea. *Geology*, *26*(2), 103–106. http://doi.org/10.1130/0091-7613(1998)026<0103:DFOLPH>2.3.CO;2

Hill, P. S., Tripati, A. K., & Schauble, E. A. (2014). Theoretical constraints on the effects of pH, salinity, and temperature on clumped isotope signatures of dissolved inorganic carbon species and precipitating carbonate minerals. *Geochimica et Cosmochimica Acta*, *125*, 610–652. http://doi.org/10.1016/j.gca.2013.06.018

Hillaire-Marcel, C. (1994). Isotope stratigraphy , sedimentation rates , deep circulation , and carbonate events in the Labrador Sea during the last ~ 200ka, (February 2016). http://doi.org/10.1139/e94-007

Hillaire-Marcel, C., & Bilodeau, G. (2000). Instabilities in the Labrador Sea water mass structure during the last climatic cycle. *Canadian Journal of Earth Science*, *37*(February), 795 – 809. http://doi.org/10.1139/cjes-37-5-795

Hillaire-Marcel, C., De Vernal, A., Bilodeau, G., & Weaver, A. J. (2001). Absence of deep-water formation in the Labrador Sea during the last interglacial period. *Nature*, *410*(6832), 1073–1077. http://doi.org/10.1038/35074059

Hillaire-Marcel, C., de Vernal, A., Candon, L., Bilodeau, G., & Stoner, J. (2001). Changes of potential density gradients in the Northwestern north Atlantic during the last climatic cycle based on a multiproxy approach. *Geophysical Monograph Series*, *126*, 83–100. http://doi.org/10.1029/GM126p0083

Hillaire-Marcel, C., de Vernal, A., & Piper, D. J. W. (2007). Lake Agassiz Final drainage event in the northwest North Atlantic. *Geophysical Research Letters*, *34*(15), 1–5. http://doi.org/10.1029/2007GL030396

Hillaire-Marcel, C., DeVernal, Bilodeau, & Wu. (1994). Isotope stratigraphy , sedimentation rates , deep circulation , and carbonate events in the Labrador Sea during the last ~ 200ka, (February 2016). http://doi.org/10.1139/e94-007

Hillaire-Marcel, C., Vernal, A. de, Lucotte, M., & Mucci, A. (1994). The Labrador Sea during the late Quaternary: Introduction. *Canadian Journal of Earth Sciences*, *31*(1), 1–4.

Hillaire-Marcel, C., Vernal, A. De, & Mckay, J. (2011a). Foraminifer isotope study of the Pleistocene Labrador Sea , northwest North Atlantic (IODP Sites 1302 / 03 and 1305), with emphasis on paleoceanographical differences between its “ inner ” and “ outer ” basins. *Marine Geology*, *279*(1-4), 188–198. http://doi.org/10.1016/j.margeo.2010.11.001

Hillaire-Marcel, C., Vernal, A. De, & Mckay, J. (2011b). Foraminifer isotope study of the Pleistocene Labrador Sea , northwest North Atlantic (IODP Sites 1302 / 03 and 1305), with emphasis on paleoceanographical differences between its “ inner ” and “ outer ” basins. *Marine Geology*, *279*(1-4), 188–198. http://doi.org/10.1016/j.margeo.2010.11.001

Hiscott, R. N., Aksu, A. E., Mudie, P. J., & Parsons, D. F. (2001). A 340 , 000 year record of ice rafting , palaeoclimatic fluctuations , and shelf-crossing glacial advances in the southwestern Labrador Sea.

Hiscott, R. N., Cremer, M., & Aksu, A. (1989). Evidence from Sedimentary sturctures for processes of sediment transport and deposition during Post-Miocene time at sites 645, 646 and 647, Baffin Bay and thr Labrador Sea. *Proceedings of the Ocean Drilling Program*, *105*, 53–63.

Hodell, D. A., Channeil, J. E. T., Curtis, J. H., Romero, O. E., & Röhl, U. (2008). Onset of “Hudson Strait”

Heinrich events in the eastern North Atlantic at the end of the middle Pleistocene transition (~640 ka)? *Paleoceanography*, *23*(4), 1–16. http://doi.org/10.1029/2008PA001591

Hodell, D. A., & Curtis, J. H. (2008). Oxygen and carbon isotopes of detrital carbonate in North Atlantic Heinrich Events. *Marine Geology*, *256*(1-4), 30–35. http://doi.org/10.1016/j.margeo.2008.09.010

Hodell, D. A., Evans, H. F., Channell, J. E. T., & Curtis, J. H. (2010). Phase relationships of North Atlantic ice-rafted debris and surface-deep climate proxies during the last glacial period. *Quaternary Science Reviews*, *29*(27-28), 3875–3886. http://doi.org/10.1016/j.quascirev.2010.09.006

Hodell, D. A., Minth, E. K., Curtis, J. H., McCave, I. N., Hall, I. R., Channell, J. E. T., & Xuan, C. (2009). Surface and deep-water hydrography on Gardar Drift (Iceland Basin) during the last interglacial period. *Earth and Planetary Science Letters*, *288*(1-2), 10–19. http://doi.org/10.1016/j.epsl.2009.08.040

Holliday, N. P., Bacon, S., Allen, J., & McDonagh, E. L. (2009). Circulation and transport in the western boundary currents at Cape Farewell, Greenland. *Journal of Physical Oceanography*, *39*(8), 1854–1870. http://doi.org/10.1175/2009JPO4160.1

Honjo, S. (1976). No Title, *1*.

Honjo, S., & Erez, J. (1978). Dissolution rates of calcium carbonate in the deep ocean; an in-situ experiment in the North Atlantic Ocean. *Earth and Planetary Science Letters*, *40*(2), 287–300. http://doi.org/10.1016/0012-821X(78)90099-7

Hu, A., Meehl, G. A., Han, W., & Yin, J. (2009). Transient response of the MOC and climate to potential melting of the Greenland Ice Sheet in the 21st century. *Geophysical Research Letters*, *36*(10), 1–6. http://doi.org/10.1029/2009GL037998

Huang, X., Meyers, P. A., Yu, J., Wang, X., Huang, J., Jin, F., … Xie, S. (2012). Moisture conditions during the Younger Dryas and the early Holocene in the middle reaches of the Yangtze River, central China. *Holocene*, *22*(12), 1473–1479. http://doi.org/10.1177/0959683612450202

Huber. (1964). Robust Estimation of a location parameter.

Hulbe, C. L. (1997). An ice shelf mechanism for Heinrich layer production. *Paleoceanography*, *12*(5), 711–717. http://doi.org/10.1029/97PA02014

Hume. (2018a). *The Last Interglacial in the Labrador Sea*. *PhD Thesis*. University of East Anglia.

Hume, L. (2018b). The Last Interglacial in the Labrador Sea.

Huntington, K. W., Eiler, J. M., Affek, H. P., Guo, W., Bonifacie, M., Yeung, L. Y., … Came, R. (2009). Methods and limitations of "clumped" CO $_2$ isotope (Δ $_{47}$) analysis by gas-source isotope ratio mass spectrometry. *Journal of Mass Spectrometry*, *44*(9), 1318–1329. http://doi.org/10.1002/jms.1614

Hut, G. (1987). Consultants' group meeting on stable isotope reference samples for geochemical and hydrological investigations.

Hutson, W. H. (1980). The agulhas current during the late pleistocene: analysis of modern faunal analogs. *Science*, *207*(11), 64–66. http://doi.org/10.1126/science.207.4426.64

Imbrie, J., Hays, J. D., Martinson, D. G., McIntyre, A., Mix, A. C., Morley, J. J., … Shackleton, N. J. (1984). The orbital theory of Pleistocene climate: Support from a revised chronology of the marine d18O record. *Milankovitch and Climate: Understanding the Response to Astronomical Forcing*, (November 2015), 269–305. http://doi.org/-

Imbrie, J., Kipp, N. G., & Turekian, K. K. (1971a). *A new micropaleontological method for quantitative paleoclimatology : Application to a late Pleistocene Caribbean Core*. *The late Cenozoic glacial ages*. Yale University Press, New Haven, Conn.

Imbrie, J., Kipp, N. G., & Turekian, K. K. (1971b). The late Cenozoic glacial ages. *Yale University Press, New Haven, Conn*, 71–182.

Imbrie, Van-Donk, & Kipp. (1973). Paleoclimatic investigation of a late Pleistocene Carribean deep-sea core: Comparison of isotopic and Faunal Methods. *Quaternary Research*, *38*, 10–38.

Irval, N., Ninnemann, U. S., Galaasen, E. V., Rosenthal, Y., Kroon, D., Oppo, D. W., … Kissel, C. (2012). Rapid switches in subpolar North Atlantic hydrography and climate during the Last Interglacial (MIS 5e). *Paleoceanography*, *27*(2), 1–16. http://doi.org/10.1029/2011PA002244

Irvalı, N., Ninnemann, U. S., Kleiven, H. K. F., Galaasen, E. V., Morley, A., & Rosenthal, Y. (2016). Evidence for regional cooling, frontal advances, and East Greenland Ice Sheet changes during the demise of the last interglacial. *Quaternary Science Reviews*, *150*, 184–199. http://doi.org/10.1016/j.quascirev.2016.08.029

Iversen, J. (1944). Viscum, Hedera and Ilex as Climate Indicators. *Geologiska Föreningen I Stockholm Förhandlingar*, *66*(3), 463–483. http://doi.org/10.1080/11035894409445689

Jautzy, J. J., Savard, M. M., Dhillon, R. S., & Bernasconi, S. M. (2020). Clumped isotope temperature calibration for calcite: Bridging theory and experimentation. *Geochemical Perspectives Letters*, (2020), 36–41. http://doi.org/10.7185/geochemlet.2021

Jimenez-Lopez, Caballero, Huertas, & Romanek. (2001). Chemical , mineralogical and isotope behavior , and phase transformation during the precipitation of calcium carbonate minerals from intermediate ionic solution at 25 ° C. *Geochimica et Cosmochimica Acta*, *65*(19), 3219–3231.

Johnsen, Clausen, Dansgaard, Fuhrer, Gundestrup, Hammer, … Steffensen. (1992). Irregular glacial interstadials recorded in a new Greenland ice core. *Nature*, *359*(24 September), 311–313.

Johnsen, S. J., Dahl-Jensen, D., Gundestrup, N., Steffensen, J. P., Clausen, H. B., Miller, H., … White, J. (2001). Oxygen isotope and palaeotemperature records from six Greenland ice-core stations: Camp Century, Dye-3, GRIP, GISP2, Renland and NorthGRIP. *Journal of Quaternary Science*, *16*(4), 299–307. http://doi.org/10.1002/jqs.622

Johnson, C., Sherwin, T., Smythe-Wright, D., Shimmield, T., & Turrell, W. (2010). Wyville Thomson Ridge Overflow Water: Spatial and temporal distribution in the Rockall Trough. *Deep-Sea Research Part I: Oceanographic Research Papers*, *57*(10), 1153–1162. http://doi.org/10.1016/j.dsr.2010.07.006

Johnson, R. G., & Lauritzen, S. E. (1995). Hudson Bay-Hudson Strait jökulhlaups and Heinrich events:

a hypothesis. *Palaeogeography, Palaeoclimatology, Palaeoecology*, *117*(1-2), 123–137. http://doi.org/10.1016/0031-0182(94)00120-W

Johnson, R. G., & McClure, B. T. (1976). A model for Northern Hemisphere continental ice sheet variation. *Quaternary Research*, *6*(3), 325–353. http://doi.org/10.1016/0033-5894(67)90001-4

Jonkers, & Kucera. (2016). Quantifying the effect of seasonal and vertical habitat tracking on planktonic foraminifera proxies. *Biogeosciences*, *1*(December), 1–34. http://doi.org/10.5194/cp-2016-125

Jonkers, L., Brummer, G. J. A., Peeters, F. J. C., Aken, H. M. Van, & Jong, M. F. De. (2010). Seasonal stratification , shell flux , and oxygen isotope dynamics of left - coiling N . pachyderma and T . quinqueloba in the western subpolar North Atlantic, *25*, 1–13. http://doi.org/10.1029/2009PA001849

Juggins, S. (2017a). rioja: Analysis of Quaternary Science Data.

Juggins, S. (2017b). rioja: Analysis of Quaternary Science Data. Retrieved from http://www.staff.ncl.ac.uk/stephen.juggins/

Jungclaus, J. H., Haak, H., Esch, M., Roeckner, E., & Marotzke, J. (2006). Will Greenland melting halt the thermohaline circulation? *Geophysical Research Letters*, *33*(17), 1–5. http://doi.org/10.1029/2006GL026815

Keigwin, L. D. (2004a). Radiocarbon and stable isotope constraints on Last Glacial Maximum and Younger Dryas ventilation in the western North Atlantic. *Paleoceanography*, *19*(4), n/a–n/a. http://doi.org/10.1029/2004PA001029

Keigwin, L. D. (2004b). Radiocarbon and stable isotope constraints on Last Glacial Maximum and Younger Dryas ventilation in the western North Atlantic. *Paleoceanography*, *19*(4), n/a–n/a. http://doi.org/10.1029/2004PA001029

Kele, Breitenbach, Sebastian, Capezzuoli, Meckler, Ziegler, … Bernasconi. (2015). Temperature dependence of oxygen- and clumped isotope fractionation in carbonates: A study of travertines and tufas in the 6-95 C temperature range. *Geochimica et Cosmochimica Acta*, *168*, 172–192. http://doi.org/10.1016/j.gca.2015.06.032

Kelson, Huntington, Schauer, Saenger, & Lechler. (2017). ScienceDirect Toward a universal carbonate clumped isotope calibration : Diverse synthesis and preparatory methods suggest a single temperature relationship. *Geochimica et Cosmochimica Acta*, *197*, 104–131. http://doi.org/10.1016/j.gca.2016.10.010

Kennett, J. P., & Srinivasan, M. S. (1983). *Neogene planktonic foraminifera: a phylogenetic atlas*. Hutchinson Ross.

Killingley, J. S. (1983). Effects of diagenetic recrystallization on 18O/16O values of deep-sea sediments. *Nature*, *301*(5901), 594–597. http://doi.org/10.1038/301594a0

Kim, S., Hillaire-marcel, C., & Mucci, A. (2006). Mechanisms of equilibrium and kinetic oxygen isotope effects in synthetic aragonite at 25 ° C, *70*, 5790–5801. http://doi.org/10.1016/j.gca.2006.08.003

Kim, S., Neil, J. R. O., Hillaire-marcel, C., & Mucci, A. (2007). Oxygen isotope fractionation between synthetic aragonite and water : Influence of temperature and Mg 2 + concentration, *71*, 4704–4715. http://doi.org/10.1016/j.gca.2007.04.019

Kim, S.-T., & O'Neil, J. (1997). Equilibrium and nonequilibrium oxygen isotope effects in synthetic carbonates. *Geochimica et Cosmochimica Acta*, *61*(16), 3461–3475. http://doi.org/10.1016/S0016-7037(97)00169-5

Kirk, R. (2017). Development of clumped isotope techniques and their application to palaeoclimate studies. *PhD Thesis*.

Kisakürek, B., Eisenhauer, A., Böhm, F., Garbe-Schönberg, D., & Erez, J. (2008). Controls on shell Mg/Ca and Sr/Ca in cultured planktonic foraminiferan, Globigerinoides ruber (white). *Earth and Planetary Science Letters*, *273*(3-4), 260–269. http://doi.org/10.1016/j.epsl.2008.06.026

Kleiven, H. F., Kissel, C., Laj, C., Ninnemann, U. S., Richter, T. O., & Cortijo, E. (2008). Reduced North Atlantic deep water coeval with the glacial lake agassiz freshwater outburst. *Science*, *319*(5859), 60–64. http://doi.org/10.1126/science.1148924

Kluge, John, Jourdan, Davis, & Crawshaw. (2015). ScienceDirect Laboratory calibration of the calcium carbonate clumped isotope thermometer in the 25 – 250 ° C temperature range. *Geochimica et Cosmochimica Acta*, *157*, 213–227. http://doi.org/10.1016/j.gca.2015.02.028

Kluge, John, M., Jourdan, A., Davis, S., Kluge, T., & Crawshaw, J. (2015). Laboratory calibration of the calcium carbonate clumped isotope thermometer in the 25 – 250 ° C temperature range. *Geochimica et Cosmochimica Acta*, *157*, 213–227. http://doi.org/10.1016/j.gca.2015.02.028

Knutz, P. C., Austin, W. E. N., & John W Jones, E. (2001). Millennial-scale depositional cycles related to British ice sheet variability and North Atlantic paleocirculation since 45 kyr B.P., Barra Fan, U.K. margin. *Paleoceanography*, *16*(1), 53–64. http://doi.org/10.1029/1999PA000483

Kohfeld, K. E., Fairbanks, R. G., Smith, S. L., & Walsh, I. D. (1996). Neogloboquadrina pachyderma (sinistral coiling) as paleoceanographic tracers in polar oceans: Evidence from Northeast Water Polynya plankton tows, sediment traps, and surface sediments. *Paleoceanography*, *11*(6), 679–699. http://doi.org/10.1029/96PA02617

Kotilainen, A. T., & Shackleton, N. J. (1995). Rapid climate variability in the North Pacific Ocean during the past 95,000 years. *Nature*, *377*(6547), 323–326.

Kozdon, R., Eisenhauer, A., Ifm-geomar, K., Kiel, D.-, Weinelt, M., & Kiel, D.-. (2009). Reassessing Mg/Ca temperature calibrations of Neogloboquadrina pachyderma (sinistral) using paired d 44/40 Ca and Mg/Ca measurements, *13*. http://doi.org/10.1029/2008GC002169

Kozdon, R., Kelly, D. C., Kitajima, K., Strickland, A., Fournelle, J. H., & Valley, J. W. (2013). In situ δ 18 O and Mg/Ca analyses of diagenetic and planktic foraminiferal calcite preserved in a deep-sea record of the Paleocene-Eocene thermal maximum. *Paleoceanography*, *28*(3), 517–528. http://doi.org/10.1002/palo.20048

Kroon, D., Austin, W. E. N., Chapman, M. R., & Ganssen, G. M. (1997). Deglacial surface circulation changes in the northeastern Atlantic: Temperature and salinity records off NW Scotland on a century scale. *Paleoceanography*, *12*(6), 755. http://doi.org/10.1029/97PA02289

Kroopnick, P. M. (1985). The distribution of 13C of ΣCO2 in the world oceans. *Deep Sea Research Part A. Oceanographic Research Papers*, *32*(1), 57–84. http://doi.org/10.1016/0198-0149(85)90017-2

Kuhlbrodt, T., Griesel, A., Montoya, M., Levermann, A., Hofmann, M., & Rahmstorf, S. (2007). On the driving processes of the Atlantic meridional overturning circulation. *Reviews of Geophysics*, *45*(2). http://doi.org/10.1029/2004RG000166

Lacroix, B., Baumgartner, L. P., Bouvier, A. S., Kempton, P. D., & Vennemann, T. (2018). Multi fluid-flow record during episodic mode I opening: A microstructural and SIMS study (Cotiella Thrust Fault, Pyrenees). *Earth and Planetary Science Letters*, *503*, 37–46. http://doi.org/10.1016/j.epsl.2018.09.016

Lajeunesse, P., & St-Onge, G. (2008). The subglacial origin of the Lake Agassiz-Ojibway final outburst flood. *Nature Geoscience*, *1*(3), 184–188. http://doi.org/10.1038/ngeo130

Langmuir, I. (1918). THE ADSORPTION OF GASES ON PLANE SURFACES OF GLASS, MICA AND PLATINUM. *ACS Publications*, *345*.

Lavender, K. L., Owens, W. B., & Davis, R. E. (2005). The mid-depth circulation of the subpolar North Atlantic Ocean as measured by subsurface floats, *52*, 767–785. http://doi.org/10.1016/j.dsr.2004.12.007

Lazier, J., Hendry, R., Clarke, A., Yashayaev, I., & Rhines, P. (2002). Convection and restratification in the Labrador Sea, 1990-2000. *Deep-Sea Research Part I: Oceanographic Research Papers*, *49*(10), 1819–1835. http://doi.org/10.1016/S0967-0637(02)00064-X

Lazier, J. R. N., & Wright, D. G. (1993). Annual velocity variations in the Labrador Current. *Journal of Physical Oceanography*. http://doi.org/10.1175/1520-0485(1993)023<0659:AVVITL>2.0.CO;2

Lea, Mashiotta, & Spero. (1999). Controls on magnesium and strontium uptake in planktonic foraminifera determined by live culturing. *Geochimica et Cosmochimica Acta*, *63*(16), 2369–2379.

Leckrone, K. J., & Hayes, J. M. (1998). Water-Induced Errors in Continuous-Flow Carbon Isotope Ratio Mass Spectrometry, *70*(13), 2737–2744. http://doi.org/10.1021/ac9803434

Legrande, A. N., & Schmidt, G. A. (2006). Global gridded data set of the oxygen isotopic composition in seawater, *33*(February), 1–5. http://doi.org/10.1029/2006GL026011

LeGrande, & Wunsch. (1995). Constraints from paleotracer data on the North Atlantic circulation during the last glacial maximum the. *Paleoceanography*, *10*(6), 1011–1045.

Lemieux-Dudon, B., Blayo, E., Petit, J. R., Waelbroeck, C., Svensson, A., Ritz, C., … Parrenin, F. (2010). Consistent dating for Antarctic and Greenland ice cores. *Quaternary Science Reviews*, *29*(1-2), 8–20. http://doi.org/10.1016/j.quascirev.2009.11.010

Leutert, T. J., Sexton, P. F., Tripati, A., Piasecki, A., Ho, S. L., & Meckler, A. N. (2019). Sensitivity of clumped isotope temperatures in fossil benthic and planktic foraminifera to diagenetic alteration. *Geochimica et Cosmochimica Acta*, *257*, 354–372. http://doi.org/10.1016/j.gca.2019.05.005

Li, C., Battisti, D. S., & Bitz, C. M. (2010). Can North Atlantic sea ice anomalies account for Dansgaard-Oeschger climate signals? *Journal of Climate*, *23*(20), 5457–5475. http://doi.org/10.1175/2010JCLI3409.1

Lisiecki, L. E., & Raymo, M. E. (2005). A Pliocene-Pleistocene stack of 57 globally distributed benthic δ 18O records. *Paleoceanography*, *20*(1), 1–17. http://doi.org/10.1029/2004PA001071

Lisiecki, L. E., & Stern, J. V. (2016). Regional and global benthic δ18O stacks for the last Glacial Cycle. *Paleoceanography*, 1368–1394. http://doi.org/10.1002/2016PA003002.Received

Locarnini, Mishonov, Baranova, Boyer, Zweng, Garcia, … Smolyar. (2018). NOAA National Centers for Environmental Information. *World Ocean Atlas 2018. Volume 1: Temperature*, (September), 1–20.

Lowell, T. V, Heusser, C. J., Andersen, B. G., Moreno, P. I., Hauser, A., Heusser, L. E., … Denton, G. H. (1995). Interhemispheric Correlation of Late Pleistocene Glacial Events. *Science*, *269*(September). http://doi.org/10.4172/2324-9307.1000133

Lowell, T. V., Fisher, T. G., Hajdas, I., Glover, K., Loope, H., & Henry, T. (2009). Radiocarbon deglaciation chronology of the Thunder Bay, Ontario area and implications for ice sheet retreat patterns. *Quaternary Science Reviews*, *28*(17-18), 1597–1607. http://doi.org/10.1016/j.quascirev.2009.02.025

Lozier, M. S., Owens, W. B., & Curry, R. G. (1995). The climatology of the North Atlantic. *Progress in Oceanography*, *36*(1), 1–44.

Lynch-Stieglitz, J., Adkins, J. F., Curry, W. B., Dokken, T., Hall, I. R., Herguera, J. C., … Mcmanus, J. F. (2007). Atlantic Meridional Overturning Glacial Maximum, *316*(April), 66–69.

Lynch-Stieglitz, J., Curry, W. B., Oppo, D. W., Ninneman, U. S., Charles, C. D., & Munson, J. (2006). Meridional overturning circulation in the South Atlantic at the last glacial maximum. *Geochemistry Geophysics Geosystems*, *7*, -. http://doi.org/10.1029/2005GC001226

Lynch-Stieglitz, J., Schmidt, M. W., Gene Henry, L., Curry, W. B., Skinner, L. C., Mulitza, S., … Chang, P. (2014). Muted change in Atlantic overturning circulation over some glacial-aged Heinrich events. *Nature Geoscience*, *7*(2), 144–150. http://doi.org/10.1038/ngeo2045

MacAyeal, D. R. (1993a). A low-order model of the Heinrich event cycle. *Palaeoceanography*, *8*(6), 767–773.

MacAyeal, D. R. (1993b). Binge/purge oscillations of the Laurentide Ice Sheet as a cause of the North Atlantic's Heinrich Events. *Palaeoceanography*, *8*(6), 775–784.

Malmgren, & Nordlund. (1996). Application of artificial neural networks to chemostratigraphy imagery. *Palaeoceanography*, *11*(4), 505–512.

Manabe, S., & Broccoli, a. J. (1985). The influence of continental ice sheets on the climate of an ice age. *Journal of Geophysical Research*, *90*(D1), 2167. http://doi.org/10.1029/JD090iD01p02167

Marchant, M., Hebbeln, D., & Wefer, G. (1999). High resolution planktic foraminiferal record of the last 13,300 years from the upwelling area off Chile. *Marine Geology*, *161*(2-4), 115–128. http://doi.org/10.1016/S0025-3227(99)00041-9

Marchitto, T. M., & Broecker, W. S. (2006). Deep water mass geometry in the glacial Atlantic Ocean: A review of constraints from the paleonutrient proxy Cd/Ca. *Geochemistry, Geophysics, Geosystems*, *7*(12), n/a–n/a. http://doi.org/10.1029/2006GC001323

Marchitto, T. M., Curry, W. B., Lynch-stieglitz, J., Bryan, S. P., Cobb, K. M., & Lund, D. C. (2014). ScienceDirect Improved oxygen isotope temperature calibrations for cosmopolitan benthic foraminifera. *Geochimica et Cosmochimica Acta*, *130*, 1–11. http://doi.org/10.1016/j.gca.2013.12.034

Maslin, M., Seidov, D., Lowe, J., Maslin, M, Seidov D, L. J., Maslin, M., Seidov, D., & Lowe, J. (2001). Synthesis of the Nature and Causes of Rapid Climate Transitions During the Quaternary. *The Oceans and Rapid Climate Change*, 9–52. http://doi.org/10.1029/GM126p0009

Mauritzen. (1996). Production of dense overflow waters feeding the North Atlantic across the Greenland-Scotland Ridge . Part 1 : Evidence for a revised circulation scheme. *Dee*, *43*(6), 769–806.

McCarthy, G. D., Gleeson, E., & Walsh, S. (2015). The influence of ocean variations on the climate of Ireland. *Weather*, *70*(8), 242–245. http://doi.org/10.1002/wea.2543

McCarthy, G. D., Smeed, D. A., Cunningham, S. A., & Roberts, C. D. (2017). Atlantic Meridonal Overturning Circulation. *Marine Climate Change Impacts Partnership*, (July), 1–7. http://doi.org/10.14465/2017.arc10.002-atl

McCave. (1994). *R.R.S Charles Darwin Cruise 88*.

McCrea, J. M. (1950). On the isotopic chemistry of carbonates and a paleotemperature scale. *The Journal of Chemical Physics*, *18*(6), 849–857. http://doi.org/10.1063/1.1747785

McManus, J. F. (1999). A 0.5-Million-Year Record of Millennial-Scale Climate Variability in the North Atlantic. *Science*, *283*(5404), 971–975. http://doi.org/10.1126/science.283.5404.971

McManus, J. F., Francois, R., Gherardi, J., & Keigwin, L. D. (2004). Collapse and rapid resumption of Atlantic meridional circulation linked to deglacial climate changes, *428*(April), 1–4.

McManus, J. F., Francois, R., Gherardl, J. M., Kelgwin, L., & Drown-Leger, S. (2004). Collapse and rapid resumption of Atlantic meridional circulation linked to deglacial climate changes. *Nature*, *428*(6985), 834–837. http://doi.org/10.1038/nature02494

McManus, J. F., Major, C. O., Flower, B. P., & Fronval, T. (1996). VARIABILITY IN SEA-SURFACE CONDITIONS IN THE NORTH ATLANTIC-ARCTIC GATEWAYS DURING THE LAST 140 , 000 YEARS. *Proceedings of the Ocean Drilling Program*, *151*.

Meckler, A. N., Ziegler, M., Millán, M. I., Breitenbach, S. F. M., & Bernasconi, S. M. (2014). Long-term performance of the Kiel carbonate device with a new correction scheme for clumped isotope measurements, (March), 1705–1715. http://doi.org/10.1002/rcm.6949

Meehl, G. A., Stocker, T. F., Collins, W. D., Friedlingstein, P., Gaye, T., Gregory, J. M., … others. (2007). Global climate projections.

Meese, D. A., Gow, A. J., Alley, R. B., Zielinski, G. A., Grootes, P. M., Ram, M., … Bolzan, J. F. (1997). The Greenland Ice Sheet Project 2 depth-age scale: Methods and results. *Journal of Geophysical Research: Oceans*, *102*(C12), 26411–26423. http://doi.org/10.1029/97JC00269

Meinicke, N., Ho, S. L., Hannisdal, B., Nürnberg, D., Tripati, A., Schiebel, R., & Meckler, A. N. (2020). A robust calibration of the clumped isotopes to temperature relationship for foraminifers. *Geochimica et Cosmochimica Acta*, *270*, 160–183. http://doi.org/10.1016/j.gca.2019.11.022

Menviel, L., Timmermann, A., Friedrich, T., & England, M. H. (2014). Hindcasting the continuum of Dansgaard-Oeschger variability: Mechanisms, patterns and timing. *Climate of the Past*, *10*(1), 63–77. http://doi.org/10.5194/cp-10-63-2014

Miller, K. R., Chapman, M. R., Andrews, J. E., & Koç, N. (2011). Diatom phytoplankton response to Holocene climate change in the Subpolar North Atlantic. *Global and Planetary Change*, *79*(3-4), 214–225. http://doi.org/10.1016/j.gloplacha.2011.03.001

Mokeddem, Z., McManus, J. F., & Oppo, D. W. (2014). Oceanographic dynamics and the end of the last interglacial in the subpolar North Atlantic. *Proceedings of the National Academy of Sciences of the United States of America*, *111*(31), 11263–11268. http://doi.org/10.1073/pnas.1322103111

Monnin, E., Indermühle, A., Dällenbach, A., Flückiger, J., Stauffer, B., Stocker, T. F., … Barnola, J. M. (2001). Atmospheric CO2 concentrations over the last glacial termination. *Science*, *291*(5501), 112–114. http://doi.org/10.1126/science.291.5501.112

Morey, Mix, & Pisias. (2005). Planktonic foraminiferal assemblages preserved in surface sediments correspond to multiple environment variables. *Quaternary Science Reviews*, *24*(24), 925–950. http://doi.org/10.1016/j.quascirev.2003.09.011

Mortensen, Hovland, Fossa, & Furevik. (2001). Distribution , abundance and size of Lophelia pertusa coral reefs in mid-Norway in relation to seabed characteristics. *J. Mar. Biol*, *81*, 581–597.

Mulitza, S., Arz, H., Kemle-von Mücke, S., Moos, C., Niebler, H.-S., Pätzold, J., & Segl, M. (1999). The South Atlantic Carbon Isotope Record of Planktic Foraminifera. *Use of Proxies in Paleoceanography*, 427–445. http://doi.org/10.1007/978-3-642-58646-0_17

Mulitza, S., Hale, W., & Niebler, H. S. (1997). Planktonic foraminifera as recorders of past surface-water stratification, (4), 335–338.

Müller, I. A., Violay, M. E. S., Storck, J., Fernandez, A., Dijk, J. Van, Madonna, C., & Bernasconi, S. M. (2017). Clumped isotope fractionation during phosphoric acid digestion of carbonates at 70 ° C. *Chemical Geology*, *449*, 1–14. http://doi.org/10.1016/j.chemgeo.2016.11.030

Munk, & Wunsch. (1998). Abyssal recipes II: energetics of tidal and wind mixing. *Deep-Sea Research Part I*, *45*, 1977 – 2010.

Naafs, B. D. A., Hefter, J., & Stein, R. (2013). Millennial-scale ice rafting events and Hudson Strait Heinrich(-like) Events during the late Pliocene and Pleistocene: A review. *Quaternary Science Reviews*, *80*, 1–28. http://doi.org/10.1016/j.quascirev.2013.08.014

Natland, M. L. (1938). *New species of foraminifera from off the west coast of North America and from the later Tertiary of the Los Angeles Basin*. University of California Press Berkeley.

Nicholl, J. A. L., Hodell, D. A., Naafs, B. D. A., Hillaire-Marcel, C., Channell, J. E. T., & Romero, O. E. (2012). A Laurentide outburst flooding event during the last interglacial period. *Nature Geoscience*, *5*(12), 901–904. http://doi.org/10.1038/ngeo1622

Nier, A. O. (1947). A Mass Spectrometer for Isotope and Gas Analysis, *398*. http://doi.org/10.1063/1.1740961

Norris, R. D., & Nishi, H. (2001). Paleontological Society Evolutionary Trends in Coiling of Tropical Paleogene Planktic Foraminifera Author (s): Richard D . Norris and Hiroshi Nishi Published by : Paleontological Society Stable URL : http://www.jstor.org/stable/2666077 REFERENCES Linked, *27*(2), 327–347.

Nuernberg, D. (1995). Magnesium in tests of Neogloboquadrina pachyderma sinistral from high northern and southern latitudes. *Journal of Foraminiferal Research*, *25*(4), 350–368. http://doi.org/10.2113/gsjfr.25.4.350

Nurnberg, D. (1995). Magnesium in tests of Neogloboquadrina pachyderma sinistral from high northern and southern latitudes. *Journal of Foraminiferal Research*, *25*(4), 350–368. http://doi.org/10.2113/gsjfr.25.4.350

Nürnberg, D., Bijma, J., & Hemleben, C. (1996). Assessing the reliability of magnesium in foraminiferal calcite as a proxy for water mass temperatures. *Geochimica et Cosmochimica Acta*, *60*(5), 803–814. http://doi.org/10.1016/0016-7037(95)00446-7

Nyland, B., Eystein, J., Elderfield, H., & Andersson, C. (2006). Neogloboquadrina pachyderma (dex. and sin.) Mg/Ca and d 18 O records from the Norwegian Sea. http://doi.org/10.1029/2005GC001055

Obrochta, S. P., Crowley, T. J., Channell, J. E. T., Hodell, D. a., Baker, P. a., Seki, A., & Yokoyama, Y. (2014a). Climate variability and ice-sheet dynamics during the last three glaciations. *Earth and Planetary Science Letters*, *406*, 198–212. http://doi.org/10.1016/j.epsl.2014.09.004

Obrochta, S. P., Crowley, T. J., Channell, J. E. T., Hodell, D. A., Baker, P. A., Seki, A., & Yokoyama, Y. (2014b). Climate variability and ice-sheet dynamics during the last three glaciations. *Earth and Planetary Science Letters*, *406*, 198–212. http://doi.org/10.1016/j.epsl.2014.09.004

Obrochta, S. P., Miyahara, H., Yokoyama, Y., & Crowley, T. J. (2012). A re-examination of evidence for the North Atlantic “ 1500-year cycle” at Site 609. *Quaternary Science Reviews*, *55*, 23–33. http://doi.org/10.1016/j.quascirev.2012.08.008

Ono, S., Wang, D. T., Gruen, D. S., Sherwood Lollar, B., Zahniser, M. S., McManus, B. J., & Nelson, D. D. (2014). Measurement of a doubly substituted methane isotopologue, 13CH3D, by tunable infrared laser direct absorption spectroscopy. *Analytical Chemistry*, *86*(13), 6487–6494. http://doi.org/10.1021/ac5010579

Oppo, D. W., & Lehman, S. J. (1993). Mid-depth circulation of the subpolar north atlantic during the last glacial maximum. *Science (New York, N.Y.)*, *259*(5098), 1148–1152. http://doi.org/10.1126/science.259.5098.1148

Oppo, D. W., McManus, J. F., & Cullen, J. L. (1998). Abrupt climate events 500,000 to 340,000 years ago: Evidence from subpolar North Atlantic sediments. *Science*, *279*(5355), 1335–1338. http://doi.org/10.1126/science.279.5355.1335

Oppo, D. W., McManus, J. F., & Cullen, J. L. (2006). Evolution and demise of the Last Interglacial warmth in the subpolar North Atlantic. *Quaternary Science Reviews*, *25*(23-24), 3268–3277. http://doi.org/10.1016/j.quascirev.2006.07.006

Ortiz, Mix, Rugh, Watkins, & Collier. (1996). Deep-dwelling plaktonic formainifera of the northeastern Pacific Ocean reveal environmental control of oxygen and carbon isotopic disequilibria. *Geochim*, *60*(22), 4509–4523.

Ottens, J. J. (1992). APRIL AND AUGUST NORTHEAST ATLANTIC SURFACE WATER MASSES REFLECTED IN PLANKTIC FORAMINIFERA, *28*(4), 261–283.

Otto-Bliesner. (2007). Last Glacial Maximum ocean thermohaline circulation : PMIP2 model intercomparisons and data constraints. *Science*, *34*, 1–6. http://doi.org/10.1029/2007GL029475

Pados, T., Spielhagen, R. F., Bauch, D., Meyer, H., & Segl, M. (2015). Oxygen and carbon isotope composition of modern planktic foraminifera and near-surface waters in the Fram Strait (Arctic Ocean) – a case study, 1733–1752. http://doi.org/10.5194/bg-12-1733-2015

Pak, D. K., Lea, D. W., & Kennett, J. P. (2004). Seasonal and interannual variation in Santa Barbara Basin water temperatures observed in sediment trap foraminiferal Mg/Ca. *Geochemistry, Geophysics, Geosystems*, *5*(12). http://doi.org/10.1029/2004GC000760

Patterson, R. T., & Fishbein, E. (1989). RE-EXAMINATION OF THE STATISTICAL METHODS USED TO DETERMINE THE NUMBER OF POINT COUNTS NEEDED FOR MICROPALEONTOLOGICAL QUANTITATIVE RESEARCH. *Palaeontlogy*, *63*(2), 245–248.

Peeters, F. J. C., Brummer, G. J. A., & Ganssen, G. (2002). The effect of upwelling on the distribution and stable isotope composition of Globigerina bulloides and Globigerinoides ruber (planktic foraminifera) in modern surface waters of the NW Arabian Sea. *Global and Planetary Change*, *34*(3-4), 269–291. http://doi.org/10.1016/S0921-8181(02)00120-0

Peltier, W. R., & Fairbanks, R. G. (2006). Global glacial ice volume and Last Glacial Maximum duration from an extended Barbados sea level record. *Quaternary Science Reviews*, *25*(23-24), 3322–3337. http://doi.org/10.1016/j.quascirev.2006.04.010

Peral, M., Daëron, M., Blamart, D., Bassinot, F., Dewilde, F., Smialkowski, N., … Waelbroeck, C. (2018). Updated calibration of the clumped isotope thermometer in planktonic and benthic foraminifera. *Geochimica et Cosmochimica Acta*, *239*, 1–16. http://doi.org/10.1016/j.gca.2018.07.016

Peters, C., Walden, J., & Austin, W. E. N. (2008). Magnetic signature of European margin sediments: Provenance of ice-rafted debris and the climatic response of the British ice sheet during Marine Isotope Stages 2 and 3. *Journal of Geophysical Research: Earth Surface*, *113*(3), 1–16. http://doi.org/10.1029/2007JF000836

Petersen, Defliese, W. F., Saenger, C., Daëron, M., Huntington, K. W., John, C. M., … Winkelstern, I. Z. (2019). Effects of Improved 17O Correction on Interlaboratory Agreement in Clumped Isotope Calibrations, Estimates of Mineral-Specific Offsets, and Temperature Dependence of Acid Digestion Fractionation. *Geochemistry, Geophysics, Geosystems*, *20*(7), 3495–3519. http://doi.org/10.1029/2018GC008127

Petersen, S. V., Winkelstern, I. Z., Lohmann, K. C., & Meyer, K. W. (2015). The effects of Porapak(TM) trap temperature on d18O, d13C, and D47 values in preparing samples for clumped isotope analysis. *Rapid Communications in Mass Spectrometry*, *30*(October 2015), 1–10.

http://doi.org/10.1002/rcm.7438

Pflaumann, U. (2003). Glacial North Atlantic: Sea-surface conditions reconstructed by GLAMAP 2000. *Paleoceanography*, *18*(3), 1065. http://doi.org/10.1029/2002PA000774

Pflaumann, U., Duprat, J., Pujol, C., & Labeyrie, L. (1996). SIMMAX: A modern analog technique to deduce Atlantic sea surface temperatures from planktonic foraminifera in deep-sea sediments. *Paleoceanography*, *11*(1), 15–35.

Pflaumann, U., Duprat, Pujol, & Labeyrie. (1996). SIMMAX: A modern analogue technique to deduce Atlantic sea surface temperatures from planktonic foraminifera in deep-sea sediments. *Paleoceanography*, *11*(1), 15–35.

Pflaumann, U., Sarnthein, M., Chapman, M., Abreu, L., Funnell, B., Huels, M., … Weinelt, M. (2003). Glacial North Atlantic : Sea-surface conditions reconstructed by GLAMAP 2000, *18*(3). http://doi.org/10.1029/2002PA000774

Piasecki, A., Bernasconi, S. M., Grauel, A. L., Hannisdal, B., Ho, S. L., Leutert, T. J., … Meckler, N. (2019). Application of Clumped Isotope Thermometry to Benthic Foraminifera. *Geochemistry, Geophysics, Geosystems*, *20*(4), 2082–2090. http://doi.org/10.1029/2018GC007961

Pickart, R. S., & Smethie, W. M. (1993). How Does the Deep Western Boundary Current Cross the Gulf Stream? *Journal of Physical Oceanography*. http://doi.org/10.1175/1520-0485(1993)023<2602:hdtdwb>2.0.co;2

Piotrowski, A. M., Goldstein, S. L., Hemming, S. R., & Fairbanks, R. G. (2005). Temporal Relationships of Carbon Cycling and Ocean Circulation at Glacial Boundaries, (March).

Pouthier, J., & Gonthier, E. (1978). Sur la susceptibilit{é} magn{é}tique des s{é}diments, indicateurs de la dispersion du mat{é}riel volcanoclastique {à} partir de l'Islande et des Faeroes. *Bull. Inst. G{é}ol. Aquitaine*, *23*, 214–226.

Poutiers, J.-A. (1975). *Sur les propri{é}t{é}s magn{é}tiques de certains s{é}diments continentaux et marins: applications*. Sciences: Bordeaux, univ. de Bordeaux 1: 1975; 492.

Prasanna, K., Ghosh, P., Bhattacharya, S. K., Mohan, K., & Anilkumar, N. (2016). Isotopic disequilibrium in Globigerina bulloides and carbon isotope response to productivity increase in Southern Ocean. *Scientific Reports*, *6*(October 2015), 1–12. http://doi.org/10.1038/srep21533

Prokhorov, I., Kluge, T., & Janssen, C. (2019). Optical clumped isotope thermometry of carbon dioxide. *Scientific Reports*, *9*(1), 1–11. http://doi.org/10.1038/s41598-019-40750-z

Rahmstorf, S. (2002). Ocean circulation and climate during the past 120,000 years. *Nature*, *419*(6903), 207–214. http://doi.org/10.1038/nature01090

Rahmstorf, S., Box, J. E., Feulner, G., Mann, M. E., Robinson, A., Rutherford, S., & Schaffernicht, E. J. (2015). Exceptional twentieth-century slowdown in Atlantic Ocean overturning circulation. *Nature Climate Change*, *5*(5), 475–480. http://doi.org/10.1038/nclimate2554

Rahmstorf, S., & Ganopolski, A. (1999). Long-term global warming scenarios computed with an efficient coupled climate model. *Climatic Change*, *43*(2), 353–367. http://doi.org/10.1023/A:1005474526406

Ramsey, M. H., Thompson, M., & Walton, S. J. (1987). Self-matrix effects as a cause of calibration curvature in inductively coupled plasma atomic emission spectrometry. *Journal of Analytical Atomic Spectrometry*, *2*(1), 33–38. http://doi.org/10.1039/JA9870200033

Rashid, H., Hesse, R., & Piper, D. J. W. (2003). Evidence for an additional Heinrich event between H5 and H6 in the Labrador Sea. *Paleoceanography*, *18*(4), 1–15. http://doi.org/10.1029/2003PA000913

Rasmussen, S. O., Bigler, M., Blockley, S. P., Blunier, T., Buchardt, S. L., Clausen, H. B., … Winstrup, M. (2014). A stratigraphic framework for abrupt climatic changes during the Last Glacial period based on three synchronized Greenland ice-core records : re fi ning and extending the INTIMATE event stratigraphy. *Quaternary Science Reviews*, *106*, 14–28. http://doi.org/10.1016/j.quascirev.2014.09.007

Rasmussen, S. O., Bigler, M., Blockley, S. P., Blunier, T., Buchardt, S. L., Clausen, H. B., … Winstrup, M. (2014). A stratigraphic framework for abrupt climatic changes during the Last Glacial period based on three synchronized Greenland ice-core records: Refining and extending the INTIMATE event stratigraphy. *Quaternary Science Reviews*, *106*, 14–28. http://doi.org/10.1016/j.quascirev.2014.09.007

Rasmussen, T. L., Oppo, D. W., Thomsen, E., & Lehman, S. J. (2003). Deep sea records from the southeast Labrador Sea: Ocean circulation changes and ice-rafting events during the last 160,000 years. *Paleoceanography*, *18*(1), n/a–n/a. http://doi.org/10.1029/2001pa000736

Rasmussen, T. L., Thomsen, E., Labeyrie, L., & Van Weering, T. C. E. (1996). Circulation changes in the Faeroe-Shetland Channel correlating with cold events during the last glacial period (58-10 ka). *Geology*, *24*(10), 937–940. http://doi.org/10.1130/0091-7613(1996)024<0937:CCITFS>2.3.CO;2

Rasmussen, T. L., Thomsen, E., & Moros, M. (2016). North Atlantic warming during Dansgaard-Oeschger events synchronous with Antarctic warming and out-of-phase with Greenland climate. *Nature Publishing Group*, (January), 1–12. http://doi.org/10.1038/srep20535

Rasmussen, T. L., Thomsen, E., Van Weering, T. C. E., & Labeyrie, L. (1996). Rapid changes in surface and deep water conditions at the Faeroe Margin during the last 58,000 years. *Paleoceanography*, *11*(6), 757–771. http://doi.org/10.1029/96PA02618

Rasmussen, Wastegard, S., Kuijpers, A., Weering, T. C. E. Van, Heinemeier, J., & Thomsen, E. (2003). Stratigraphy and distribution of tephra layers in marine sediment cores from the Faeroe Islands , North Atlantic. *Marine*, *199*, 263–277. http://doi.org/10.1016/S0025-3227(03)00219-6

Raymo, M. E., Oppo, D. W., Flower, B. P., Hodell, D. A., McManus, J. F., Venz, K. A., … McIntyre, K. (2004). Stability of North Atlantic water masses in face of pronounced climate variability during the Pleistocene. *Paleoceanography*, *19*(2), 1–13. http://doi.org/10.1029/2003PA000921

Renssen, H., & Isarin, R. F. B. (2001). *Renssen-Isarin-GPC2001*.

Revel, Cremer, Grousset, & Labeyrie. (1996). Grain-size and Sr-Nd isotopes as tracer of paleo-bettom current strength, Northeast Atlantic Ocean. *Marine Geology*, (131), 233–249.

Robinson, S. G. (1986). The late Pleistocene palaeoclimatic record of North Atlantic deep-sea sediments revealed by mineral-magnetic measurements. *Physics of the Earth and Planetary Interiors*, *42*(1-2), 22–47. http://doi.org/10.1016/S0031-9201(86)80006-1

Rodríguez-Sanz, Bernasconi, S. M., Marino, G., Heslop, D., Müller, I. A., Fernandez, A., … Rohling, E. J. (2017). Penultimate deglacial warming across the Mediterranean Sea revealed by clumped isotopes in foraminifera. *Scientific Reports*, *7*(1), 1–11. http://doi.org/10.1038/s41598-017-16528-6

Rooth, C. (1982). Hydrology and ocean circulation. *Progress in Oceanography*, *11*(2), 131–149. http://doi.org/10.1016/0079-6611(82)90006-4

Rosenheim, B. E., Tang, J., & Fernandez, A. (2013). Measurement of multiply substituted isotopologues (' clumped isotopes ') of CO 2 using a 5 kV compact isotope ratio mass spectrometer : Performance , reference frame , and carbonate paleothermometry. *Rapid Communications in Mass Spectrometry*, *1*(February), 1847–1857. http://doi.org/10.1002/rcm.6634

Rossby, T. (1996). The North Atlantic Current and surrounding waters: At the crossroads. *Reviews of Geophysics*, *34*(4), 463–481. http://doi.org/10.1029/96RG02214

Roux. (1979a). Estimation des paléoclimats d'après l'écologie des foraminifères. *Article Numérisé Dans Le Cadre Du Programme Numérisation de Documents Anciens Mathématiques*.

Roux, M. (1979b). Estimation des paleoclimats d'apres l'ecologie des foraminiferes. *Les Cahiers de L'analyse Des Donnees*, *1*, 61–79.

Ruddiman, W. F. (1977). Late Quaternary deposition of ice-rafted sand in the subpolar North Atlantic (lat 40 ° to 65 ° N), (71213).

Rudnicki, M. D., Wilson, P. A., & Anderson, W. T. (2001). Numerical models of diagenesis, sediment properties, and pore fluid chemistry on a paleoceanographic transect: Blake Nose, Ocean Drilling Program Leg 171B. *Paleoceanography*, *16*(6), 563–575. http://doi.org/10.1029/2000PA000551

Sachs, J. P., & Lehman, S. J. (1999). Subtropical North Atlantic temperatures 60,000 to 30,000 years ago. *Science*, *286*(5440), 756–760. http://doi.org/10.1126/science.286.5440.756

Sandström, J. W. (1916). *Meteorologische studien im schwedischen hochgebirge*.

Santrock, J., Studley, S. A., & Hayes, J. M. (1985). Isotopic Analyses Based on the Mass Spectrum of Carbon Dioxide, (12), 1444–1448.

Savin, & Douglas. (1973). Stable Isotope and Magnesium Geochemistry of Recent Planktonic Foraminifera from the South Pacific. *GSA Bulletin*, *84*(7), 2327–2342. http://doi.org/10.1130/0016-7606(1973)84<2327:SIAMGO>2.0.CO;2

Schauble, E. A., Ghosh, P., & Eiler, J. M. (2006). Preferential formation of 13C-18O bonds in carbonate minerals, estimated using first-principles lattice dynamics. *Geochimica et Cosmochimica Acta*, *70*(10), 2510–2529. http://doi.org/10.1016/j.gca.2006.02.011

Schauer, U. (1997). Impact of eastern Arctic shelf waters on the Nansen Basin intermediate layers. *Journal of Geophysical Research C: Oceans*, *102*(C2), 3371–3382.

http://doi.org/10.1029/96JC03366

Schiebel, Bijma, & Hemleben. (1997). Population dynamics of the planktic foraminifer Globigerina bulloides from the eastern North Atlantic. *Deep Sea Research*, *44*(9).

Schiebel, R., Waniek, J., Bork, M., & Hemleben, C. (2001). Planktic foraminiferal production stimulated by chlorophyll redistribution and entrainment of nutrients, *48*.

Schmidt, G., Bigg, G., & Rohling, E. (1999). Global seawater oxygen-18 database, NASA Goddard Inst. for Space Stud. New York.

Schmittner, A., Chiang, J. C. H., & Hemming, S. R. (2013). Introduction: The Ocean's Meridional Overturning Circulation. *Ocean Circulation: Mechanisms and Impacts - Past and Future Changes of Meridional Overturning*, 1–4. http://doi.org/10.1029/173GM02

Schott, F. A., Zantopp, R., Stramma, L., Dengler, M., Fischer, J., & Wibaux, M. (2004). Circulation and deep-water export at the western exit of the subpolar north Atlantic. *Journal of Physical Oceanography*, *34*(4), 817–843. http://doi.org/10.1175/1520-0485(2004)034<0817:CADEAT>2.0.CO;2

Schrag, D. P., Adkins, J. F., McIntyre, K., Alexander, J. L., Hodell, D. A., Charles, C. D., & McManus, J. F. (2002). The oxygen isotopic composition of seawater during the Last Glacial Maximum. *Quaternary Science Reviews*, *21*(1-3), 331–342. http://doi.org/10.1016/S0277-3791(01)00110-X

Seidov, D., & Maslin, M. (2001a). Atlantic ocean heat piracy and the bipolar climate see-saw during Heinrich and Dansgaard-Oeschger events. *Journal of Quaternary Science*, *16*(4), 321–328. http://doi.org/10.1002/jqs.595

Seidov, D., & Maslin, M. (2001b). Atlantic Ocean heat piracy and the bipolar climate see-saw during Heinrich and Dansgaard-Oeschger events. *Journal of Quaternary Science*, *16*(4), 321–328. http://doi.org/10.1002/jqs.595

Sexton, P. F., Wilson, P. A., & Pearson, P. N. (2006). Microstructural and geochemical perspectives on planktic foraminiferal preservation: "glassy" versus "frosty." *Geochemistry, Geophysics, Geosystems*, *7*(12). http://doi.org/10.1029/2006GC001291

Shackleton, N. (1967). Oxygen Isotope Analyses and Pleistocene Temperatures Re-assessed. *Nature*, *215*(5096), 15–17. http://doi.org/10.1038/215015a0

Shackleton, N. J. (1974). Attainment of isotopic equilibrium between ocean water and benthonic foraminifera genus Uvigerina: Isotopic changes in the ocean during the last glacial. In *Les Methodes Quantitatives D'e´tude des Variations du Climat au Cours du Pleistocene,* (pp. 203–209).

Shackleton, N. J. (1984). Oxygen and carbon isotope stratigraphy of Deep Sea Drilling Project hole 552A: Plio-Pleistocene glacial history. *Init. Rep. DSDP*, *81*, 599–609.

Shackleton, N. J., Chapman, M., Sánchez-Goni, M. F., Pailler, D., & Lancelot, Y. (2002). The classic marine isotope substage 5e. *Quaternary Research*, *58*(1), 14–16. http://doi.org/10.1006/qres.2001.2312

Shackleton, N. J., Fairbanks, R. G., Chiu, T. C., & Parrenin, F. (2004). Absolute calibration of the

Greenland time scale: Implications for Antarctic time scales and for Δ14C. *Quaternary Science Reviews*, *23*(14-15), 1513–1522. http://doi.org/10.1016/j.quascirev.2004.03.006

Shackleton, N. J., Hall, M. a, & Pate, D. (1995). Pliocene Stable Isotope Stratigraphy of Site 846. *Proceedings of the Ocean Drilling Program, Scientific Results, Vol. 138*, *138*, 337–355. http://doi.org/10.2973/odp.proc.sr.138.117.1995

Shackleton, N. J., Hall, M. A., & Vincent, E. (2000). Phase relationships between millennial-scale events 64 , 000-24 , 000 years ago the benthie study b • SO Stratigraphy, *15*(6), 565–569.

Shackleton, N. J., & Opdyke, N. D. (1973). Oxygen isotope and palaeomagnetic stratigraphy of Equatorial Pacific core V28-238: Oxygen isotope temperatures and ice volumes on a 105 year and 106 year scale. *Quaternary Research*, *3*(1), 39–55. http://doi.org/10.1016/0033-5894(73)90052-5

Shaffer, G., Olsen, S. M., & Bjerrum, C. J. (2004). Ocean subsurface warming as a mechanism for coupling Dansgaard-Oeschger climate cycles and ice-rafting events. *Geophysical Research Letters*, *31*(24), 1–4. http://doi.org/10.1029/2004GL020968

Shuman, B., Newby, P., Huang, Y., & Webb, T. (2004). Evidence for the close climatic control of new England vegetation history. *Ecology*, *85*(5), 1297–1310. http://doi.org/10.1890/02-0286

Siddall, M., Rohling, E. J., Thompson, W. G., & Waellbroeck, C. (2008). Marine isotope stage 3 sea level fluctuations: Data synthesis and new outlook. *Reviews of Geophysics*, *46*(4), 1–29. http://doi.org/10.1029/2007RG000226

Simstich, J., Sarnthein, M., & Erlenkeuser, H. (2003). Paired N 18 O signals of Neogloboquadrina pachyderma (s) and Turborotalita quinqueloba show thermal strati ¢ cation structure in Nordic Seas, *48*. http://doi.org/10.1016/S0377-8398(02)00165-2

Singarayer, J. S., Richards, D. a., Ridgwell, A., Valdes, P. J., Austin, W. E. N., & Beck, J. W. (2008). An oceanic origin for the increase of atmospheric radiocarbon during the Younger Dryas. *Geophysical Research Letters*, *35*(14), 1–6. http://doi.org/10.1029/2008GL034074

SINKA, K. J., & ATKINSON, T. C. (1999). A mutual climatic range method for reconstructing palaeoclimate from plant remains. *Journal of the Geological Society*, *156*(2), 381 LP – 396. http://doi.org/10.1144/gsjgs.156.2.0381

Skinner, L. C., & Elderfield, H. (2005). Constraining ecological and biological bias in planktonic foraminiferal Mg / Ca and D 18 O cc : A multispecies approach to proxy calibration testing, *20*, 1–15. http://doi.org/10.1029/2004PA001058

Skinner, L. C., & Shackleton, N. J. (2006). Deconstructing Terminations I and II: revisiting the glacioeustatic paradigm based on deep-water temperature estimates. *Quaternary Science Reviews*, *25*(23-24), 3312–3321. http://doi.org/10.1016/j.quascirev.2006.07.005

Sohn, R. A., & Menke, W. (2002). Application of maximum likelihood and bootstrap methods to nonlinear curve-fit problems in geochemistry, 1–17.

Sowers, T., & Bender, M. (1995). Climate records covering the last deglaciation. *Science*, *269*(5221), 210–214. http://doi.org/10.1126/science.269.5221.210

Spero, H. J., Bijma, J., Lea, D. W., & Bernis, B. E. (1997). Effect of seawater carbonate concentration on foraminiferal carbon and oxygen isotopes. *Nature*, *390*(6659), 497–500. http://doi.org/10.1038/37333

Spooner, P. T., Guo, W., Robinson, L. F., Thiagarajan, N., Hendry, K. R., Rosenheim, B. E., & Leng, M. J. (2016). Clumped isotope composition of cold-water corals : A role for vital effects ? *GEOCHIMICA ET COSMOCHIMICA ACTA*, *179*, 123–141. http://doi.org/10.1016/j.gca.2016.01.023

Staines-urías, F., Kuijpers, A., & Korte, C. (2013). Evolution of subpolar North Atlantic surface circulation since the early Holocene inferred from planktic foraminifera faunal and stable isotope records. *Quaternary Science Reviews*, *76*, 66–81. http://doi.org/10.1016/j.quascirev.2013.06.016

Stangeew, E. (2001). Distribution and Isotopic Composition of Living Planktonic Foraminifera N. pachyderma (sinistral) and T. quinqueloba in the High Latitude North Atlantic. *PhD Dissertation*, *Kiel Unive*, 90.

Steens, T. N. F., Ganssen, G., & Kroon, D. (1992). Oxygen and carbon isotopes in planktonic foraminifera as indicators of upwelling intensity and upwelling-induced high productivity in sediments from the northwestern Arabian Sea. *Geological Society Special Publication*, *64*(64), 107–119. http://doi.org/10.1144/GSL.SP.1992.064.01.07

Stolper, D. A., Eiler, J. M., & Higgins, J. A. (2018). Modeling the effects of diagenesis on carbonate clumped-isotope values in deep- and shallow-water settings. *Geochimica et Cosmochimica Acta*, *227*, 264–291. http://doi.org/10.1016/j.gca.2018.01.037

Stoner, J. S., Channell, J. E. T., & Hillaire-Marcel, C. (1998). A 200 ka geomagnetic chronostratigraphy for the Labrador Sea: indirect correlation of the sediment record to SPECMAP. *Earth and Planetary Science Letters*, *159*(3-4), 165–181. http://doi.org/10.1016/S0012-821X(98)00069-7

Stoner, J. S. Y., Channell, J. E. T., Hillaire-marcel, C., & Kissel, C. (2000). Geomagnetic paleointensity and environmental record from Labrador Sea core MD95-2024 : global marine sediment and ice core chronostratigraphy for the last 110 kyr, *183*, 161–177.

Stoner, S., & Hillaire-marcel, C. (1996). The magnetic signature of rapidly deposited detrital layers from the Deep Labrador Sea: Relationship to North Atlantic Heinrich layers, *11*(3), 309–325.

Stromberg, A. J. (2004). Why write statistical software? the case of robust statistical methods, 1–8.

Stuiver, Reimer, Bard, Beck, Burr, Hughen, … Spurk. (1998). INTCAL98 RADIOCARBON AGE CALIBRATION, 24,000-0 cal BP. *Radiocarbon*, *40*(3), 1041–1083.

Subhas, A. V., Rollins, N. E., Berelson, W. M., Erez, J., Ziveri, P., Langer, G., & Adkins, J. F. (2018). The dissolution behavior of biogenic calcites in seawater and a possible role for magnesium and organic carbon. *Marine Chemistry*, *205*(August), 100–112. http://doi.org/10.1016/j.marchem.2018.08.001

Svensson, A., Andersen, K. K., Bigler, M., Clausen, H. B., Dahl-Jensen, D., Davies, S. M., … Vinther, B. M. (2008). A 60 000 year Greenland stratigraphic ice core chronology. *Climate of the Past*, *4*(1), 47–57. http://doi.org/10.5194/cp-4-47-2008

Swart, Murray, S. T., Staudigel, P. T., & Hodell, D. A. (2019). Oxygen Isotopic Exchange Between CO2 and Phosphoric Acid: Implications for the Measurement of Clumped Isotopes in Carbonates. *Geochemistry, Geophysics, Geosystems*, *20*(7), 3730–3750. http://doi.org/10.1029/2019GC008209

Swart, P. K., Burns, S. J., & Leder, J. J. (1989). Fractionation of the stable isotopes of oxygen and carbon in carbon dioxide during the reaction of calcite with phosphoric acid as a function of temperature and technique, *86*, 89–96.

Szeremeta, N., Bassinot, F., Balut, Y., & Pagel, M. (2004). Oversampling of sedimentary series collected by giant piston corer : Evidence and corrections based on 3 . 5-kHz chirp profiles. *Palaeoceanography*, *19*, 1–8. http://doi.org/10.1029/2002PA000795

Tang, J., Dietzel, M., Fernandez, A., Tripati, A. K., & Rosenheim, B. E. (2014). Evaluation of kinetic effects on clumped isotope fractionation (δ47) during inorganic calcite precipitation. *Geochimica et Cosmochimica Acta*, *134*, 120–136. http://doi.org/10.1016/j.gca.2014.03.005

Tarutahi, T., & Clayton, R. N. (1969). The effect of polymorphism and magnesium substitution on oxygen isotope fractionation between calcium carbonate and water, *33*.

ter Braak, C. J. F., & Looman, C. W. N. (1986). Weighted averaging, logistic regression and the Gaussian response model. *Vegetatio*, *65*(1), 3–11. http://doi.org/10.1007/BF00032121

Ter-Braak, Juggins, Birks, & Van-der-Voet. (1993). *Weighted averaging partial least squares regression (WA-PLS): definition and comparison with other methods for species-environment calibration. Chapter 25 in: Multivariate Environmental Statistics*. Amsterdam: Elsevier Science Publishers B.V. (North- Holland).

Thompson, W. G., & Goldstein, S. L. (2006). A radiometric calibration of the SPECMAP timescale. *Quaternary Science Reviews*, *25*(23-24), 3207–3215. http://doi.org/10.1016/j.quascirev.2006.02.007

Thornalley, D. J. R., Bauch, H. A., Gebbie, G., Guo, W., Ziegler, M., Bernasconi, S. M., … Yu, J. (2015). A warm and poorly ventilated deep Arctic Mediterranean during the last glacial period. *Science*, *349*(6249), 706–710. http://doi.org/10.1126/science.aaa9554

Thornalley, D. J. R., Elderfield, H., & Mccave, I. N. (2008). Holocene oscillations in temperature and salinity of the surface subpolar North Atlantic. *Nature*, *457*(7230), 711–714. http://doi.org/10.1038/nature07717

Toggweiler, J. R., & Samuels, B. (1998). On the ocean’s large-scale circulation near the limit of no vertical mixing. *Journal of Physical Oceanography*, *28*(9), 1832–1852. http://doi.org/10.1175/1520-0485(1998)028<1832:OTOSLS>2.0.CO;2

Tripati, A. K., Eagle, R. a., Thiagarajan, N., Gagnon, A. C., Bauch, H., Halloran, P. R., & Eiler, J. M. (2010). 13C–18O isotope signatures and “clumped isotope” thermometry in foraminifera and coccoliths. *Geochimica et Cosmochimica Acta*, *74*(20), 5697–5717. http://doi.org/10.1016/j.gca.2010.07.006

Tripsanas, E. K., & Piper, D. J. W. (2008). Late Quaternary stratigraphy and sedimentology of Orphan Basin : Implications for meltwater dispersal in the southern Labrador Sea, *260*, 521–539. http://doi.org/10.1016/j.palaeo.2007.12.016

Tukey, J. W. (1977). *Exploratory Data Analysis*. *Biometrical Journal* (XVI,688 S, Vol. 23). Addison-Wesley Publishing Company Reading, Mass. — Menlo Park, Cal., London, Amsterdam, Don Mills, Ontario, Sydney. http://doi.org/doi:10.1002/bimj.4710230408

Tzedakis, P. C., Drysdale, R. N., Margari, V., Skinner, L. C., Menviel, L., Rhodes, R. H., … Zanchetta, G. (2018). Enhanced climate instability in the North Atlantic and southern Europe during the Last Interglacial. *Nature Communications*, *9*(1). http://doi.org/10.1038/s41467-018-06683-3

Tzedakis, P. C., Lawson, I. T., Frogley, M. R., Hewitt, G. M., & Preece, R. C. (2002). Buffered tree population changes in a Quaternary refugium: Evolutionary implications. *Science*, *297*(5589), 2044–2047. http://doi.org/10.1126/science.1073083

Urey. (1947). The thermodynamic properties of isotopic substances, (582).

Urey, H. C., Lowenstam, H. a., Epstein, S., & McKinney, C. R. (1951). Measurement of Paleotemperatures and Temperatures and the Southeastern United States. *Bulletin of the Geological Society of America*, *62*(April), 399–416. http://doi.org/10.1130/0016-7606(1951)62[399:MOPATO]2.0.CO;2

Usdowski, Michaelis, Bottcher, & Hoefs. (1991). Factors for the oxygen isotope equilibrium fractionation between aqueous and gaseous CO2, carbonic acid, bicarbonate, carbonate, and water (19-degrees-C). *Zeitschrift Fur Physikalische Chemie-International Journal of Research in Physical Chemistry & Chemical Physics*, *170*, 237–249.

Van Kreveld, S. A., Knappertsbusch, M., Ottens, J., Ganssen, G. M., & Van Hinte, J. E. (1996). Biogenic carbonate and ice-rafted debris (Heinrich layer) accumulation in deep-sea sediments from a Northeast Atlantic piston core. *Marine Geology*, *131*(1-2), 21–46. http://doi.org/10.1016/0025-3227(95)00143-3

Van Kreveld, S., Sarnthein, M., Erlenkeuser, H., Grootes, P., Jung, S., Nadeau, M. J., … Voelker, A. (2000). Potential links between surging ice sheets, circulation changes, and the Dansgaard-Oeschger cycles in the Irmiger Sea, 60-80 kyr. *Paleoceanography*, *15*(4), 425–442. http://doi.org/10.1029/1999PA000464

Van-Aken, & Becker. (1997). Hydrography and through-flow in the north-eastern North Atlantic Ocean : the NANSEN project. *Progress in Oceanography*, *38*(97), 297–346.

Vellinga, M., & Wood, R. A. (2002). Global climatic impacts of a collapse of the atlantic thermohaline circulation. *Climatic Change*, *54*(3), 251–267. http://doi.org/10.1023/A:1016168827653

Verbitsky, M., & Saltzman, B. (1995). A diagnostic analysis of Heinrich glacial surge events. *Paleoceanography*, *10*(1), 59–65. http://doi.org/10.1029/94PA02815

Vernal, D., Hillaire-Marcel, & Bilodeau. (1996). Reduced meltwater outflow from the Laurentide ice margin during the Younger Dryas. *Nature*, *381*(JUNE), 346–348.

Vernal, A. De, Hillaire-marcel, C., Peltier, W. R., & Weaver, A. J. (2002). Structure of the upper water column in the northwest North Atlantic : Modern versus Last Glacial Maximum conditions, *17*(4), 1–15. http://doi.org/10.1029/2001PA000665

Vidal, L., Labeyrie, L., Cortijo, E., Arnold, M., Duplessy, J.-C., Michel, E., … van Weering, T. C. E. (1997). Evidence for changes in the North Atlantic Deep Water linked to meltwater surges during the

Heinrich events. *Earth and Planetary Science Letters*, *146*, 13–27. http://doi.org/10.1016/S0012-821X(96)00192-6

Volkmann, R. (2000). Planktic foraminifers in the outer Laptev Sea and the Fram Strait—modern distribution and ecology. *The Journal of Foraminiferal Research*, *30*(3), 157–176.

Wacker, U., Fiebig, J., To, J., Scho, B. R., Friedrich, O., Tu, T., … Joachimski, M. M. (2014). ScienceDirect Empirical calibration of the clumped isotope paleothermometer using calcites of various origins, *141*, 127–144. http://doi.org/10.1016/j.gca.2014.06.004

Wacker, U., & Mainz, J. G. (2013). Clumped isotope analysis of carbonates : comparison of two different acid digestion Clumped isotope analysis of carbonates : comparison of two different acid digestion techniques, (JULY). http://doi.org/10.1002/rcm.6609

Waelbroeck, C., Labeyrie, L., Duplessy, J., Guiot, J., Labracherie, M., Leclaire, H., & Duprat, J. (1998). Improving past sea surface temperature estimates based on planktonic fossil faunas Abstract . A new method of past sea surface temperature reconstruction based on the modem analog technique on the indirect approach has been developed : the revised analog . *Atlantic*, *13*(3), 272–283. http://doi.org/10.1029/98pa00071

Waelbroeck, C., Lougheed, B. C., Vazquez Riveiros, N., Missiaen, L., Pedro, J., Dokken, T., … Ziegler, M. (2019). Consistently dated Atlantic sediment cores over the last 40 thousand years. *Scientific Data*, *6*(1), 165. http://doi.org/10.1038/s41597-019-0173-8

Wang, L., Sarnthein, M., Erlenkeuser, H., Grimalt, J., Grootes, P., Heilig, S., … Pflaumann, U. (1999). East Asian monsoon climate during the Late Pleistocene: High-resolution sediment records from the South China Sea. *Marine Geology*, *156*(1-4), 245–284. http://doi.org/10.1016/S0025-3227(98)00182-0

Wang, Z., Schauble, E. a., & Eiler, J. M. (2004). Equilibrium thermodynamics of multiply substituted isotopologues of molecular gases. *Geochimica et Cosmochimica Acta*, *68*(23), 4779–4797. http://doi.org/10.1016/j.gca.2004.05.039

Ward, J. H. (1963). Hierarchical Grouping to Optimize an Objective Function. *Journal of the American Statistical Association*, *58*(301), 236–244. http://doi.org/10.1080/01621459.1963.10500845

Wary, M., Eynaud, F., Marjolaine, S., Zaragosi, S., Rossignol, L., Malaizé, B., … Charlier, K. (2015). Stratification of surface waters during the last glacial millennial climatic events: a key factor in subsurface and deep water mass dynamics. *Climate of the Past Discussions*, *11*(3), 2077–2119. http://doi.org/10.5194/cpd-11-2077-2015

Watkins, & Hunt, J. D. (2015). A process-based model for non-equilibrium clumped isotope effects in carbonates. *Earth and Planetary Science Letters*, *432*, 152–165. http://doi.org/10.1016/j.epsl.2015.09.042

Watkins, J. M., Hunt, J. D., Ryerson, F. J., & DePaolo, D. J. (2014). The influence of temperature, pH, and growth rate on the δ18O composition of inorganically precipitated calcite. *Earth and Planetary Science Letters*, *404*, 332–343. http://doi.org/10.1016/j.epsl.2014.07.036

Watkins, J. M., Nielsen, L. C., Ryerson, F. J., & DePaolo, D. J. (2013). The influence of kinetics on the oxygen isotope composition of calcium carbonate. *Earth and Planetary Science Letters*, *375*, 349–360. http://doi.org/10.1016/j.epsl.2013.05.054

Weaver, A. J., Sedláček, J., Eby, M., Alexander, K., Crespin, E., Fichefet, T., … Zickfeld, K. (2012). Stability of the Atlantic meridional overturning circulation: A model intercomparison. *Geophysical Research Letters*, *39*(20), 1–8. http://doi.org/10.1029/2012GL053763

Weber, M. E., Mayer, L. a, Bilodeau, G., Hiscott, R. N., & Sediment, A. (2001). Derivation of δ18O from sediment core log data ’ Implications for millennial-scale climate change scale climate change in the Labrador Sea. *Palaeoceanography*, *16*(5), 503–514.

Winter, A., & Siesser, W. (1994). Coccolithophores Cambridge University Press. *Cambridge 242p*.

Wu, G., & Hillaire-Marcel, C. (1994). Oxygen isotope compositions of sinistral Neogloboquadrina pachyderma tests in surface sediments: North Atlantic Ocean. *Geochimica et Cosmochimica Acta*, *58*(4), 1303–1312. http://doi.org/10.1016/0016-7037(94)90383-2

Wunsch, C. (2002). What Is the Predictive Ecology. *Science*, *298*(November), 1179–1180. http://doi.org/DOI 10.1126/science.1079329

Yohai. (1986). High breakdown-point and high efficiency robust estimates for regression. *The Annals of Statistics*, *15*(20), 642–656.

Yokoyama, Y., Lambeck, K., & Deckker, P. De. (2000). Timing of the Last Glacial Maximum from observed sea-level minima, *406*(August), 1998–2001.

York, D. (1968). Least squares fitting of a straight line with crrelated errors. *Earth and Planetary Science Letters*, *5*(Xi), 320–324.

Yoshida, N., Vasilev, M., Ghosh, P., Abe, O., Yamada, K., & Morimoto, M. (2013). Precision and long-term stability of clumped-isotope analysis of CO 2 using a small-sector isotope ratio mass spectrometer, *46*(July 2012), 207–215. http://doi.org/10.1002/rcm.6431

Zaarur, S., Affek, H. P., & Brandon, M. T. (2013). A revised calibration of the clumped isotope thermometer. *Earth and Planetary Science Letters*, *382*, 47–57. http://doi.org/10.1016/j.epsl.2013.07.026

Zahn, R., & Mix, A. C. (1991). Benthic foraminiferal δ18O in the ocean’s temperature-salinity-density field: Constraints on Ice Age thermohaline circulation. *Paleoceanography*, *6*(1), 1–20. http://doi.org/10.1029/90PA01882

Zahn, R., Schönfeld, J., Kudrass, H. R., Park, M. H., Erlenkeuser, H., & Grootes, P. (1997). Thermohaline instability in the North Atlantic during melt water events: Stable isotope and ice-rafted detritus records from core SO75-26KL, Portuguese margin. *Paleoceanography*, *12*(5), 696–710. http://doi.org/10.1029/97PA00581

Zhang, N., Yamada, K., Kano, A., Matsumoto, R., & Yoshida, N. (2018). Equilibrated clumped isotope signatures of land-snail shells observed from laboratory culturing experiments and its environmental implications. *Chemical Geology*, *488*(March), 189–199. http://doi.org/10.1016/j.chemgeo.2018.05.001

Zhang, X., Lohmann, G., Knorr, G., & Purcell, C. (2014). Abrupt glacial climate shifts controlled by ice sheet changes. *Nature*, *512*(7514), 290–294. http://doi.org/10.1038/nature13592

Zhuravleva, A., Bauch, H. A., & Van Nieuwenhove, N. (2017a). Last Interglacial (MIS5e) hydrographic shifts linked to meltwater discharges from the East Greenland margin. *Quaternary Science Reviews*, *164*, 95–109. http://doi.org/10.1016/j.quascirev.2017.03.026

Zhuravleva, A., Bauch, H. A., & Van Nieuwenhove, N. (2017b). Last Interglacial (MIS5e) hydrographic shifts linked to meltwater discharges from the East Greenland margin. *Quaternary Science Reviews*, *164*, 95–109. http://doi.org/10.1016/j.quascirev.2017.03.026

Ziveri, P., Stoll, H., Probert, I., Klaas, C., Geisen, M., Ganssen, G., & Young, J. (2003). Stable isotope “vital effects” in coccolith calcite. *Earth and Planetary Science Letters*, *210*(1-2), 137–149. http://doi.org/10.1016/S0012-821X(03)00101-8

Zweng, Reagan, Seidov, Boyer, Locarnini, Garcia, … Smolyar. (2018). NOAA National Centers for Environmental Information. *World Ocean Atlas 2018. Volume 2: Salinity*, *1*(September), 1–20.